

LANCASTER UNIVERSITY

DOCTORAL THESIS

---

**A study of neutral pion production from  
charged-current  $\nu_{\mu}$  interactions in the T2K  
near detector (Tracker + ECal)**

---

*Author:*  
Dave SHAW

*Supervisor:*  
Dr. Helen O'KEEFFE

*A thesis submitted in fulfillment of the requirements  
for the degree of Doctor of Philosophy*

*in the*

Experimental Particle Physics Group  
Physics Department

June 14, 2018



# Declaration of Authorship

I, Dave SHAW, declare that this thesis titled, “A study of neutral pion production from charged-current  $\nu_\mu$  interactions in the T2K near detector (Tracker + ECal)” and the work presented in it are my own. I confirm that:

- This work was done wholly or mainly while in candidature for a research degree at this University.
- Where any part of this thesis has previously been submitted for a degree or any other qualification at this University or any other institution, this has been clearly stated.
- Where I have consulted the published work of others, this is always clearly attributed.
- Where I have quoted from the work of others, the source is always given. With the exception of such quotations, this thesis is entirely my own work.
- I have acknowledged all main sources of help.
- Where the thesis is based on work done by myself jointly with others, I have made clear exactly what was done by others and what I have contributed myself.

Signed:

---

Date:

---



*“Now I did a job. I got nothing but trouble since I did it, not to mention more than a few unkind words as regard to my character, so let me make this abundantly clear. I do the job. And then I get paid.”*

- Malcom Reynolds



# Abstract

Tokai to Kamioka (T2K) is a long-baseline neutrino oscillation experiment, whose beam is produced at the J-PARC accelerator complex in Tokai, Japan. This beam is sampled by a near detector, ND280, 280 m from the beam origin and a far detector, Super-Kamiokande, 295 km from the beam origin. The primary systematic uncertainties dominating the oscillation analyses for T2K are related to the neutrino beam flux, cross-section and final state interaction uncertainties. Within this thesis, a first attempt is made to develop an analysis in the ND280 highland2 analysis framework which selects  $\nu_\mu$  induced charged-current events containing at least one  $\pi^0$ . In order to investigate potential differences in the conversion channels of the  $\pi^0$  decay  $\gamma$ s, exclusively those which finally convert in the Tracker + ECal regions of the ND280 are considered. The analysis presented selects  $\nu_\mu$  CC $\pi^0$  inclusive events in the ND280, reconstructed in the Tracker + ECal regions, with an efficiency of  $3.2 \pm 0.06\%$  and a purity of  $71.7 \pm 0.71\%$ . The analysis detailed within was carried out using data taken from the T2K run periods 2 - 4, which corresponds to  $55.19 \times 10^{19}$  protons on target (P.O.T). This leads to a prediction of  $262.1 \pm 32.8$  (Stat. + Det. + Flux + Model Error) events being selected for the NEUT Monte-Carlo (MC), and a total of  $316 \pm 17.8$  events being selected within the real data. These figures imply general agreement between Monte Carlo and real data. A number of suggestions for future work are described. It is expected that the implementation of these will allow a total CC $1\pi^0$  inclusive final state cross-section measurement and also allow this work to be used in data samples used to constrain future T2K oscillation analyses. Secondly, a portion of this thesis describes work completed by the author which focused on the implementation of a software solution to a hardware problem, which arised during construction of the ECal modules which form part of the ND280.



# Acknowledgements

In a fair and reasonable universe, this would be by far the longest section of this thesis. However, in this particular universe, I will have to make use of this ever-shrinking single blank page. I am not the same person who began this doctorate four years ago. My years working on the T2K experiment have been formative and horizon broadening. In a professional context, I have been able to work alongside many excellent scientists, and provide (if only minor) contributions to global scientific research. Perhaps more importantly, I have gained friends and experiences, incomparable to those I had before, which despite their singularity can both be essentially grouped into the activities of karaoke (Soho or Tokai!), Station Ramen and Shinchan's.

Thanks to those who made a significant and positive impact to me during the PhD. Without Jon and Matt, there is a reasonable likelihood that I would still be struggling to compile highland2. To Stephen, for your moral and scientific support for the duration, you're the real four chord song. To Luke, to mirror the opening sentence of this section, you might deserve this more than me, but you've already got one, so tough luck. I would like to thank my supervisor, Helen, who has provided consistent encouragement, understanding and tea, and without whom I would certainly not be finishing.

For those in Lancaster, I would like to thank those who have provided me with indispensable help and friendship in recent years. Laura, for allowing me the chance to take this step, and the many students and postdocs who have ensured that I did not spend all of my time in Lancaster either working or drinking alone. Luke, Iain, Andy, Tom, Dom, Steve, Ben, Adam, Charlotte, Amy, Will and Alasdair, you have all provided adequate diversions and kept me more or less on the path to what could be loosely termed, success.

I would like to thank my family and my partner's family for their support throughout, and especially towards the end of, my PhD. I would like to thank my Dad for providing me with the belief that I could achieve what I set my mind to, and my Mum for providing me with the means to do so.

Finally, I would especially like to thank Elle for her constant support. It has not been an easy time for me, and I know that this has inevitably made things difficult for both of us. I appreciate everything that you have had to deal with, and look forward to a (fractionally) more normal time. To the future!



# Contents

<b>Declaration of Authorship</b>	<b>iii</b>
<b>Abstract</b>	<b>vii</b>
<b>Acknowledgements</b>	<b>ix</b>
<b>1 Introduction and Theory of Neutrinos</b>	<b>1</b>
1.1 Introduction	1
1.2 The Standard Model	2
1.3 Postulation and Description	2
1.4 Original Detection	5
1.5 Three Neutrino Flavours	8
1.6 Discrepancy between model and experiment	10
1.7 Neutrino Oscillations	12
1.8 MSW Effect - Matter Enhanced Oscillations	20
1.9 Neutrino Mass	20
1.10 Majorana Neutrinos	23
1.11 Neutrinoless Double Beta Decay	24
1.12 Experimental Searches - Recent and Future	25
1.12.1 Kamiokande/Super-K	25
1.12.2 IceCube	26
1.12.3 Daya Bay	28
1.12.4 SNO and SNO+	30
1.12.5 Katrin	32
1.12.6 $\text{NO}\nu\text{A}$	33
1.12.7 DUNE	35
1.12.8 Hyper-Kamiokande	36
1.12.9 Other Key Neutrino Experiments	37
<b>2 The T2K Experiment</b>	<b>39</b>
2.1 Experiment Running	40
2.2 Physics Goals	41
2.3 J-PARC Accelerator Complex	42
2.3.1 Neutrino Beam Energy	44
2.3.2 Beam Contamination and Helicity Suppression	45
2.4 Super-K Detector	47
2.5 ND280 Complex	51
2.5.1 INGRID	51
2.5.2 ND280	51

	UA1 Magnet . . . . .	52
	$\pi^0$ Detector . . . . .	53
	Time Projection Chambers . . . . .	53
	Fine Grain Detectors . . . . .	53
	Side Muon Range Detector (SMRD) . . . . .	54
	The Electromagnetic Calorimeter Modules (ECals) . . . . .	55
2.6	ND280 Software and Neutrino Interaction Event Generators . . . . .	58
2.6.1	Data Acquisition Software . . . . .	59
2.6.2	ND280 Reconstruction . . . . .	59
2.6.3	Tracker and Global Reconstruction . . . . .	59
2.6.4	ECal Object Reconstruction . . . . .	62
	Hit preparation . . . . .	62
	2D Clustering . . . . .	62
	3D Clustering . . . . .	63
2.6.5	Simulation . . . . .	64
2.6.6	Neutrino Interaction Generation . . . . .	64
	Quasi-Elastic Scattering . . . . .	65
	Resonance Production . . . . .	66
	Deep Inelastic Scattering . . . . .	67
	Neutrino Event Generators . . . . .	67
2.7	T2K Measurements . . . . .	68
<b>3</b>	<b>Reconfiguring Mis-mapped Channels in the ECal</b> . . . . .	<b>73</b>
3.1	Motivation . . . . .	73
3.2	Mis-mapped Channels . . . . .	74
3.3	Relevant ECal Electronics and Software . . . . .	76
3.4	The Process of Determining Mis-mappings . . . . .	78
3.4.1	Plotting the Channel Output for Simple Track Fitted Cosmic Data . . . . .	79
3.4.2	Plotting the Cosmic Data in a 3D Histogram . . . . .	81
3.4.3	Plotting Events Using post-Simple Track Fitted Data . . . . .	84
3.4.4	Plotting Events Using pre-Simple Track Fitted Data . . . . .	86
3.4.5	Noise Reduction - Timing Cuts . . . . .	87
3.4.6	Subtracting the Histograms - Post-STF and Pre-STF . . . . .	88
3.5	Re-mapping the ECal : Validation . . . . .	90
3.6	Results . . . . .	91
3.6.1	Results for RMM0 and RMM1 (DSECal) . . . . .	91
3.6.2	Results for RMM3 (Barrel Top Left ECal) . . . . .	95
3.6.3	Results for RMM4 (Barrel Bottom Left ECal) . . . . .	97
3.6.4	Results for RMM10 and RMM11 Anomaly (Barrel Bottom Right ECal) . . . . .	101
3.7	Reconstruction Efficiency Improvements . . . . .	105
3.8	Conclusion . . . . .	105
<b>4</b>	<b>Selecting <math>\nu_\mu</math> Induced Charged-Current <math>\pi^0</math> Events in FGD1</b> . . . . .	<b>107</b>
4.1	Analysis Motivation . . . . .	107
4.1.1	Brief History of Neutral Pions . . . . .	108

4.1.2	Physics of Charged-Current Neutrino Interactions Producing Neutral Pions . . . . .	108
4.1.3	Measurements of $CC\pi^0$ Production . . . . .	111
4.2	Reconstructing Neutrino Energy in Events . . . . .	113
4.2.1	Signal Definition . . . . .	115
4.3	Data and Monte Carlo Samples . . . . .	118
4.4	highland2 . . . . .	119
4.5	Actions and Cuts in the $CC\pi^0$ Inclusive Analysis . . . . .	123
4.5.1	Selecting the Muon . . . . .	123
4.5.2	Finding True Vertex $\pi^0$ s . . . . .	126
4.5.3	Finding Signal Relevant Objects . . . . .	126
4.5.4	Building $\pi^0$ Decay Photon Candidates . . . . .	132
4.5.5	ECal and Track Object Multiplicity Cut . . . . .	134
4.5.6	ECal Object Energy Cut . . . . .	138
4.5.7	ECal Object to Muon Vertex Distance Cut . . . . .	139
4.5.8	ECal Object MIPeM Cut . . . . .	140
4.5.9	ECal Object Collinearity Cut . . . . .	142
4.5.10	FGD1 Tracks Pion Pull Cut . . . . .	144
4.5.11	TPC Tracks Likelihood Cut . . . . .	149
4.5.12	Build Tracker Decay Photon Candidates . . . . .	152
4.5.13	Tracker Decay Photon Candidate - Muon Vertex Distance Cut . . . . .	154
4.5.14	Tracker Decay Photon Candidate - Collinearity Cut . . . . .	155
4.5.15	Tracker Decay Photon Candidate - Pair Separation Cut . . . . .	157
4.5.16	Tracker Decay Photon Candidate - Pair Invariant Mass Cut . . . . .	160
4.5.17	Make Tracker + ECal $\pi^0$ s Candidates . . . . .	162
4.6	Optimisation of Selection . . . . .	164
4.7	Efficiency and Purity of Selection . . . . .	173
4.7.1	Acting upon Selection Objects in Addition to Events . . . . .	176
4.8	Reconstructed $\pi^0$ Candidates . . . . .	179
4.9	Choosing a $\pi^0$ Candidate . . . . .	181
4.9.1	Half the Photons Away . . . . .	184
<b>5</b>	<b>Systematic Uncertainties</b> . . . . .	<b>189</b>
5.1	Detector Systematics . . . . .	191
5.1.1	Discussion of Completeness and Importance of Detector Systematics . . . . .	194
5.2	Validation of Detector Systematics . . . . .	195
5.2.1	Assessment of Individual and Total Systematics . . . . .	196
	Assessing Systematic Impact on Specific Toy Variables . . . . .	201
	Events Passing The Selection For Each Toy Experiment . . . . .	203
	Sand Muon Contamination . . . . .	205
5.3	Flux Systematics . . . . .	206
5.3.1	Flux Simulation and Tuning . . . . .	206
5.3.2	Flux Uncertainties . . . . .	209
5.4	Neutrino Interaction Uncertainties . . . . .	213
5.4.1	Most Relevant Neutrino Interaction Uncertainties . . . . .	216
5.5	Propagation of Systematic Errors Using T2KReWeight . . . . .	216

<b>6</b>	<b>Results</b>	<b>219</b>
6.1	Overview	219
6.2	Kinematic Distributions	224
6.2.1	$\pi^0$ Invariant Mass	225
6.2.2	$\pi^0$ Momentum	230
6.2.3	$\pi^0 \cos(\theta)$ With Respect to $\nu_\mu$ Beam Direction	234
6.2.4	$\mu^-$ Candidate Momentum	237
6.2.5	$\mu^- \cos(\theta)$ With Respect to $\nu_\mu$ Beam Direction	239
6.3	Summary of Results	241
<b>7</b>	<b>Conclusions and Future Work</b>	<b>243</b>
7.1	Future Work	243
7.1.1	Completion of a full branched analysis	243
7.1.2	Moving Towards Modular $\pi^0$ Analyses	245
7.1.3	Combinatorics and MVAs	245
7.1.4	Running with more data	246
7.1.5	Run Analysis on $\bar{\nu}_\mu$ Data	247
7.1.6	Improved Detector Reconstruction	247
7.1.7	Improved Truth Matching	248
7.1.8	More detailed assessment of systematic errors	249
7.1.9	Cross-section Measurement	250
7.1.10	Including FGD2	251
7.1.11	Run Analysis Using Multiple Neutrino Generators	252
7.2	Conclusions	253
<b>A</b>	<b>Appendix</b>	<b>255</b>

# List of Figures

1.1	The Standard Model of particle physics details all known fundamental particles discovered [2]. . . . .	3
1.2	The measured electron kinetic energy spectrum (blue) and the expected theoretical discrete energy (red) peak for a zero neutrino beta decay [5]. . . . .	4
1.3	The quark flow diagram for beta decay. Illustrating the conversion of a down to an up quark via the flavour changing weak interaction . . . . .	4
1.4	Schematic of The Savannah River Neutrino Detector : Capable of discerning anti-neutrino induced signals and distinguishing them from the background. [9] . . . . .	7
1.5	Feynman diagram showing the three possible particle production mechanisms for an $e^+e^-$ interaction. . . . .	8
1.6	A combined data fit from ALEPH, DELPHI, L3 and OPAL. A model of three light neutrino flavours fits this exceptionally well . . . . .	9
1.7	The well understood proton-proton chain, which takes place in all main sequence, hydrogen burning stars. The expected neutrino flux at the earth can be calculated using this model [20] . . . . .	11
1.8	The energy spectrum of neutrinos emitted by the Sun by detected flux for various astrophysical nuclear processes. Experiments sensitive to those processes are shown at the top . . . . .	12
1.9	The probability of an initially muon neutrino to be measured as another flavour state as it travels. Shown for the short range and long range case. Muon probability is shown in blue, tau neutrino in red and electron neutrino in black . . . . .	17
1.10	The theoretical expected flux vs the detected neutrino flux for a number of experiments. On the far right we can see that the SNO measurements for all neutrino flavours matches up very well with the theory. [35] . . . . .	18
1.11	$-2\Delta\ln(L)$ (equivalent of $\Delta\chi^2$ ) as a function of $\delta_{CP}$ for the normal (black) and inverted (red) mass ordering. The vertical lines show the corresponding allowed 95% confidence interval, calculated using the Feldman-Cousins method. [28] . . . . .	19
1.12	The normal and inverted mass hierarchies for the neutrino mass states. In the normal case the difference between mass states one and two is much smaller than the difference between two and three. The colours in this schematic show the various mass eigenstate contributions to the overall flavour eigenstate [39]. . . . .	21

1.13 A prediction of the energy spectra in electron-neutrino beta decay at Katrin for a model of a 1eV electron-neutrino mass vs a massless electron-neutrino. Tiny deviations can be seen at the endpoint of the spectrum representing the minimum energy taken away by a neutrino (its mass energy) [41]. . . . . 23

1.14 Distribution of events as a function of reconstructed L/E. Data are compared to the best fit and expectation with no oscillations (top) and the ratio of data and best fit to the expectation without oscillations is also shown (bottom). Bands indicate estimated systematic uncertainties [48]. 27

1.15 90% confidence contours of the result in the  $\sin^2 \theta_{23} - \Delta m_{32}^2$  plane in comparison with the ones of the most sensitive experiments. The log-likelihood profiles for individual oscillation parameters are also shown (right and top). A normal mass ordering is assumed [48]. . . . . 28

1.16 Allowed regions for the  $\sin^2(2\theta_{13})$  and  $\Delta m_{ee}^2$  parameter phase space at the 68.3%, 95.5% and 99.7% confidence levels [49]. . . . . 29

1.17 Figure 3.3 shows the PMT outer shell which surrounds the 6 m radius acrylic vessel used to contain the heavy water used as the SNO detector. Two people can be seen at the bottom of the picture to judge the scale [53]. 30

1.18 The three possible neutrino interactions detectable by SNO. A comparison of the rates at which these proceed was used to illustrate oscillation in solar neutrinos. The charged-current process here is only sensitive to  $\nu_e$  interactions, whereas the neutral current reaction is equally sensitive to all flavours of neutrino. [52]. . . . . 31

1.19 Katrin being moved in the land travel portion of it's journey from Deggen-dorf to Karlsruhe [41]. . . . . 32

1.20 The reconstructed energy for far detector selected events. The black data points show the statistical uncertainties. The green histogram corresponds to the predicted unoscillated spectrum. The brown and red histograms represent best fit predictions including certain systematics. The blue points represent the backgrounds. [56]. . . . . 34

1.21 The best-fit (solid black circles) and allowed values (solid black curve) of  $\sin^2 \theta_{23}$  and  $\Delta m_{32}^2$  from this analysis assuming the normal mass hierarchy. The dashed contour lines are results from T2K and MINOS [56]. . . 34

1.22 Schematic of the proposed DUNE experiment, showing the initial accelerator at Fermilab, followed by the near and far detectors. . . . . 35

1.23 A recent proposal for the detector tanks of Hyper-K. Filled with ultra pure water, doped with gadolinium and lined with cutting edge technology PMT detectors [59]. . . . . 37

2.1 Figure showing the total baseline for the T2K experiment. Beginning at the J-PARC accelerator complex in Tokai, Ibaraki and ending at the Super-Kamiokande detector near the city of Hida in the Gifu prefecture [65]. . . . . 39

2.2 Figure showing accumulated protons on target over time (in blue), with neutrino mode (red) and anti-neutrino running (purple). Periods of no running can be seen, in particular two which correspond to the incidents mentioned above [65]. . . . . 40

2.3	A map of Japan with the J-PARC facility in Tokai on the east coast and the Super-K detector 295 km away in Kamioka [25]. . . . .	42
2.4	An aerial view of the J-PARC facility in Tokai. Outlined on the image are different stages of the accelerator used in the T2K experiment. The off-axis neutrinos from this accelerator have an energy range of 600 MeV to 800 MeV [68]. . . . .	43
2.5	A Feynman diagram for pion decay, producing anti-muons and muon neutrinos [69]. . . . .	43
2.6	A plot illustrating the narrow spread of energies at an off-axis angle of $2.5^\circ$ . It also shows the minimum survival probability for $\nu_\mu$ at that off-axis angle and T2K energy range. This represents a maximal chance of oscillation from $\nu_\mu$ to $\nu_e$ [71]. . . . .	45
2.7	T2K beam flux prediction, showing relative flavour fractions for neutrinos and antineutrinos at Super-K. The left plot is for the neutrino beam mode made by focusing the positively charged particles, and the right is for the anti-neutrino mode made by focusing the negative ones [72]. . .	47
2.8	A schematic view of the SuperK detector in Kamioka. Outlined on the image are various important features of the detector used in the T2K experiment [68]. . . . .	48
2.9	Example Super-K event displays from a muon-neutrino interaction (left) and electron-neutrino interaction (right) showing the characteristic sharp and fuzzy Cherenkov radiation rings for these interaction types. [75] . .	48
2.10	An electron ring (left) and a $\pi^0$ fuzzy double ring (right) in the Super-K event display. The similarities of these structures is apparent, although the $\pi^0$ does fully occur within a much shorter time period (as indicated by the z-axis colours) [78]. . . . .	49
2.11	An exploded view of the ND280 detector, where each sub-detector can clearly be seen [80]. . . . .	52
2.12	Reconstructed track range and energy deposited for tracks that stop in FGD1, having traversed more than three FGD1 layers. The data plotted is Run 1 and Run 2 ND280 data, with the expected energy loss curves based on Monte Carlo studies for muons, pions and protons overlaid [85].	55
2.13	The charge-weighted positions of hits in the ECals (not including P0D ECal) are shown. The position of the centre of the beam is to the lower right, and as a result, more events occur in the bottom right of the ECal than the top left. . . . .	56
2.14	The flow of the signal from hitting a scintillator bar in the ECal, to the MPPC, a TFB and finally the RMM, before being read out to Data Acquisition. . . . .	57
2.15	An overview of the various packages which comprise the T2K software, from the data/MC input stages through detector reconstruction and to the final analysis stage. [94] . . . . .	58

2.16	An ND280 data event showing (a) calibrated hits and (b) the globally reconstructed track. The event (number 146768) is from a beam spill trigger in ND280 run 6829, sub-run 34. The beam direction is from left to right. The track traverses the P0D, TPC1, FGD1, TPC2, FGD2, TPC3 and the DsECAL. . . . .	61
2.17	Results for the normal (left) and inverted (right) hierarchies. The areas between coloured lines show allowed regions of $\sin^2(2\theta_{13})$ for each value of $\delta_{CP}$ at 68% (green) and 90% (blue) confidence levels. The black solid line is the best fit value of $\sin^2(2\theta_{13})$ for each assumed value of $\delta_{CP}$ and the mass hierarchy [64]. . . . .	69
2.18	The T2K total flux-averaged cross-section with the NEUT and the GENIE prediction for T2K and SciBooNE. The T2K data point is placed at the flux mean energy. The vertical error represents the total (statistical and systematic) uncertainty, and the horizontal bar represent 68% of the flux at each side of the mean energy. The T2K flux distribution is shown in grey. [109] . . . . .	70
2.19	The total $\nu_e$ CC inclusive cross-section for a wide range of neutrino energy. The T2K data point is placed at the $\nu_e$ flux mean energy. The vertical error represents the total uncertainty, and the horizontal bar represents 68% of the flux each side of the mean. The T2K flux distribution is shown in grey. The NEUT and GENIE predictions are the total $\nu_e$ CC inclusive predictions as a function of neutrino energy. The NEUT and GENIE averages are the flux-averaged predictions [110]. . . . .	71
3.1	Illustrates a summary of the flow of data and processes in the determination of the swaps. Data is represented by ellipses and processes by boxes. STF represents the T2K software, Simple Track Fitter. . . . .	78
3.2	An event display representation of a cosmic muon passing through the ND280. . . . .	79
3.3	Plot showing the number of hits for each channel on TFB7 on RMM1. A clear deficit can be seen at channel 40, indicating a dead channel. The ECal group maintains a list of dead channels. The repeated slopes are due to the physical geometry of the modules and the Trip-T cosmic trigger. . . . .	80
3.4	Plot showing the number of hits for each channel on TFB0 on RMM1. A clear deficit can be seen at channels 12 and 28, indicating a swap. However, this summed over data does not give a definitive indication that these missing hits occurred at the same time. Although, the fact that the deficit for both channels is similar is encouraging. . . . .	81
3.5	The number of hits for each channel for the entire Downstream ECal for hits of hit end -1 in the 3D bar/layer representation. A clear deficit can be seen for a few bins, and four clear non-hit bins illustrating dead channels in white. The even numbered layers on this plot represent bars running from left to right and the odd numbers represent bars running top to bottom, which have been combined to create this plot. . . . .	82

3.6	The number of hits for each channel for the entire Barrel Top Left Module for single ended bars. Every other layer in this view is entirely white, which represents the other orientation of the bar which is readout by other TFBs. Additionally, a number of interesting features can be seen in this plot, including dead channels (white spaces), anomalous or mis-mapped channels and a strange artefact hit deficit near the centre top of the plot, which is due to an intermittently bad channel in the outermost layer of the ECal (Layer 30, Bar 52). . . . .	83
3.7	Shows the simple track fitted particle track for event 1956015 on RMMs 8 and 9. Known dead channels can be seen, plotted with the bin content 60 in this case, the large red block representing an entire dead TFB on RMM9, which could not be used in particle reconstruction. This TFB was lost in the 2011 earthquake. . . . .	84
3.8	A simple-track-fitted particle track for event 3299 in RMM3. The channel plotted as bin content 162 is channel 62 from RMM3 TFB6, plotted with a 100 surplus to differentiate this from the other hits in the track. . . . .	85
3.9	A pre-STF plot for a cosmic event. In this case the bin content is simply the number of hits on that channel. A clear space can be seen and many outlying noise hits, which may contain the mis-mapped channel. . . . .	86
3.10	Left : A cosmic ray event with the bin content as channel number. Right : Most of the noise has been excluded using the integration cycle cut and 50 ns restriction. . . . .	87
3.11	Event 3299 : pre-STF and post-STF histograms. For left post-STF plot, we can see where channel 62 has been artificially superimposed). For the right pre-STF and post noise reduction plot, we see the space where we would expect to see channel 62, and channel 55 being triggered instead on the same TFB. Finally, the result after subtraction is shown. The remaining residual channels are likely to represent a mis-mapping. . . . .	89
3.12	Another two examples of the residual hits left after the subtraction of Post-STF minus Pre-STF has taken place. This case shows that channels 12 and 28 on RMM1 TFB0 are likely to be swapped with each other. This is a persistent case which is reflected later in the results. The black rectangles on the plot outline the area where other same TFB mis-mappings could have occurred. . . . .	89
3.13	Plot showing cosmic hits for the DS ECal (amalgamated RMM0 and RMM1) for the downstream view before re-mapping. . . . .	92
3.14	Plot showing cosmic hits for the DS ECal (amalgamated RMM0 and RMM1) for the downstream view after re-mapping. The improvement can be seen in the fewer low hit channels (in blue), and the increase in the total number of histogram entries. . . . .	92
3.15	Plot showing cosmic hits for the DS ECal (amalgamated RMM0 and RMM1) for the upstream view before re-mapping. . . . .	93
3.16	Plot showing cosmic hits for the DS ECal (amalgamated RMM0 and RMM1) for the upstream view after re-mapping. The improvement can be seen in the fewer low hit channels (in blue), and the increase in the total number of histogram entries. . . . .	93

3.17	Plots illustrating the swap of channel 5 with channel 7 on RMM0 TFB23. There is an equivalent number of spaces in events involving one of these channels as additional hits in the other channel. . . . .	94
3.18	Plots illustrating the swap of channel 61 with channel 63 on RMM1 TFB5. There is an equivalent number of spaces in events involving one of these channels as additional hits in the other channel. . . . .	94
3.19	Plot showing cosmic hits for RMM3 for the single ended bars view before re-mapping. . . . .	96
3.20	Plot showing cosmic hits for RMM3 for the single ended bars view after re-mapping. The improvement here is not as easy to discern by eye due to the complexity of the swaps on RMM3 TFB 6 in the upper left region of Figure 3.19. However, the overall improvement can be seen by the increased number of matched tracks represented by the additional $\sim 27k$ entries in this histogram. . . . .	96
3.21	Plot showing cosmic hits for RMM4 for the single ended bars view before re-mapping. . . . .	99
3.22	Plot showing cosmic hits for RMM4 for the single ended bars view after re-mapping. This plot includes the special case re-mapping for RMM4, discussed in this section. It is clear that the deficit in the TFB34 region (around bar 70) has greatly improved. . . . .	99
3.23	Another example of a vertical line of mis-mapped channels in the RMM4 TFB34 region. . . . .	100
3.24	Another example of a vertical line of mis-mapped channels in the RMM4 TFB34 region. . . . .	100
3.25	Plot Another example of a vertical line of mis-mapped channels in the RMM4 TFB34 region. In this case the particle is moving in the opposite direction. . . . .	101
3.26	Shows all cosmic hits for RMM11 TFB19 after fitting. The channels exhibiting a hit deficit visually suggest mis-mapping in this area, although this turned out not to be the case. . . . .	103
3.27	shows the LI plot for the Barrel Top Right (RMM11 Single Ended Bars). Clearly, an anomalous region can be seen in the centre of this plot, as well as the bottom right. [120] . . . . .	104
3.28	Plot showing cosmic hits for RMM11 for the single ended bars view before re-mapping. Improvement made by re-mapping was negligible, due to the fact that most of the hit deficit artefacts are caused by other phenomena, unrelated to mis-mapping. . . . .	104
3.29	Shows the general improvement seen in RMM3 after subtraction. . . . .	106
4.1	Illustrative Feynman diagrams for the three dominant interaction modes : charged-current quasi-elastic (CCQE), resonant (CCRES) and deep inelastic (CCDIS) neutrino-nucleon interaction processes. Where $\nu_\mu$ is the incoming muon neutrino, $\mu^-$ is the muon, n is the neutron, p is the proton, and X represents a fragmented nucleon. . . . .	110
4.2	Historic $CC1\pi^0$ cross-section measurements compared to the Nuance Monte Carlo generator prediction [90]. . . . .	112

4.3	The MiniBooNE CC1 $\pi^0$ , flux averaged, differential cross-section measurement on a mineral oil target compared to the Nuance Monte-Carlo generator cross-section prediction [91]. . . . .	113
4.4	Neutrino and antineutrino charged-current cross-sections per nucleon for interactions as a function of neutrino energy. Cross-section measurements are shown for quasi-elastic interactions along with the total for all interactions from a selection of experiments. The Nuance [89] Monte Carlo generator cross-section prediction is shown for CCQE, CCRES and CCDIS interactions, along with the total [90]. Figure 2.18 can be used as a comparison to the NEUT MC generator, though in this case not delineated by interaction type. . . . .	114
4.5	Schematic diagram representing a typical Tracker + Tracker $\pi^0$ conversion in the ND280 detector. . . . .	115
4.6	Schematic diagram representing a typical ECal + ECal $\pi^0$ conversion in the ND280 detector. . . . .	116
4.7	Schematic of a charged-current resonant neutrino interaction, producing a $\pi^0$ and its subsequent decay to two photons and ultimately two $e^+e^-$ pairs. . . . .	117
4.8	Schematic diagram representing a typical Tracker + ECal $\pi^0$ conversion in the ND280 detector. Many other conversion topologies are possible for a Tracker + ECal $\pi^0$ and are illustrated in the Appendix (A.1 to A.5) . . . . .	117
4.9	An overview of the data flow when running an analysis using highland2 [123]. . . . .	119
4.10	Momentum of muon candidates which pass the charged-current inclusive selection by interaction type. . . . .	125
4.11	Momentum of muon candidates which pass the charged-current inclusive selection by $\pi^0$ reaction type. . . . .	125
4.12	Number of True $\pi^0$ s in Events Passing the Charged-Current Inclusive Selection . . . . .	127
4.13	The number of tracks with both an FGD1 and TPC component, by number of events. This excludes the main muon track of the reconstructed charged-current interaction. . . . .	128
4.14	The number of true negative tracks with both an FGD1 and TPC component per event. This excludes the main muon track of the reconstructed charged-current interaction. . . . .	128
4.15	The number of true positive tracks with both an FGD1 and TPC component per event. . . . .	129
4.16	The number of reconstructed isolated FGD1 tracks per event. . . . .	131
4.17	The number of ECal DPCs built in each event which pass the muon selection. . . . .	133
4.18	A visual representation of the track and isolated ECal object phase space which delineates each branch. The muon track is counted among NTPC-Tracks, therefore no charged-current muon neutrino events could occupy the bottom row. . . . .	135

4.19	A visual representation of the track and isolated ECal object phase space for CCN $\pi^0$ signal events. All events shown are those which contain at least one $\pi^0$ in the MC truth. The black box shows an area of high signal, followed by the yellow and then red boxes. As the parameter space is expanded, more signal events are retained but this also leads to the inclusion of further backgrounds. The black, yellow and red boxes contain 23.9%, 37.7% and 52.7% of the total signal events respectively. . . . .	136
4.20	A visual representation of the track and isolated ECal object phase space for MC truth Non-CCN $\pi^0$ , i.e. background events. The green, yellow and red boxes contain 12.6%, 17.2% and 19.7% of the total background events respectively. . . . .	137
4.21	A visual representation of the track and isolated ECal object phase space for all events, both signal + background. The percentage of Signal/Signal + Background events in the green, yellow and red boxes is 20.8%, 23.4% and 25.5% respectively. . . . .	137
4.22	Distribution of the energies of all ECal DPC in events which have passed the multiplicity cuts. . . . .	138
4.23	Distribution of the distance of the start position of all ECal DPCs from the $\mu^-$ vertex. . . . .	140
4.24	Values of MIPEM for all ECal DPC passing the unoptimised cut detailed in Subsection 4.5.7. . . . .	141
4.25	Collinearity for all ECal DPCs passing the unoptimised cut detailed in Subsection 4.5.8. . . . .	143
4.26	Full range of PDG codes which make up the FGD1 isolated tracks. This shows a large proportion of electrons and positrons ( $\pm 11$ ), but also large backgrounds from charged pions ( $\pm 211$ ) and protons (2212). The truth categories used are those described in Table 4.3. . . . .	144
4.27	Restricted range of PDGs for FGD1 isolated tracks, showing $\mu^-$ (and anti- $\mu^+$ ) contamination, as well as the electron and positron candidates. The truth categories used are those described in Table 4.3. . . . .	145
4.28	FGD track pion pull of all FGD1 isolated tracks passing the unoptimised cut detailed in Subsection 4.5.14. A large peak can be seen below zero and a smaller bump above. The large peak and the smaller bump are due to the way in which pion pull is calculated for particles of different species. True pions will tend to have a pull around zero (Figure 4.29, electrons and positrons less than zero (Figure 4.31) and protons larger than zero (although a significant portion may be mistaken for pions (Figure 4.29). . . . .	146
4.29	FGD track pion pull of true proton FGD1 isolated tracks passing the unoptimised cut detailed in Subsection 4.5.14. The true protons occupy a broad range of pulls, making some of them more difficult to remove using this variable than other particle species. The double peak is due to protons of certain momenta behaving in a similar fashion to pions in terms of $dE/dx$ . . . . .	147

4.30	FGD track pion pull of true pion FGD1 isolated tracks passing the unoptimised cut detailed in Subsection 4.5.14. This is mostly centred around zero as we would expect for true pions matching the pull hypothesis. We can see that all events which contain a true pion track, necessarily satisfy an ‘Other’ event category. . . . .	148
4.31	FGD track pion pull of true electron and positron FGD1 isolated tracks passing the unoptimised cut detailed in Subsection 4.5.14. This is a narrow peak predominantly below zero. By placing a sensible cut on FGD pion pull it is possible to remove a significant amount of proton background and a small amount of pion background. . . . .	148
4.32	PDG Codes for TPC Electron Candidate Tracks before the cut detailed in Subsection 4.5.11. There are very few backgrounds for the negative tracks, the main one being positrons which are difficult to discern from electrons. . . . .	150
4.33	PDG Codes for TPC Electron Candidate Tracks after the cut detailed in Subsection 4.5.11. The likelihood cut fractionally decreases the positron and pion background, but significantly cuts out a large portion of potential signal. This cut is not worthwhile due to the initially low background. . . . .	150
4.34	PDG Codes for TPC Positron Candidate Tracks before the cut detailed in Subsection 4.5.11. A large proton background and a small pion background can be seen for the positive track candidates. . . . .	151
4.35	PDG Codes for TPC Positron Candidate Tracks after the cut detailed in Subsection 4.5.11. The proton and pion backgrounds which were present prior to the TPC track likelihood cut have been significantly reduced. . . . .	151
4.36	The multiplicity of NTrackerDPCs after all basic tracks cuts described in Section 4.5. Most events remaining contain one Tracker DPC, although non- $\pi^0$ backgrounds are large in this bin. . . . .	153
4.37	Distance to Muon Vertex for all Tracker DPCs Made. This represents all events (signal + background) which are retained after the basic track cuts described in Section 4.5. All optimisation was carried out using a Monte Carlo sample of Run 4 Air of $4.27 \times 10^{20}$ P.O.T . . . . .	154
4.38	Schematic to show function of the tracker DPC collinearity cut. FGD1 and TPC2 are shown, with a illustrative event taking place, producing a $\pi^0$ and other backgrounds. The converted pair (in blue) which has vector direction b (in yellow) should be close to the constructed vector direction a (also in yellow). . . . .	155
4.39	Collinearity of all tracker DPCs passing the muon distance cut. Most DPC candidates have a collinearity close to one, with event contributions being uniform for all values. No immediate analytical distinction can be seen for this variable. . . . .	156
4.40	Schematic to show function of the tracker DPC pair separation cut. The pair converted in the lower part of TPC2 will have track start positions which are very close together. Whereas pairing up the negative pion and the upper electron track would result in a very large pair separation. . . . .	158

4.41	Pair separation for all tracker DPC candidates passing the collinearity cut. There is a large peak in the first bin, containing separation values of 0 to 40 mm. In terms of event category, the distribution seems to be even for all values, however this is somewhat meaningless and needs to be analysed in terms of a true DPC rather than a true $\pi^0$ event. . . . .	159
4.42	Pair invariant mass for all tracker DPC candidates passing the pair separation cut. Most DPC candidates have a reconstructed invariant mass of $< 200 \text{ MeV}/c^2$ . The event category distribution is uniform. . . . .	161
4.43	All possible $\pi^0$ s candidates built for this sample for the unoptimised selection. This plot illustrates perfectly that the selection is in dire need of optimisation in order to construct only reasonable $\pi^0$ candidates from which to choose. The fact that some events contain as many as 28 $\pi^0$ candidates illustrates the combinatoric problem appositely. . . . .	162
4.44	Reconstructed mass of all possible $\pi^0$ s candidates built for this sample for the unoptimised selection. This has the expected wide gaussian profile and uniform event type distribution. . . . .	163
4.45	Reconstructed mass of the highest momentum $\pi^0$ s candidate built for this sample for the unoptimised selection. Selecting only the highest momentum $\pi^0$ in each event does not help to identify true $\pi^0$ candidates. . . . .	163
4.46	Momentum Optimisation for FGD1 + TPC Tracks in the Selection. Signal is shown in blue and background in red, illustrating that generally $e^+$ and $e^-$ particles have lower momentum than others. This does seem like a good candidate for a cut to preferentially retain signal over background. Values from the optimisation algorithm are superimposed on to the plot as text. . . . .	168
4.47	Optimisation of the Pair Separation for True and False Tracker DPCs. The majority of the signal exists for DPCs whose pair constituents are $< 20$ mm apart. Values from the optimisation algorithm are superimposed on to the plot as text. . . . .	170
4.48	Optimisation of the Pair Invariant Mass for True and False Tracker DPCs. The amount of signal increases as the value of pair invariant mass tends to zero, with a reasonable maximum value of $40 \text{ MeV}/c^2$ calculated by the optimisation process. Values from the optimisation algorithm are superimposed on to the plot as text. . . . .	171
4.49	Optimisation of the Collinearity for True and False Tracker DPCs. Most DPC candidates for both signal and background have a value close to one. At extremely fine binning there is some separation, although this may be beyond the capability of the detector to resolve accurately. Values from the optimisation algorithm are superimposed on to the plot as text. . . . .	172
4.50	Efficiency and Purity of the Selection After Optimisation. The steady increase in signal event purity at each cut stage can be seen. This is accompanied by significant drops in signal efficiency, which is unavoidable for this type of analysis. Some cuts which do not seem to affect event purity, actually serve to reduce combinatoric backgrounds and increase object purity. . . . .	174

4.51	Accompanying plot to Table 4.7 showing the number of events surviving each selection cut in data and MC. The selection here starts after the Charged-Current pre-selection has been applied. There is very good agreement between data and MC throughout for the Run 4 Air sample (normalised to $1.76 \times 10^{20}$ P.O.T).	176
4.52	Reconstructed invariant mass of all $\pi^0$ s passing the selection. This appears to have the expected peak at the known $\pi^0$ mass of $135 \text{ MeV}/c^2$ , which implies that the actual $\pi^0$ objects are being correctly built. There is an associated width which could be due to detector resolution smearing or wrong combinations of $\pi^0$ decay particles. Additionally, the 80.4% purity can be seen, with the background event contributions being flat (not peaked at $135 \text{ MeV}/c^2$ ).	179
4.53	Reconstructed invariant mass of all true $\pi^0$ s passing the selection. This shows a very well defined peak as expected. However, this does illustrate that even for true $\pi^0$ s there is an associated width, and a contribution from 'Other', due to neutral current interactions.	180
4.54	Reconstructed invariant mass of all false $\pi^0$ s passing the selection. A broad peak built from the incorrect combination of $\pi^0$ decay products in (mostly) actual $\pi^0$ events. This represents one of the biggest hurdles to overcome in this and future $\pi^0$ analyses.	180
4.55	The $\pi^0$ candidate with the invariant mass closest to that of the known $\pi^0$ mass in a given event is chosen and plotted here. We see the characteristic $\pi^0$ mass peak around $135 \text{ MeV}/c^2$ . Of course we cannot use this to measure the $\pi^0$ mass as we are now biased, but it is a useful metric which helps to correctly identify the true $\pi^0$ .	183
4.56	Reconstructed $\pi^0$ candidates where both photons are from a true $\pi^0$ . For all candidates within the 0 to $500 \text{ MeV}/c^2$ range.	185
4.57	Reconstructed $\pi^0$ candidates where exactly one photon is from a true $\pi^0$ . For all candidates within the 0 to $500 \text{ MeV}/c^2$ range.	185
4.58	Reconstructed $\pi^0$ candidates where neither photon is from a true $\pi^0$ . For all candidates within the 0 to $500 \text{ MeV}/c^2$ range. This is low statistics (due to the high event purity of the selection) and has an irregular structure. These objects are mostly built from 'Other' particles.	186
5.1	The distribution of all muon candidates passing the selection for the entirety of the Monte Carlo used for this analysis result ( $87.39 \times 10^{20}$ P.O.T)	197
5.2	The detector error which defines secondary pion interactions is expectedly high in this analysis (due to pions providing a major background to the positive tracks being built to form decay photon candidates), however it is reasonably stable at lower energies. The total relative error contribution from this source is $\sim 5\%$	198
5.3	The secondary interaction proton detector error becomes erratic at high momenta, due to low statistics. Perhaps limiting the upper momentum of the muon candidate to 2 GeV would be beneficial. The error contribution from this source is $\sim 3\%$	198

5.4	TPC Track Efficiency is an unavoidable systematic in any T2K analysis which utilises the tracker. The error here is relatively uniform except at very high momenta, which is likely due to the low number of events in that bin. The overall contribution from this source is ( $\sim 3\%$ ) . . . . .	199
5.5	FGD Track Efficiency turns out to be the highest source of detector uncertainty in this analysis ( $\sim 6\%$ ). This is not too surprising given that all track objects used must begin within FGD1. In future it should be considered whether the statistics boost gained from reconstructing $\pi^0$ decay products which fully convert in FGD1 (FGDIso DPCs) is well-motivated, and worth the added error. . . . .	199
5.6	The relative error contribution from the determination of ECal PID. This is one of the highest sources of detector systematic in this analysis, due to the importance of ECal objects. The averaged error contribution is $\sim 5\%$ , which potentially could be mitigated by limiting the analysis to muon candidates with momentum of 2 GeV and under. . . . .	200
5.7	The total relative error contribution from all sources of detector error. The total averaged differential error for this is in agreement with other methods, at $\sim 11\%$ ( $\sim \pm 5.5\%$ ). Once again there is a dramatic increase in error for events with a high momenta muon candidate. In a future analysis it could be beneficial to cut off this high muon energy tail, although in reality it is unlikely to contain many selected events. . . . .	201
5.8	The reconstructed FGD track pion pull for the first four toys, variation in the shape and the number of events retained can be seen. . . . .	204
5.9	The number of events passing the FGD track pion pull for each toy was plotted. This variation illustrates that the systematics are having an effect, and that it is within expectations. We would not expect estimate of the error from this figure to be in-keeping with the overall $\sim 11\%$ ( $\sim \pm 5.5\%$ ), as this is early in the selection and only takes into account systematics which affect this specific variable. However, it is reasonably Gaussian, with a mean of 1050, a standard deviation of 4.5 and a variance of 20.6. . . . .	205
5.10	The number of events passing the entire selection for 500 toy throws of the experiment (all detector systematics switched-on) is shown. A reasonably gaussian distribution can be seen, centred around a mean of $\sim 217$ events. The weight contribution to each toy is shown, with the integral of all events summing to one. . . . .	206
5.11	The Fluka2008.3b neutrino flux prediction for the ND280 detector for $\nu_{\mu}$ , re-weighted to the NA61 target data. The contribution from pion, kaon and muon decays to the total neutrino flux are shown [132]. . . . .	207
5.12	The final tuning weights for the flux predictions at the ND280 for $\nu_{\mu}$ . The secondary pion tuning is substantial, and without it the neutrino flux would be considerably underestimated [70]. . . . .	209
5.13	The fractional error for the total neutrino flux uncertainty, for a wide range of energy. Also shown are the individual contributions from three primary sources of uncertainty : hadronic interactions, beam parameters and horn current [70]. . . . .	211

5.14	Correlations of the flux for a given flavor, energy and detector. The binning on the y-axis is identical to the binning on the x-axis. [70] . . . . .	211
5.15	Correlations of the flux uncertainties for a range of neutrino energy. . . . .	212
5.16	Correlations of the interaction and FSI uncertainties considered in this analysis. . . . .	215
6.1	The number of events in data and MC after each selection cut for $87.39 \times 10^{20}$ NEUT T2K Production 6B MC P.O.T and $55.19 \times 10^{19}$ T2K Real Data Production (RDP) P.O.T. The first two cuts, which can be seen in Table 6.1 have been intentionally removed from this plot in order to focus more clearly on the later stages of the selection. As stated, these first two stages show a large data/MC disparity, which is largely rectified by the quality and fiducial volume cuts. . . . .	222
6.2	The ratio of remaining events in data and MC after each selection cut for $87.39 \times 10^{20}$ NEUT T2K Production 6B MC P.O.T and $55.19 \times 10^{19}$ T2K Real Data Production (RDP) P.O.T. The first two cuts, which can be seen in Table 6.1 have been intentionally removed from this plot in order to focus more clearly on the later stages of the selection. It can clearly be seen that the later stages of the selection, specifically the TPC Tracks Likelihood cut, introduce a data/MC disparity. The post-selection cut which selects the $\pi^0$ candidate is not shown, but brings the ratio to 1.21, as outlined in the results. . . . .	223
6.3	Reconstructed invariant mass distribution of $\pi^0$ candidates passing the selection, scaled to $55.19 \times 10^{19}$ P.O.T of RDP from T2K Runs 2-4. Compared with $87.39 \times 10^{20}$ P.O.T of NEUT Monte Carlo from T2K Runs 2-4 Production 6B. The total RDP statistical error corresponds to $\pm 8.6\%$ and the total MC error is $\pm 12.5\%$ . . . . .	225
6.4	Reconstructed invariant mass distribution of $\pi^0$ candidates passing the selection, scaled to $55.19 \times 10^{19}$ P.O.T of RDP from T2K Runs 2-4. Compared with $87.39 \times 10^{20}$ P.O.T of NEUT Monte Carlo from T2K Runs 2-4 Production 6B. Only the MC flux source of error is shown, which corresponds to $\pm 5.8\%$ . . . . .	227
6.5	Reconstructed invariant mass distribution of $\pi^0$ candidates passing the selection, scaled to $55.19 \times 10^{19}$ P.O.T of RDP from T2K Runs 2-4. Compared with $87.39 \times 10^{20}$ P.O.T of NEUT Monte Carlo from T2K Runs 2-4 Production 6B. Only the MC interaction source of error is shown, which corresponds to $\pm 6.7\%$ . . . . .	228
6.6	Reconstructed invariant mass distribution of $\pi^0$ candidates passing the selection, scaled to $55.19 \times 10^{19}$ P.O.T of RDP from T2K Runs 2-4. Compared with $87.39 \times 10^{20}$ P.O.T of NEUT Monte Carlo from T2K Runs 2-4 Production 6B. Only the MC FSI source of error is shown, which corresponds to $\pm 6.9\%$ . . . . .	228
6.7	Reconstructed invariant mass distribution of $\pi^0$ candidates passing the selection, scaled to $55.19 \times 10^{19}$ P.O.T of RDP from T2K Runs 2-4. Compared with $87.39 \times 10^{20}$ P.O.T of NEUT Monte Carlo from T2K Runs 2-4 Production 6B. Only the MC detector source of error is shown, which corresponds to $\pm 5.1\%$ . . . . .	229

6.8	Reconstructed invariant mass distribution of $\pi^0$ candidates passing the selection, scaled to $55.19 \times 10^{19}$ P.O.T of RDP from T2K Runs 2-4. Compared with $87.39 \times 10^{20}$ P.O.T of NEUT Monte Carlo from T2K Runs 2-4 Production 6B. Only the MC statistical source of error is shown, which corresponds to $\pm 1.5\%$ . . . . .	229
6.9	Reconstructed momentum distribution of $\pi^0$ candidates passing the selection, scaled to $55.19 \times 10^{19}$ P.O.T of RDP from T2K Runs 2-4. Compared with $87.39 \times 10^{20}$ P.O.T of NEUT Monte Carlo from T2K Runs 2-4 Production 6B. . . . .	230
6.10	Reconstructed $\cos(\theta)$ distribution of $\pi^0$ candidates passing the selection, scaled to $55.19 \times 10^{19}$ P.O.T of RDP from T2K Runs 2-4. Compared with $87.39 \times 10^{20}$ P.O.T of NEUT Monte Carlo from T2K Runs 2-4 Production 6B.	234
6.11	Reconstructed momentum distribution of $\mu^-$ candidates passing the selection, scaled to $55.19 \times 10^{19}$ P.O.T of RDP from T2K Runs 2-4. Compared with $87.39 \times 10^{20}$ P.O.T of NEUT Monte Carlo from T2K Runs 2-4 Production 6B. . . . .	237
6.12	Reconstructed $\cos(\theta)$ distribution of $\mu^-$ candidates passing the selection, scaled to $55.19 \times 10^{19}$ P.O.T of RDP from T2K Runs 2-4. Compared with $87.39 \times 10^{20}$ P.O.T of NEUT Monte Carlo from T2K Runs 2-4 Production 6B.	239
A.1	This represents the ideal circumstance for a ND280 Tracker+ECal $\pi^0$ conversion, where there is a clear TPC Pair which forms a pair. These tracks may have FGD and TPC components, but it is possible that the photon has entirely converted in the TPC, thus giving the tracks only TPC components. . . . .	257
A.2	In this instance the Tracker DPC has fully converted in FGD1 and the tracks produced by this photon are also entirely contained there. Although this is a pair, it may not result in building an ideal $\pi^0$ candidate, due to the inferior reconstruction capabilities when compared with the TPC. For example, charge reconstruction is not reliable in the FGD. . . .	257
A.3	In this instance the Tracker DPC photon has converted in FGD1 but one of the resultant tracks is fully contained within FGD1 and the other in TPC2. The underlying idea is that these are from the same pair and can be reconstructed as such. Additional complications do arise due to the dead space between the subdetectors, as well as the lack of reliable charge reconstruction in the FGD. An isolated track in the FGD (passing cuts) will be matched up with all available tracks in the TPC to form Tracker DPC Pair candidates. . . . .	258
A.4	In this instance the assumption is being made that the photon conversion has resulted in an asymmetric electron/positron pair, such that only one of the tracks is reconstructed (and the other missed due to a sufficient number of track segments in the FGD+TPC). The particular DPC built from this track will not be subject to a number of the cuts which can act only on pairs, meaning that it is likely to build a less reliable $\pi^0$ object. .	259

A.5	In this instance the assumption is being made that the photon conversion has resulted in an asymmetric electron/positron pair, such that only one of the tracks is reconstructed (and the other missed due to a sufficient number of track hits in the FGD). This topology would likely not result in a good Tracker DPC and thus $\pi^0$ object, due to the lack of a complementary pair track and inferior reconstruction. . . . .	259
A.6	Reconstructed invariant mass of highest momentum $\pi^0$ candidates passing the selection. . . . .	260
A.7	Reconstructed invariant mass of randomly selected $\pi^0$ candidates passing the selection. . . . .	260
A.8	Reconstructed invariant mass of $\pi^0$ candidates passing the selection which are selected by the nMVA. . . . .	260
A.9	Reconstructed invariant mass of $\pi^0$ candidates passing the selection, whose ECal DPC has the highest energy. . . . .	261
A.10	Reconstructed invariant mass of $\pi^0$ candidates passing the selection, whose Tracker DPC has the smallest TPC pair invariant mass. . . . .	261
A.11	Reconstructed invariant mass of $\pi^0$ candidates passing the selection, whose Tracker DPC has the smallest TPC pair separation. . . . .	261
A.12	Reconstructed momentum of highest momentum $\pi^0$ candidates passing the selection. . . . .	262
A.13	Reconstructed momentum of randomly selected $\pi^0$ candidates passing the selection. . . . .	262
A.14	Reconstructed momentum of $\pi^0$ candidates passing the selection, which are selected by the nMVA. . . . .	262
A.15	Reconstructed momentum of $\pi^0$ candidates passing the selection, whose ECal DPC has the highest energy. . . . .	263
A.16	Reconstructed momentum of $\pi^0$ candidates passing the selection, whose Tracker DPC has the smallest TPC pair invariant mass. . . . .	263
A.17	Reconstructed momentum of $\pi^0$ candidates passing the selection, whose Tracker DPC has the smallest TPC pair separation. . . . .	263
A.18	Two dimensional distribution of the reconstructed invariant mass vs reconstructed momentum for selected $\pi^0$ candidates passing the selection in the NEUT MC. There does not appear to be any obvious sources of discrepancy between the MC and data, although this would benefit from higher statistics. . . . .	264
A.19	Two dimensional distribution of the reconstructed invariant mass vs reconstructed momentum for selected $\pi^0$ candidates passing the selection in the observed data. There does not appear to be any obvious sources of discrepancy between the MC and data, although this would benefit from higher statistics. . . . .	264
A.20	Two dimensional distribution of the reconstructed momentum vs reconstructed $\cos(\theta)$ (w.r.t to $\mu^-$ direction) for selected $\pi^0$ candidates passing the selection in the NEUT MC. There does not appear to be any significant sources of discrepancy between the MC and data, although this would benefit from higher statistics. . . . .	265

A.21 Two dimensional distribution of the reconstructed momentum vs reconstructed $\cos(\theta)$ (w.r.t to $\mu^-$ direction) for selected $\pi^0$ candidates passing the selection in the observed data. There does not appear to be any significant sources of discrepancy between the MC and data, although this would benefit from higher statistics. . . . .	265
A.22 Two dimensional distribution of the reconstructed momentum vs reconstructed $\cos(\theta)$ (w.r.t to the assumed neutrino beam direction) for all $\mu^-$ candidates passing the selection in the NEUT MC. There does not appear to be any significant sources of discrepancy between the MC and data, although this would benefit from higher statistics. . . . .	266
A.23 Two dimensional distribution of the reconstructed momentum vs reconstructed $\cos(\theta)$ (w.r.t to the assumed neutrino beam direction) for all $\mu^-$ candidates passing the selection in the observed data. There does not appear to be any significant sources of discrepancy between the MC and data, although this would benefit from higher statistics. . . . .	266

# List of Tables

1.1	Known values of neutrino mixing parameters for a normal neutrino mass hierarchy. All values taken from the PDG (2016) [37]. . . . .	20
3.1	Name, RMM number and number of TFBS for each of the ECal modules. *Two of these TFBS were lost in the 2011 earthquake. . . . .	76
3.2	Mis-mapped Channels in the Downstream ECal module. 6 Mis-mappings are listed with the determined correct mapping. . . . .	95
3.3	Mis-mapped Channels in the Barrel Top Left ECal. 14 Mis-mappings are listed with the determined correct mapping. . . . .	97
4.1	The P.O.T of the NEUT Monte Carlo samples used for this analysis. . . . .	118
4.2	The P.O.T of the data samples used for this analysis. . . . .	118
4.3	Definitions of the signals which define the subsets for the ‘reactionpi0’ drawing category, used throughout this analysis. All particles described are those present in the final state. ‘Other’ particles includes : charged-pions, neutral etas, neutral rhos, kaons, electrons, positrons and anti-muons. Percentage of events is passing muon selection. . . . .	122
4.4	The number of minimum track and isolated ECal object requirements for each branch. *NTracks is all tracker objects (TPC and FGD) and includes the main muon track. . . . .	134
4.5	Selection Optimisation Results - Figure Of Merit : Efficiency $\times$ Purity <sup>2</sup> . . . . .	166
4.6	Selection Second Optimisation Results - Figure Of Merit : Efficiency $\times$ Purity <sup>2</sup> . . . . .	169
4.7	The number of events in data and MC after each selection cut. All normalised to the P.O.T of the available Run 4 Air RDP - $1.76 \times 10^{20}$ . . . . .	175
4.8	Breakdown of the Monte Carlo for Run 4 Air Optimisation Sample (Normalised to $1.76 \times 10^{20}$ P.O.T as in Table 4.7 and Figure 4.51) in terms of the possible reactionpi0 event categories. Illustrated at each stage in the selection process to convey the effect which each cut has on the relative signal and background contributions. Full descriptions of each of the contributing categories can be found in Table 4.3. . . . .	177
4.9	Probability of correctly identifying the true $\pi^0$ in a selected event. All values subject to a statistical error of $\pm 6.7\%$ for this sample. These values may seem low as often only one of the two true $\pi^0$ decay photons are correctly identified. . . . .	184

5.1	Detector Systematics in the $\nu_{\mu}\text{CC}\pi^0$ Inclusive Selection. Each of the fundamental error sources was varied to $\pm 1\sigma$ uncertainty level. It is detailed whether each error source is applied at the object or event level, and implemented as a variation or weight systematic. This total relative detector error translates to a propagated associated uncertainty of $\sim \pm 5.1\%$ on the final result. . . . .	193
5.2	Monte Carlo statistical errors in the muon momentum bins for candidates passing the selection. . . . .	197
5.3	Parameters and relevant values of the NIWG group 2015 model parameter covariance matrix. The values shown here are consistent with those plotted in the model error covariance matrix used for this analysis. More detail can be found in the T2K technical note [137]. . . . .	214
5.4	All sources of systematic error which affect the NEUT Monte Carlo are shown. These are separated into four major sources, which are all similar in scale. . . . .	217
6.1	The number of events in data and MC after each selection cut for $87.39 \times 10^{20}$ NEUT T2K Production 6B MC P.O.T and $55.19 \times 10^{19}$ T2K Real Data Production (RDP) P.O.T. This represents 0.66% of the events passing the quality and fiducial cuts for the RDP and 0.59% for the NEUT MC. . . .	221
6.2	The statistical error for the real data production is shown here. This is comparable to the Monte Carlo errors, and can be mitigated in future by the use of more data. . . . .	241
6.3	All sources of systematic error which affect the NEUT Monte Carlo are shown. These are separated into five major sources, with comparable contributions from all stated sources aside from MC statistical. . . . .	241
A.1	Selection Optimisation Results - Figure Of Merit : Efficiency $\times$ Purity . .	255
A.2	Selection Second Optimisation Results - Figure Of Merit : Efficiency $\times$ Purity . . . . .	256
A.3	Mis-mappings found in the work described in Chapter 3. . . . .	267

## Chapter 1

# Introduction and Theory of Neutrinos

### 1.1 Introduction

This thesis sets its focus directly upon the elusive particle, the neutrino, and its place in historical and modern experimental physics. Chapter one focuses on the history of neutrinos in the 20th and 21st centuries, including an overview of experiment and theory. This is followed by a more in-depth look at a specific neutrino experiment, T2K (Tokai to Kamioka) in chapter two. The T2K experiment began its search for neutrino oscillations in 2006, and it is data taken by this experiment which is the primary focus of this thesis. Chapter three contains a detailed look at work completed by the author, which focused on one subdetector of the T2K near detector, the Electromagnetic Calorimeter. Chapter four contains a comprehensive account of the physics analysis undertaken using data from the near detector, an investigation of the charged-current muon neutrino interactions in which one or more neutral pions are produced. This account includes a description of the stages of development, optimisation and results of the analysis. Chapter five contains a thorough treatment of the systematic uncertainties associated with this analysis. This is followed by the analysis results in chapter six, which contains several distributions of relevant reconstructed kinematic variables and a comparison of data and Monte Carlo for events retained by the analysis selection. Finally, the work is summarised, with pertinent discussion points and conclusions in chapter seven, which

also contains a description of various avenues for future work.

## 1.2 The Standard Model

The Standard Model of particle physics is widely accepted to be one of the greatest achievements of modern physics, and provides a description of the fundamental elementary particles which comprise all known matter and energy within the universe, the current notable exception being dark matter. A graphical representation of the Standard Model is shown in Figure 1.1, split into groups for quarks, leptons and bosons. Historically the neutrinos described in the Standard Model are massless, however research which illustrated a phenomena described as ‘neutrino oscillation’ [1] indicated that neutrinos have a small but finite mass. The nature of the neutrino is discussed at length in this chapter, with attention paid to their production, behaviour and detection.

A neutrino is an electrically neutral, weakly interacting subatomic particle. Neutrinos are produced in radioactive decay, certain nuclear reactions (such as those which occur in our Sun), cosmic ray interactions, supernovae and accelerators. These sources of neutrinos help us to gain a further understanding of their properties. There are three active types of neutrino: electron, muon and tau, which correspond to the three charged leptons of the Standard Model. A neutrino of a given flavour can be produced in reactions involving charged leptons of the same flavour.

## 1.3 Postulation and Description

The neutrino was first postulated by Wolfgang Pauli in 1930. Pauli had already made great contributions to physics even before this point, and continued to do so, possibly most notably in the Pauli Exclusion Principle, as well as leading a historically fascinating life. One of Pauli’s most famous achievements would come in the form of the postulation of a seemingly undetectable particle. The neutrino’s tiny mass, at the time

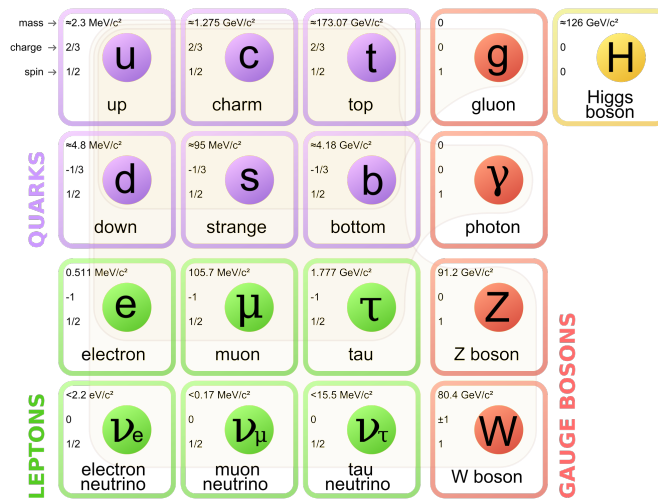


FIGURE 1.1: The Standard Model of particle physics details all known fundamental particles discovered [2].

thought to be zero, and lack of electrical charge severely decrease its chance of interacting with matter, as it cannot interact via the electromagnetic force. Pauli's 'desperate remedy' led him to humourously exposit,

*'I have done a terrible thing. I invented a particle that cannot be detected.'* W.

Pauli [3].

Prior to Pauli's postulate, it had been noted that the nuclear process, beta decay seemed to defy a number of conservation laws, with apparent violation of the conservation of energy, momentum and angular momentum. It was clearly shown that the emitted electron in beta decay was allowed to have a continuous spectrum of energies, as opposed to a well defined discrete peak, which would be expected in a two-body decay. Despite his outward misgivings, Pauli even going so far as to wager a case of champagne against the discovery of the neutrino [4], the particle hypothesised would solve the aforementioned problems.

Shortly after Pauli's initial postulation of the neutrino, the Italian physicist Enrico Fermi entered the metaphorical playing field. Fermi was able to develop a mathematical formulation which described the production of the neutrino via his 'weak force', otherwise known as Fermi's Interaction [6], which was capable of converting a neutron

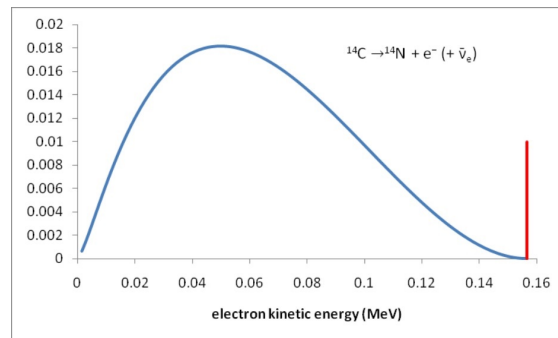


FIGURE 1.2: The measured electron kinetic energy spectrum (blue) and the expected theoretical discrete energy (red) peak for a zero neutrino beta decay [5].

to a proton, with the additional emission of an electron and an anti-neutrino, in a process known as neutrino beta decay. This atomic conversion is achieved via the weak interaction, where a down type quark in the bound neutron becomes an up quark, resulting in a bound proton, as shown in Figure 1.3.

Even at this early stage in neutrino physics it was facing an uphill struggle, with the journal ‘Nature’ replying to Fermi’s submission with the following,

*‘because it contained speculations too remote from reality to be of interest to the reader’ [7].*

though they later admitted that the rejection was one of the great editorial blunders in its history.

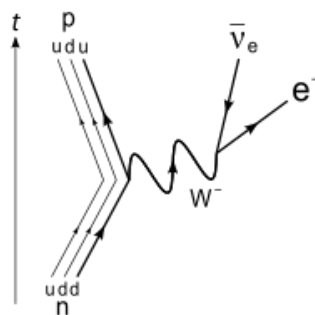


FIGURE 1.3: The quark flow diagram for beta decay. Illustrating the conversion of a down to an up quark via the flavour changing weak interaction [8].

Not long after this formulation, Hans Bethe and Robert Bache suggested an interaction by which the neutrino could potentially be observed.

*'It seems practically impossible to detect neutrinos in the free state...There is only one process which neutrinos can certainly cause. That is the inverse beta process, consisting of the capture of a neutrino by a nucleus together with the emission of an electron (or positron).'* H.Bethe, R.Bacher[9]

The process of inverse beta decay would give hope to experimentalists wishing to detect the neutrino. However, given the strength of the weak force, an interaction was still extremely unlikely, with an estimated light-year of lead required in order to stop a single neutrino. This low probability of interaction is a fundamental constant of reality, which still plagues neutrino physicists today, leading to a community understanding of 'intense sources, big detectors'.

## 1.4 Original Detection

A number of experiments have been built to directly detect the neutrino and discern its properties. The first experiment to successfully detect the neutrino was the Cowan-Reines experiment in 1956 [10]. Famously, and perhaps setting the tone for work in the field of neutrino physics, they did not receive the Nobel Prize until 1995, nearly 40 years later. As stated above, the process of inverse beta decay was the key to detecting the first neutrinos.

Fred Reines was a member of the Theoretical Division of the Manhattan Project at Los Alamos from 1944. Scientists working on the development of nuclear weapons would use this period as an opportunity to study new physical phenomena, utilising the unique conditions which can be generated by fission chain reactions in atomic nuclei. Clyde Cowan joined Reines and in 1951 they set upon building 'Project Poltergeist', an unlikely experiment requiring the detonation of a 20 kilo-ton nuclear bomb. Perhaps the familiarity of working with nuclear weapons on a daily basis was explanation for this ambitious project, an assertion strengthened by Reines' notes.

*'Anyone untutored in the effects of nuclear explosions would be deterred by the challenge of conducting an experiment so close to the bomb, but we knew otherwise from experience and pressed on.'* F. Reines [9]

This project was ultimately abandoned in favour of a more conventional experiment, with much more repeatability. J.M.B. Kellogg suggested that by using a nuclear fission reactor, Cowan and Reines could search for a steady signal of anti-neutrinos rather than those from a single signal blast. The Savannah River neutrino detector was built in 1955. The target of this detector was a 200 litre tank of water, in which anti-neutrinos would interact with the protons to produce positrons and neutrons. This was doped with cadmium chloride in order to capture neutrons on cadmium nuclei. In an effort to reduce backgrounds, a coincidence method using three liquid scintillation veto chambers was used. The layout of this set up is shown in Figure 1.4.

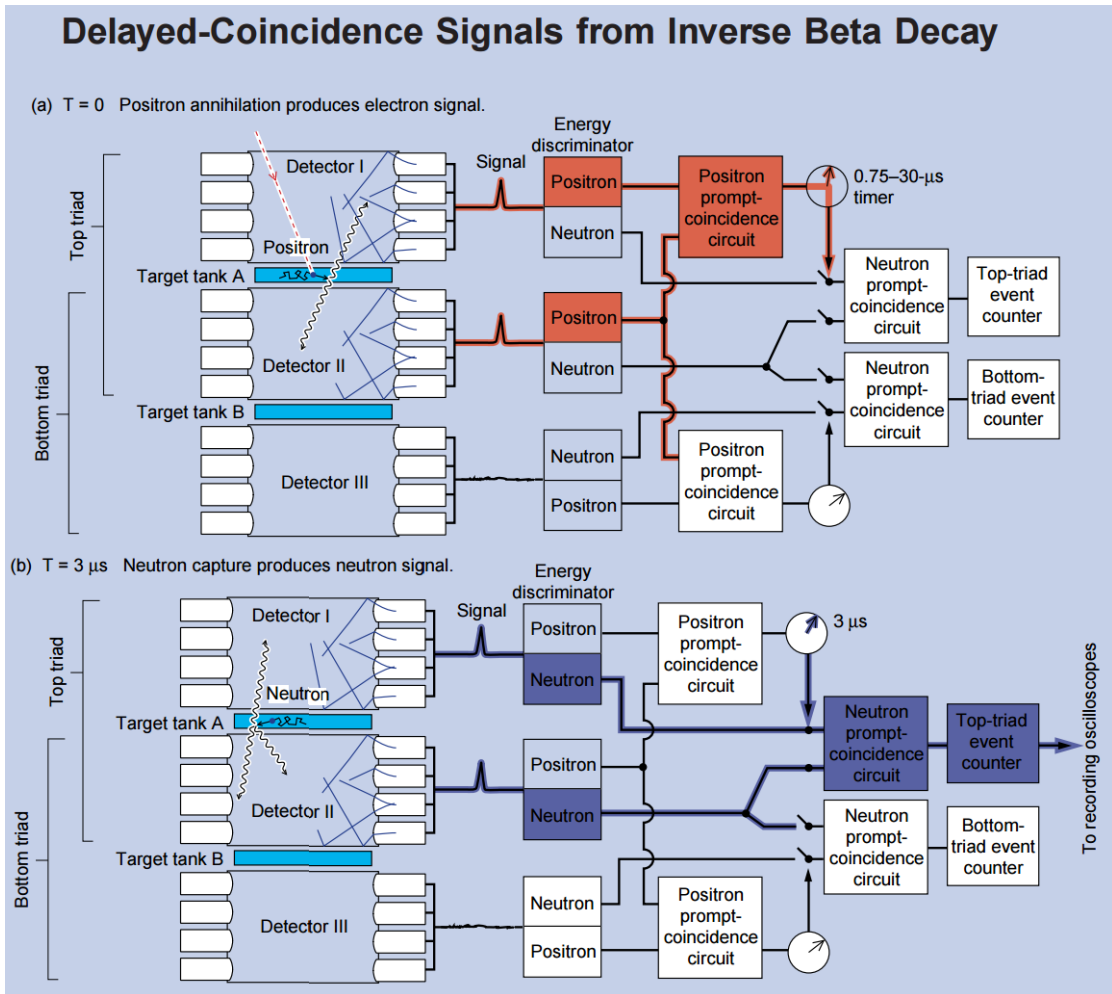


FIGURE 1.4: Schematic of The Savannah River Neutrino Detector : Capable of discerning anti-neutrino induced signals and distinguishing them from the background. [9]

Anti-neutrino detection was achieved by placing two targets between vertically stacked scintillation tanks. Any anti-neutrino induced signal in the uppermost target would cause a positron to be produced, almost instantly annihilate, and for the resultant gamma photons to be detected by the photomultiplier tubes, surrounding the tanks either side of that target. This would shortly be followed by a characteristic neutron capture on cadmium signal approximately 3 - 10  $\mu\text{s}$  later in those same scintillation chambers. Products of this interaction would not be energetic enough to reach the third (bottom) scintillation chamber, which would only see interactions from other events. This configuration helped to eschew false delayed-coincidence signals induced

by stray neutrons, gamma rays, and other stray particles from cosmic showers or from the reactor, which would be more likely to cause random firing of the tubes in all three chambers.

On June 14, 1956, after the counting of the events had been completed, Reines and Cowan contacted Wolfgang Pauli by telegram to inform him of their discovery. Presciently setting the tone for the future of experimental neutrino physics, Pauli replied, ‘*thanks for the message. Everything comes to him who knows how to wait*’.

## 1.5 Three Neutrino Flavours

The  $\nu_\mu$  neutrino was discovered at Brookhaven National Laboratory in 1962 [11], and the  $\nu_\tau$  at the DONUT experiment in 2000 [12]. Consequently, we know that there are at least three neutrino flavour states and three mass states. Initially the idea of three neutrino flavours was motivated by symmetries within the standard model, which currently contains three generations of quarks and leptons. This hypothesis was investigated by experiments at the Large Electron-Positron collider (LEP) [13], such as ALEPH, DELPHI, L3 and OPAL. We know now from their studies of  $Z^0$  boson production in electron-positron collisions that there are indeed three light neutrino types [14] (sterile neutrinos will be discussed later). The  $Z^0$  particle can decay into pairs of charged leptons ( $e^+e^-$ ,  $\mu^+\mu^-$ ,  $\tau^+\tau^-$ ), into  $\nu\bar{\nu}$  pairs, or into  $q\bar{q}$  pairs (as shown in Figure 1.5), which can then form hadrons via hadronization.

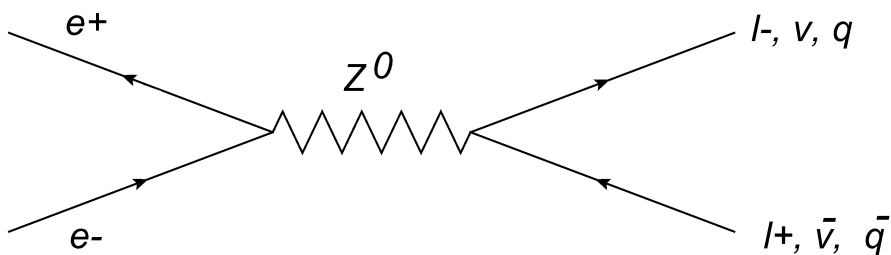


FIGURE 1.5: Feynman diagram showing the three possible particle production mechanisms for an  $e^+e^-$  interaction.

Therefore, the branching ratio of all  $\nu\bar{\nu}$  states can be determined by subtracting the measured partial widths of experimentally observable channels (charged lepton

and quark) from the total  $Z^0$  width at the resonance peak (See Eq. 1.1). Using then a theoretical value for  $\Gamma_{\nu\bar{\nu}}$ , the number of interacting  $\nu$  flavours which couple to the  $Z^0$  can be determined. In experimental terms,  $N_\nu$  has a damping effect on the measured hadronization cross-section from the  $Z^0$  decay, which consequently affects the height and width of the measured resonance peak, as shown in Figure 1.6.

$$\Gamma_{Total} = 3\Gamma_{q\bar{q}} + \Gamma_{ee} + \Gamma_{\mu\mu} + \Gamma_{\tau\tau} + N_\nu\Gamma_{\nu\bar{\nu}} \quad (1.1)$$

Where  $\Gamma_{Total}$  is the branching ratio of all contributing processes, equivalent to that measured. Each of the subsequent branching ratios represents the contributions from the couplings of quarks (in three colours), charged-leptons and finally, neutrinos.

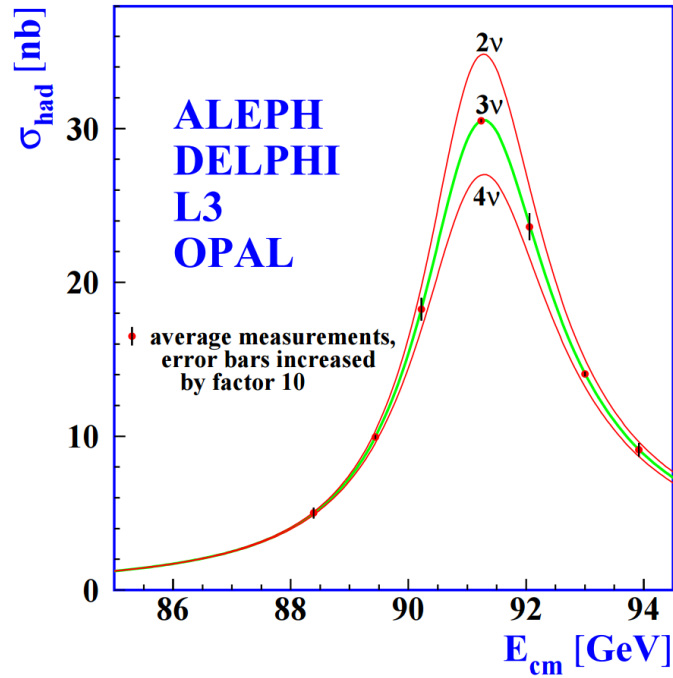


FIGURE 1.6: A combined data fit from ALEPH, DELPHI, L3 and OPAL. A model of three light neutrino flavours fits this exceptionally well [14].

Multiple models were fit to the combined data, provided by the experiments discussed. It was clearly seen that three flavours strongly agrees with the results, though the best fit to the data points was  $2.984 \pm 0.008$  [14], which is technically not consistent with an integer number, but is within two standard deviations. Whether this has any real significance has yet to be seen, with other combined results being consistent with an integer three flavours [15].

If we consider analysis of the cosmic neutrino background and its effect on big bang nucleosynthesis (BBN) then we obtain a value of  $3.14 \pm 0.7$  [16] for  $N_\nu$ , which is in very good agreement with the Standard Model expectation. A determination of  $N_\nu$  from cosmic microwave background anisotropies has previously yielded tension with the BBN result, stating  $N_\nu = 4.34 \pm 0.87$  [17]. However, more recently the Planck spacecraft collaboration has published a tighter bound on the effective number of neutrino species, at  $N_\nu = 3.15 \pm 0.23$  [18]. This leads to the conclusion that there are three active flavours of light neutrino, which is consistent with the Standard Model prediction.

## 1.6 Discrepancy between model and experiment

One of the most puzzling problems of elementary particle physics in the 20th century was the ‘Solar Neutrino Problem’, which illustrated a discrepancy between the measured number of neutrinos coming from the Sun and the number expected from theory. Fusion reactions taking place in the Sun are now known to produce a flux of electron-neutrinos, which are emitted isotropically and can be detected on Earth. In the late 1960s, Ray Davis and John Bacall performed an experiment [19] with the purpose of detecting neutrinos passing through the Earth, which had been created in nuclear fusion in the proton-proton chain of the Sun. If the experiment was successful in finding these solar neutrinos, it would prove that the Sun runs on thermonuclear power and not one of the many other mechanisms suggested, such as it being a giant ball of iron, slowly cooling by radiative emission. During this endeavour he made a fascinating discovery which would dominate neutrino physics throughout the 20th and into the 21st

century.

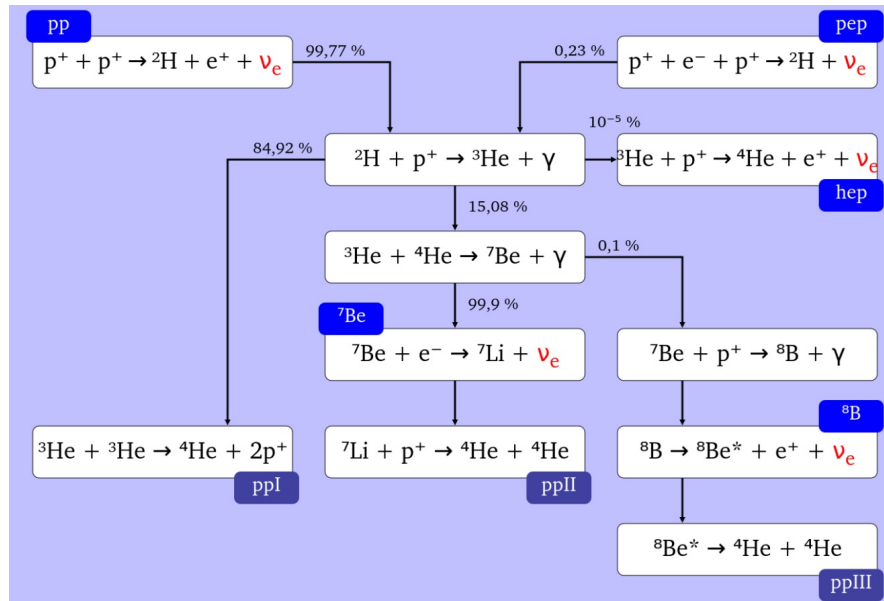


FIGURE 1.7: The well understood proton-proton chain, which takes place in all main sequence, hydrogen burning stars. The expected neutrino flux at the earth can be calculated using this model [20]

In their experiment, the Sun was the required neutrino source and the detector was based in the Homestake mine in South Dakota. This was placed 1478 m underground and contained 100,000 gallons of perchloroethylene, a common dry-cleaning fluid. The signal required was inverse beta decay, producing an electron and an argon atom, which could then be extracted from the tank, by bubbling helium throughout the fluid, and counted. Despite the magnitude of this detector, it still only yielded an interaction rate of approximately one argon atom produced every 2 days, once again due to the low interaction rate of the weak force.

The experiment famously found that the measured the solar neutrino flux significantly differed from that which was predicted by the theory, with only one third of the expected number arriving at the detector [19]. The theoretical calculations which Bahcall had produced were very precise, but it was widely believed within the scientific community that he or Davis had made a mistake.

Ultimately, this conundrum was resolved by modifying our understanding of the

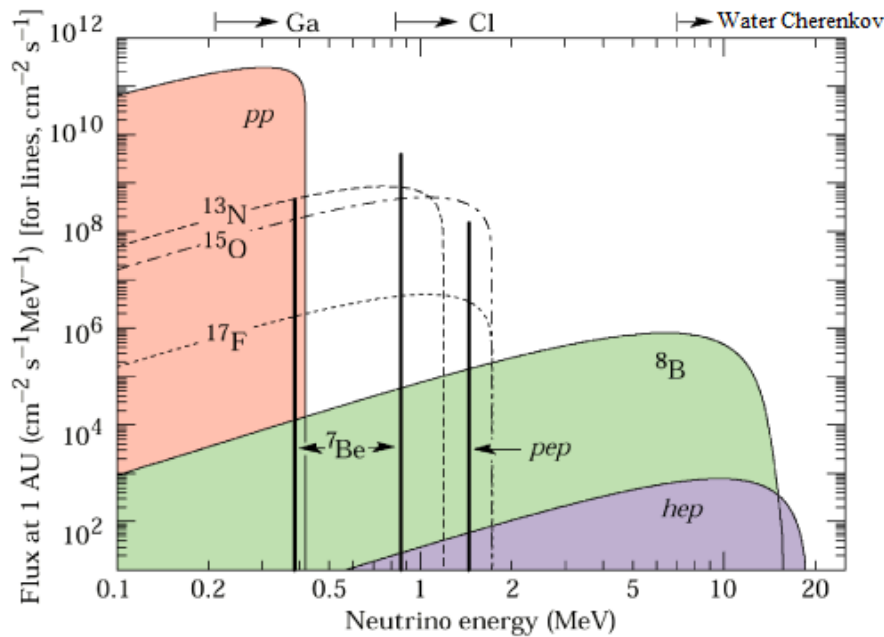


FIGURE 1.8: The energy spectrum of neutrinos emitted by the Sun by detected flux for various astrophysical nuclear processes. Experiments sensitive to those processes are shown at the top [21].

properties of neutrinos rather than of the astrophysical models. This new understanding invokes the phenomena of neutrino oscillation, and is discussed in Section 1.7.

## 1.7 Neutrino Oscillations

While neutrinos travel through space and time they have a distinct probability of transforming from one type or ‘flavour’ to another. The fact that neutrinos oscillate is an example of physics beyond the Standard Model. This was well illustrated by the aforementioned ‘Solar Neutrino Problem’, which arose from discrepancies between the predicted number of neutrinos arriving at the Earth from the Sun and the number actually detected by experiment. The first proposal of neutrino oscillations was by Bruno Pontecorvo in 1957 [22]. An expansion of this theory after the discovery of the  $\nu_\mu$ , explains why the  $\nu_e$  created in the Sun could have changed flavour into another type (later found to be  $\nu_\mu$  and  $\nu_\tau$ ), which were undetectable by Davis’ experiment.

When a neutrino is created it has a specific lepton flavour (i.e  $e$ ,  $\mu$  or  $\tau$ ), which has a direct relationship with the charged-lepton produced in the same interaction. However, this flavour eigenstate is in fact a linear superposition of three separate neutrino mass states. As the neutrinos propagate through vacuum or matter, these mass states propagate at slightly different rates. This means that after a certain amount of time, the neutrino will be in a state composed of a mixture of the three potential mass states, which form the make up of the flavour state. The formalism which governs these oscillations is similar to that of well-understood quark mixing [23], and indicates that this is only possible if the neutrino mass is non-zero.

The likelihood of a neutrino of a given flavour being in another flavour state at some time after its creation can be modelled using a mathematical construction known as the Pontecorvo, Maki, Nakagawa and Sakata (PMNS) [24] matrix. This is a unitary matrix, which relates the flavour states of the neutrinos to the mass states. It is a description of how the weak force couples together these two fields, shown in Equations 1.2 and 1.3.

$$\begin{pmatrix} \nu_e \\ \nu_\mu \\ \nu_\tau \end{pmatrix} = \begin{pmatrix} U_{e1} & U_{e2} & U_{e3} \\ U_{\mu1} & U_{\mu2} & U_{\mu3} \\ U_{\tau1} & U_{\tau2} & U_{\tau3} \end{pmatrix} \begin{pmatrix} \nu_1 \\ \nu_2 \\ \nu_3 \end{pmatrix} \quad (1.2)$$

Eq. 1.2 shows the flavour states which the neutrino may occupy on the left and the mass states on the far right. The middle matrix term describes the probability of a given flavour state corresponding to a given mass state, and is known as the PMNS mixing matrix [24].

The parameters of the PMNS matrix describe the physical characteristics of neutrinos which contribute to oscillations. These parameters are three mixing angles and one phase:  $\theta_{13}, \theta_{23}, \theta_{12}, \delta_{CP}$ . It is also often split into three components, which we call the atmospheric, reactor and solar components, due to the fact that oscillations of neutrinos have been clearly observed in all three sectors (Equation 1.3). It has been the primary goal of the T2K experiment to put stringent constraints on several of these parameters, so that we can gain a further understanding of neutrino oscillations [25]. The PMNS

matrix [24] is defined as follows :

$$U = \begin{pmatrix} 1 & 0 & 0 \\ 0 & \cos \theta_{23} & \sin \theta_{23} \\ 0 & -\sin \theta_{23} & \cos \theta_{23} \end{pmatrix} \begin{pmatrix} \cos \theta_{13} & 0 & \sin \theta_{13} e^{-i\delta_{CP}} \\ 0 & 1 & 0 \\ -\sin \theta_{13} e^{i\delta_{CP}} & 0 & \cos \theta_{13} \end{pmatrix} \begin{pmatrix} \cos \theta_{12} & \sin \theta_{12} & 0 \\ -\sin \theta_{12} & \cos \theta_{12} & 0 \\ 0 & 0 & 1 \end{pmatrix} \quad (1.3)$$

Eq. taken from [24].

Where  $\theta_{13}$ ,  $\theta_{23}$  and  $\theta_{12}$  represent the mixing angles between the defined neutrino mass states ( $\nu_1$ ,  $\nu_2$  and  $\nu_3$ ). The middle matrix contains a term called the CP violating phase  $\delta_{CP}$ , which if non-zero could give rise to some new and interesting physics.

CP conservation dictates that the successive operation of charge conjugation and parity is conserved, such that if particles in nature were inverted in a coordinate and charge conjugation, the probability of interactions occurring would remain the same. This is particularly relevant to a popular problem in physics known as the matter/anti-matter asymmetry of the Universe [26]. This problem states that if no asymmetry existed, then the Universe would have been created with equal amounts of matter and anti-matter, and consequently due to annihilation, there should be no residual matter or anti-matter remaining today. However, this is clearly not the case, implying a physical reason for this imbalance.

Due to a phenomenon known as leptogenesis, the mechanism by which leptons were created, there could be a link between CP and this matter/anti-matter problem. In the currently accepted Standard Model, lepton number is conserved and it is not possible to create leptons directly without corresponding anti-leptons. Leptogenesis can only take place in theories of physics beyond the Standard Model, such as neutrino oscillation [27]. Therefore, if the CP violating phase is shown to be non-zero in the PMNS matrix, neutrino oscillations could be the key to the one of the biggest mysteries in modern science. Recently, the T2K experiment has rejected the hypothesis that  $\nu_e$  and  $\bar{\nu}_e$  oscillate with the same probability at a 95% confidence level [28].

In 1.3, the first matrix is attributed to the atmospheric/accelerator part and  $\theta_{23}$ , often referred to as the atmospheric mixing angle, is associated with the dominant atmospheric  $\nu_\mu$  oscillations. The second matrix, referred to as the reactor part, contains parameters associated with CP violation. Finally, the third matrix describes the solar mixing angle  $\theta_{12}$  that is predominantly responsible for solar neutrino oscillations. Accurately measuring the parameters of this matrix is essential to unravelling the mystery of neutrino oscillations.

In Eq. 1.4, the following symbols are used :  $\nu_\mu$  - muon flavour neutrino,  $\nu_e$  - electron flavour Neutrino, E - total energy of the neutrino, p - momentum of the neutrino, x - distance travelled, m - mass,  $\theta$  - generic mixing angle (indices denote specific mixing angles).

The derivation of the mathematical probability of a  $\nu_\mu$  oscillating to a  $\nu_e$  for the two flavour case is shown in Eq. 1.4. This probability will reach a peak at certain combinations of neutrino energy and distance travelled.

$$\begin{pmatrix} \nu_e \\ \nu_\mu \end{pmatrix} = \begin{pmatrix} \cos \theta & \sin \theta \\ \sin \theta & \cos \theta \end{pmatrix} \begin{pmatrix} \nu_1 \\ \nu_2 \end{pmatrix} \quad (1.4)$$

$$\therefore |\nu_e\rangle = \cos(\theta) |\nu_1\rangle + \sin(\theta) |\nu_2\rangle$$

$$|\nu_\mu\rangle = -\sin(\theta) |\nu_1\rangle + \cos(\theta) |\nu_2\rangle$$

Time and position dependence mean that :

$$|\nu_e\rangle = \cos(\theta) |\nu_1(x, t)\rangle + \sin(\theta) |\nu_2(x, t)\rangle$$

$$Use : |\nu_n(x, t)\rangle = e^{-i(E_n t - p_n x)} |\nu_n(0, 0)\rangle$$

$$\therefore |\nu_e\rangle = \cos(\theta) e^{-i(E_1 t - p_1 x)} |\nu_1\rangle + \sin(\theta) e^{-i(E_2 t - p_2 x)} |\nu_2\rangle$$

Energy is conserved and the waves are coherent, so :

$$E_1 = E_2 = E$$

$$|\nu_e\rangle = e^{-i(E_1 t - p_1 x)} (\cos(\theta) |\nu_1\rangle + \sin(\theta) e^{-i(p_2 - p_1)x} |\nu_2\rangle)$$

Now consider the momenta :

$$p_1 = \sqrt{(E^2 - m_1^2)}$$

$$p_2 = \sqrt{(E^2 - m_2^2)}$$

$m \ll E$  so can use binomial expansion

$$p_1 = \sqrt{(E^2 - m_1^2)} = (E + 1/2(-m_1^2)(E)) = E - \frac{m_1^2 E}{2}$$

and likewise for  $p_2$ , so that :

$$p_2 - p_1 = \frac{m_1^2 - m_2^2}{2E} = \frac{\Delta m^2}{2E}$$

Now,

$$|\nu_e\rangle = e^{-i(E_1 t - p_1 x)} (\cos(\theta) |\nu_1\rangle + \sin(\theta) e^{-i(\frac{\Delta m^2}{2E})x} |\nu_2\rangle)$$

$$P(\nu_e \rightarrow \nu_e) = |\langle \nu_e | \nu_e(x, t) \rangle|^2 = \cos^4 \theta + \sin^4 \theta + \cos^2 \theta \sin^2 \theta (e^{i\frac{\Delta m^2 x}{2E}} - e^{-i\frac{\Delta m^2 x}{2E}})$$

USING TRIGONOMETRIC IDENTITIES WE OBTAIN :

$$P(\nu_e \rightarrow \nu_e) = 1 - \sin^2(2\theta) \sin^2\left(\frac{\Delta m^2 x}{4E}\right)$$

Converting to natural units of energy (GeV) and replacing  $x$  with the commonly used  $L$  as distance travelled (km) gives :

$$P(\nu_e \rightarrow \nu_e) = 1 - \sin^2(2\theta) \sin^2\left(\frac{1.27\Delta m^2 L}{E}\right)$$

For the two flavour case shown in Eq. 1.4, the oscillation probability  $P(\nu_\mu \rightarrow \nu_e)$  can be expressed as  $1 - P(\nu_e \rightarrow \nu_e)$ . A visualisation of the more complex but realistic three flavour case is shown in Figure 1.9.

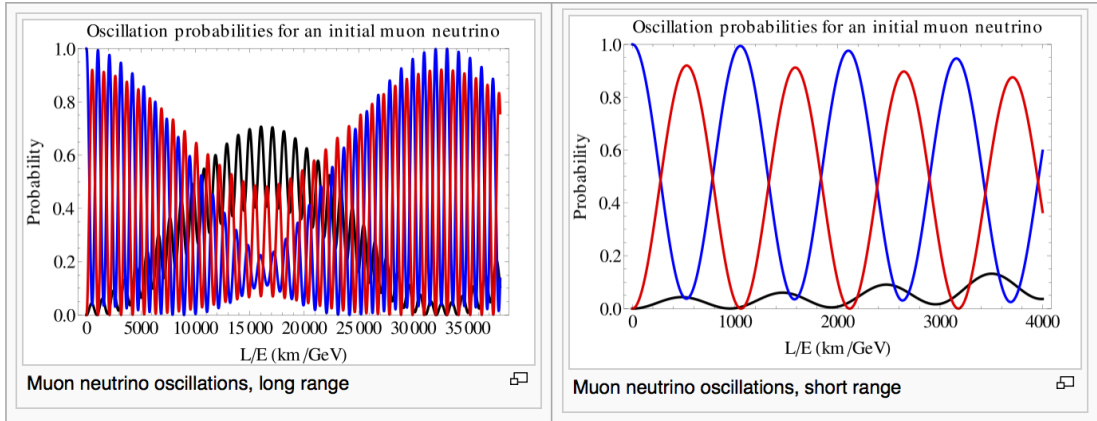


FIGURE 1.9: The probability of an initially muon neutrino to be measured as another flavour state as it travels. Shown for the short range and long range case. Muon probability is shown in blue, tau neutrino in red and electron neutrino in black [29].

In reality there are three active neutrino flavours. The oscillation probability formula for the three flavour case for  $\nu_\mu$  to  $\nu_e$  is shown here :

$$P(\nu_\mu \rightarrow \nu_e) = \sin^2 2\theta_{23} \sin^2 \theta_{13} \sin^2\left(\Delta m_{32}^2 \frac{L}{4E}\right) - \frac{\sin^2 \theta_{12} \sin 2\theta_{23}}{2 \sin \theta_{13}} \sin\left(\Delta m_{21}^2 \frac{L}{4E}\right) \sin^2 \theta_{13} \sin^2\left(\Delta m_{32}^2 \frac{L}{4E}\right) \sin \delta_{CP} \quad (1.5)$$

Eq. taken from [30].

This neutrino oscillation hypothesis was ultimately confirmed by two neutrino experiments; Super-K observed neutrino oscillations in the atmosphere [31] and the Sudbury Neutrino Observatory (SNO) resolved the solar neutrino problem [32]. SNO achieved this by using a detector which was sensitive to all flavours of neutrino (discussed more in Section 1.12.4), and the total flux of all neutrino flavours agreed with the theoretical prediction. A description of the detection mechanisms of both SNO and Super-K is included later. A comparison of the neutrino flux detectable by a number of experiments, illustrating the sensitivity of SNO to all flavours is shown in Figure 1.10.

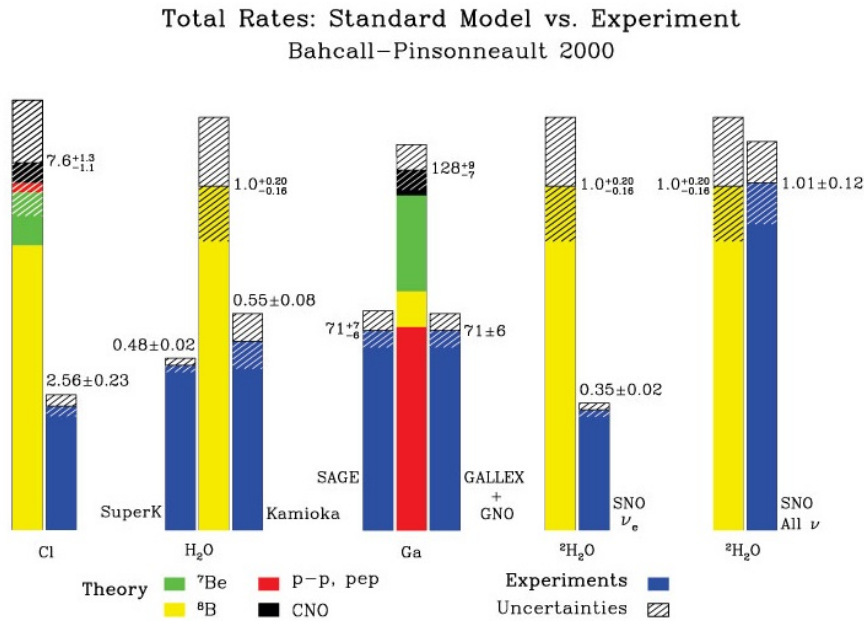


FIGURE 1.10: The theoretical expected flux vs the detected neutrino flux for a number of experiments. On the far right we can see that the SNO measurements for all neutrino flavours matches up very well with the theory. [35]

It has been the focus of many global neutrino experiments to determine the values of the PMNS parameters. However, as there are a number of degrees of freedom, a number of parameter sets are possible. Variations could depend on the mass difference between the second and third neutrino mass eigenstates, the neutrino mixing angles, the mass hierarchy and the CP violating phase  $\delta_{CP}$ . The angles  $\theta_{12}$  and  $\theta_{23}$  are fairly well known, and are large. This is quite unexpected, as in the Cabibbo-Kobayashi-Maskawa (CKM) mixing matrix for quarks, all of the angles are quite small. The third

angle  $\theta_{13}$  however, was believed to be small, and as of June 2011 had not yet been directly measured. In 2012, the Daya Bay experiment released a  $5.2\sigma$  significance measurement of  $\theta_{13}$  [36], illustrating that it was non-zero, which is important for CP violation searches, as this angle precedes  $\delta_{CP}$  in the PMNS matrix (Eq. 1.3). In 2013, T2K released a measurement of the neutrino oscillation parameters from muon neutrino disappearance with an off-axis beam, more precisely measuring various mixing parameters [33]. In 2014,  $\theta_{23}$  was measured much more precisely by the T2K experiment [34], as illustrated in Figure 1.11, and these results agree with previous assertions. Recently, in a T2K measurement, it has been indicated that  $\delta_{CP}$  is likely non-zero with 95% confidence [28]. This was achieved by running the beam at different times in neutrino and anti-neutrino mode, and measuring differences in the oscillation probabilities, which provides sensitivity to  $\delta_{CP}$ . T2K is described in much more detail in Chapter 2.

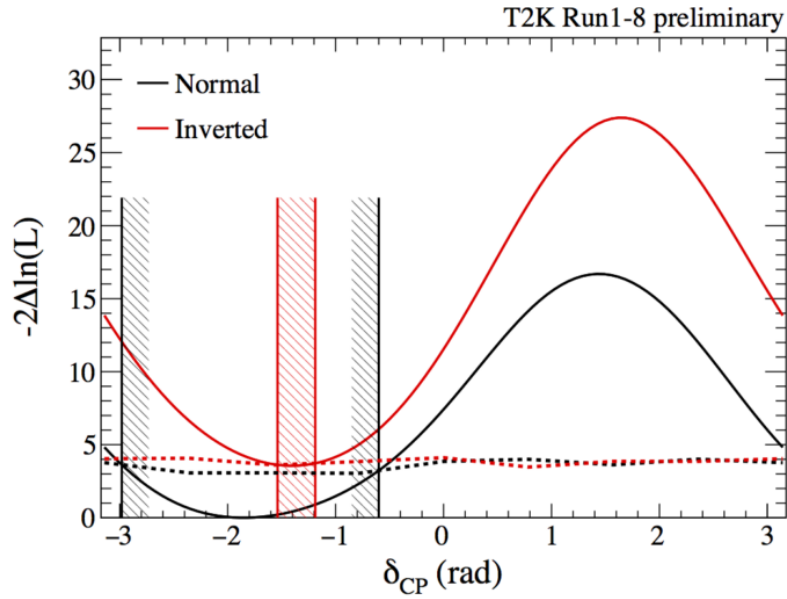


FIGURE 1.11:  $-2\Delta\ln(L)$  (equivalent of  $\Delta\chi^2$ ) as a function of  $\delta_{CP}$  for the normal (black) and inverted (red) mass ordering. The vertical lines show the corresponding allowed 95% confidence interval, calculated using the Feldman-Cousins method. [28]

Parameter	Best Fit Value	$3\sigma$ Allowed Range	Experiment(s)
$\sin^2 \theta_{13}$	0.0214	0.0185 - 0.0246	Daya Bay, RENO and Chooz
$\sin^2 \theta_{12}$	0.297	0.250 - 0.354	KamLAND (and Solar)
$\sin^2 \theta_{23}$	0.437	0.379 - 0.616	T2K, MINOS, Daya Bay, Super-K, NO $\nu$ A
$\Delta m_{21}^2$	$7.37 \cdot 10^{-5} eV^2/c^4$	6.93 - 7.97	KamLAND (and Solar)
$\Delta m_{31}^2$	$2.50 \cdot 10^{-3} eV^2/c^4$	2.37 - 2.63	Daya Bay, MINOS, T2K, Super-K, NO $\nu$ A

TABLE 1.1: Known values of neutrino mixing parameters for a normal neutrino mass hierarchy. All values taken from the PDG (2016) [37].

## 1.8 MSW Effect - Matter Enhanced Oscillations

The Mikheyev-Smirnov-Wolfenstein (MSW) effect is a process by which matter promotes oscillation in neutrinos as they pass through [38]. The electrons contained in matter cause changes to the energy levels in the propagation eigenstates (mentioned in the Section 1.7) of the neutrinos, which causes an effect similar to that of light passing through a medium with a non-zero refractive index. As the neutrino oscillation probabilities depend upon the mass squared differences of the three known generations of neutrinos, the mass variations cause the neutrinos to behave differently in matter of varying densities. This is particularly prevalent in very dense areas such as the Sun, where many neutrinos are produced in proton-proton chain reactions (see Figure 1.7). Ultimately, this means that the oscillation from the electron-neutrino flavour neutrinos in the Sun to the other flavours measured at the Earth occurs almost completely in the Sun and negligibly in the vacuum of space. T2K encounters minimal matter effects due to its comparatively short 295 km baseline.

## 1.9 Neutrino Mass

We know that the probability of a neutrino oscillation is dependent on the mixing angles discussed above. It is also dependent on the differences in the masses of the neutrino states squared (i.e.  $\Delta m_{21}^2 = m_2^2 - m_1^2$ ). It is extremely difficult to directly detect the

masses of the neutrinos, but it is possible to infer the mass differences between them. For a three flavour neutrino system, the hierarchies shown in Figure 1.12 have been suggested. These two hierarchies arise from the fact that the sign of  $\Delta m_{21}^2$  is known, but the sign of  $\Delta m_{31}^2$  is yet to be determined, positioning that state either above or below the other two.

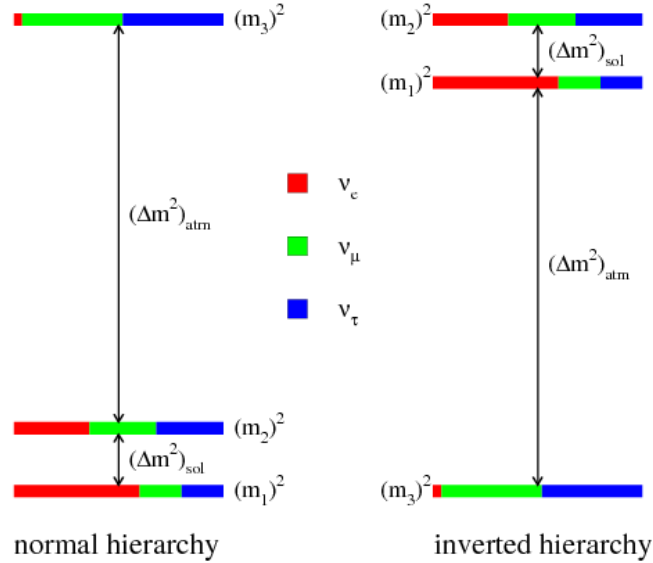


FIGURE 1.12: The normal and inverted mass hierarchies for the neutrino mass states. In the normal case the difference between mass states one and two is much smaller than the difference between two and three. The colours in this schematic show the various mass eigenstate contributions to the overall flavour eigenstate [39].

Due to the extremely low mass of neutrinos, it has previously been stated in the Standard Model that their mass is zero. This idea was reinforced by the fact that they travel at a speed essentially indistinguishable from that of light. We now know that there are mass differences between the combinations of the mass eigenstates ( $\nu_1$ ,  $\nu_2$ ,  $\nu_3$ ) which comprise the three flavour eigenstates, therefore they must have a non-zero mass. In fact, it is this intrinsic property of mass which allows the quantum mechanical oscillation phenomena to take place. Additionally, if we can determine one of the masses, we can then calculate the other two. The mass hierarchy can be determined in accelerator experiments utilising earth matter effects, which modify the oscillation probability in such a way that provides sensitivity to the hierarchy. In terms of mass

measurements, known oscillations place a lower limit on the neutrino mass scale. More direct measurements of the neutrino mass come from the three areas : cosmological constraints, neutrinoless double beta decay and endpoint beta decay (usually using tritium).

An analysis of current cosmological observations, such as the anisotropies of the cosmic microwave background or the distribution of large-scale structure, currently provides an upper bound on the sum of neutrino masses of order 1 eV or less, and future cosmological measurements are expected to be sensitive to neutrino masses well into the sub-electronvolt regime [40]. Considering that this is a sum of all three mass eigenstates and that the mass of the hitherto lightest elementary particle, the electron, is 0.511 MeV, it is no surprise that there have been no definitive measurements as yet.

Attempts to measure the absolute mass of neutrinos involves examining well-known decays of particles, which decay to a neutrino and some other particles. If the momentum of these particles can be measured, and the mass of the decaying parent, and the decay products are well known, then energy-momentum conservation can, in principle, allow one to determine the mass of the outgoing neutrino. One potential method of a direct neutrino mass measurement is the use (once again) of the beta decay channel.

The general theory of  $\beta$ -decay (formulated by Fermi) describes the shape of the energy of the electron emitted from the decay by :

$$\frac{dN}{dE_e} = Cp(E + m_e)(E_0 - E_e)\sqrt{(E_0 - E_e)^2 - m_\nu^2}F(E_e)\theta(E_0 - E_e - m_\nu) \quad (1.6)$$

where C is a normalisation constant,  $m_e$  is the electron mass,  $E_e$  is the electron energy, and  $E_0$  is the maximum allowable energy for the electron from the decay kinematics, and is called the end point. The function  $F(E_e)$  is called the Fermi function, and takes it account the interactions of the electron with the electromagnetic field of the daughter nucleus. The final term,  $\theta(E_0 - E_e - m_\nu)$ , imposes energy conservation. We can visualise this function like so :

It can be seen that if the neutrino were massless, the spectrum would fully extend to

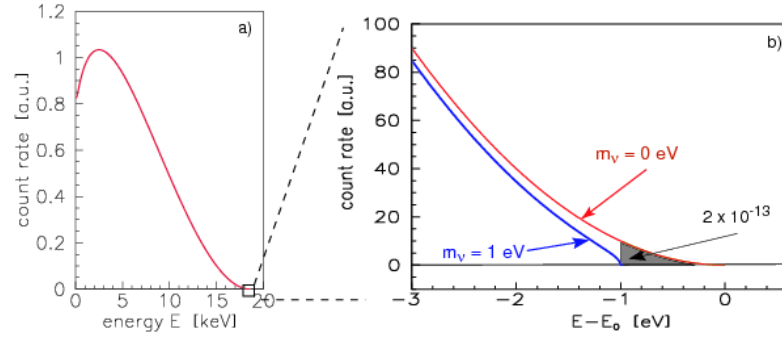


FIGURE 1.13: A prediction of the energy spectra in electron-neutrino beta decay at Katrin for a model of a 1eV electron-neutrino mass vs a massless electron-neutrino. Tiny deviations can be seen at the endpoint of the spectrum representing the minimum energy taken away by a neutrino (its mass energy) [41].

the endpoint representing the remaining energy available in the decay. However, if the neutrino has some mass then spectrum must be cut short of this total, and the point at which the neutrinos have been emitted with zero effective momentum will reveal the rest mass.

Direct neutrino mass measurements have already pushed down our current upper limit to  $m(\nu_e)$  less than 2 eV. The next generation of beta spectroscopy experiments such as Katrin aim to improve this further and reach a sensitivity limit of  $m(\nu_e)$  greater than 0.2 eV [42].

## 1.10 Majorana Neutrinos

When Paul Dirac first formulated his famous ‘Dirac Equation’ in 1928 as a relativistic equation of motion for the wave function of the electron, it became apparent that negative energy solutions existed for electrons and therefore antiparticles must exist [43]. Carl Anderson discovered the antimatter partner of the electron which Dirac had predicted in 1932 [45]. He called it the positron as it seemed identical to an electron but with a positive charge.

Elementary particles which interact with the Higgs field are known as Dirac fermions; a category to which (within the Standard Model) quarks, electrons and neutrinos all belong. The mass of these particles is due to that interaction, and is well understood.

However, a discussion of the absolute mass of neutrinos would be incomplete if only Dirac masses were considered, as it is possible that the neutrino mass is generated by another mechanism. This mechanism is a unique self-interaction, leading to the consequence that neutrinos may be their own anti-particle, otherwise known as Majorana Fermions. In 1937, Ettore Majorana hypothesised these eponymous particles as ones which can be their own anti-particle, in contrast to Dirac fermions which cannot. In the Standard Model, thus far all elementary fermions except neutrinos have been shown to be Dirac fermions, which can be easily seen due to the electromagnetic charge of the particles, as Majorana particles necessarily must have zero charge.

Dirac masses for neutrinos do not seem to account for the large discrepancy in the masses of them and of other fermions (quarks and charged leptons), which are on the order of millions of times heavier. It is therefore necessary to invoke another mechanism known as the seesaw, which is possible only for Majorana fermions. The simplest version of this extends the Standard Model by assuming two or more additional right-handed neutrino fields which do not interact weakly and exist on a very large mass scale. This simple seesaw mechanism would produce three light neutrinos, one for each known lepton flavour, and three heavy ‘sterile’ neutrinos which have not been observed as yet. Neutrinoless double beta decay, which can be viewed as two beta decay events where the produced anti-neutrinos immediately annihilate with one another, is only possible if neutrinos are their own antiparticles.

## **1.11 Neutrinoless Double Beta Decay**

Beta decay has been discussed at length so far, due to its core place in neutrino detection and history. Double beta decay is also possible, which emits two electrons and two antineutrinos. This balances leptonic matter and antimatter both before and after the decay process, thus conserving lepton number. However, if neutrinos are Majorana then it is possible that the ‘antineutrinos’ produced during double beta decay could annihilate one another and disappear, violating lepton number conservation. This is

called neutrinoless double beta decay and can only occur in certain atoms, such as tellurium. In order for any double beta decay to be possible, the final nucleus must have a larger binding energy than the original nucleus. For certain nuclei, such as germanium-76, the isobar one atomic number higher (arsenic-76) has a smaller binding energy, preventing single beta decay. However, the isobar with atomic number two higher, selenium-76, has a larger binding energy, so double beta decay is then allowed.

## 1.12 Experimental Searches - Recent and Future

The Cowan-Reines[10] and Davis[19] experiments were mentioned earlier, and while these did herald the dawn of modern neutrino physics, these do not represent the scale and diversity of the global initiatives we are lucky to have today. This section will describe some of the work being done in the field of neutrino oscillation physics today.

### 1.12.1 Kamiokande/Super-K

There have been multiple stages of particle physics and neutrino experiments at Kamioka in the Mozumi mine. The first of these Kamioka experiments was called KamiokaNDE (Kamioka Nucleon Decay Experiment) [44]. This was a large water Cherenkov detector which was designed to search for proton decay. If a proton were to decay in the target water or Kamiokande, it would produce other charged particles which could then be identified by their cherenkov radiation. To reduce potential backgrounds to the proton decay signal, the detector was buried deep under a mountain, which shields the detector from cosmic ray muons. The detector failed to observe proton decay, but set a contemporary world's best limit on the lifetime of the proton. A series of upgrades were carried out focusing on the reduction of radioactive backgrounds in the detector, which once completed began taking data as Kamiokande-II in 1985. The Kamiokande-II experiment happened to be running at a fortuitous time, as a supernova took place while the detector was online and taking data. With the upgrades that had taken place the detector was sensitive enough to observe the thermal neutrinos produced by Supernova

1987A, which took place approximately 160000 light years away in the Large Magellanic Cloud. The neutrinos arrived at Earth in February 1987, and the Kamiokande-II detector observed 11 events.

At the start of the 1990s, particle physicists were starting to suspect that the solar neutrino problem and atmospheric neutrino deficit had something to do with neutrino oscillation. The Super Kamiokande detector was designed to test the oscillation hypothesis for both solar and atmospheric neutrinos. The Super-Kamiokande detector consists of 50,000 tons of pure water surrounded by  $\sim 11,200$  photomultiplier tubes. The detector was again designed as a cylindrical structure, this time 41.4 m tall and 39.3 m across. The detector was surrounded with a considerably more sophisticated outer detector which could not only act as a veto for cosmic muons but could also assist in their reconstruction. Super-Kamiokande started data taking in 1996 and has made several important measurements. These include precision measurement of the solar neutrino flux using the elastic scattering interaction, the first very strong evidence for atmospheric neutrino oscillation, and a considerably more stringent limit on proton decay. A detailed description of the workings of the Super-K detector can be found in Section 2.4.

### 1.12.2 IceCube

The IceCube Neutrino Observatory is a neutrino telescope in the Amundsen-Scott South Pole Station in Antarctica. Ice Cube is focused on searching for neutrinos which have been created in high energy astrophysical sources (its observable range is approximately 100 GeV to several PeV), such as gamma ray bursts, supernovae and phenomena involving black holes and neutron stars [46]. The data is collected using thousands of spherical optical sensors (each containing a photomultiplier tube), which are placed at depths ranging from 1450 m to 2450 m under the Antarctic ice. In order to achieve this, holes were melted un the ice using a hot water drill. The depth of the detectors, purity of the surrounding ice and lack of native life helped to reduce noise and to attain a clearer signal. Observations so far have included a shadowing effect by the moon,

which blocks cosmic ray protons, creating a deficit of cosmic ray shower muons, and not long after the experiment was completed a pair of high energy neutrinos were detected. These are thought to be of astrophysical origin given their high energy and were named ‘Bert’ and ‘Ernie’ after characters from the Sesame Street TV show [47]. A key subdetector within IceCube is the Deep Core low-energy extension, which is a densely instrumented region of the IceCube array which extends the observable energies below 100 GeV. The Deep Core strings are positioned at the center of the main array, in the clearest ice at depths between 1760 m and 2450 m. In 2014, Deep Core was utilised in a neutrino oscillation analysis [48], using 3 years of data, which measured  $\nu_\mu$  disappearance in the 10 GeV to 100 GeV energy range. Assuming normal hierarchy, the best fit parameters for this analysis were  $\Delta m_{32}^2 = 2.72_{-0.20}^{+0.19} \times 10^{-3} eV^2$  and  $\sin^2 \theta_{23} = 0.53_{-0.12}^{+0.09}$ . These results are compatible and comparable in precision to those of dedicated oscillation experiments. These results, including the spectra plot and confidence countours are shown here in Figures 1.14 and 1.15.

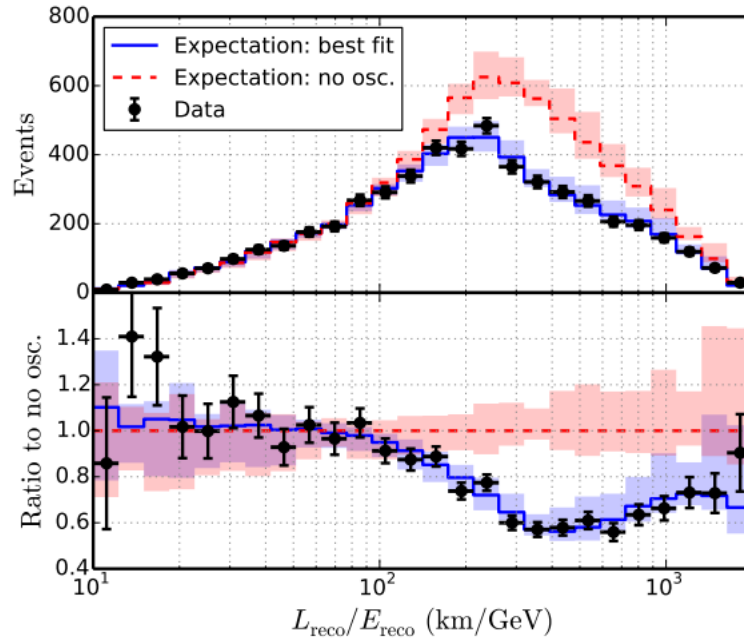


FIGURE 1.14: Distribution of events as a function of reconstructed L/E. Data are compared to the best fit and expectation with no oscillations (top) and the ratio of data and best fit to the expectation without oscillations is also shown (bottom). Bands indicate estimated systematic uncertainties [48].

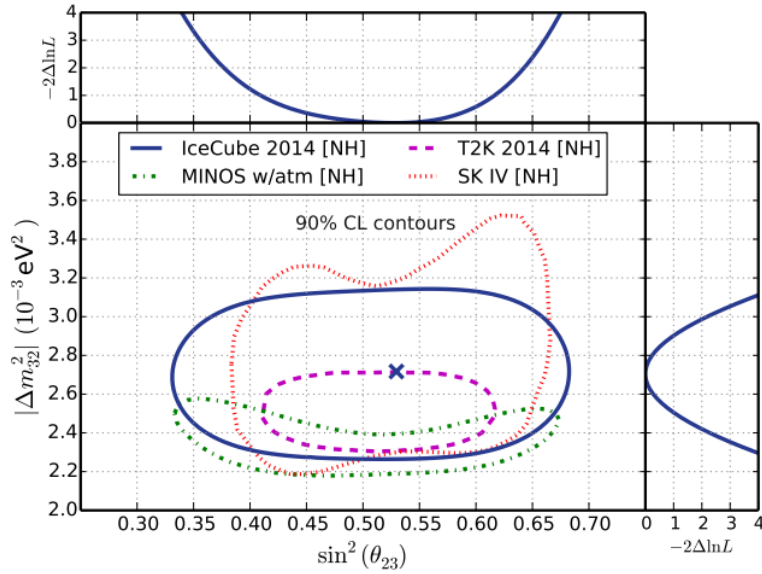


FIGURE 1.15: 90% confidence contours of the result in the  $\sin^2 \theta_{23} - \Delta m_{32}^2$  plane in comparison with the ones of the most sensitive experiments. The log-likelihood profiles for individual oscillation parameters are also shown (right and top). A normal mass ordering is assumed [48].

### 1.12.3 Daya Bay

The Daya Bay Reactor Neutrino Experiment is a China-based multinational particle physics project studying neutrinos. It is situated at Daya Bay, approximately 52 kilometers northeast of Hong Kong. The experiment consists of eight  $\bar{\nu}$  detectors, clustered in three locations within 1.9 km of six nuclear reactors. Each detector consists of 20 tonnes of liquid scintillator (linear alkylbenzene doped with gadolinium) surrounded by photomultiplier tubes and shielding. Daya Bay studies neutrino oscillations and is designed to measure the mixing angle  $\theta_{13}$  using antineutrinos produced by the reactors of the Daya Bay Nuclear Power Plant and the Ling Ao Nuclear Power Plant. By probing this value, insight can be gained into neutrino mixing and further understanding of CP violation (the value for which is conflated with  $\theta_{13}$  in the PMNS matrix). On 8 March 2012, the Daya Bay collaboration announced a  $5.2\sigma$  discovery of  $\theta_{13} \neq 0$ , with  $\sin^2(2\theta_{13}) = 0.092 \pm 0.016$  (*stat*)  $\pm 0.005$  (*syst*) [49], illustrated in Figure 1.16 This was a significant result, as its non-zero value and the fact it is surprisingly large will allow

experiments to probe CP violation in the neutrino sector. It is consistent with earlier results by T2K, MINOS and Double Chooz. The Daya Bay collaboration produced an updated analysis of their results in 2014, which used the  $\nu$  energy spectrum to improve the bounds on the mixing angle to  $\sin^2(2\theta_{13}) = 0.092 \pm 0.009$  [36].

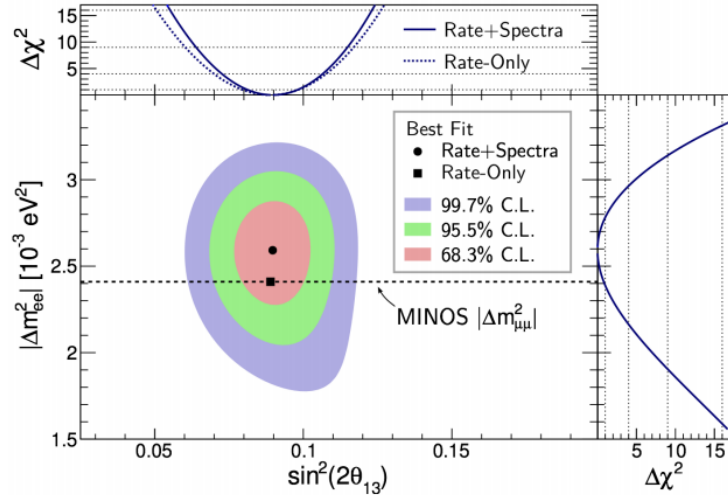


FIGURE 1.16: Allowed regions for the  $\sin^2(2\theta_{13})$  and  $\Delta m_{ee}^2$  parameter phase space at the 68.3%, 95.5% and 99.7% confidence levels [49].

#### 1.12.4 SNO and SNO+

The Sudbury Neutrino Observatory, located approximately 2 km underground in the Creighton Mine in Sudbury, Ontario, Canada has been mentioned earlier for its resolution of the solar neutrino problem. It was designed to detect solar neutrinos via their interactions with heavy water, 1000 tonnes of which is contained in a 6 metre radius acrylic vessel. Signals from events which occur in the water can be picked up by the 9,600 photomultiplier tubes placed on a sphere approximately 850 cm inside the acrylic vessel [50]. As stated above, it was the SNO experiment which provided clear evidence that neutrinos oscillate [32].

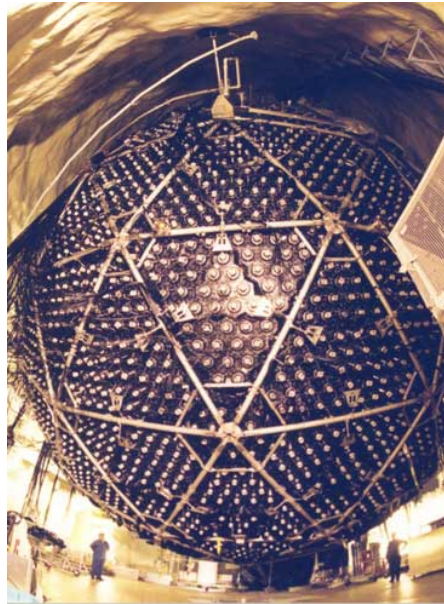


FIGURE 1.17: Figure 3.3 shows the PMT outer shell which surrounds the 6 m radius acrylic vessel used to contain the heavy water used as the SNO detector. Two people can be seen at the bottom of the picture to judge the scale [53].

The fact that SNO used heavy water for their neutrino detection allows sensitivity to both charged and neutral current interactions, which are described here. In the charged current interaction, a  $\nu$  converts a neutron in a deuteron to a proton. The  $\nu$  is absorbed in the reaction and an electron is produced. Solar neutrinos have energies smaller than the mass of muons and tau leptons, so only  $\nu_e$  can participate in this reaction. The emitted electron carries off most of the neutrino's energy, on the order of 5-15 MeV, and

is detectable. The produced proton does not have enough energy to be detected easily. In the neutral current interaction, a neutrino dissociates the deuteron, breaking it into its constituent neutron and proton. This interaction has no flavour restriction based on the energy of the incoming  $\nu$  and thus proceeds at an equal rate for all flavours. The dissociated neutron is captured by heavy water nucleus, and produces a gamma ray photon of 6 MeV energy, which allows tagging of the event. Another mechanism equally likely for all flavours of  $\nu$  and detectable by SNO was the elastic scattering of a  $\nu$  from an atomic electron. The rates of all of these types of interactions can be compared to illustrate the historic result mentioned in 1.7, unequivocally resolving the solar neutrino problem. Cartoon schematics of these processes are shown in Figure 1.18.

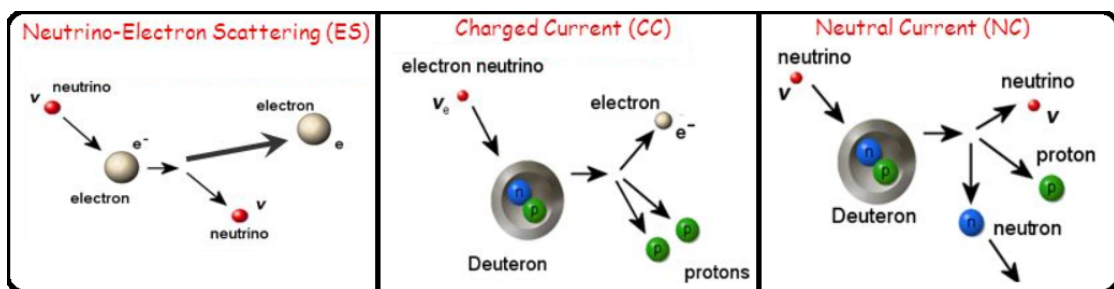


FIGURE 1.18: The three possible neutrino interactions detectable by SNO. A comparison of the rates at which these proceed was used to illustrate oscillation in solar neutrinos. The charged-current process here is only sensitive to  $\nu_e$  interactions, whereas the neutral current reaction is equally sensitive to all flavours of neutrino. [52].

The currently running, SNO+ is a relatively new experiment, which makes use of the existing SNO hardware and framework, but with the addition of liquid scintillator linear alkyl benzene to the detection medium[51]. SNO+ has a number of physics goals, the first of which is to investigate neutrinoless double beta decay, achieved via the decay of tellurium [54]. Additionally, analysis of proton-electron-proton (pep) and carbon-nitrogen-oxygen (CNO) cycles in the Sun will help to better understand neutrino-matter interaction and solar composition. SNO+ will also be capable of monitoring neutrinos produced in radioactive decays in the earth (geoneutrinos).

### 1.12.5 Katrin

Katrin (Karlsruhe Tritium Neutrino Experiment) [41] is currently undertaking a measurement of the mass of the electron-antineutrino with sub-eV precision by examining the spectrum of electrons emitted from the beta decay of tritium.



FIGURE 1.19: Katrin being moved in the land travel portion of its journey from Deggendorf to Karlsruhe [41].

The events of interest to Katrin are ones in which the electron takes almost all the energy and the neutrino almost none, so that only the mass energy difference remains. These events are extremely rare, occurring approximately 1 in  $10^{12}$  decays. In order to filter out the common events so the detector is not overwhelmed. When a  $\beta$ -decay occurs in the tritium, the ejected electron is guided along the input channel to the large spectrometer. The spectrometer imposes an electron potential along its length, stopping all but the most energetic electrons. Those electrons which have high enough energy to overcome the potential barrier are then guided into the detector. By changing the value of the potential, an integral spectrum of the electrons can be built up and the end point studied for signs of neutrino mass. If the electron neutrino mass is  $> 0.35$  eV, KATRIN will be able to measure it to a precision of  $5\sigma$  [41].

### 1.12.6 NO $\nu$ A

NO $\nu$ A is a long baseline neutrino experiment, currently producing new physics analyses [55]. NO $\nu$ A utilises Fermilab's NuMI accelerator neutrino beam to provide a supply of approximately 2 GeV energy neutrinos. The two detectors which comprise NO $\nu$ A are a near detector at Fermilab and a far detector based 810 km from the beam origin. Both detectors are made of planes of liquid scintillator stacked in a linear tunnel like geometry. The near detector weighs approximately 300 tonnes and has 18,000 instrumented channels. The far detector weighs 14,000 tonnes, 70% of which is active detector volume, and 344,000 instrumented detector cells. This configuration is very good at distinguishing electrons from  $\pi^0$  mesons. In 2016, NO $\nu$ A completed their first measurement of  $\nu_\mu$  disappearance in a  $\nu_\mu$  beam, using a 14 kton exposure of  $2.74 \times 10^{20}$  protons on target. Assuming the normal neutrino mass hierarchy, this analysis produced a measurement of  $\Delta m_{32}^2 = 2.52_{-0.18}^{+0.20} \times 10^{-3} \text{ eV}^2$  and a value for  $\sin^2 \theta_{23}$  in the range 0.38 to 0.65, both at the 68% confidence level [56]. The spectra and contour plots for this result are shown in Figures 1.20 and 1.21. This was shortly followed by an  $\nu_e$  [57] appearance measurement among others. Going forward, for the value of  $\theta_{13}$  determined by Daya Bay and others, NO $\nu$ A has about a 50% probability of being sensitive to the neutrino mass ordering.

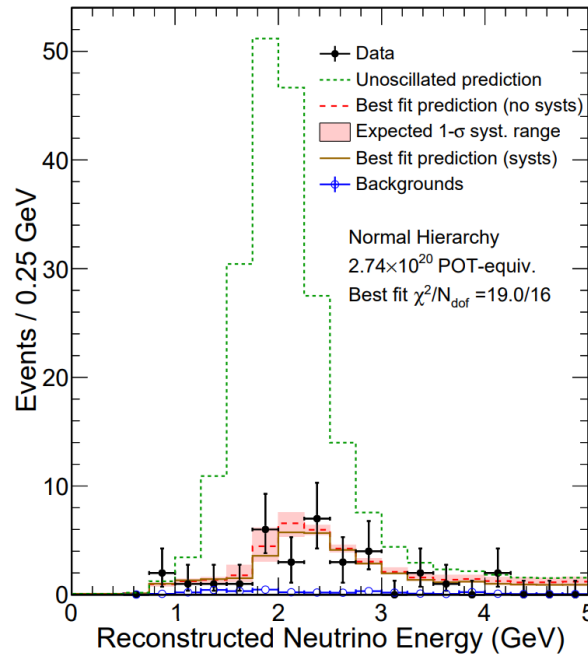


FIGURE 1.20: The reconstructed energy for far detector selected events. The black data points show the statistical uncertainties. The green histogram corresponds to the predicted unoscillated spectrum. The brown and red histograms represent best fit predictions including certain systematics. The blue points represent the backgrounds. [56].

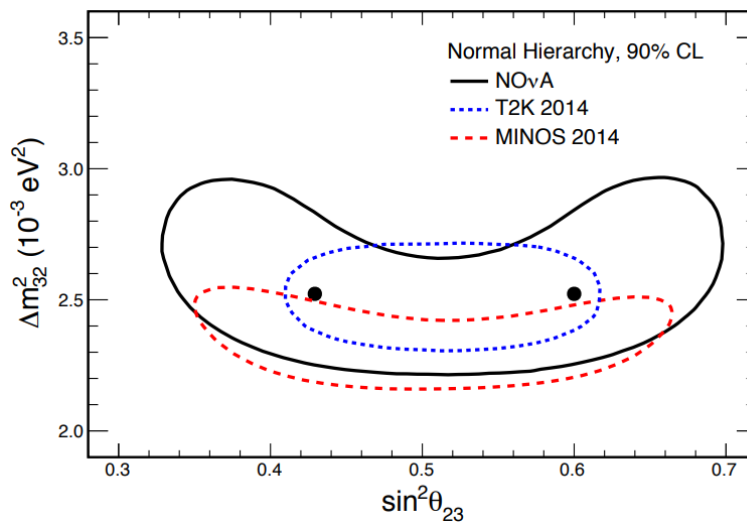


FIGURE 1.21: The best-fit (solid black circles) and allowed values (solid black curve) of  $\sin^2 \theta_{23}$  and  $\Delta m_{32}^2$  from this analysis assuming the normal mass hierarchy. The dashed contour lines are results from T2K and MINOS [56].

### 1.12.7 DUNE

The Deep Underground Neutrino Experiment (DUNE) is one of the primary global scale next generation neutrino experiments, self-described humbly as ‘An international mega-science project’ [58] and will be located at several sites in the United States. A beam of  $\nu_\mu$  will be produced using the Fermilab accelerator complex in Illinois, and is planned to be the most intense source of neutrinos on the planet. This beam will be directed across the country (approximately 1300 km), through the Earth’s crust to an instrumented multi-kiloton volume of liquid argon located at the Sanford Lab in South Dakota. The current far detector design is for four modules of instrumented liquid argon with a fiducial volume of 10 kilotons each. The first two modules are expected to be complete in 2024, with the beam operational in 2026. The final module is planned to be operational by 2027. Excavation of the cavities to house these modules began in July 2017.

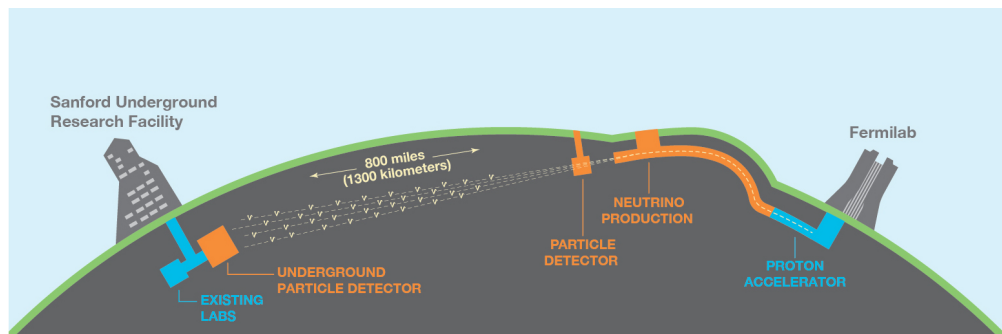


FIGURE 1.22: Schematic of the proposed DUNE experiment, showing the initial accelerator at Fermilab, followed by the near and far detectors.

DUNE’s prospective physics goals are many, including : gaining a more thorough understanding of neutrino oscillations via precision measurement of the PMNS parameters, an investigation of CP violation in the lepton sector, searches for proton decay, a determination of the neutrino mass ordering, and even a potential glimpse into core collapse supernovae in the Milky Way, essentially peering inside a newly formed neutron star or even seeing the genesis of a black hole. A determination of the mass ordering in DUNE would be possible due to probing the effect of matter enhanced neutrino oscillations, which should be significant for DUNE’s 1300 km baseline. As mentioned

previously, a discovery of CP violation in the lepton sector would be an important discovery for modern physics, and can be achieved in next generation experiments such as DUNE and Hyper-K by the comparison of neutrino oscillations in matter and anti-matter regimes. Specifically, this could be achieved by making precision measurements of  $\nu_\mu$  to  $\bar{\nu}_\mu$  and  $\nu_e$  to  $\bar{\nu}_e$  oscillations, and probing for differences.

### 1.12.8 Hyper-Kamiokande

On the other side of the world to DUNE, the natural successor to the T2K experiment, Hyper-Kamiokande (Hyper-K) is being designed. Another large next generation neutrino experiment, it will be a third generation water Cherenkov detector based in Japan. The first target tank is planned to be 260 kton in mass, which is more than ten times the fiducial volume of Super-K [59]. A second tank is projected for construction 6 years after the first. In addition to this there is a planned beam upgrade to 1.3 MW power which will be achieved via a magnet upgrade and increased repetition rate. This high powered beam will significantly increase the physics potential of the experiment. Hyper-K will also benefit from use of upgraded near detectors (INGRID and ND280), as well a new intermediate detector, E61, which will help to further constrain flux uncertainties and explore other physics such as neutron production using gadolinium doping and 4 off-axis effects on final state kinematics and reconstructed neutrino energy. Hyper-K will also utilise new designs of PMTs by Hamamatsu, which benefit from years of knowledge and experience of Super-K's electronics. The second tank is being considered for construction in Korea, which would allow for studies at a significantly larger baseline. Both DUNE and Hyper-K expect sensitivity to  $\delta_{CP}$  of  $5\sigma$  in the same areas of phase space.

The physics goals of Hyper-K are similar to DUNE and are competitive in that arena, with expected  $3\sigma$  results for CP violation and a determination of the neutrino mass hierarchy within 5 years of running. The long sought after signal of proton decay may also be found, with sensitivity to the signal significantly extended (from Super-K) up to  $10^{35}/10^{34}$  years lifetime for the  $p \rightarrow e^+ \pi^0$  / ( $p \rightarrow \bar{\nu} \bar{K}^+$ ) mode.

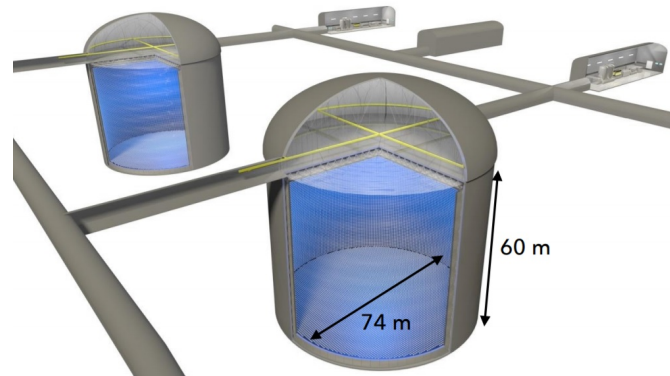


FIGURE 1.23: A recent proposal for the detector tanks of Hyper-K. Filled with ultra pure water, doped with gadolinium and lined with cutting edge technology PMT detectors [59].

### 1.12.9 Other Key Neutrino Experiments

The Kamioka Liquid Scintillator Antineutrino Detector (KamLAND) is an electron antineutrino detector at the Kamioka Observatory. The detector is located in a mine shaft in the old KamiokaNDE cavity. The site is surrounded by 53 Japanese commercial nuclear reactors. Nuclear reactors produce  $\bar{\nu}_e$  during the decay of radioactive fission products in the nuclear fuel. The isotropically emitted  $\bar{\nu}_e$  flux decreases as the inverse square of distance from the reactor. The detector is sensitive to the  $\sim 25\%$  of  $\bar{\nu}$  from nuclear reactors which exceed the threshold energy of 1.8 MeV and thus produces a signal in the detector. KamLAND started to collect data on January 17, 2002. First results were reported using only 145 days of data. Without neutrino oscillation,  $86.8 \pm 5.6$  events were expected, however, only 54 events were observed. KamLAND confirmed this result with a 515 day data sample, in which 365.2 events were predicted in the absence of oscillation, and 258 events were observed. These results established antineutrino disappearance at 99.6% statistical significance [60].

The Borexino experiment is designed to study low energy solar neutrinos. The detector is the world's most radio-pure liquid scintillator calorimeter. It is placed within a stainless steel sphere which holds the signal detectors (photomultiplier tubes and PMTs) and is shielded by a water tank to protect it against external radiation and

tag incoming cosmic muons that manage to penetrate the overburden of the mountain above. The primary aim of the experiment is to make a precise measurement of the individual neutrino fluxes from the Sun and compare them to the Standard solar model predictions. This will improve understanding of the functioning of the Sun (e.g., nuclear fusion processes taking place at the core of the Sun, solar composition, opacities, matter distribution, etc.) and will also help determine properties of neutrino oscillations, including the MSW effect. Specific goals of the experiment are to detect beryllium-7, boron-8, pp, pep and CNO solar neutrinos as well as  $\bar{\nu}$  from the Earth and nuclear power plants. It may also be able to detect neutrinos from supernovae within our galaxy.

Double Chooz is a short-baseline neutrino oscillation experiment in Chooz, France. Its goal is to measure or set a limit on the  $\theta_{13}$  mixing angle. The experiment uses reactors of the Chooz Nuclear Power Plant as a neutrino source and measures the flux of neutrinos they receive. To accomplish this, Double Chooz has a set of two detectors situated 400 m and 1050 m from the reactors. Physics data has been taken at both the near and far detectors since the beginning of 2015. In November 2011, first results of the experiment were presented, hinting at a non-zero value of  $\theta_{13}$ . In a 2012 result, utilising 228 days of data,  $\theta_{13}$  was measured and the no oscillation hypothesis was excluded at  $2.9\sigma$  significance [62].

## Chapter 2

# The T2K Experiment

The T2K experiment is a long baseline neutrino experiment designed to investigate flavour changing neutrino oscillations [25]. This is achieved by generating an intense beam of (anti-)muon neutrinos at the J-PARC facility in Tokai and directing this beam across Japan to the Super-Kamiokande detector where its composition and intensity are measured. The beam content and flux are also measured at the ND280 (Near Detector at 280 m) complex, which lies 280 m down the beam-line from its origin and  $2.5^\circ$  off-axis (which is explained in Section 2.3). Sampling the beam at this point provides valuable information about the initial beam spectrum, composition and intensity, which can be compared to results collected at the Super-K detector (295 km away and also  $2.5^\circ$  off-axis). The experiment searches for the disappearance of  $\nu_\mu/\bar{\nu}_\mu$  and appearance of  $\nu_e/\bar{\nu}_e$  in an initially predominantly  $\nu_\mu/\bar{\nu}_\mu$  beam. In 2013, a paper was published confirming that  $\nu_\mu$  to  $\nu_e$  oscillations had been observed, with  $7.3\sigma$  significance and a total of 28  $\nu_e$  events detected [64]. This was the first direct observation of  $\nu_\mu$  to  $\nu_e$ .



FIGURE 2.1: Figure showing the total baseline for the T2K experiment. Beginning at the J-PARC accelerator complex in Tokai, Ibaraki and ending at the Super-Kamiokande detector near the city of Hida in the Gifu prefecture [65].

## 2.1 Experiment Running

Commissioning of the T2K experiment began in April 2009 and the first physics beam data was collected in January 2010. Operation of the experiment was temporarily suspended after the major earthquake of March 2011, which had negative implications for both the experiment and the whole country. A thorough status check was carried out and necessary repairs were completed by early 2012, when T2K began data taking once again. There was another interruption in running over 2013 - 2014, due to an accident in another experiment's beamline. This interruption corresponded with a LINAC (linear accelerator) upgrade, which lessened the impact on physics data taking. Operations resumed in May 2014, including the first anti-neutrino data. By early 2015, the J-PARC neutrino beam was operating routinely at power levels above 300 kW. Most recently, T2K has been running at power levels of 460 kW in anti-neutrino mode, as shown in Figure 2.2.

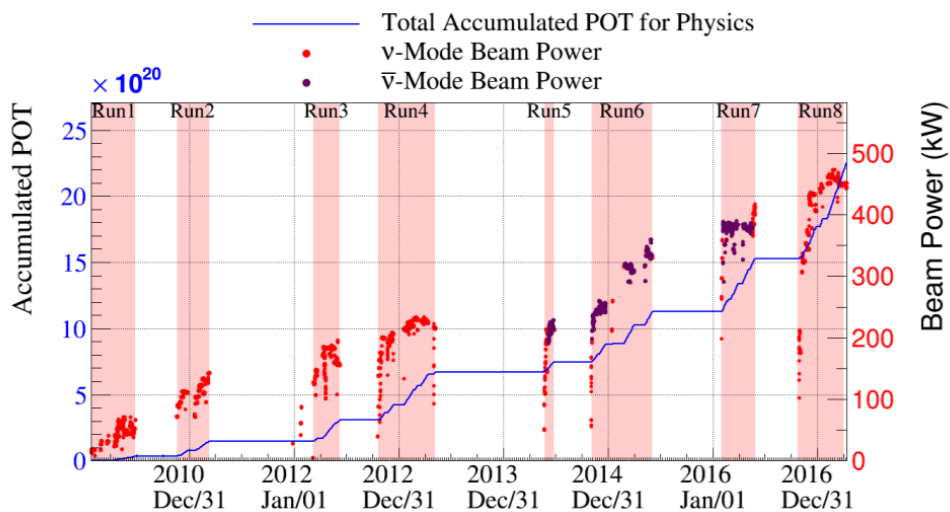


FIGURE 2.2: Figure showing accumulated protons on target over time (in blue), with neutrino mode (red) and anti-neutrino running (purple). Periods of no running can be seen, in particular two which correspond to the incidents mentioned above [65].

## 2.2 Physics Goals

The goal of the T2K experiment has always been to explore physics beyond the Standard Model and gain a more complete understanding of neutrino oscillation parameters. Two primary goals of T2K were the discovery of  $\nu_\mu$  to  $\nu_e$  oscillations and the measurement  $\theta_{13}$ . Other neutrino experiments (discussed in Chapter 1) observed the disappearance of  $\nu_\mu$  in a beam, but oscillation from  $\nu_\mu$  to  $\nu_e$  was not observed until July 2013 by T2K. The reason for this is that the mixing angle  $\theta_{13}$ , which determines the probability of this particular oscillation, is very small (See Table 1.1). Another physics goal was the precision measurement of the oscillation parameters involved in  $\nu_\mu$  disappearance down to  $|\delta\Delta m_{23}^2| = 10^{-4}\text{eV}^2$  and  $\delta(\sin^2 2\theta_{23})=0.01$ , which has been achieved. A third physics goal was the search for a sterile component in  $\nu_\mu$  disappearance, achieved by detecting neutral current events. This sterile component was ruled out at the 95% confidence level at ND280 in the  $\sin^2 2\theta_{ee} > 0.2$  and  $\Delta m_{41}^2 > 8\text{eV}^2$  region of phase space [66], which LSND and MiniBooNE suggested may contain sterile neutrino oscillations in a minimally extended 4-neutrino flavor framework. Further T2K results are discussed in Section 2.7.

The continued running goals of T2K include the determination of the octant to which  $\theta_{23}$  belongs, further understanding of cross-section models for  $\nu/\bar{\nu}$  interactions, and  $\bar{\nu}_e$  appearance in a  $\bar{\nu}_\mu$  beam. In addition to this, as with many experiments, longer running leads to better understanding of systematic uncertainties, allowing tighter constraints on physics measurements. A second stage of the experiment is envisaged. T2K-II is planned, with an upgrade of the beam to 1 MW power with an extended run at T2K for  $20 \times 10^{21}$  POT, allowing a more comprehensive search for the CP violation parameter,  $\delta_{CP}$  using T2K-II and combined reactor results [67]. T2K-II will increase the total running from  $7.8 \times 10^{21}$  protons-on-target to  $20 \times 10^{21}$  protons-on-target, and aims for an initial observation of CP violation with  $3\sigma$  or higher significance for the case of maximum CP violation. A schematic showing the positioning of the beam complex and Super-K detector of T2K is shown in Figure 2.3.

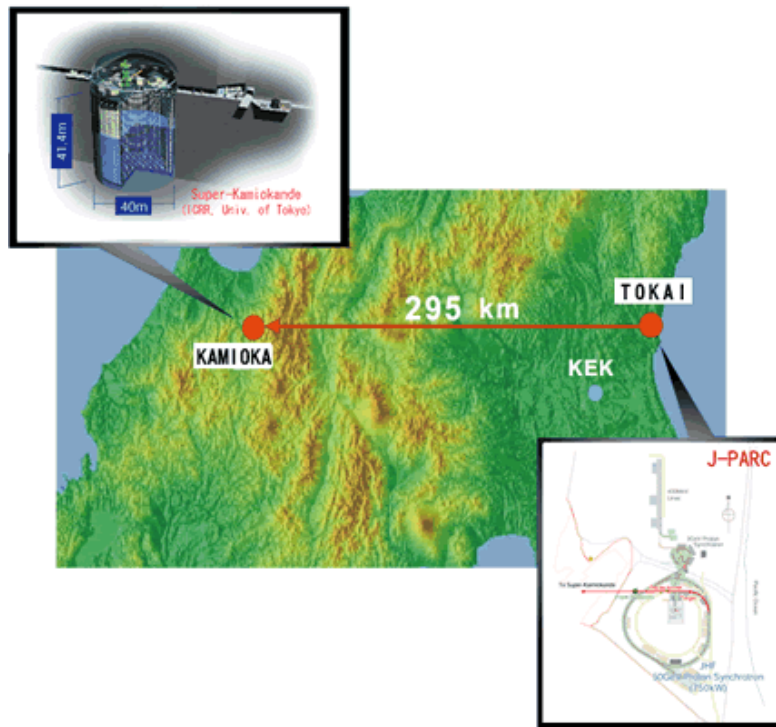


FIGURE 2.3: A map of Japan with the J-PARC facility in Tokai on the east coast and the Super-K detector 295 km away in Kamioka [25].

## 2.3 J-PARC Accelerator Complex

The J-PARC (Japan Proton Accelerator Research Complex) facility is located in Tokai, Ibaraki, Japan. It is a joint project between the High Energy Accelerator Research Organisation and the Japan Atomic Energy Agency. The particle accelerators based here are used to generate the neutrino beam, which is directed at a  $2.5^\circ$  angle to the ND280 and Super-K detectors [25]. An aerial view of the accelerator complex is shown in Figure 2.4.

The neutrino beam is created by first accelerating protons in the LINAC up to 400 MeV, then passing these into the Rapid Cycling Synchrotron (RCS) up to 3 GeV and the final stage of acceleration is in the Main Ring Synchrotron (MRS) which can accelerate the H-ions. up to 30 GeV. Once the protons have reached maximum energy they are extracted using a magnetic guiding system. Each proton beam ‘spill’ is split into eight bunches and these are directed towards a graphite block, which then produces

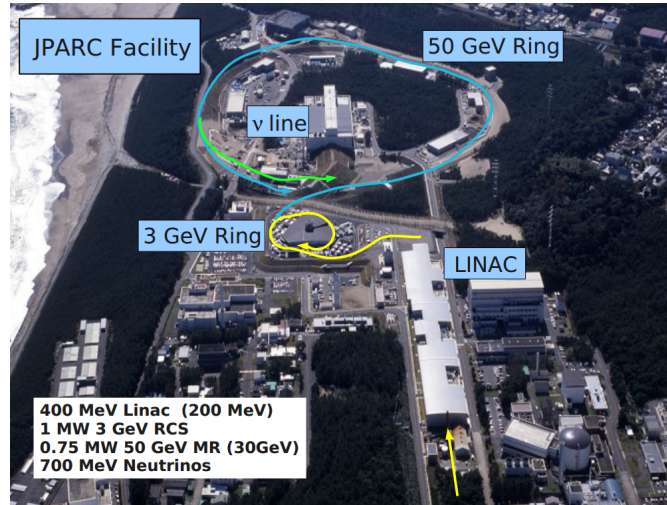


FIGURE 2.4: An aerial view of the J-PARC facility in Tokai. Outlined on the image are different stages of the accelerator used in the T2K experiment. The off-axis neutrinos from this accelerator have an energy range of 600 MeV to 800 MeV [68].

secondary hadrons, predominantly pions and kaons. These pions are preferentially selected and focused by a series of magnetic horns and subsequently decay to produce neutrinos [25]. An example of this is shown in Figure 2.5.

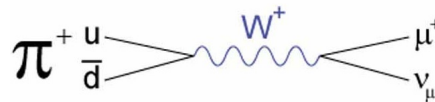


FIGURE 2.5: A Feynman diagram for pion decay, producing anti-muons and muon neutrinos [69].

The charge of the pion determines whether a  $\nu_\mu$  or  $\bar{\nu}_\mu$  is produced in its decay. By changing the horn polarity, a  $\pi^-$  can be selected, resulting in a  $\bar{\nu}_\mu$  beam. This can be of great benefit when investigating CP violation, as explained in Chapter 1. The T2K experiment will be spending a significant portion of its running time in the near future running in  $\bar{\nu}_\mu$  mode. The charged (of chosen polarity) meson beam then enters a long helium filled decay volume. The decay volume is constructed of thick steel walls surrounded by concrete shielding. Water cooling keeps the steel and concrete below 100 °C. Most of the charged meson beam decays within this volume, predominantly via:

$$\pi^+ \rightarrow \mu^+ + \nu_\mu \quad (2.1)$$

or

$$\pi^- \rightarrow \mu^- + \bar{\nu}_\mu \quad (2.2)$$

in the case of  $\bar{\nu}_\mu$  beam production.

At the end of the decay volume lies the beam dump. This is a water cooled block of graphite, which weighs 75 tons, along with 15 iron plates with a combined depth of 2.40 m. Only muons with an energy greater than approximately 5 GeV are able to penetrate this [70]. As the number of protons hitting the target is directly correlated to the number of charged-pions produced, and this in turn is directly correlated to the number of neutrinos produced, we can see the direct proportionality between Protons On Target (P.O.T) and total number of neutrinos produced.

### 2.3.1 Neutrino Beam Energy

The maximum sensitivity to the oscillation parameters is achieved by tuning the neutrino beam energy to the oscillation maximum for the T2K baseline. The oscillation maximum occurs at a neutrino energy ( $E_\nu$ ) less than 1 GeV for the 295 km baseline with  $\Delta m_{23}^2 \sim 3 \times 10^{-3} \text{ eV}^2$ . The narrower band flux at the off-axis angle and the neutrino survival probability is shown in Figure 2.6.

The energy of the neutrino beam produced using the aforementioned methods is shown in Eq. 2.3.

$$E_\nu = \frac{m_\pi^2 - m_\mu^2}{2(E_\pi - p_\pi \cos\theta)} \quad (2.3)$$

where  $m_\pi$  and  $m_\mu$  are the masses of the pion and muon,  $E_\pi$ ,  $p_\pi$  and  $\theta$  are the energy, momentum, and angle of the pion relative to the muon direction, respectively.

Figure 2.6 illustrates that by choosing a  $2.5^\circ$  off-axis angle, it is ensured that a narrow band beam is produced, at the energies required, calculated using 2.3. This can be

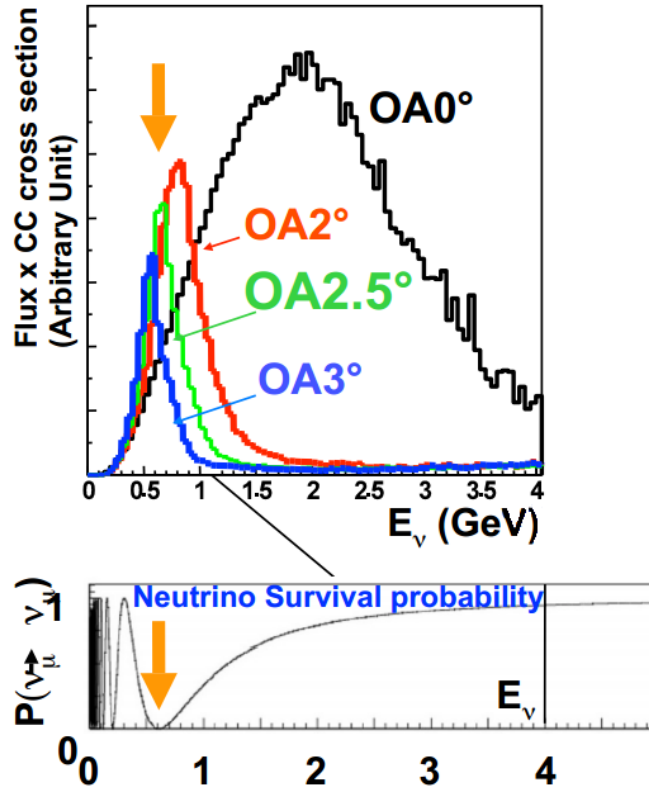


FIGURE 2.6: A plot illustrating the narrow spread of energies at an off-axis angle of  $2.5^\circ$ . It also shows the minimum survival probability for  $\nu_\mu$  at that off-axis angle and T2K energy range. This represents a maximal chance of oscillation from  $\nu_\mu$  to  $\nu_e$  [71].

tuned to the oscillation maximum such that those neutrinos in our energy range of interest have a high probability of oscillation whereas the long high energy tail represents those which have very little chance of oscillation.

### 2.3.2 Beam Contamination and Helicity Suppression

As stated, there is a small contribution of kaons to the the charged meson beam, produced when protons collide with the target. These will decay via either of the following, producing on average higher energy neutrinos than their pion counterparts:

$$K^+ \rightarrow \mu^+ + \nu_\mu \quad (2.4)$$

$$K^+ \rightarrow \mu^+ + \nu_\mu + \pi^0 \quad (2.5)$$

Additionally there is a small background contamination from :

$$K^+ \rightarrow e^+ + \nu_e + \pi^0 \quad (2.6)$$

$$\mu^+ \rightarrow e^+ + \nu_e + \bar{\nu}_\mu \quad (2.7)$$

There is also a background from the following :

$$\pi^+ \rightarrow e^+ + \nu_e \quad (2.8)$$

which occurs in  $< 1.3 \times 10^{-4}$  of cases. This mode could be expected to be the main decay mode of the pion, but it is heavily suppressed due to spin and helicity considerations.

A charged (positive in this case) pion has spin zero, therefore the anti-lepton and neutrino must be emitted with opposite spins to preserve net zero spin and conserve angular momentum. However, because the weak interaction is sensitive only to the left chirality component of fields, the neutrino always has left chirality, which means it is left-handed, since for relativistic particles the helicity is the same as chirality. This means that the anti-lepton must be emitted with spin in the direction of its linear momentum (i.e. also left-handed). However, considering the case if the anti-leptons were massless, they would only interact with the pion via the weak force in the right-handed form (because for relativistic particles helicity is opposite to chirality) and this decay mode would be prohibited. The anti-leptons are not always relativistic, so it is not required for the helicity to be exactly opposite. Therefore, suppression of the  $e^+$  decay channel comes from the fact that its mass is much smaller than the  $\mu^+$ . The  $e^+$  is relatively massless compared to the muon, and thus the  $e^+$  mode is highly suppressed.

The overall prediction for the T2K beam flux, showing relative flavour fractions for neutrinos and antineutrinos at Super-K is shown in Figure 2.7.

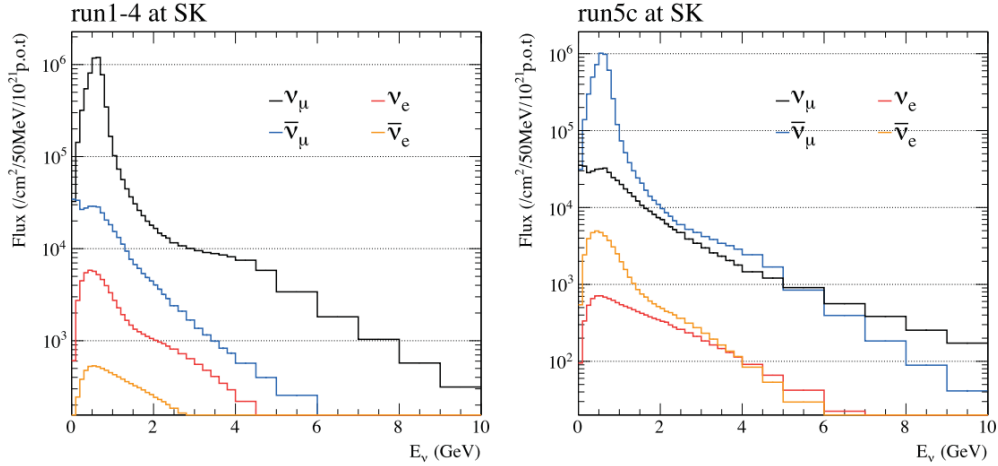


FIGURE 2.7: T2K beam flux prediction, showing relative flavour fractions for neutrinos and antineutrinos at Super-K. The left plot is for the neutrino beam mode made by focusing the positively charged particles, and the right is for the anti-neutrino mode made by focusing the negative ones [72].

## 2.4 Super-K Detector

The Super-K detector is a neutrino observatory, located near the Kamioka section of the city of Hida in Gifu prefecture, Japan [73]. It is located 1000 m under Mount Ikeno and consists of a cylindrical stainless steel tank filled with 50,000 tonnes of ultra pure water. Mounted around the detector are approximately 11,000 photomultiplier tubes (PMTs) which can detect tiny flashes of light in the large water volume. A schematic of the Super-K detector is shown in Figure 2.8.

When a neutrino from a natural source or from the neutrino beam interacts with electrons or nuclei in the water, a charged particle can be produced. If this charged particle is travelling faster than the local speed of light in that medium (i.e. ultra pure water), a cone of light is produced. This is known as ‘Cherenkov Radiation’ [74]. The Cherenkov light cone projects a ring on to the wall of the detector. This is detected by the PMTs and a recorded ring is reconstructed by the software. If the event is caused

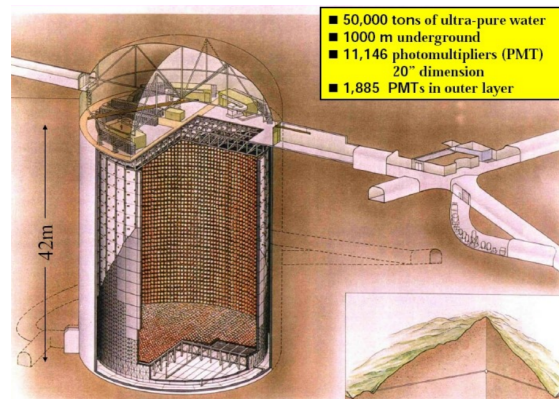


FIGURE 2.8: A schematic view of the SuperK detector in Kamioka. Outlined on the image are various important features of the detector used in the T2K experiment [68].

by an electron-neutrino, in the charged-current case it will produce an electron in the interaction. Due to electromagnetic scattering in the water with atomic electrons, this results in a fuzzy ring projected on to the wall of the detector. If the event is caused by a muon neutrino, in the charged-current case then a muon will be created in the interaction. These are often highly relativistic and therefore travel in a straight line through the detector, creating a sharp edged ring in the detector. Example Super-K event displays of both of these typical cases are shown in Figure 2.9.

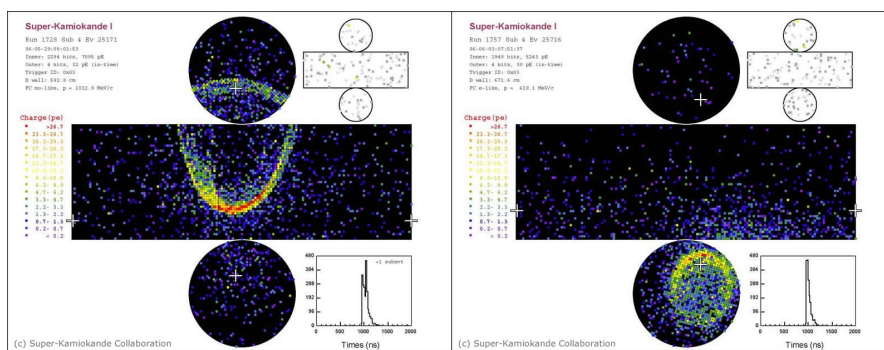


FIGURE 2.9: Example Super-K event displays from a muon-neutrino interaction (left) and electron-neutrino interaction (right) showing the characteristic sharp and fuzzy Cherenkov radiation rings for these interaction types. [75]

We know that neutrinos come in three weakly interacting flavours, and oscillate between these states. Therefore, we would expect some  $\nu_\tau$  to interact in Super-K and

produce charged  $\tau$  leptons. However, this does not happen commonly for three primary reasons : the mass of the  $\tau$  is large (1777 MeV) and thus a neutrino would require a significant amount of energy to produce a  $\tau$  in a charged-current interaction. Most neutrinos produced by the T2K beam have a peak energy of 600-800 MeV, which is not sufficient to produce a  $\tau$  in a charged-current interaction. Therefore they could only be produced by neutral current modes, which are more difficult to detect due to the absence of a charged-lepton in the final state. Even if a  $\tau$  is produced, due to its large mass, it is unlikely that a  $\tau$  would reach super-local-luminal speeds in the detector, and given the  $\tau$  lifetime is very short ( $6.99 \times 10^{-13}$ s) it would be unlikely to emit Cherenkov radiation in that time. Nonetheless, Super-K has performed an analysis of atmospheric  $\tau$  neutrinos, reconstructing  $\sim 180.1 \pm 44.3$  (statistical)  $\pm_{15.2}^{17.8}$  (systematic) [76]  $\tau$  leptons produced in the 22.5 kton fiducial volume of the detector by tau neutrinos during the 2806 day running period. This was not achieved by direct observation of Cherenkov light from  $\tau$  leptons, but instead by selecting a statistical sample of the hadronic decays of  $\tau$  leptons using its multi-ring event sample.

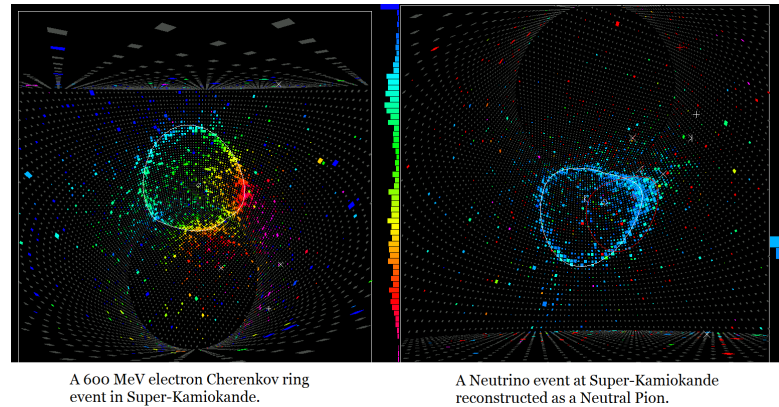


FIGURE 2.10: An electron ring (left) and a  $\pi^0$  fuzzy double ring (right) in the Super-K event display. The similarities of these structures is apparent, although the  $\pi^0$  does not fully occur within a much shorter time period (as indicated by the z-axis colours) [78].

$\pi^0$  particles can be reconstructed by Super-K, as the two photons produced by its decay ( $\pi^0 \rightarrow \gamma\gamma$  98.8% of the time [77]) create two separate electromagnetic showers,

which then produce electron-like Cherenkov radiation rings. These rings can be combined to reconstruct the original  $\pi^0$  meson (by recombining its decay products). However, in Super-K, if either of the decay photons is not energetic enough to produce an electromagnetic shower above the Cherenkov threshold, or the two electron-like Cherenkov rings indistinguishably overlap, then the event may be mis-identified as an electron-neutrino event. The Cherenkov threshold energies for Super-K are given for relevant particles here : Electron : 0.8 MeV, Muon : 160 MeV, Pion : 213 MeV, Proton : 1.4 GeV. Therefore  $\pi^0$  from Neutral-Current interactions are potentially one of the most significant backgrounds to electron-neutrino appearance searches by the T2K experiment, and one of the motivations for this analysis.

In 2013, a new method for event reconstruction in large Cherenkov detectors was developed called FiTQun [79], which then supplemented the existing set of reconstruction algorithms in Super-K. FitQun uses a likelihood fitting approach, utilising charge and time probability distribution functions and fitting using a number of kinematic variables (vertex position, track momentum, track direction) simultaneously. Before the implementation of FiTQun, 40% of the  $\nu_e$  appearance background was from  $\pi^0$ s [79], where the second photon was missed. The FitQun  $\pi^0$  fitter uses the result of a single track fit, yields an electron hypothesis, and then performs an additional fit, taking into account the momenta and conversion lengths of each decay photon. Using a 2D likelihood ratio vs  $\pi^0$  mass cut, this new approach removes 75 % of the remaining  $\pi^0$  background, without any depreciation in electron signal efficiency. Nonetheless, despite these significant improvements, it is still beneficial to understand  $\pi^0$  production in charged-current events, not only for further background reduction, but for a multitude of physics reasons, explored in the motivation section of Chapter 4.

## 2.5 ND280 Complex

The ND280 complex is split into two main detectors; the eponymously titled ND280 and INGRID (Interactive Neutrino Grid) [80]. INGRID lies directly in the beam line and therefore receives the largest flux at the highest spread of energies [81]. The ND280 detector lies 280 m from the beam origin at an off-axis angle of  $2.5^\circ$ . There is a well justified scientific case for this, which states that the neutrinos created with the energy spectrum of the off-axis beam are more likely to oscillate in transit. An off-axis beam also produces a narrower spread of energies which is tuned to maximise the oscillation probabilities at the required distance and energy. These effects can be clearly seen in Figure 2.6. The maximal oscillation from  $\nu_\mu$  to  $\nu_e$  at this distance and energy is due to the L/E factor in the survival probability equation, which was discussed in the introduction (Eq. 1.4). In this case, the beam energy peaks at 600 MeV to 800 MeV and at a distance of 295 km this provides a maximal probability of oscillation from a  $\nu_\mu$  to a  $\nu_e$ .

### 2.5.1 INGRID

Precision measurement of the  $\nu$  beam direction and intensity is achieved using modular  $\nu$  detectors. INGRID (Interactive Neutrino GRID) [81] is an on-axis near detector which consists of sixteen identical modules arranged in horizontal and vertical rows around the beam centre. The module has a sandwich structure of iron target plates and scintillator trackers. INGRID monitors the neutrino beam profile centre and intensity by using the number of observed  $\nu$  events in each module. The  $\nu$  beam direction is measured with accuracy better than 0.4 mrad from the measured beam centre. The normalised event rate is measured with 4% precision. INGRID is not directly used in this analysis, as it is focused entirely on the off-axis detector.

### 2.5.2 ND280

The off-axis near detector is located 280 m downstream of the target [80], shown in Figure 2.11. It is composed of a  $\pi^0$  Detector (P $\emptyset$ D), three Time Projection Chambers

(TPCs), two Fine Grain Detectors (FGDs), a Side Muon Range Detector (SMRD), three Electromagnetic Calorimeter (ECAL) modules enclose these, and it is all surrounded by a large magnet. The ND280 is used to sample the beam in order to determine its composition and intensity as well as to reduce total systematic errors in the experiment. An overview of these systematic errors for this analysis is discussed in Chapter 5.

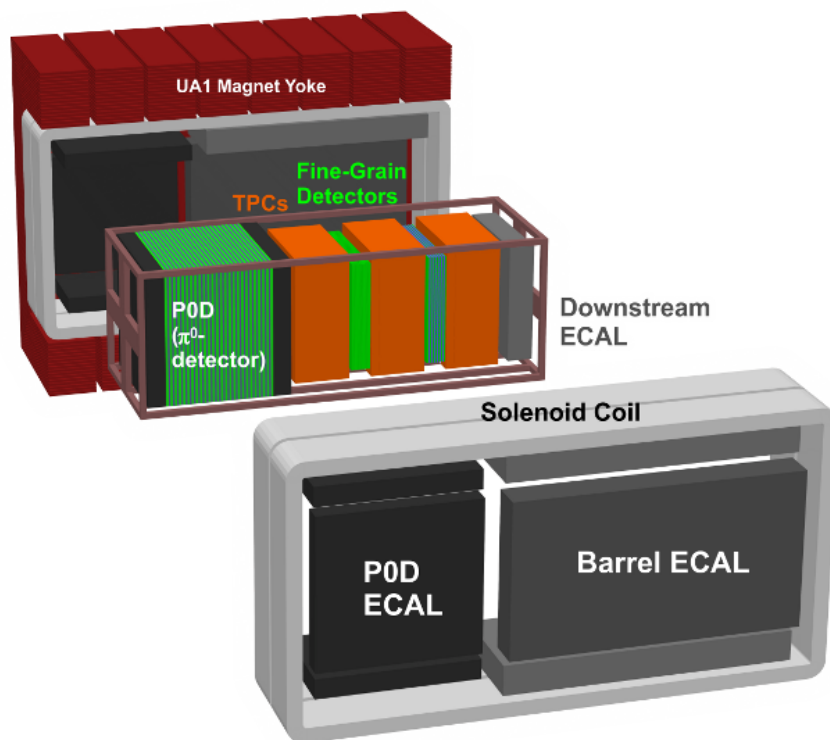


FIGURE 2.11: An exploded view of the ND280 detector, where each sub-detector can clearly be seen [80].

### UA1 Magnet

The detectors described in Section 2.5.2 are enclosed by the UA1 Magnet yoke and solenoid coils. The magnet is 4 m in height, and produces a field of 0.2 T. The resultant curved tracks of charged particles can be used to determine their charge and momentum [82].

### $\pi^0$ Detector

The P $\emptyset$ D [83] is used to detect  $\pi^0$  particles which immediately decay into two photons and is comprised of alternate layers of lead and brass and active plastic scintillator bars. The experiment can be run with the P $\emptyset$ D filled with water, giving a total cross-section of neutrinos on water + carbon + brass, or without water, giving a total cross-section of air + carbon + brass. These cross-sectional measurements can be subtracted from one another to get a value of the cross-section on water (the air being negligible). Events which have interactions occurring in the P $\emptyset$ D are not considered for this analysis, the reasoning for this is explained further in Chapter 4.

### Time Projection Chambers

There are three large TPCs for charged-particle tracking. The TPCs contain a gas mixture of argon, tetrafluoromethane and isobutane in the proportions 95:3:2. This particular mixture was chosen for its high speed, low diffusion, and good performance with the micromegas detectors used in the TPC electronics. The gas mixture ionises as charged particles pass through, resulting in the release of electrons, which then drift to an electrified plate at the sides of the sub-detector, where they are detected as they cause a brief electric current. The TPC allows a measurement of the energy deposition over distance,  $dE/dx$ , along with charge identification from track curvature, thus a particle identification can be achieved. For example, the ionisation energy loss of electrons in 1 atmosphere of argon gas is roughly 45% larger than for muons in the momentum range of interest, leading to good discrimination between these particle types [84].

### Fine Grain Detectors

The FGDs are composed of active scintillator bars of cross-sectional size  $\sim 1 \text{ cm}^2$  and length  $\sim 1864 \text{ mm}$ . It could be compared with the P $\emptyset$ D but without the lead layers, to ensure that the mass is kept low, reducing scattering and increasing track resolution. The FGD has the following characteristics: it is capable of detecting almost all charged particles produced at the interaction vertex with good efficiency in order to determine

the type of interaction, it is thin enough that charged leptons penetrate into the TPCs (where their momenta and flavour can be determined), it is capable of distinguishing protons from muons and pions (see the pull plots in Subsection 4.5.10), and it contains  $\sim 1$  tonne of target mass for neutrino interactions in order to yield a sufficiently large sample of events. The FGD is capable of detecting all charged particles produced at the interaction vertex due to it being entirely constructed of the extruded polystyrene scintillator bars, which effectively convert particle energy deposition into light. The same bars are used in the ECal subdetector, which is described in much greater detail in Section 2.5.2 and Chapter 3 due to its central role in this analysis work and the T2K service work described. The energy-distance travelled profiles of common particles produced in the FGD are shown in 2.12. The second FGD (FGD2) is downstream of FGD1 and also contains water. This mirrors the target material of Super-K, thus removing the need for the understanding of complex nuclear effects when migrating from a cross-sectional measurement on one material to another. The combination of the FGDs and TPCs is known as the Tracker region of the ND280 detector [85]. FGD1 forms the target for this analysis, with forward going tracks and showers being reconstructed there and in the TPCs and ECals. The justification for this choice is explained further in Chapter 4. FGD2 was not used incorporated in this analysis due to time constraints, but this will be rectified in future work (see Chapter 7).

### Side Muon Range Detector (SMRD)

Scintillator bars have been placed in the iron magnet surrounding the rest of the detector modules, this forms the SMRD. Its main functions within the ND280 detector include the role of active veto detector and cosmic trigger, as well as being optimised for energy measurements of large angle muons which may be created via charged-current neutrino interactions in the inner detectors [86].

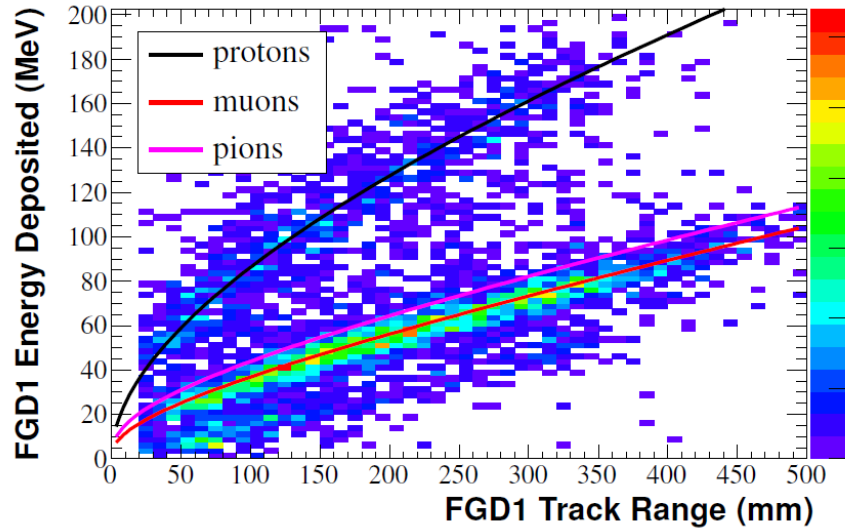


FIGURE 2.12: Reconstructed track range and energy deposited for tracks that stop in FGD1, having traversed more than three FGD1 layers. The data plotted is Run 1 and Run 2 ND280 data, with the expected energy loss curves based on Monte Carlo studies for muons, pions and protons overlaid [85].

### The Electromagnetic Calorimeter Modules (ECals)

The ECals are an integral part of the ND280 detector, essential in the reconstruction of neutral particles and the identification of charged particle species [87]. There are three ECals; the  $P\emptyset D$  ECal which surrounds the  $P\emptyset D$ , the Barrel ECal which surrounds the Tracker region and the Downstream ECal (DSECal) which is located at the far (i.e. downstream) end of the detector. The Barrel ECal is comprised of six modules in order to provide hermetic coverage of the tracker, as can be seen in Figure 2.13 and Figure 2.11.

The ECal is a lead-active scintillator sampling calorimeter, which means that a particle travelling through the lead is likely to interact and deposit energy in a nearby scintillator bar. The scintillator bars are composed of extruded polystyrene doped with organic fluors at concentrations of 1% PPO and 0.03% POPOP. This energy is converted into light and travels along the bar through a wavelength shifting fibre (WLS) to a Multi-Pixel Photon Counter (MPPC), converting the light to an electrical signal. The WLS fibres are used to collect the light produced in the scintillator bars. The plastic

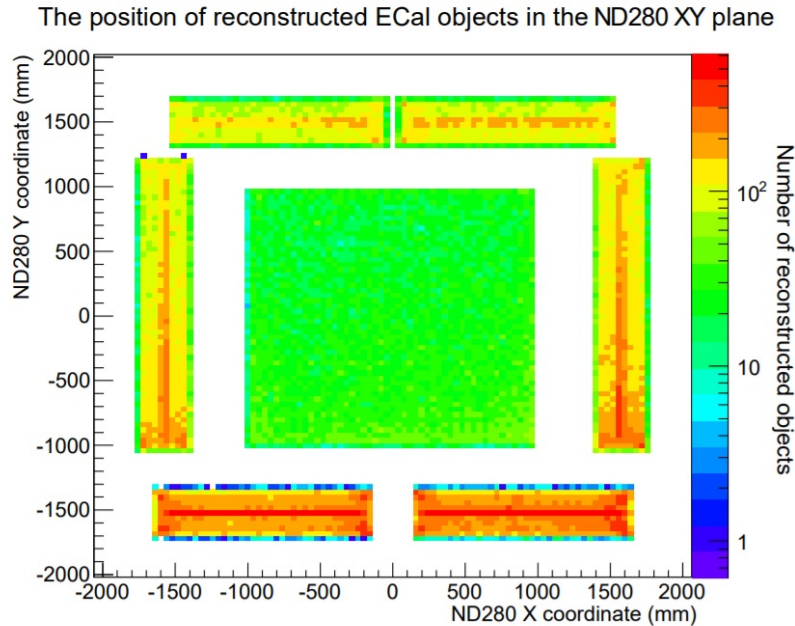


FIGURE 2.13: The charge-weighted positions of hits in the ECals (not including POD ECal) are shown. The position of the centre of the beam is to the lower right, and as a result, more events occur in the bottom right of the ECal than the top left.

in these fibres is doped with dyes which absorb the predominantly blue light from the scintillator and re-emit green light, to which the MPPCs are more sensitive. The MPPCs which readout the scintillator bars consist of many independent sensitive pixels, each of which operates as a Geiger micro-counter. The use of Geiger-mode avalanches gives them a gain similar to that of a vacuum PMT. The output of the device is the analogue sum of all the fired pixels, and is expressed in terms of a ‘pixel energy unit’ (PEU). A specially designed 667-pixel MPPC, with a sensitive area of  $1.3 \times 1.3 \text{ mm}^2$ , was developed for T2K by Hamamatsu [88]. The scintillator bars are positioned in alternating and perpendicular directions by layer, ensuring that a particle’s movement can be tracked in 3 dimensions.

As illustrated in Figure 2.14, the light from a particle interaction will travel down the scintillator bar and activate an MPPC, registering a signal. Up to 64 of these MPPCs or channels are connected to a Trip-T Front End Board (TFB) and up to 48 TFBs are read out by a Readout Merger Module (RMM) [87]. In the Barrel ECal, the shorter scintillator

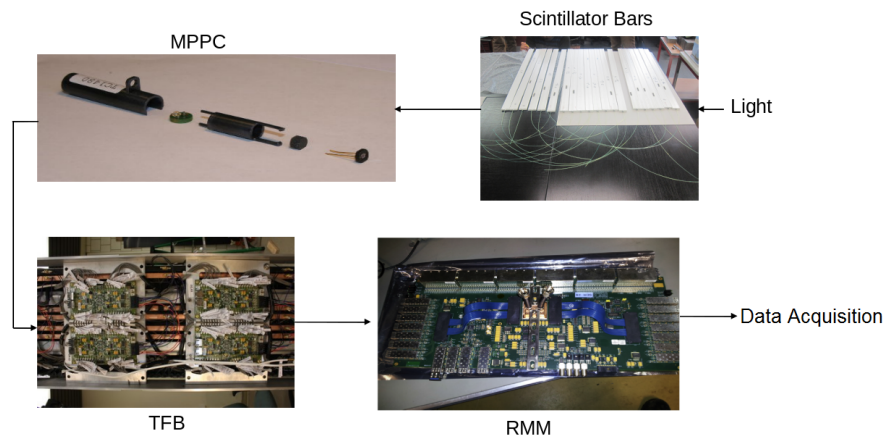


FIGURE 2.14: The flow of the signal from hitting a scintillator bar in the ECal, to the MPPC, a TFB and finally the RMM, before being read out to Data Acquisition.

bars run perpendicular to the beam direction whereas the longer scintillator bars run parallel to the beam direction. The shorter bars can only be read out from one end, whereas the longer bars are read out from both. In the DSECal, both configurations of bars run perpendicular to the beam direction, with all bars being read out at both ends. Further details about the ECal are included in Chapter 3.

## 2.6 ND280 Software and Neutrino Interaction Event Generators

The ND280 software has a modular structure of packages which perform specific tasks, a diagram of the software suite is shown in Figure 2.15. This structure reflects the modular nature of the ND280 detector, with each sub-detector group having control over packages specific to that sub-detector. It is predominantly written in C++ and Python and is split into two categories; online and offline. The online software is responsible for collecting the data and recording it into a readable format ready for later analysis. The offline software is run on the raw data recorded by the online software, and is responsible for calibration, reconstruction of particle and shower objects and their analysis.

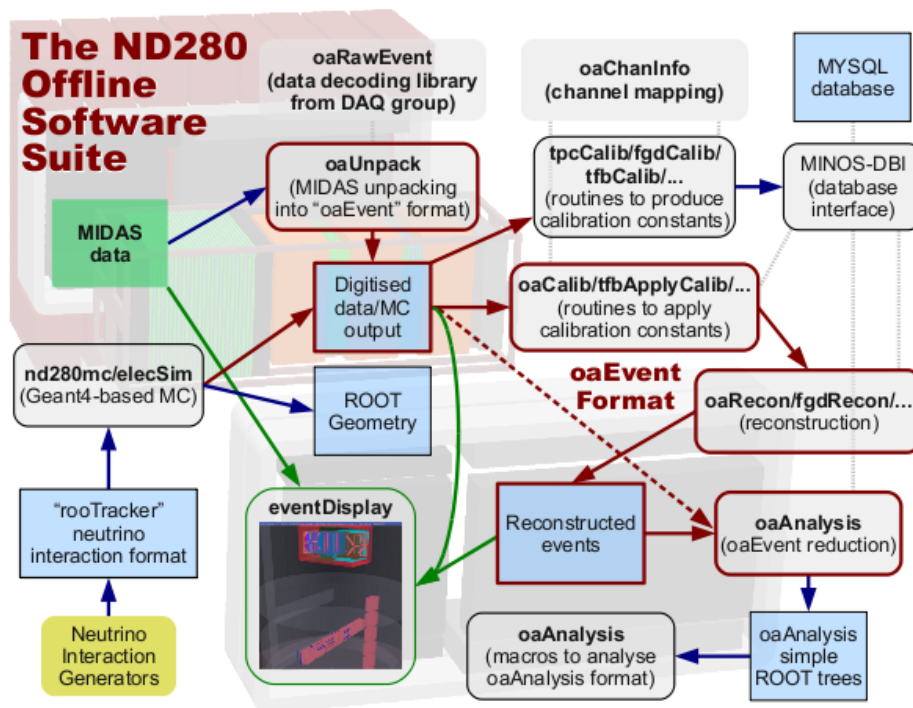


FIGURE 2.15: An overview of the various packages which comprise the T2K software, from the data/MC input stages through detector reconstruction and to the final analysis stage. [94]

### 2.6.1 Data Acquisition Software

The ND280 detectors use the Maximum Integrated Data Acquisition System (MIDAS) framework, which was developed as a general purpose data acquisition system for small and medium scale experiments [95]. As standard, MIDAS provides a complete DAQ system, the main features of which are: a front-end template for acquiring your hardware information, a data transfer mechanism to a local/remote computer, data logging capability, a data analysis framework, data monitoring, full run control, and a web interface for monitoring and controlling the experiment during running. This interface is regularly used by DAQ experts and DAQ shifters in the ND280 site control room. Other additional features which the ND280 takes full advantage of include: sub-runs, messages, history, alarms, and event notification. Despite these built-in features, extensive changes were still made for use with ND280.

### 2.6.2 ND280 Reconstruction

For the data, raw events are unpacked into a C++ based `oaEvent` format. This `oaEvent` format is used throughout the ND280 software chain until events are saved into purely ROOT-based objects (in `oaAnalysis`), which are then passed in flattrees or minitrees to be used by an analyst in Highland2. After some calibration, the events are then reconstructed, first on a sub-detector basis and then using a global reconstruction package. Finally, events are processed through the `oaAnalysis` package, which saves ROOT-based objects and significantly reduces the output file size. Highland2 extracts a cut down version of the pertinent information from these files, which can then be used by analysts to build selections, analyses, make plots and investigate the impact of systematics within that one framework. Highland2 is described in detail in Section 4.4 and the use of it throughout Chapter 4.

### 2.6.3 Tracker and Global Reconstruction

The ND280 tracker and global reconstruction uses routines provided by an external reconstruction toolkit called RecPack. RecPack provides a series of functions for track

fitting, propagation and matching between subdetectors, taking into consideration the ND280 geometry, the uniform magnetic field, multiple scattering effects and energy loss of particles. Firstly, the TPC reconstruction algorithms are applied to the calibrated data and MC for each individual TPC. This is done by simply grouping hits together if they are close in time and space and uses basic pattern recognition algorithms to join the groups of hits together. A likelihood fit is then performed on the fitted track to determine its coordinates, angle and curvature.

In addition, the ionisation energy released in the TPC gas as a function of the track length is calculated, which can be used later on for particle identification. In the next stage, the TPC tracks are used to seed FGD reconstruction, and a Kalman filter is used to incrementally match tracks from the TPC to hits in the FGD. Any hits which remain in the FGD after this incremental matching process are assumed to have no TPC component, and are reconstructed using algorithms that focus exclusively on the FGD. In the isolated FGD reconstruction, pattern recognition algorithms are used to group hits together in the two planar views (XZ and YZ). These two dimensional views are then matched to form a three dimensional track. The charge weighted position of any remaining hits or unmatched two dimensional tracks is saved. Finally, the tracker reconstruction algorithms use a Kalman filter to join all TPC and FGD tracks together. The track direction is determined using timing information from the FGDs. The purpose of the global reconstruction is to combine results from all subdetector reconstruction packages. An example event reconstructed in this fashion is shown in Figure 2.16. Attempts are made to match the reconstructed objects in the tracker to their neighbouring subdetectors (ECal and P $\emptyset$ D). This is done by extrapolating the tracker track into the subdetector in question and performing a search for reconstructed objects which reside close to the entry position of the track. Objects are successfully matched together if the resultant  $\chi^2$  of a fit performed using the position and direction of the object is less than 100. A loose time cut requiring reconstructed objects to be within 300 ns of each other is also made. Finally, the track is built using a Kalman filter and track properties such as the overall position, direction and momentum are recalculated, taking into account

expected energy losses and the individual reconstructed momentum for the objects. The global reconstruction repeats this procedure until no more objects can be matched together.



FIGURE 2.16: An ND280 data event showing (a) calibrated hits and (b) the globally reconstructed track. The event (number 146768) is from a beam spill trigger in ND280 run 6829, sub-run 34. The beam direction is from left to right. The track traverses the P0D, TPC1, FGD1, TPC2, FGD2, TPC3 and the DsECAL.

## 2.6.4 ECal Object Reconstruction

This section describes the barrel and downstream ECal reconstruction, which plays a large role in the analysis detailed in this thesis. ECal Reconstruction is performed by a package called `ecalRecon`, which takes as inputs calibrated hits, and outputs three dimensional reconstructed objects in a fashion similar to the track object reconstruction.

### Hit preparation

Each calibrated ECal hit has a recorded time and position in two dimensions based on the bar and layer location of the hit. At this stage in the reconstruction the position of the hit along the bar is not known. Therefore, hits can only be considered in two views, local XZ and local YZ. A minimum charge cut of 0.3 PEU<sup>1</sup> is applied to all calibrated hits before these are placed into groups of hits falling into 50 ns time window blocks. The recombination of the charge and time associated with a hit may be necessary if the bar containing the hit has double ended readout. All DsECAL bars and the longer BrECAL bars have double ended readout. For these bars, each hit may actually correspond to two calibrated hits, the charge and time of which are recombined and an estimate of the unknown coordinate is made. A correction is applied to account for the light attenuation in the WLS fibre and to equalise all the channels connected to a TFB. At this stage all charges are recorded in MIP equivalent units (MEU), which is the expected most probable value of charge deposited by a minimum-ionising particle (MIP) (1 MEU is approximately 25 PEU).

### 2D Clustering

Two dimensional clustering algorithms consider clusters in the (local) XZ and (local) YZ views separately. The hit in a given 50 ns group with the highest charge is used as a seed, and a search is carried out for nearby hits which may form a cluster. If a hit is within  $\pm 15$  ns of the seed, is in the neighbouring or next to neighbouring bar and is in

---

<sup>1</sup>PEU stands for pixel-equivalent units and is obtained by converting the charge from each MPPC sensor into a number of activated pixels.

the neighbouring or next to neighbouring layer, it is clustered with the seed hit. This process is then repeated iteratively, using every hit in the cluster as a seed. The second stage of clustering combines the clusters formed in the first step, provided there are three or more hits in that cluster. The cluster with the most hits is used as a seed and is combined with another if the mean hit time of the candidate cluster is within 40 ns of the seed. A discriminator, based on the width of the clusters and a charge weighted axis output from a principal component analysis (PCA), is also used. Finally, attempts are made to match any unclustered hits with the two dimensional clusters.

### 3D Clustering

A likelihood calculation is performed which uses as inputs the ratio of the charge of two clusters and the difference in starting layer. The result of this calculation is used to decide if two dimensional clusters should be matched to make one three dimensional cluster. The matching algorithm also considers any clusters produced from the tracker reconstruction as a seed. By forming the likelihood variable for all possible combinations of clusters, the best possible match is selected. There is an additional matching step, which makes attempts to associate unclustered hits with any two dimensional clusters which have not successfully matched to form three dimensional clusters. This step is important for the reconstruction of low energy particles (namely photons), where it is possible that only a single hit in one view and a cluster in the other is available. Any single hits are required to be within 10 ns of the mean cluster time, and restrictions on the layer containing the hit are :  $L_{Min} - 1 \geq L_{Hit} \geq L_{Max} + 1$ , where  $L_{Min}$  is the minimum hit layer of the two dimensional cluster and  $L_{Max}$  is the maximum. The built three dimensional clusters inform the position of the unknown coordinate for combined hit estimates and the initial attenuation corrections and MIP equalisation are reapplied based on the new reconstructed position of that hit.

### 2.6.5 Simulation

The simulation software for the ND280 can be split into four sections. The first is a beam generator (FLUKA) [97] which models the production of neutrinos starting with the proton beam colliding with the graphite target and concluding with meson decay in the decay chamber. The simulated hadron production is then passed to JNUBEAM [70], which models the secondary parts of the beamline such as the baffle, target and horn magnets. The next simulation package models neutrino interactions GENIE [101] and passes this information to (GEANT4) [98], which handles interactions inside the detector. The detector itself is then simulated, modelling the detector and how particles propagate and decay within it. Finally the electronic response of each detector is simulated. The output of these simulation packages mirrors the data output in the file format. This allows calibration, reconstruction and analysis packages to be run over both simulated data and real data reliably. More detail of the flux simulation is given in Section 5.3, due to its relevance to flux model tuning and uncertainty.

### 2.6.6 Neutrino Interaction Generation

A large amount of neutrino event data has been collected from a multitude of sources (solar, atmospheric, reactor, accelerator), at a number of experiments, allowing thorough analysis of neutrino oscillation phenomena and neutrino interactions with nuclei. Of course, in order to understand the underlying physical properties of these processes, sophisticated models need to be developed. In modern experimental neutrino physics, these come in the form of generators, which produce simulated data, based on computational models of neutrino-nucleus interactions, to which real data distributions may be compared [99]. These sophisticated models can be used to provide information on how signal and background events are handled in a given detector, in this case ND280. An ideal generator would perfectly simulate all possible interactions and nuclear effects, but this is not possible, due to limitations in our understanding of the underlying physical phenomena, and assumptions inherent in any generator. The nuclear effects, in particular, are a major problem when attempting to match models with data. An

example of this is the modelling of nuclear Fermi motion using effective spectral functions. Due to these issues, generators now attempt to model the full 4-momentum of any target nucleon, all outgoing leptons and all hadrons and gammas emitted from the target nuclei.

In this analysis, the various backgrounds as well as simulated  $\pi^0$  particles are simulated at given neutrino interaction vertices by NEUT. By constructing an analysis which can accurately assess the rate and particle kinematics of these interactions and comparing data to Monte Carlo, we can improve models and grow closer to fully understanding neutrinos and their interactions with nuclei.

The four primary modes of neutrino interaction modelled by generators are :

- Quasi-elastic scattering :  $\nu + N \rightarrow l + N^*$
- Production of mesons via resonance :  $\nu + N \rightarrow l + N^* + m$
- Coherent pion production :  $\nu + X \rightarrow l + \pi + X$
- Deep inelastic scattering :  $\nu + N \rightarrow l + N^*$  (Multiple Hadrons)

where  $N$  ( $N^*$ ),  $l$ ,  $m$ , and  $X$  denote nucleon (excited nucleus), lepton, meson and nucleus, respectively.

Event generators usually begin with free-nucleon cross-sections which are used as simplistic starting point in a more complex nuclear physics model. As stated above, the key processes are quasi-elastic (elastic for NC) scattering, resonance production, and non-resonant inelastic scattering, each of which make comparable contributions to interactions taking place in the few-GeV energy range.

### Quasi-Elastic Scattering

The interaction cross-section for neutrino induced charged-current quasi-elastic scattering is described in terms of the leptonic and hadronic weak currents, where dominant contributions to the hadronic current come from the vector and axial-vector form factors. There is also a pseudo-scalar term in the hadronic current, but this is small for  $\nu_\mu$

and  $\nu_e$ . The vector form factors required for this calculation have been measured by recent high precision electron scattering experiments and has been shown to have some deviation from the simple dipole form. As a consequence, most neutrino interaction generators use parametrizations of this form factor taken directly from the data. The axial form factor does not benefit from the same high precision experiments and most the generators use the dipole form. Generally, the value of axial form factor at  $q^2 = 0$  is extracted from the polarized nucleon beta decay experiment. However, the axial vector mass parameter varies with each generator, with values typically  $\sim 1.00 \text{ GeV}/c^2$ .

### Resonance Production

The majority of generators use the Rein-Sehgal description to simulate neutrino induced single pion production. To obtain the cross-section for a particular channel, they calculate the amplitude for the production of each resonance and multiply that by the probability for the decay of that resonance into that particular channel. Generators may vary in ways such as : the number of resonances included, whether the amplitudes are added coherently or incoherently, the invariant mass range over which the model is used, how non-resonant backgrounds are included, the inclusion of lepton mass terms, and the model parameter values (in particular the axial mass). In the Rein-Sehgal model, it is also possible to calculate the cross-sections of single photon, kaon and eta productions by changing the decay probability of the resonances, which are available in some of the generators. It is known that discrepancies exist between recent pion electro/photoproduction data and results from the simulation data with the same framework, i.e. the vector part of this model. There have been attempts to overcome this issue and some generators have started using more appropriate form factors. The GiBUU and NuWRO [102] generators do not use the Rein-Sehgal model, and instead rely directly on electro-production data for the vector contribution and fit bubble chamber data to determine the remaining parameters for the axial contribution. Similar methods of utilising experimental data from dedicated experiments are used to inform the T2K flux model and tuning, which is described in 5.3.1. Resonant production is one

of the primary mechanisms which results in neutral pions in the analysis described in this thesis.

### **Deep Inelastic Scattering**

For this process, the target shifts from the nucleon to its quark constituents. Therefore, generators use the standard expression for the constructions for the nucleon structure functions  $F_2$  and  $xF_3$  from parton distributions for high  $Q^2$  (the DIS regime) to calculate direction and momentum of lepton. Generators also include a handling of shallow inelastic scattering which takes place at lower  $Q^2$ . It is important that these processes are not confused or double counted, and efforts are made to ensure that these processes are understood distinctly. For this analysis, it is unlikely that shallow inelastic scattering would result in a significant portion of neutral pions, whereas DIS is a significant source.

### **Neutrino Event Generators**

There are several neutrino event generators available for use in an experiment. In the past, each experiment would develop their own event generators, which could easily lead to inconsistencies when comparing results on a global scale. NEUT [100] was developed initially for the Kamiokande experiment and adapted for integration with the experiments : Super-Kamiokande, K2K, SciBooNE and T2K. General purpose event generators, intended to be used across a multitude of experiments have been developed, including FLUKA and GENIE [101], with FLUKA including geometry handling as mentioned and GENIE handling neutrino interactions, and designed for use with a number of neutrino experiments including : ArgoNeut, MicroBooNE, MINOS, MINER $\nu$ A, and T2K. Another generator, NuWro began development in  $\sim$  2004 [102], and is capable of simulating neutrino interactions, taking into account beam profile and composition, detailed detector geometry as well as FSI in the nuclear target. Although it is not an official Monte Carlo generator for any experiment, it is widely used as a tool for development and testing of new physical models in MC generators. This analysis

was completed using Monte Carlo produced by the NEUT neutrino generator. The use of NEUT as part of this analysis and in terms of results is discussed further in Chapter's 2 and 6 respectively.

## 2.7 T2K Measurements

The T2K experiment has provided many valuable measurements since it began running. One important early measurement was the indication of electron-neutrino appearance from an accelerator produced off-axis muon neutrino beam in 2011 [103]. In these results, 6 electron-neutrino events were detected, compared with an expected  $1.5 \pm 0.3$  (syst). Further to this, a first muon neutrino disappearance study with the same off-axis beam was conducted [104]. This study found that with a beam of initially  $1.43 \times 10^{20}$  protons on target, only 31 fully contained muon events were seen at SuperK, compared with  $104 \pm 14$  expected events if there was no oscillation. This also helped to put further constraints on a number of mixing parameters. An important result was found in the electron-neutrino appearance in a muon neutrino beam study, published in 2013. In this study 11 electron-neutrino events were observed at the far detector, where only  $3.3 \pm 0.4$  were expected [105]. This was further corroborated later in that year with a more comprehensive observation of  $\nu_e$  in a  $\nu_\mu$  beam. In this instance, a total of 28 electron-neutrino events were detected with an energy distribution consistent with an appearance signal and corresponding to a statistical significance of  $7.3\sigma$  when compared to  $4.92 \pm 0.55$  expected events [64], see Figure 2.17. This result illustrated with great confidence that the mixing angle  $\theta_{13}$  is non-zero, and was in agreement with the existing Daya Bay measurement, which had been published in March 2012 [106].

In 2014, new data from T2K produced a high precision measurement of the mixing parameter  $\theta_{23}$  from muon neutrino disappearance in the beam [107]. It is important to understand the qualities of the beam being used in these measurements. It is known that the muon neutrino beam used has an intrinsic irreducible electron component ( $\sim 0.1\%$  of the flux) from the decay of muons and kaons (described in Subsection 2.3.2),

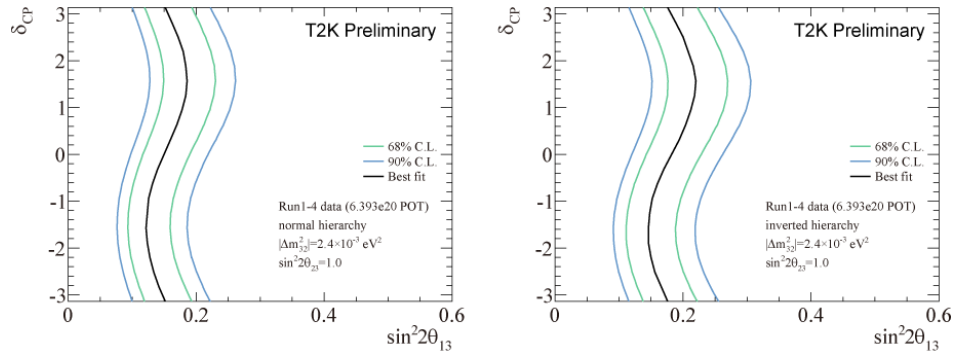


FIGURE 2.17: Results for the normal (left) and inverted (right) hierarchies. The areas between coloured lines show allowed regions of  $\sin^2(2\theta_{13})$  for each value of  $\delta_{CP}$  at 68% (green) and 90% (blue) confidence levels. The black solid line is the best fit value of  $\sin^2(2\theta_{13})$  for each assumed value of  $\delta_{CP}$  and the mass hierarchy [64].

which if misunderstood could give false results. In 2014, this component was measured using the ND280 [108]. These results indicated that previous predictions of this component were correct. All of the up to date known mixing parameters can be found in Table 1.1.

However, not all studies conducted at T2K are oscillation based. In 2013, T2K performed the first measurement of the  $\nu_\mu$  inclusive charged current interactions on carbon at neutrino energies of approximately 1 GeV [109], shown in Figure 2.18. T2K also performed the first differential cross-section measurements of electron neutrino charged current interactions at energies  $\sim 1$  GeV as a function of electron momentum, electron scattering angle and four-momentum transfer of the interaction [110], the total cross-section for which is shown in Figure 2.19.

While the scientific community has made great strides towards a complete understanding of neutrinos and their properties, there are still a number of remaining mysteries. One of the most pronounced of these is the absolute mass of neutrinos, as it is only possible to infer the squares of the differences between the mass states.

Another big question is that of CP violation and the measurement of  $\delta_{CP}$ . This is of tremendous importance in determining if neutrinos and leptogenesis had a major role in the matter/asymmetry in the Universe. If this is non-zero this could be the case, and measurements from T2K with constraints from reactor experiments in 2014 hinted at a

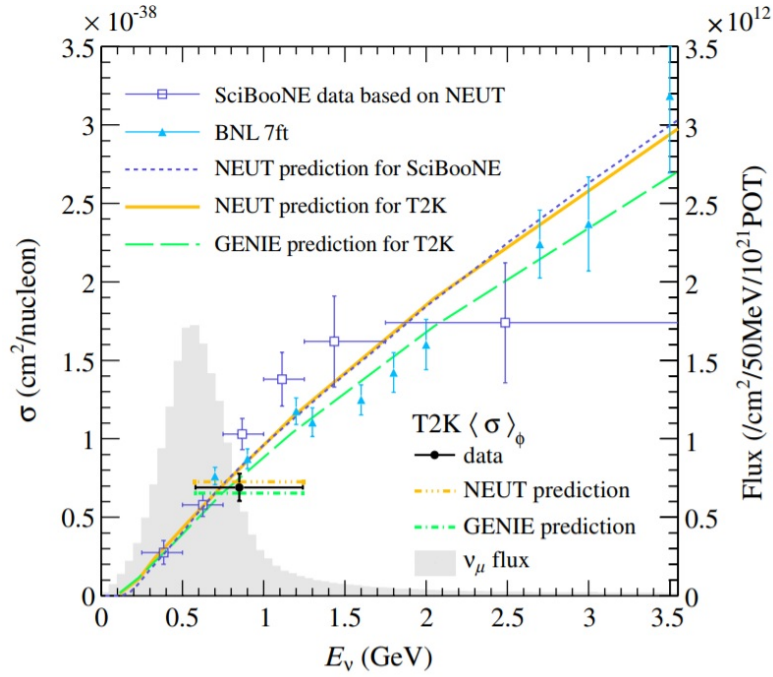


FIGURE 2.18: The T2K total flux-averaged cross-section with the NEUT and the GENIE prediction for T2K and SciBooNE. The T2K data point is placed at the flux mean energy. The vertical error represents the total (statistical and systematic) uncertainty, and the horizontal bar represent 68% of the flux at each side of the mean energy. The T2K flux distribution is shown in grey. [109]

best fit point of  $-\pi/2$  [111]. A recent announcement by T2K states that  $\delta_{CP}$  is non-zero, with 95% confidence [28], as illustrated in Figure 1.11 in Chapter 1.

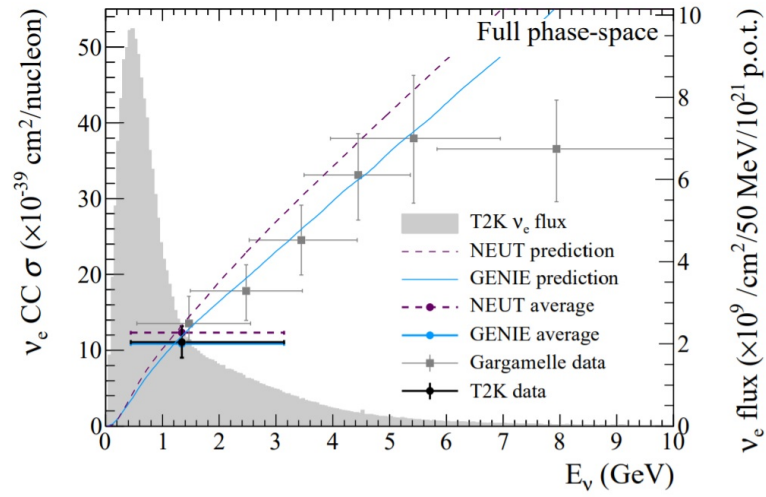


FIGURE 2.19: The total  $\nu_e$  CC inclusive cross-section for a wide range of neutrino energy. The T2K data point is placed at the  $\nu_e$  flux mean energy. The vertical error represents the total uncertainty, and the horizontal bar represents 68% of the flux each side of the mean. The T2K flux distribution is shown in grey. The NEUT and GENIE predictions are the total  $\nu_e$  CC inclusive predictions as a function of neutrino energy. The NEUT and GENIE averages are the flux-averaged predictions [110].



## Chapter 3

# Reconfiguring Mis-mapped Channels in the ECal

A comprehensive and systematic study of the mapping of each electronic channel to a specific scintillator bar location within the ND280 Electromagnetic Calorimeter [87] was performed. Several instances of an electronic channel being connected with the wrong Multipixel Photon Counter, and thus scintillator bar, were identified. Such a mis-mapping causes reconstruction of a particle's trajectory and energy deposition in the ECal to be inaccurate. In this work, 65 mis-mapped channels in the ECal have been identified out of a total possible 22336, and the issue was resolved at the software level.

### 3.1 Motivation

The ability of the ECal to detect events and for the software to reconstruct them accurately is very important for analyses using the ND280. The current reconstruction efficiency in the ECal at low energies ( $E < 100$  MeV) is very low and is presently under review. There is an effort in the ECal group [112] to improve the low energy reconstruction. The work detailed here has been part of ongoing efforts to improve this efficiency, by searching for incorrectly connected (i.e. mis-mapped) channels, so that this issue may be resolved at the software level. It would not have been possible to fix this issue at the hardware level as this would require removing all of the ECal modules, which would be expensive, impractical, and risk further damage to the detector.

## 3.2 Mis-mapped Channels

A particle is detected in the ECal when it deposits energy in a scintillator bar, which directs the light produced to a wavelength shifting fibre (WLS) and finally to an Multi-Pixel Photon Counter (MPPC). Each of these MPPCs corresponds to a ‘channel’ in the T2K event reconstruction software, and there are a total of 22,336 channels in the ECal [87]. When reconstructing objects such as showers or tracks, it is extremely important that all of these channels are connected correctly when a particle deposits energy in its corresponding bar. For example, it is possible that a channel would not register a particle ‘hit’ when has energy has been deposited, due to the response voltage of the channel being set too high. Conversely, channels could register hits when there are none, due to noise. Therefore, it is important to calibrate these channels so that their hit response is accurate and uniform.

Calibration of the ECal channels can be performed using cosmic rays. Because these sources are minimum ionising particles, the charge deposited in each bar should be the same, and bar to bar response calibration can be performed. Additionally, events used are ones which satisfy the the Trip-T ‘Cosmic Trigger’ [86], and these should conform to a well understood hit distribution. The cosmic trigger ensures that a through-going particle has entered at one detector face and exits at another detector face, which means that a transiting particle must hit every ECal layer <sup>1</sup> between those two points. Using this data we can create a two dimensional map of the channels (See Figures 3.5 and 3.6), which shows how many hits each channel registered in a period of time. By analysing this data, we can see that some channels register fewer hits than we would expect for cosmic data, when compared with neighbouring channels. This could be due to the bias voltage of the MPPC being miscalculated or other electronic noise issues.

However, there is another potential problem that could cause a seemingly incorrect response from the channels, which is not related to their calibrated sensitivity. It is possible that channels were ‘mis-mapped’ during detector construction. This means that

---

<sup>1</sup>There is a very low probability that a particle may slip between the bar gaps and therefore not be reconstructed

a given channel in the software will not necessarily correspond to the correct bar and layer in the physical detector. If we look at one of the two dimensional maps and locate a channel which does not seem to be responding appropriately, then it is plausible that this could be mis-mapped to a different physical channel in the ECal. For 22,336 channels it would be a potentially insurmountable task to correct these mis-mappings if they were not restricted to the same Trip-T Front End Board. Fortunately, due to the nature of the electronics in the ECal, the majority of readout cables available would not be of sufficient length to sensibly reach across TFBs, therefore it is unlikely that a channel would be swapped with one on another TFB. There were some instances of cross-TFB swaps, but these were fixed before this work began. There are up to 64 channels linked to each TFB and so any mis-mapping should be between one anomalous channel and any of the other 63 on that same board. The few that were mis-mapped across TFBs are geometrically obvious, and these have previously been rectified in the software at the `oaChanInfo` level.

### 3.3 Relevant ECal Electronics and Software

There are up to 64 channels on each TFB, which comprises four Trip-T chips, each reading in data for up to 16 channels. Each Trip-T chip is numbered 0 to 3 or A to D. There are between 26 and 44 TFBs on each RMM of the ECal, and a total of 12 RMMs. These RMMs make up different ECal modules, which are shown in Table 3.1.

Module Name	RMM Number	Number of TFBs
Downstream ECal	0	28
Downstream ECal	1	28
P0D ECal Left (South)	2	15
Barrel Top Left (South)	3	44
Barrel Bottom Left (South)	4	44
Barrel Side Left (South)	5	26
Barrel Side Left (South)	6	26
P0D ECal Right (North)	7	15
Barrel Side Right (North)	8	26
Barrel Side Right (North)	9	24*
Barrel Bottom Right (North)	10	44
Barrel Top Right (North)	11	44

TABLE 3.1: Name, RMM number and number of TFBs for each of the ECal modules. \*Two of these TFBs were lost in the 2011 earthquake.

RMM9 has 24 TFBs as two were lost in the 2011 Earthquake. Most of these modules have scintillator bars running parallel to the  $x, y$  and  $z$  dimensions of the ND280. However, the Downstream ECal has perpendicular bars in the  $x$  and  $y$  planes, all of which are double ended read out. Therefore, there are no single ended view plots in this work for the DS ECal.

A tool used extensively throughout this process was the Simple Track Fitter (STF) [114]. This basic reconstruction algorithm is used exclusively in the ECal subdetector, and produces simple tracks from data, in this case from cosmic events. As input, the

Simple Track Fitter takes in known quantities including: number of hits, number of layers, and upstream and downstream layer. These quantities are used to produce 2D clusters of hits which were then connected by a straight line, forming a simple track. This is a quick and simple tool to use, which was not designed to reconstruct every track, but to reconstruct clean and well understood tracks as quickly and accurately as possible. This was a very effective tool in this process, as it was able to cleanly differentiate between hits forming a track (and retain those) and those hits outside of a basic track.

RMM2 and RMM7 are excluded from this analysis. These RMMs readout the P $\emptyset$ D ECal, in which the bars/layers have a very different geometry, with all bars running parallel to the beam direction and therefore no third dimensional position marker. Simple Track Fitter was therefore not previously used on the P $\emptyset$ D ECal. Since the initial application of this re-mapping tool, a version of Simple Track Fitter has been created for the P $\emptyset$ D ECal by Stephen Dolan [113], however there are very few layers in the P $\emptyset$ D ECal and this is likely to render this re-mapping method unreliable. Notably, preliminary plotting of the cosmic data for the P $\emptyset$ D ECal did indicate an entire swapped TFB, which occurred after repair work carried out in 2014. This later confirmed by other methods, but this is much more obvious than individual channel mis-mapping.

Collect Muon Data (CMUD) is a data compression tool, which may take simple track fitted ROOT files as an input and convert them into a trimmed down format. After conversion, the ROOT files contain much fewer trees, which can then be directly accessed to retrieve pertinent variables to this process, such as event number, hitBar, hitLayer and channelNumber. It will be explained in detail in Sections 3.4.4 and 3.4.3, how comparing events at this level to ones at reconstruction level yielded information regarding mis-mappings.

### 3.4 The Process of Determining Mis-mappings

In this section, the methods used to systematically find mis-mapped channels will be described. A flow chart illustrating the stages of this process is shown in Figure 3.1. The various stages that have led towards the holistic solution will then be outlined, in order to convey a comprehensive understanding of the final results.

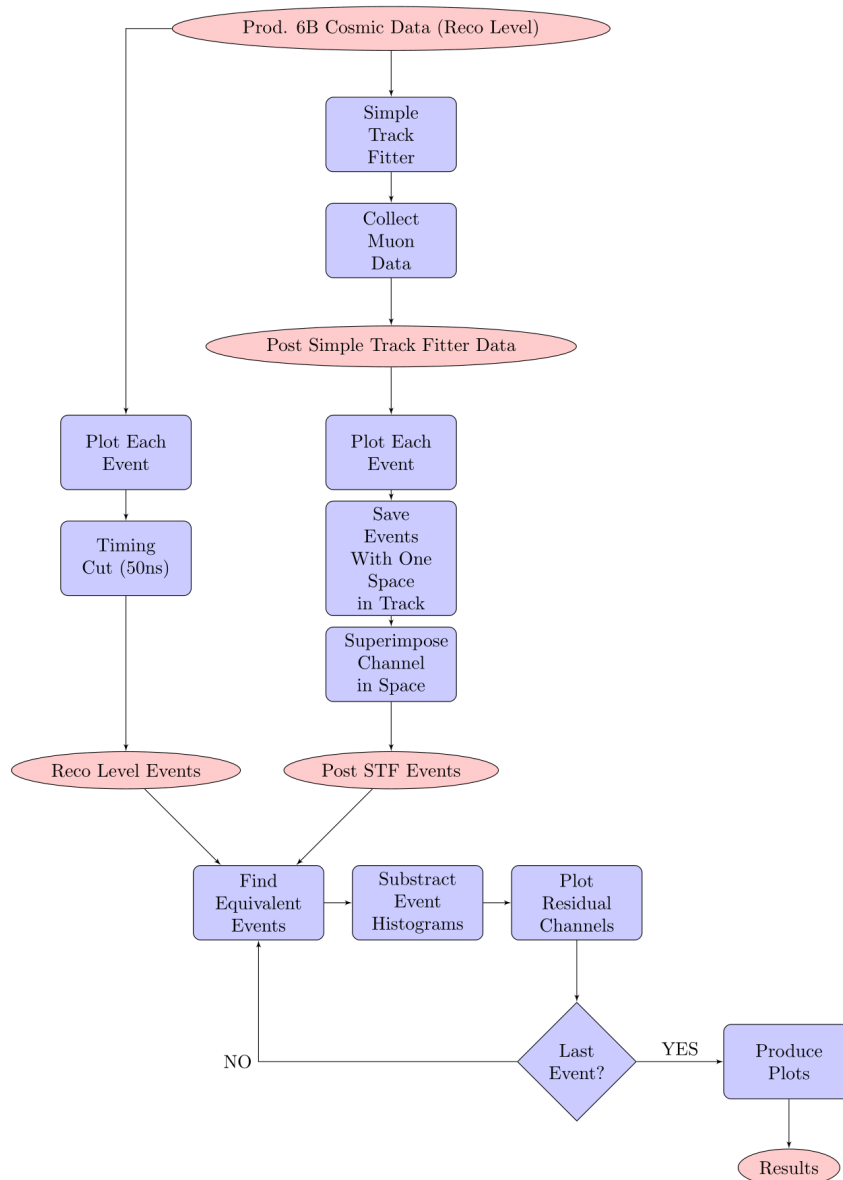


FIGURE 3.1: Illustrates a summary of the flow of data and processes in the determination of the swaps. Data is represented by ellipses and processes by boxes. STF represents the T2K software, Simple Track Fitter.

### 3.4.1 Plotting the Channel Output for Simple Track Fitted Cosmic Data

An important first step in resolving this issue was to use actual data taken from Trip-T cosmic ray events. A selection of production 6B cosmic ray data files (6,336 in total) from Run 4 were used. These were run through the basic reconstruction algorithm, Simple Track Fitter. This process ensured that only data which contributed to clearly defined single tracks was retained and any noise hits or hit channels outside of a certain physical region were dismissed. This physical region is predetermined in STF. In this particular case, this can also become a helpful diagnostic tool in finding swapped channels. If a cosmic ray passes through a module in the detector in a straight line, then it is expected that all layers along the muon trajectory are hit with no discontinuities (unless a channel is dead). However, if a channel were hit in the detector but it was being recognised in the software as an alternate channel then a discontinuity or ‘hole’ would be seen in the post simple track fitter view. The corresponding channel that has been activated in the software will be disregarded by the simple track fitter as noise, as it is unlikely to occupy a position in line with the reconstructed track.

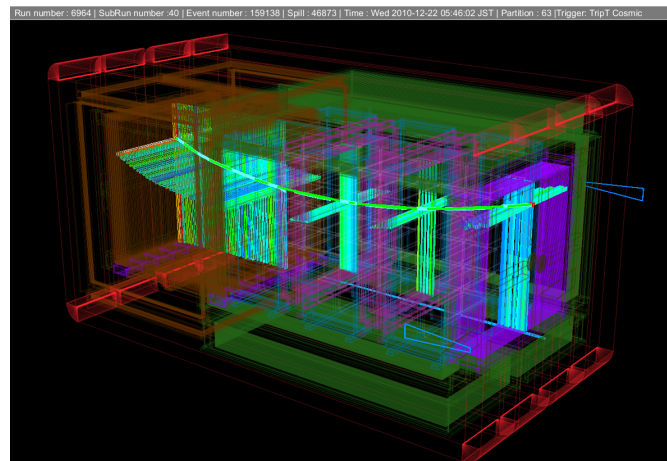


FIGURE 3.2: An event display representation of a cosmic muon passing through the ND280.

The first step in the process of determining mis-mappings was to produce plots which illustrated the number of hits for a given channel on each TFB in the ECal. After producing plots for each channel on each TFB (see Figures 3.3 and 3.4), the next stage

was to analyse these plots to find instances of ‘Dead Channels’ and potentially mis-mapped channels. Dead channels were characterised by their lack of hits within the data sample. It was initially thought important that these were catalogued, so as not to confuse them with potentially mis-mapped channels. However, the finalised mis-mapping identification method was mostly insensitive to their presence.

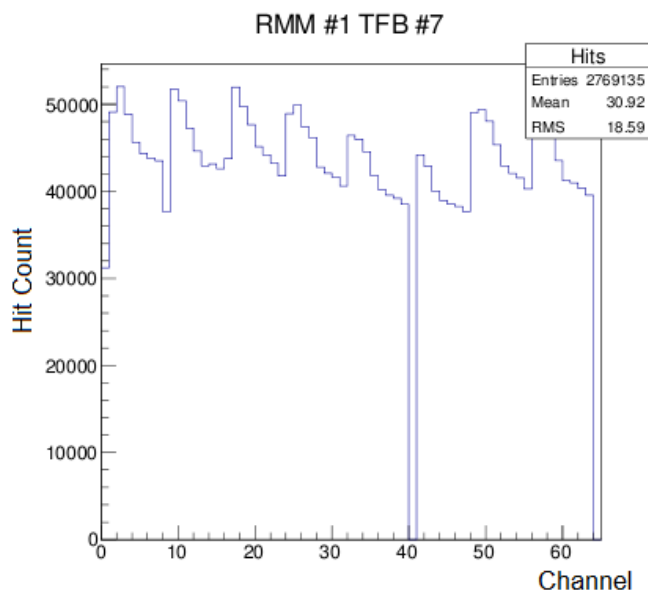


FIGURE 3.3: Plot showing the number of hits for each channel on TFB7 on RMM1. A clear deficit can be seen at channel 40, indicating a dead channel. The ECal group maintains a list of dead channels. The repeated slopes are due to the physical geometry of the modules and the Trip-T cosmic trigger.

As mentioned previously, due to the physical nature of the ECal, it is unlikely that a channel would be mis-mapped with one on another TFB. Therefore, a potentially mis-mapped channel on these plots would be represented by a deficit of hits in two channels on the same TFB. This would happen as when one channel was hit in physical space, the other would be activated in the software. As these are then disregarded by simple track fitter, for summed over tracks this would manifest as a vast decrease in total number of hits for both of those channels. They would not be zero, as occasionally the activated channel would coincidentally form part of an event track and be included. At this stage these are still only potential mis-mappings, as their hit deficit could be

due to other factors such as having a too low bias voltage or the channels having been turned off and on during the course of a run. An example is shown in Figure 3.3.

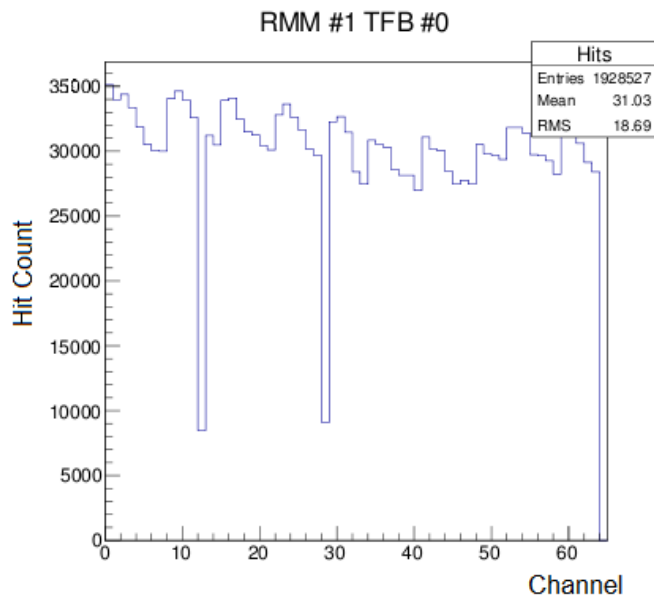


FIGURE 3.4: Plot showing the number of hits for each channel on TFB0 on RMM1. A clear deficit can be seen at channels 12 and 28, indicating a swap. However, this summed over data does not give a definitive indication that these missing hits occurred at the same time. Although, the fact that the deficit for both channels is similar is encouraging.

### 3.4.2 Plotting the Cosmic Data in a 3D Histogram

While the 2D hit count per channel plots were very useful and effective at illustrating that there is a dead channel and mis-mapped channel issue, it was time consuming to view all of them and ultimately highly inconclusive regarding mis-mappings. It was decided that hits should be plotted in bar/layer space, which also makes them more intuitive when attempting to imagine the geometry of the ECal.

Data was combined into entire modules (i.e. RMMs 0 - 11). This yielded plots which were easy to view, intuitive and not time consuming due to the number of RMMs. One important consideration at this stage was 'hit end' or 'stream direction' which retained the data of which side of a double ended bar was hit. On a TFB basis, each channel is hit from the same end and therefore there is no overlap, but when combining the data into the 'Global' RMM plots, it was necessary to split the data by this variable. If

both ends of a bar were represented on the same plot, it would be impossible to tell which end was at fault, and therefore which channel. In previous stages, this has been denoted by  $\text{hitEnd} = -1, 0, 1$ , which on the following plots is denoted by downstream, single and upstream respectively, where single refers to bars where only one end is read out. In addition some RMMs were combined to accurately represent the physical ECal Modules (RMMs 0 and 1, RMMs 5 and 6, RMMs 8 and 9). It is worth noting that all of the bars in the DSECal have double ended readout, hence the ‘single’ plot does not exist.

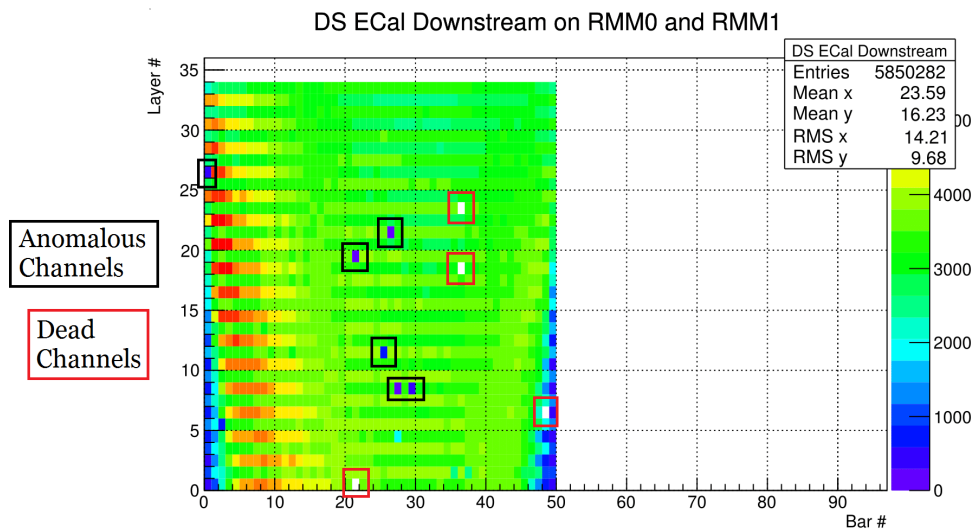


FIGURE 3.5: The number of hits for each channel for the entire Downstream ECal for hits of hit end -1 in the 3D bar/layer representation. A clear deficit can be seen for a few bins, and four clear non-hit bins illustrating dead channels in white. The even numbered layers on this plot represent bars running from left to right and the odd numbers represent bars running top to bottom, which have been combined to create this plot.

Due to the various geometries there are 5 orientations of bars for plotting purposes. For the Barrel ECal these are upstream, downstream and single ended, and for the Downstream ECal, these are upstream right to left, downstream right to left, upstream up to down and downstream up to down. The ‘global’ module plots style is also very useful when looking at actual tracks traversing the ECal. It is intuitive to see the hit channels of a given module for a given stream as these represent reconstructed tracks. Two examples of these combined bar/layer plots are shown in Figures 3.5 and 3.6. The

hit distribution has a spatial variation due to the acceptance of the Trip-T cosmic trigger.

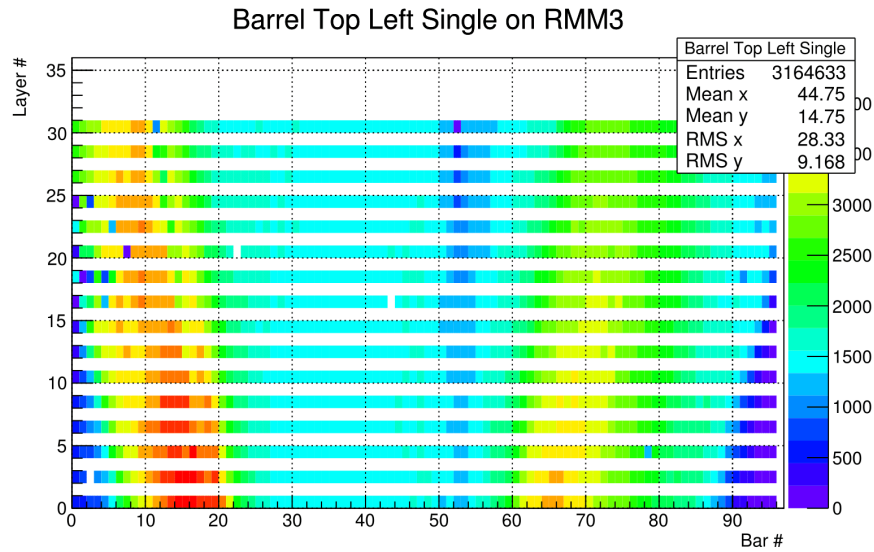


FIGURE 3.6: The number of hits for each channel for the entire Barrel Top Left Module for single ended bars. Every other layer in this view is entirely white, which represents the other orientation of the bar which is readout by other TFBs. Additionally, a number of interesting features can be seen in this plot, including dead channels (white spaces), anomalous or mis-mapped channels and a strange artefact hit deficit near the centre top of the plot, which is due to an intermittently bad channel in the outermost layer of the ECal (Layer 30, Bar 52).

The artefact seen around bar 52 in Figure 3.6 is due to a bad channel response in the top most layer of the plot, which has a knock on effect to reconstruction in STF. This particular deficit is not caused by mis-mapping, although it illustrates that low level issues in the detector and software can become bigger issues during and after reconstruction.

### 3.4.3 Plotting Events Using post-Simple Track Fitted Data

A utility was created to plot events from the data, after processing by STF. This was achieved by iterating through the data and for each event, plotting each hit in histograms similar to those produced previously. This required that a new histogram was created for each event and that these plots were saved to a postscript file and a ROOT [115] file for analysis purposes. In order to provide as much information about the event as possible, the RMM number and stream direction were included in the title and the bin content of the hit bar/layer was set to the channel number (channel number zero was set to 0.5 to avoid an empty bin). An example event, containing a typical muon track, a dead channel and an entire dead TFB is shown in Figure 3.7.

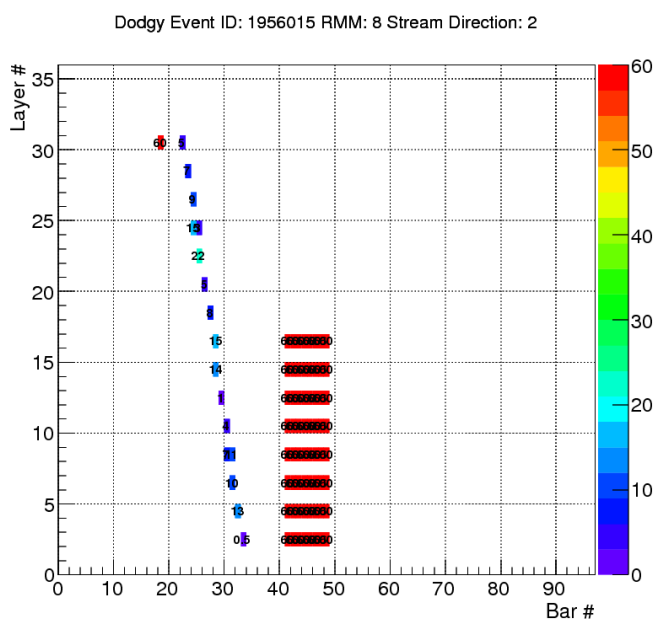


FIGURE 3.7: Shows the simple track fitted particle track for event 1956015 on RMMs 8 and 9. Known dead channels can be seen, plotted with the bin content 60 in this case, the large red block representing an entire dead TFB on RMM9, which could not be used in particle reconstruction. This TFB was lost in the 2011 earthquake.

In order to keep track of the hit channels in the data, an array was filled for each event. This array was analysed to find spaces in the event tracks. This was done by algorithmically placing conditions on an 'empty space'. Firstly, the empty space would have a bin content of zero; secondly, channels either side of it must also be zero; and

thirdly, the channels above and below the space must be greater than zero, or have direct neighbours greater than zero. Once a space had been identified, (its properties RMM, Bar, Layer, Stream, Channel Number stored) this channel was then artificially plotted on to the track with an added +100 bin content so that it could be distinguished from the hit channels (See Figure 3.8). Specific conditions to find missing channels which were on the edges of modules were included, and tracks where the space would lie in an ambiguous position were disregarded. This had a negative impact on the efficiency of the final analysis, but this was mitigated by large statistics.

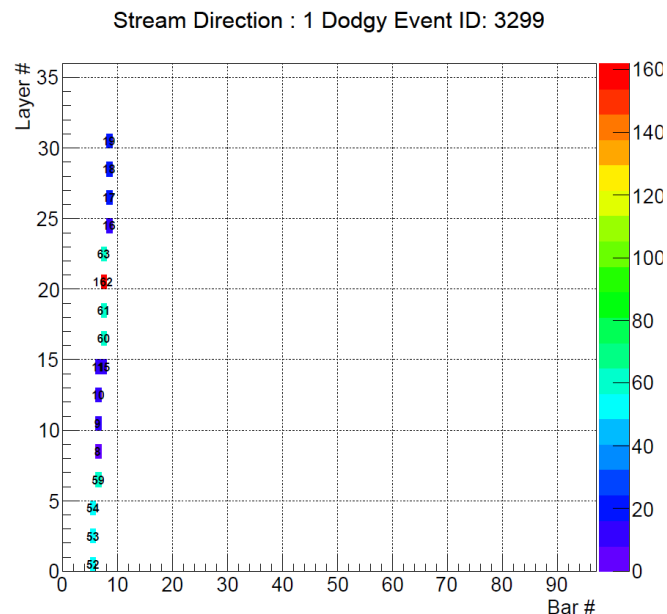


FIGURE 3.8: A simple-track-fitted particle track for event 3299 in RMM3. The channel plotted as bin content 162 is channel 62 from RMM3 TFB6, plotted with a 100 surplus to differentiate this from the other hits in the track.

The ROOT file created in this process was filled with these plots, which contained exclusively events which had holes in their tracks. Initially, it was required that this hole must correspond to a known anomalous channel. However, it was decided that this may be too restrictive, and so all events with discontinuities were compared. The ROOT file produced at this stage was used later in the determination of swaps.

### 3.4.4 Plotting Events Using pre-Simple Track Fitted Data

As stated earlier, the output from the track plotting utility described used data which had been run through simple track fitter and therefore excluded hits which did not form part of a straight line track. In order to produce plots which contain all ‘used’ and ‘unused’ hits, it was necessary to go to the ‘reco’ level and access the hits directly using a more fundamental event loop. A script was created, which would create identical plots to the ones previously illustrated, and for the same events, but would also include noise hits and channels that had not passed simple track fitter conditions. This would allow a useful comparison of regularly missed channel hits, which could be mis-mapping spaces, and regularly discarded channel hits, which could be mis-mapping hits. An example of a reconstruction level event, including noise is shown in Figure 3.9.

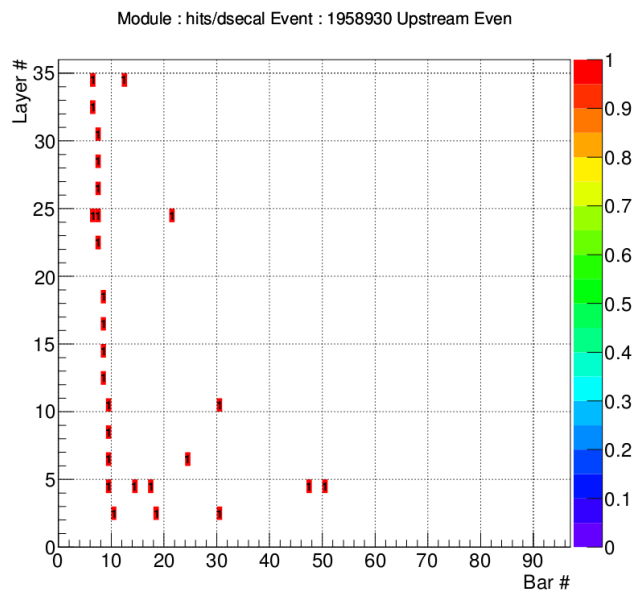


FIGURE 3.9: A pre-STF plot for a cosmic event. In this case the bin content is simply the number of hits on that channel. A clear space can be seen and many outlying noise hits, which may contain the mis-mapped channel.

This program had to be run using reconstruction files, which contain all hits in a given event, including noise. The other utilities must run on files which had been conditioned using two tools : Simple Track Fitter and Collect Muon Data. Consequently,

so that the exact same data could be used for both techniques, reconstruction files were obtained and all conditioned appropriately.

### 3.4.5 Noise Reduction - Timing Cuts

The next key step was to remove the noise from the pre-STF plots, without cutting out the mis-mappings. To removing noise hits while retaining the mis-mapped hits, the 'Integration Cycle' variable was used. Every TFB has 23 capacitors, each of which correspond to an integration cycle, a time window of 480 ns in length. This variable can take the values 0 to 22, and all hits occurring within one integration cycle will occupy the same 480 nanoseconds time period. Therefore, it is unlikely that any other hit will coincidentally occupy the same integration cycle as a cosmic hit from a track, which makes this the ideal variable for excluding noise (at a suppression factor of 1/23). This worked well and started to yield very promising plots indicating mis-mappings on the same TFBs. As with the program running on STF data, these histograms were stored in a ROOT file to be accessed by the final comparative analysis tool later.

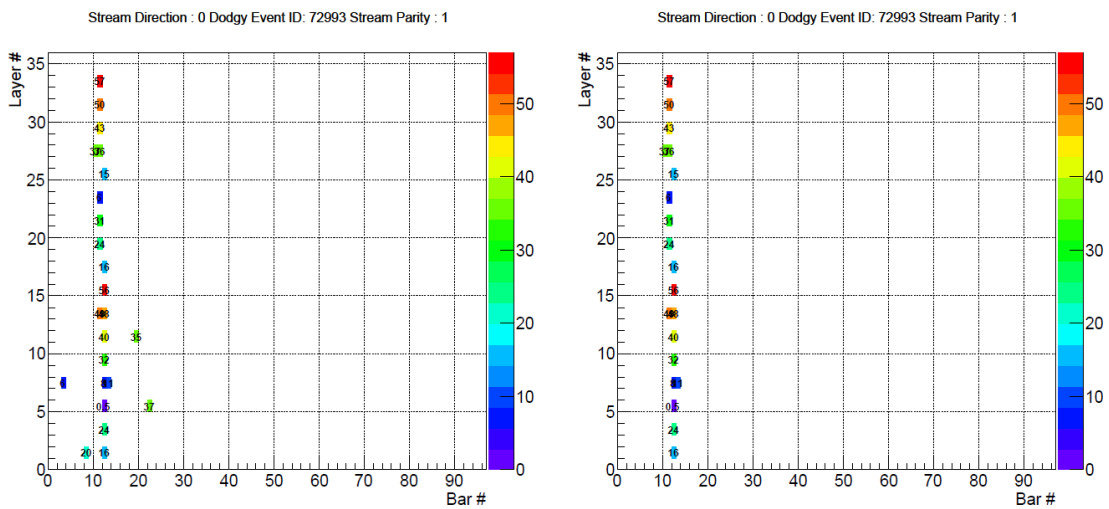


FIGURE 3.10: Left : A cosmic ray event with the bin content as channel number. Right : Most of the noise has been excluded using the integration cycle cut and 50 ns restriction.

The integration cycle cut was very effective at removing noise from these events. However, due to the high importance of removing consistently noisy channels, other

methods were also investigated. The most effective of which was to restrict all of the hits to a 50 ns window. This was done by iterating over the event twice. In the first iteration, the time of each hit was recorded and stored in a histogram, which was then used to determine the single peak time and gaussian distribution about this point. In the second iteration, the restriction was implemented such that each hit must be within 50 ns either side of this peak time. This timing cut was used in addition to the integration cycle cut and did manage to remove even more noise, by an additional suppression factor of 100/480 (the ratio of the two time intervals). An example of this noise reduction for a single event is shown in Figure 3.10.

### 3.4.6 Subtracting the Histograms - Post-STF and Pre-STF

The goal through this entire process has been to determine which channels in the ECal are mis-mapped or swapped with other channels. The program written to subtract the histograms produced in the aforementioned utilities and analyse this result does exactly that, via a number of stages. Firstly, the program will take in as arguments the two ROOT files which have been produced, both of which contain the same events, one post-STF (as outlined in Subsection 3.4.3) and one pre-STF (Subsection 3.4.4) with timing cut based noise reduction. An example of this is shown in Figure 3.11. Each of these events contains a hole in the through-going track, although it is artificially filled in the post-STF case.

For each event, the stored pre-STF histograms are subtracted from the post-STF histograms, and the absolute value of this result is saved to a third histogram. As the bin content of these histograms is channel number, this subtraction will result in no hits for most of the channels in the track. However, for an event containing a mis-mapped channel, the missing 'hole' bin will remain with its channel number bin content from the post-STF histogram, and the remaining channels which were not incorporated into the STF track and which survived the noise cuts, will remain (also with their bin content indicating their channel number). An example of a subtracted plot is shown in Figure 3.11, and a further two in Figure 3.12. The absolute value of each bin is used, and after

subtraction all that remains are histograms populated with very few hits, which should be comprised of mostly mis-mapped channels and residual noise.

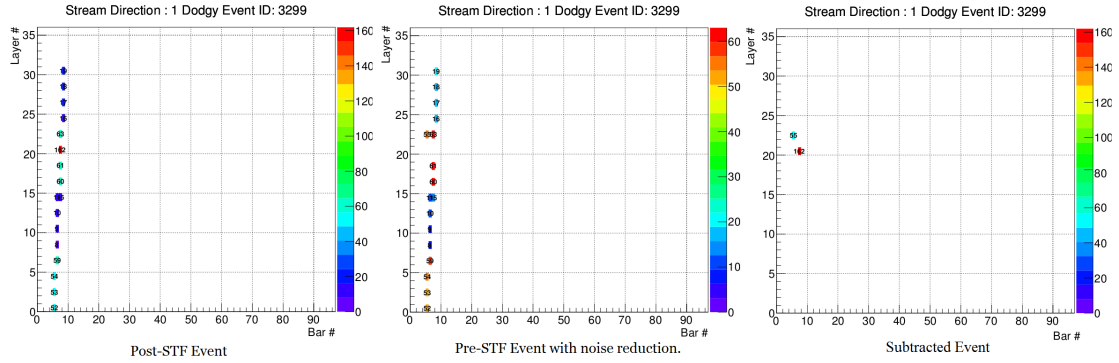


FIGURE 3.11: Event 3299 : pre-STF and post-STF histograms. For left post-STF plot, we can see where channel 62 has been artificially superimposed). For the right pre-STF and post noise reduction plot, we see the space where we would expect to see channel 62, and channel 55 being triggered instead on the same TFB. Finally, the result after subtraction is shown. The remaining residual channels are likely to represent a mis-mapping.

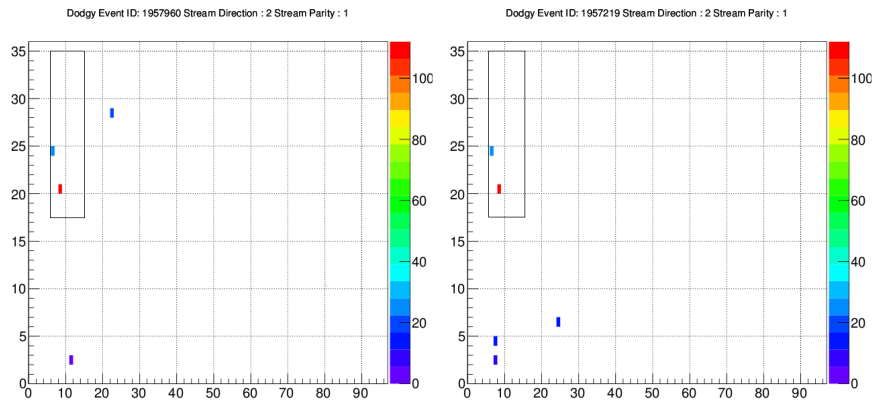


FIGURE 3.12: Another two examples of the residual hits left after the subtraction of Post-STF minus Pre-STF has taken place. This case shows that channels 12 and 28 on RMM1 TFB0 are likely to be swapped with each other. This is a persistent case which is reflected later in the results. The black rectangles on the plot outline the area where other same TFB mis-mappings could have occurred.

The analysis was then run for high statistics, which was necessary to clearly determine actual swaps. Initially this constituted a large number of events, but this was reduced by only using ones which contain a discontinuity in the track. During this process, a 2D histogram for each channel is produced (see Figures 3.17 and 3.18). For

each time a channel residually appears in a bar/layer event plot after subtraction, we may fill the bins of the channel histogram for any other channels on that subtracted bar/layer plot. The restriction is also imposed that these channels must occupy the same TFB. Therefore, each time more than one residual channel remains on a bar/layer subtracted plot, that channel's corresponding 2D channel plot is filled. This will happen repeatedly if a swap is systematic, and so peaks will emerge in these 2D channel plots.

After all events have been examined and the channel plots filled, only those plots which have more than zero hits, and therefore retain mostly useful information, are saved. Ultimately this utility provides a handful of plots for each module, illustrating which channels are also hit when a given channel is hit. These are a clear indication of mis-mappings and running over high statistics gives unequivocal swaps for many of the TFBs. This information was then collated into tables, listing swaps for each module. Plots illustrating each RMM (0 - 11) (excluding the P $\emptyset$ D ECal - RMM7) in each view were produced for the situation before and after the provisional re-mapping was done.

### 3.5 Re-mapping the ECal : Validation

Once the channel plots had been produced for the above modules, and these results distilled into lists of swapped channels, it was important to validate this work, before it was submitted to the calibration group for implementation in the ND280 software. An optional extension was added to Simple Track Fitter [116] by Luke Pickering. This extension took as an input, the list of swapped channels (as an .xml parameters file) and ran over the reconstruction level files, with these swaps now implemented. Then the CMUD utility was run over these files, so that cosmic data files comparable to those we started with were produced, in terms of access to variables in a ROOT tree. The utilities created in the early stages of this work were used to produce 3D bar/layer plots of this data, which could be compared to the plots made using pre-swapped data. In the pre-swap case, a deficit of hits in these plots could indicate a potential mis-mapping.

Therefore, if this swap had been correctly deduced and implemented, this deficit of hits should disappear. After re-mapping many of these low hit channels did improve, accompanied an overall increase in number of retained hits and tracks, as shown in the plots of Section 3.6.

## 3.6 Results

The results of the work described are included here. However, a much more comprehensive treatment can be found in the T2K technical note [117] describing this work, with only a representative selection being included here as examples. With respect to this, a full treatment of the DS ECal results is included here, with only a few plots for the other modules retained.

### 3.6.1 Results for RMM0 and RMM1 (DSECal)

In this first part of the results section, the analysis results plots are included, so that the reader has a better comprehension of the methods used. It would be too cumbersome to include these for each swap, so for later modules these are omitted. The final improvement for the DSECal is shown in the comparison of Figures 3.13 and 3.14 and Figures 3.15 and 3.16.

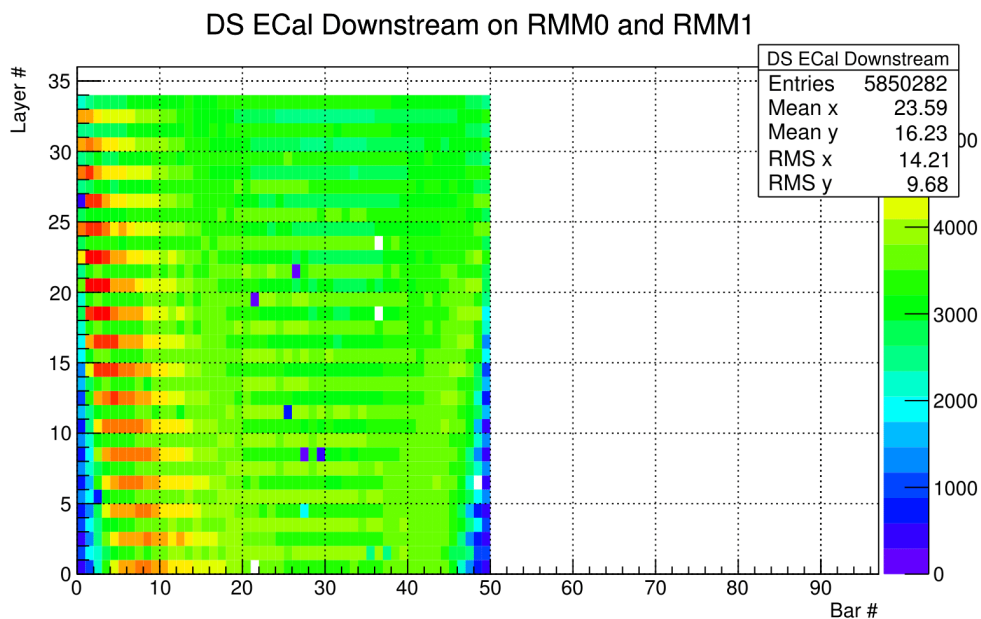


FIGURE 3.13: Plot showing cosmic hits for the DS ECal (amalgamated RMM0 and RMM1) for the downstream view before re-mapping.

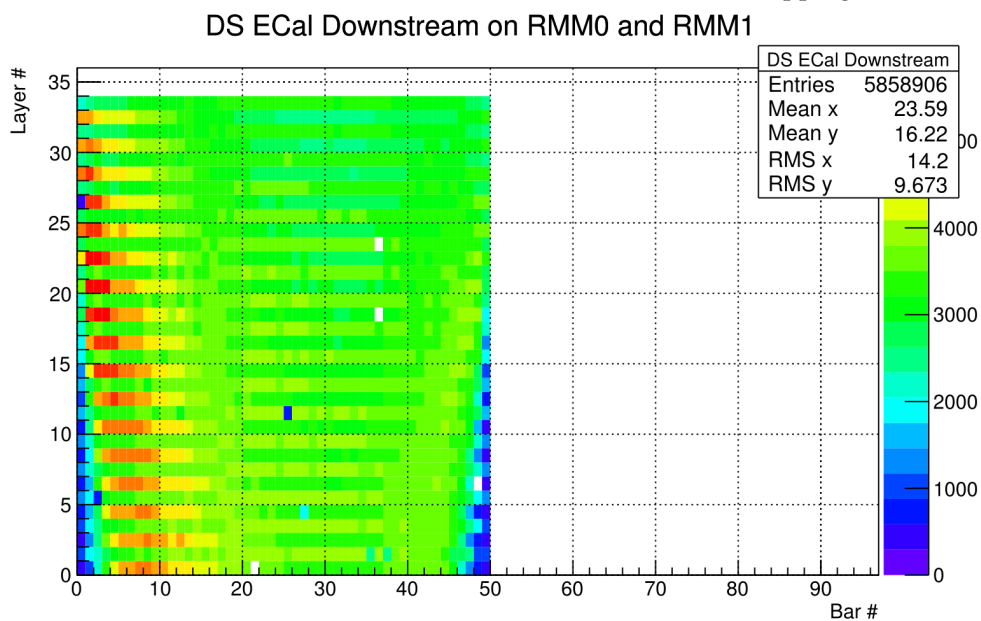


FIGURE 3.14: Plot showing cosmic hits for the DS ECal (amalgamated RMM0 and RMM1) for the downstream view after re-mapping. The improvement can be seen in the fewer low hit channels (in blue), and the increase in the total number of histogram entries.

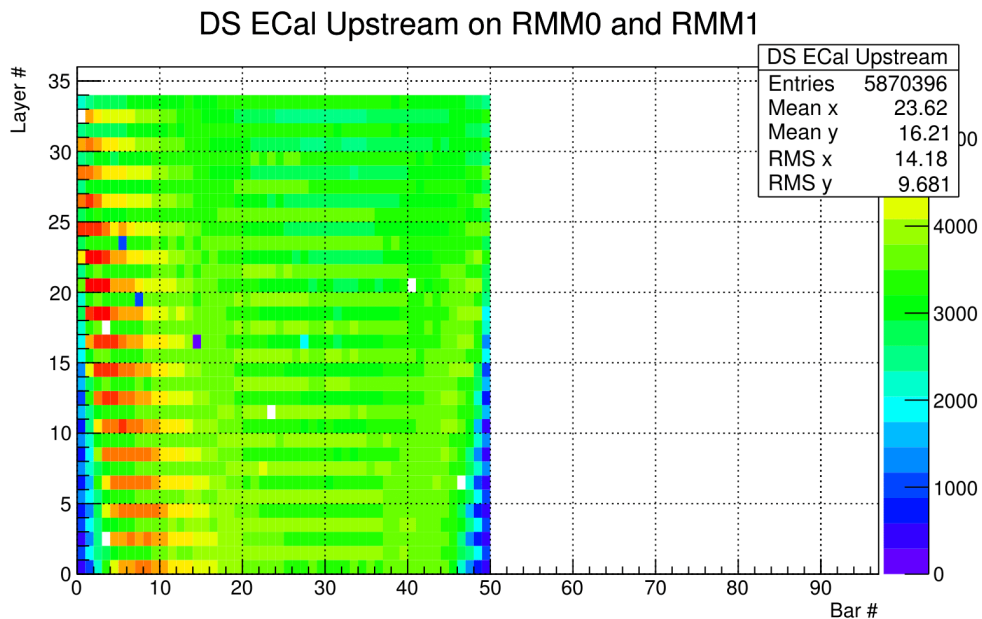


FIGURE 3.15: Plot showing cosmic hits for the DS ECal (amalgamated RMM0 and RMM1) for the upstream view before re-mapping.

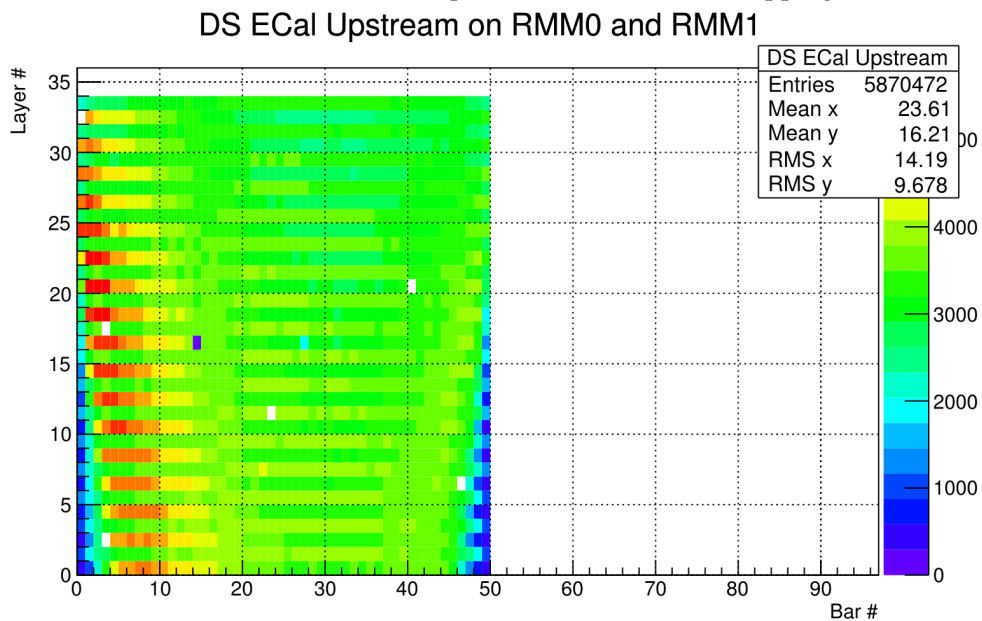


FIGURE 3.16: Plot showing cosmic hits for the DS ECal (amalgamated RMM0 and RMM1) for the upstream view after re-mapping. The improvement can be seen in the fewer low hit channels (in blue), and the increase in the total number of histogram entries.

The following plots show some of the direct swaps found on RMM0 and RMM1:

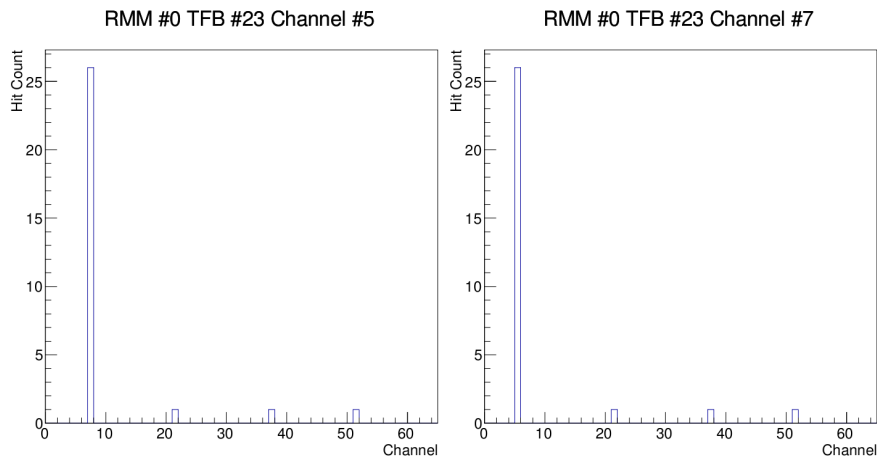


FIGURE 3.17: Plots illustrating the swap of channel 5 with channel 7 on RMM0 TFB23. There is an equivalent number of spaces in events involving one of these channels as additional hits in the other channel.

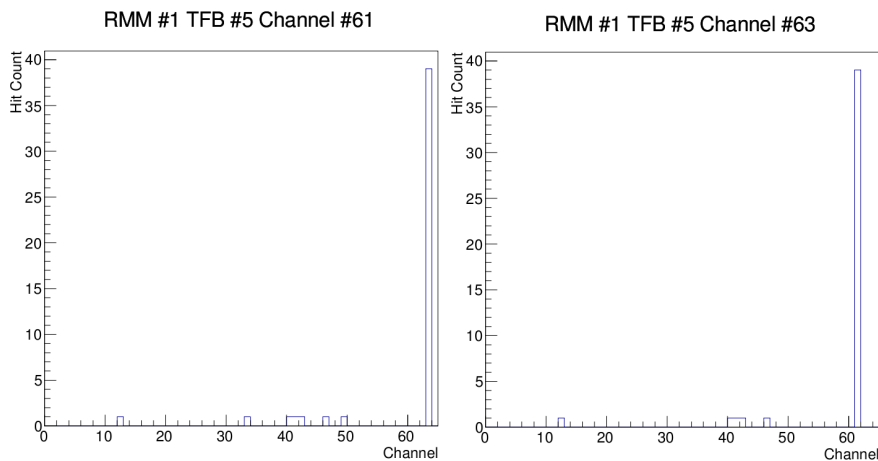


FIGURE 3.18: Plots illustrating the swap of channel 61 with channel 63 on RMM1 TFB5. There is an equivalent number of spaces in events involving one of these channels as additional hits in the other channel.

It is clear to see that there is a distinct correlation between the peaks of a given hit channel and its swap. For example, Channel 61 has been residually hit exactly the same number of times as Channel 63 on RMM1 TFB5 (See Figure 3.18). For clarification, this translates to one of those channels being consistently missing in a reconstructed track and being superimposed in by the utility, and the other being retained after noise

cuts on the pre-simple track fitted histograms and therefore not disappearing when one histogram is subtracted from the other.

RMM Number	TFB Number	Channel Number	Swapped with Channel
0	23	5	7
0	23	7	5
1	0	12	28
1	0	28	12
1	5	61	63
1	5	63	61

TABLE 3.2: Mis-mapped Channels in the Downstream ECal module. 6 Mis-mappings are listed with the determined correct mapping.

Table 3.2 shows which channels are swapped within the DS ECal according to the output of the utilities discussed.

### 3.6.2 Results for RMM3 (Barrel Top Left ECal)

For RMM3 there are three views, as we have single ended and double ended bars being readout. There are a few mis-mappings, but most of these are confined to TFB6, which has previously been cursorily investigated by Callum Wilkinson [118] during layer efficiency calibrations. This previous analysis did not yield conclusive results, due to the complexity of the swaps and their geometrical closeness. These factors were also prevalent in this analysis, but were mostly overcome by large statistics and reducing the complexity of the problem one swap at a time. There was an increase in hits retained in all views, not just the ones which have re-mapped channels. This is due to increased reconstruction of tracks, extending to their views. The plots are shown for the interesting case of the single ended bars and the complex region of TFB6. The major improvement for the Barrel Top Left ECal is shown in the comparison of Figures 3.19 and 3.20.

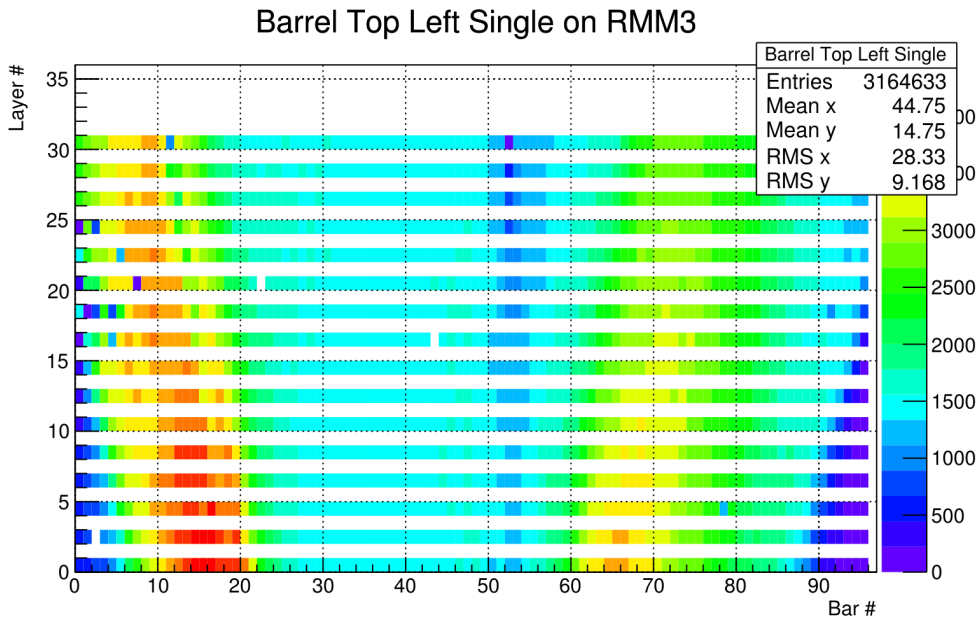


FIGURE 3.19: Plot showing cosmic hits for RMM3 for the single ended bars view before re-mapping.

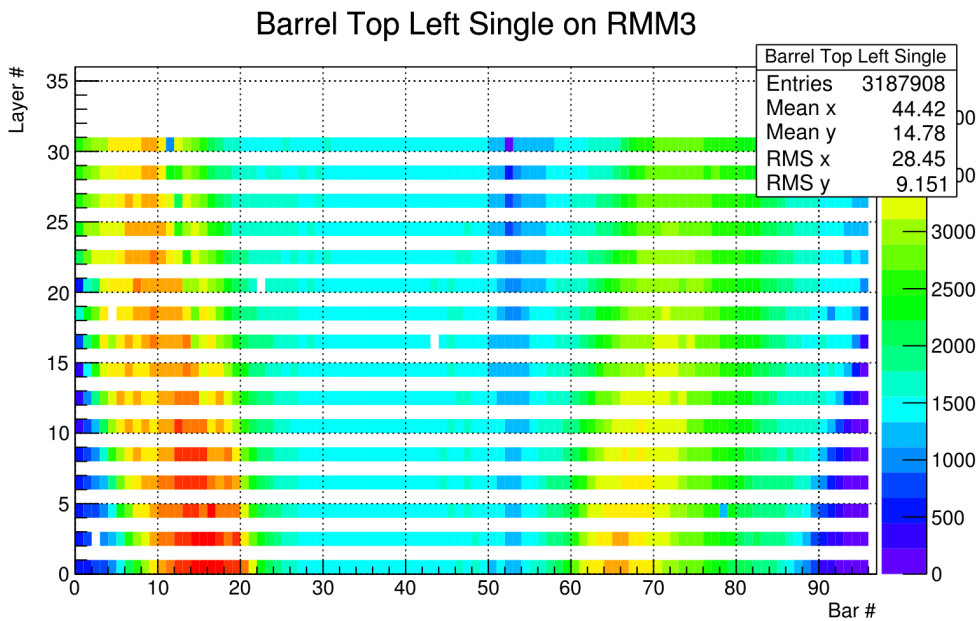


FIGURE 3.20: Plot showing cosmic hits for RMM3 for the single ended bars view after re-mapping. The improvement here is not as easy to discern by eye due to the complexity of the swaps on RMM3 TFB 6 in the upper left region of Figure 3.19. However, the overall improvement can be seen by the increased number of matched tracks represented by the additional  $\sim 27k$  entries in this histogram.

RMM Number	TFB Number	Channel Number	Swapped with Channel
3	6	16	24
3	6	24	16
3	6	32	41
3	6	41	32
3	6	48	53
3	6	53	48
3	6	37	45
3	6	45	37
3	6	49	55
3	6	55	49
3	6	55	62
3	6	62	55
3	6	49	62
3	6	62	49

TABLE 3.3: Mis-mapped Channels in the Barrel Top Left ECal. 14 Mis-mappings are listed with the determined correct mapping.

The last six lines in Table 3.3 may seem counter-intuitive, as they do not represent a direct swap. Oddly, it seems that on an individual basis, both channels 49 and 62 are swapped with channel 55. This may be due to a fix being implemented in the software, making this a time dependent issue, to which this analysis was not sensitive. The configuration described in Table 3.3 was chosen to maximise the number of hits gained. This is under further investigation.

### 3.6.3 Results for RMM4 (Barrel Bottom Left ECal)

As can be seen in Figure 3.21, there is a particularly complex region of mis-mapping on RMM4 for the single ended bars. This region is located around Bar 70 and Layer 3 on the aforementioned figure, this is all due to swaps on TFB34. Poor reconstruction in

this region may be particularly damaging, due to the fact that it is close to the boundary between FGD2 and TPC3. A small number of swaps were found for RMM4. However many of these were special cases, which initially were not deduced by the systematic analysis described. By looking at hit maps and individual plots, some of these swaps were found and then validated using the re-mapping tool. Significant improvement for the Barrel Bottom Left ECal is shown in Figures 3.21 and 3.22.

Three swaps were found for RMM4 using the standard method, that has been used throughout this process. However, upon validating these, there was only a small improvement in the complex region of TFB34. Much of the hit deficit, caused by mis-mappings still remained. It was clear that for this highly mis-mapped region, the analysis being used was only partially effective.

The final analysis utility which produces these results analyses events on an individual basis, subtracting the tracks to leave the residual hits. Therefore, it was possible to print out events which specifically intersected RMM4 TFB34 and visually analyse them to understand why the method might be partially failing, and where the mis-mappings actually lie. Examples are shown in Figures 3.23 to 3.25.

It became clear from these events and others, that there was a systematic mis-mapping on this TFB, where a row of four vertically arranged channels were swapped with another vertical row. However, they are not necessarily swapped symmetrically. Using this information and results from the analysis, the order of the swaps for these 8 channels was determined. These swaps were implemented and validated, with the region now showing a significant improvement in number of hits. Once these were established, it was clear that the 8 channels internal to these two rows were also mis-mapped.

The standard method was failing in this instance due to its reliance on simple track fitter. The method expects that simple track fitter will disregard anything outside of what could be considered to be part of a track. However, due to the large amount of mis-mapping in this area, simple track fitter was retaining tracks with quite large departures from a sensible track. This can be seen in the above track plots, where a

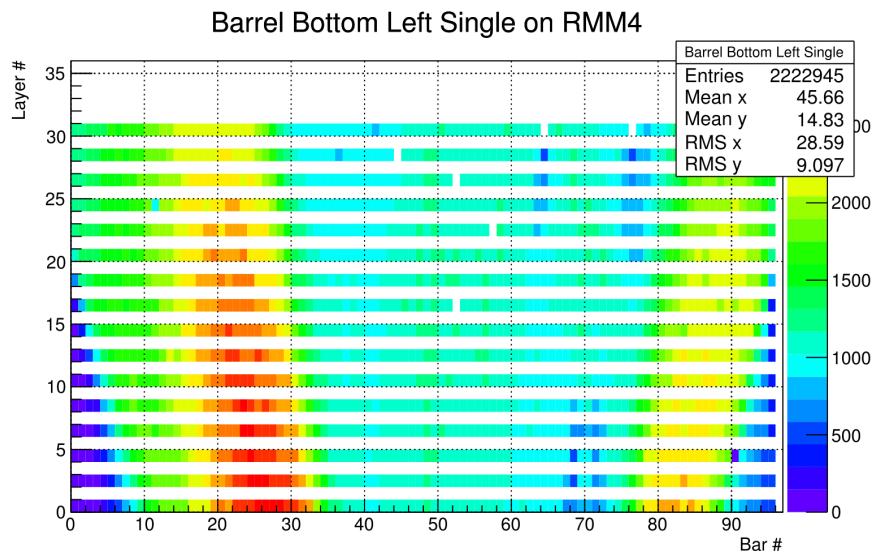


FIGURE 3.21: Plot showing cosmic hits for RMM4 for the single ended bars view before re-mapping.

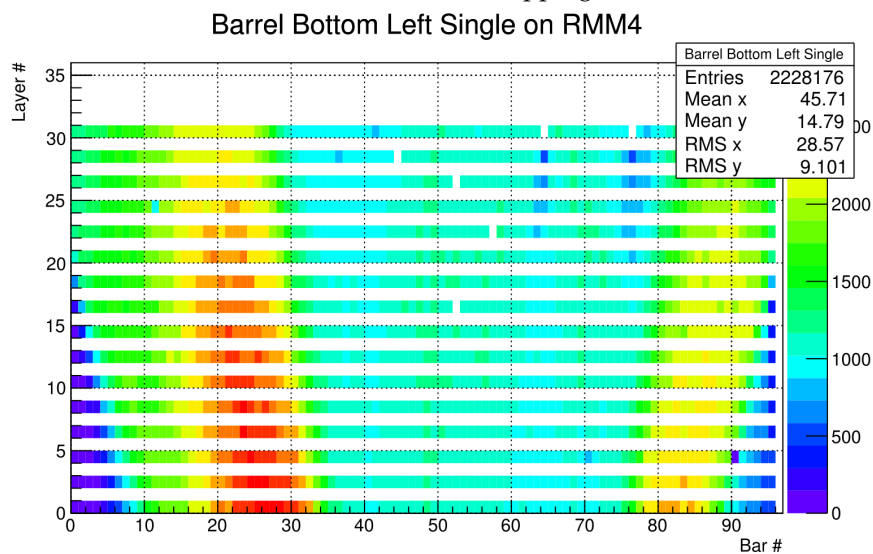


FIGURE 3.22: Plot showing cosmic hits for RMM4 for the single ended bars view after re-mapping. This plot includes the special case re-mapping for RMM4, discussed in this section. It is clear that the deficit in the TFB34 region (around bar 70) has greatly improved.

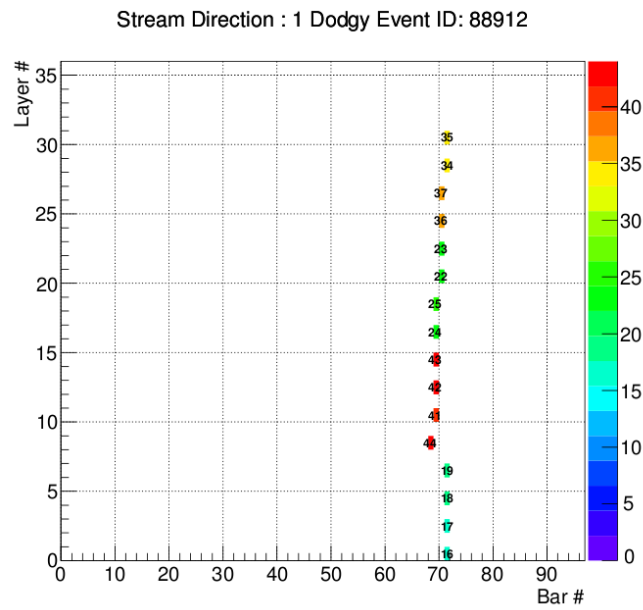


FIGURE 3.23: Another example of a vertical line of mis-mapped channels in the RMM4 TFB34 region.

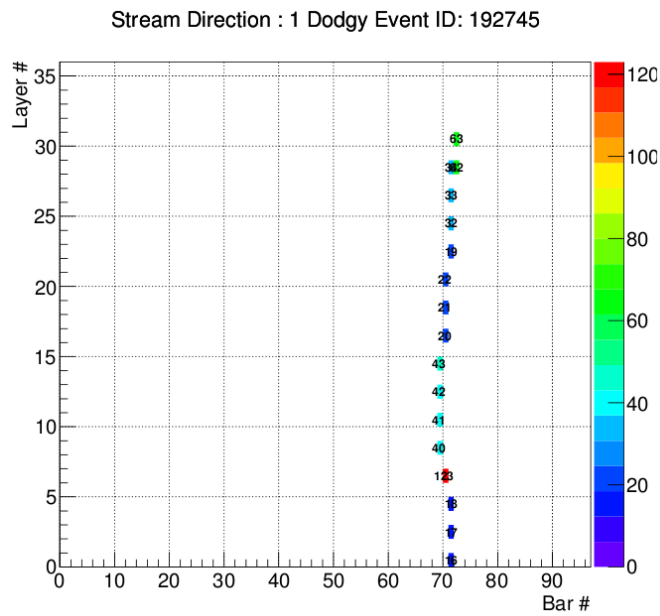


FIGURE 3.24: Another example of a vertical line of mis-mapped channels in the RMM4 TFB34 region.

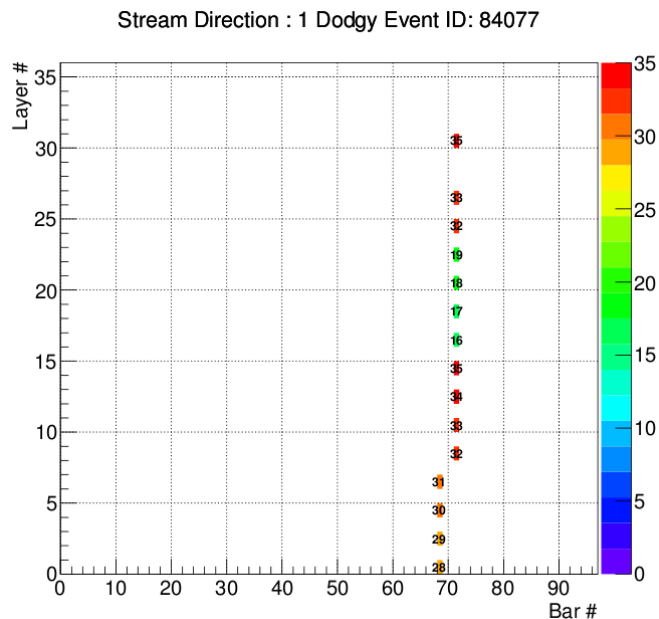


FIGURE 3.25: Plot Another example of a vertical line of mis-mapped channels in the RMM4 TFB34 region. In this case the particle is moving in the opposite direction.

reconstructed particle is heading in one direction through the ECal, and suddenly has a branch off from this direction, which is not physically possible. Of course it could be argued that this effect is simply from showering electrons, but this is consistent and systematic in a specific region.

#### 3.6.4 Results for RMM10 and RMM11 Anomaly (Barrel Bottom Right ECal)

Only two statistically significant swaps were found for RMM10. Others that did emerge were ambiguous, and validation showed no discernible improvement when they were implemented. This is not a surprise, as when viewing the RMM10 bar/layer cosmic hit plots, there are very few deficit channels. There were no statistically significant swaps found for RMM11, but there are large regions which are candidates for swaps. The cause of this deficit was not mis-mapping, and is considered to be an anomaly. It is clear from the results of this process what constitutes a swap and what may be a consistently anomalous channel. Most of the anomalous channels found by this work are ratified by the 'hot channels' list produced as part of the ECal subsystem logs. However, one

striking region of interest was found on RMM11 in the single ended bar view, where the associated anomalous channels were not listed in the logs. This lack of mention in the logs indicated that these would be swaps and visually this region appeared very much like a typical highly mis-mapped area, with a large hit deficit on a number of channels on TFB 19 as shown in Figures [3.26](#), [3.27](#) and [3.28](#).

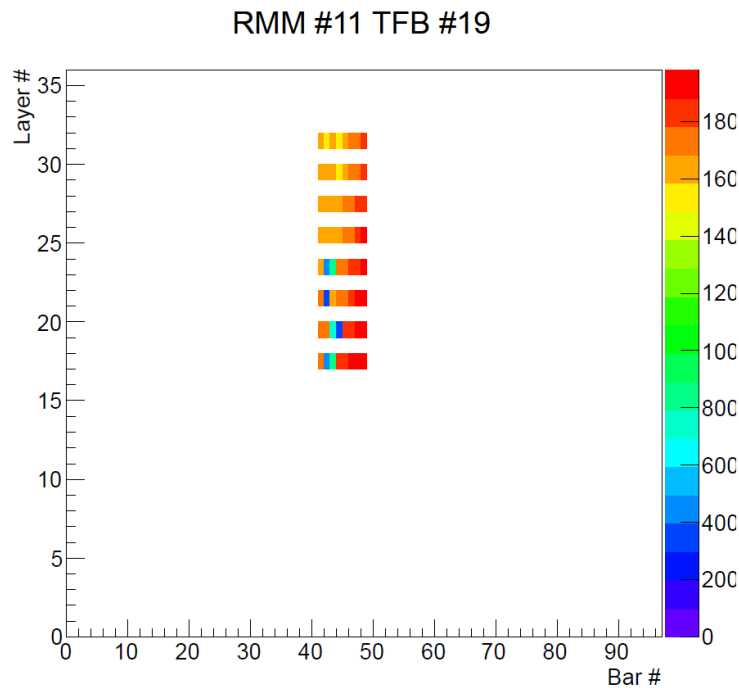


FIGURE 3.26: Shows all cosmic hits for RMM11 TFB19 after fitting. The channels exhibiting a hit deficit visually suggest mis-mapping in this area, although this turned out not to be the case.

However, upon running the analysis for this module, it became immediately apparent that nothing was being found in this area which implied a mis-mapping. This led to some consternation, until it was suggested that the ECal Light Injection (LI) [119] system could be used to rule out this region as mis-mapped. The LI system works by simply illuminating the ECal, such that every channel will trigger simultaneously. Usually, this method would not be useful in determining mis-mappings, due to the simultaneity of its illumination, which would cause a channel and its swapped partner to both light up. However, it could certainly be used to find an area of channels not reacting appropriately to outside stimulus. Previous plots had been produced of this exact area by Dr. Jonathan Perkin, and helped to clearly see that this area was not mis-mapped, as shown in Figure 3.27. This region has now been ruled out as a mis-mapping, though the cause of this deficit still remains a mystery. It is also unsolved as to why these channels are not being flagged as anomalous in the ECal subsystem scripts. It is thought that these channels may have on-board hardware issues relating to their high voltage supply.

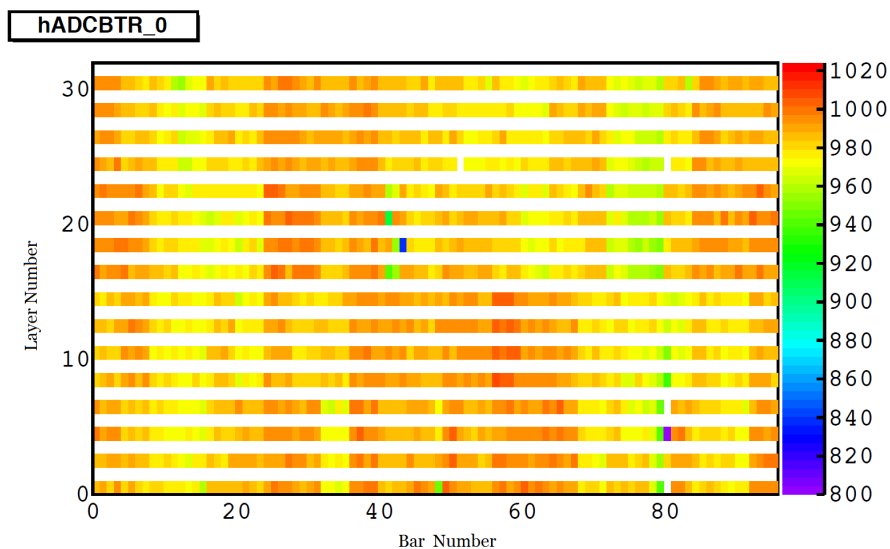


FIGURE 3.27: shows the LI plot for the Barrel Top Right (RMM11 Single Ended Bars). Clearly, an anomalous region can be seen in the centre of this plot, as well as the bottom right. [120]

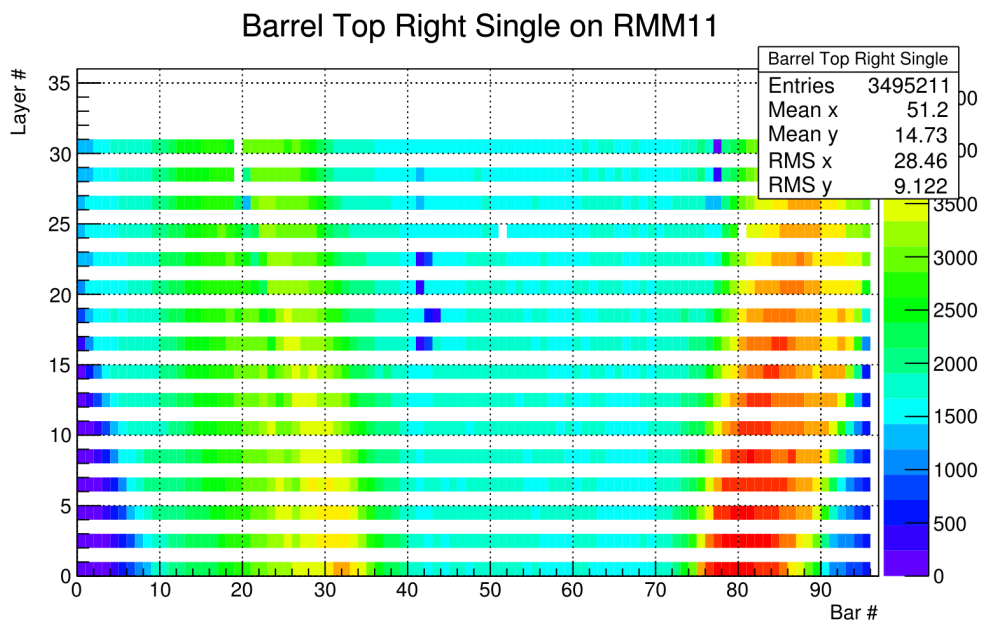


FIGURE 3.28: Plot showing cosmic hits for RMM11 for the single ended bars view before re-mapping. Improvement made by re-mapping was negligible, due to the fact that most of the hit deficit artefacts are caused by other phenomena, unrelated to mis-mapping.

### 3.7 Reconstruction Efficiency Improvements

While it is validating to see the deficit in channels disappear after being re-mapped, the situation becomes even clearer the histograms for the pre-swap situation are subtracted from the post-swap histograms. The number of additional hits retained by Simple Track Fitter can be seen in the subtracted plot and illustrates the general improvement (See Figure 3.29). In addition to this, we can see the extra tracks that have been retained as a consequence of re-mapping. These tracks had previously been discarded by the Simple Track Fitter reconstruction tool. Discarding valid hits and tracks and retaining potentially distorted or fabricated objects would have a negative impact on reconstruction efficiency and analysis efficacy. A region of mis-mapped channels could confuse established reconstruction algorithms, especially for low energy objects and showers which rely on very few hits even for the case of no mis-mapping. The fact that there is not only an improvement in the number of hits for the specific swapped channels, but also for the matched tracks shows that the effect of mis-mappings could be further reaching than previously thought. A general increase over the whole ECal of 0.2% in matched hits is seen.

While Simple Track Fitter is not the reconstruction algorithm used in the official ND280 analyses, it is a reasonable indicator of the effect which the re-mapping will have on reconstruction. Also, it is possible that mis-reconstructed tracks or discarded tracks may negatively contribute to analyses variables and conditions, i.e. causing confusion regarding whether a track is exclusively contained in the ECal or not. Complications arising from issues like these can contribute to larger systematic errors and inefficiencies.

### 3.8 Conclusion

This work will help to improve the reconstruction efficiency of the ECal. The list of swaps found in this work has been passed to the calibration group, who will enact software fix in an upcoming ND280 software release. Particular improvement will be

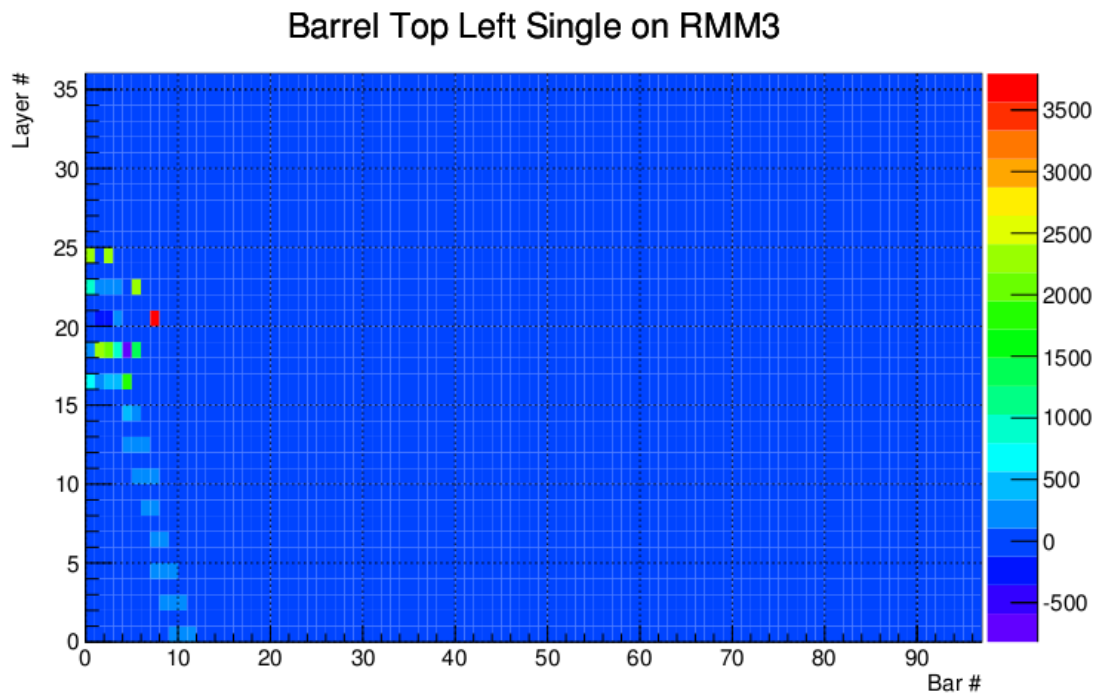


FIGURE 3.29: Shows the general improvement seen in RMM3 after subtraction.

for low energy particles which only trigger a small number of channels as they travel through the ECal, making track reconstruction more difficult. If a low energy particle activates a mis-mapped channel, then the track reconstruction algorithm will see a small number of channels in a line hit, followed by a space and accompanied by a hit elsewhere in the detector. The reconstruction algorithm will disregard this as sufficient evidence of a particle and this damages the efficiency of the detector. Once the results of this work is implemented, this will no longer happen and will be of value in particular for low energy  $\pi^0$  particle reconstruction. A table of all mis-mappings can be found in the Appendix A.

## Chapter 4

# Selecting $\nu_\mu$ Induced Charged-Current $\pi^0$ Events in FGD1

### 4.1 Analysis Motivation

The primary goal of an analysis of  $\nu_\mu$  interactions producing neutral pions is ultimately to allow better understanding of the rate and mechanisms by which these interactions proceed. More specifically, this will allow us to probe existing models of  $\pi^0$  production, better identify backgrounds and ultimately measure a production cross-section. The T2K oscillation analyses are subject to systematic uncertainty contributions from neutrino flux and cross-section models. To constrain these uncertainties, T2K produces fits to external data sets and dedicated ND280 final state samples. Currently the ND280 analyses provide CCQE, CC1 $\pi^+$  and ‘CC Other’ enhanced samples for these fits which help to constrain those uncertainties. Over time it is intended that more final state samples and cross-section measurements for specific  $\nu$  interaction modes will be produced by ND280 analyses. The analysis described in this chapter will contribute to a future dedicated CC $\pi^0$  enhanced sample and cross-section measurement. Additionally, despite the fact that Super-K now utilises new and improved reconstruction algorithms which dramatically improve  $\pi^0$  background reduction, a greater understanding of the rate of  $\pi^0$  production (predominantly in neutral current events) is useful for the development of  $\nu$  interaction models.

Specifically, in this analysis the  $\gamma$  conversion topology of Tracker + ECal is chosen

(See Subsection 4.2.1), which serves to explore potential phase space conversion differences in different regions of the ND280. For example, ‘is there a preference for  $\pi^0$ s to ultimately convert in the ECal + ECal, more so than Tracker + Tracker?’. Understanding these differences will help to further understand overall charged-current events producing  $\pi^0$ s and help to constrain uncertainties.

#### 4.1.1 Brief History of Neutral Pions

Hideki Yukawa predicted mesons as particles which would carry the strong nuclear force in 1935, hypothesising a particle with a mass of approximately  $100 \text{ MeV}/c^2$ . The neutral pion has no charge and was thus much more difficult to detect directly, an inference initially being made from cosmic ray decays to low energy electrons alongside photon showers. Shortly after this, the  $\pi^0$  was definitively identified at the University of California in 1950 [121], a discovery made possible by the use of a cyclotron and the observation of the  $\pi^0$  decay to two photons.

The quark composition of a  $\pi^0$  is one of two :  $u\bar{u}$  or  $d\bar{d}$ , most commonly stated as a quantum superposition of the two as  $(u\bar{u} - d\bar{d})/\sqrt{2}$ . The  $\pi^0$  has a rest mass of  $135.0 \text{ MeV}/c^2$  [77], with a mean lifetime of  $8.4 \times 10^{-17} \text{ s}$ . As the  $\pi^0$  decays electromagnetically, its lifetime is much shorter than that of the charged pion, which decays via the weak interaction. The primary decay mode being  $\pi^0$  to  $2\gamma$ , which occurs 98.823% of the time [77]. The secondary decay mode of the  $\pi^0$  is known as the Dalitz Decay (for Richard Dalitz), where one of the photons undergoes an internal conversion, resulting in  $\pi^0$  to  $\gamma + e^+ + e^-$ , with a probability of 1.174%. The third largest decay mode is the double Dalitz decay, where both photons internally convert, resulting in  $2e^+ + 2e^-$ , and only occurs  $3.34 \times 10^{-3}\%$  of the time.

#### 4.1.2 Physics of Charged-Current Neutrino Interactions Producing Neutral Pions

The neutrino is a neutral lepton and therefore interacts exclusively via the weak nuclear force. Consequently, direct observations of neutrinos are impossible, and instead

experiments focus on the particles produced during the exchange of a  $W$  or  $Z$  boson between a neutrino and nuclear target. Neutral current interactions proceed via the exchange of a  $Z$  boson and maintains the incoming neutrino in the outgoing state (albeit with modified kinematics). Charged-current interactions proceed via the exchange of a  $W$  boson and result in a charged lepton in the final state, which must retain the flavour of the incoming neutrino.

A range of these interactions may occur at GeV scale energies, the dominant modes being charged-current quasi-elastic (CCQE) scattering, deep inelastic scattering (DIS) and resonant (RES) production [90]. Feynman diagrams of these interactions are shown in Figure 4.1. Among the charged-current interactions, at energies less than  $\sim 2$  GeV, the CCQE mode dominates. Charged-current quasi-elastic (CCQE) interactions are useful as we can measure the kinematics of the outgoing lepton to reveal information about the energy of the incoming neutrino, and because the relatively simple nature of the process allows comparison of interaction models.

At higher interaction energies ( $\sim 1 - 5$  GeV), resonant interactions become more prevalent. These are similar to CCQE events but also cause an excitation of the nucleon to a higher energy state such as a  $\Delta^+$ . This is then followed on a very short time scale by the decay of this excited nucleon to its ground state which can involve the emission of a tertiary particle such as a charged or neutral meson. At neutrino energies of  $\sim 5$  GeV and beyond, neutrino-nucleon interactions become dominated by the DIS process. At this point the neutrino will interact directly with an individual quark within the bound nucleon. The ejection of a quark via this interaction can lead to the production of hadronic showers, potentially producing many low energy particles which are then absorbed, with the multiplicity of these particles increasing at higher energies.

The cross-section of each of the three dominant interaction modes discussed is energy dependent. This has resulted in an abundance of experimental measurements for particular modes at high energies, and a scarcity at low energies (See Figure 4.4). Additionally, it is important to analyse these interactions with a variety of nuclear materials, as the present data represents mostly interactions with carbon, oxygen and argon, so

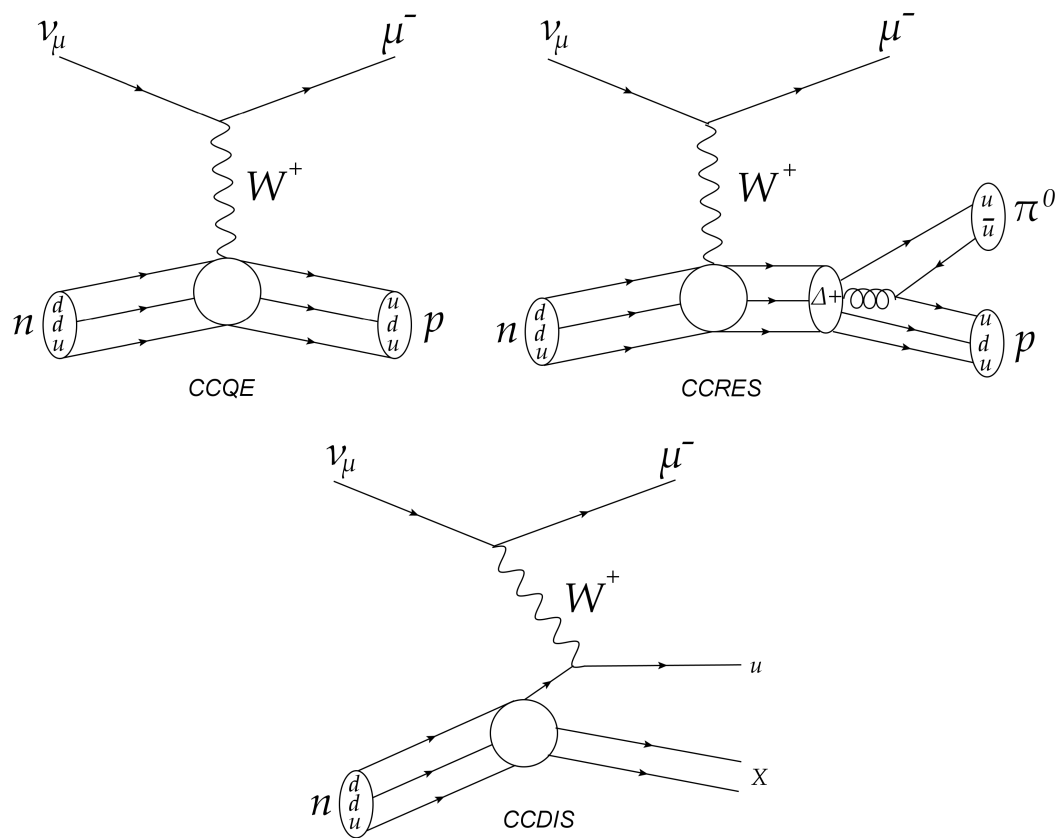


FIGURE 4.1: Illustrative Feynman diagrams for the three dominant interaction modes : charged-current quasi-elastic (CCQE), resonant (CCRES) and deep inelastic (CCDIS) neutrino-nucleon interaction processes. Where  $\nu_\mu$  is the incoming muon neutrino,  $\mu^-$  is the muon,  $n$  is the neutron,  $p$  is the proton, and  $X$  represents a fragmented nucleon.

that nuclear effects can be extricated. Finally, in future it will be interesting to probe these interactions for anti-neutrinos and to compare the results. Differences in interaction cross-section are expected and measured for  $\nu$  and  $\bar{\nu}$ , due to chirality effects which affect the interaction probabilities, these were discussed in Section 2.3.2. Beyond this, if differences are discovered between the oscillation rates (in vacuum and matter) for  $\nu$  and  $\bar{\nu}$ , this may give an insight into CP violation due to leptogenesis.

Further detail regarding the use of neutrino event generators and NEUT can be found in Section 2.6.6. For this analysis, details of specific interactions modelled in NEUT is included in Chapter 6. This is included for the cases where it specifically applies to some of the key observables of this work, such as reconstructed kinematic variables in data and MC, which are highly dependent on a good understanding of these processes.

### 4.1.3 Measurements of $CC\pi^0$ Production

The majority of previous measurements for the  $CC1\pi^0$  interaction process come from experiments undertaken in the 1980s, which used hydrogen and deuterium targets (See Figure 4.2). The data for those measurements covers a fairly comprehensive range of energies, but illustrates significant tension between the data and Nuance prediction, especially at higher energies. Additionally, there is a deficit of data at the lowest energies applicable to modern accelerator based oscillation experiments, and the use of simple target nuclei make the application of such data to complex target nuclei difficult due to the importance of complex nuclear interactions.

In 2011, the MiniBooNE [91] experiment released a flux averaged  $CC1\pi^0$  differential cross-section measurement on mineral oil (See Figure 4.3). This measurement conveys a systematically larger cross-section measurement in data when compared with the Nuance prediction. This data is currently used by the T2K experiment to constrain the model input parameters, which are used to evaluate the cross-section uncertainty for oscillation results. There is also limited additional information available from the  $CC1\pi^0$  inclusive cross-section measurements made by the SciBooNE [92] and K2K [93]

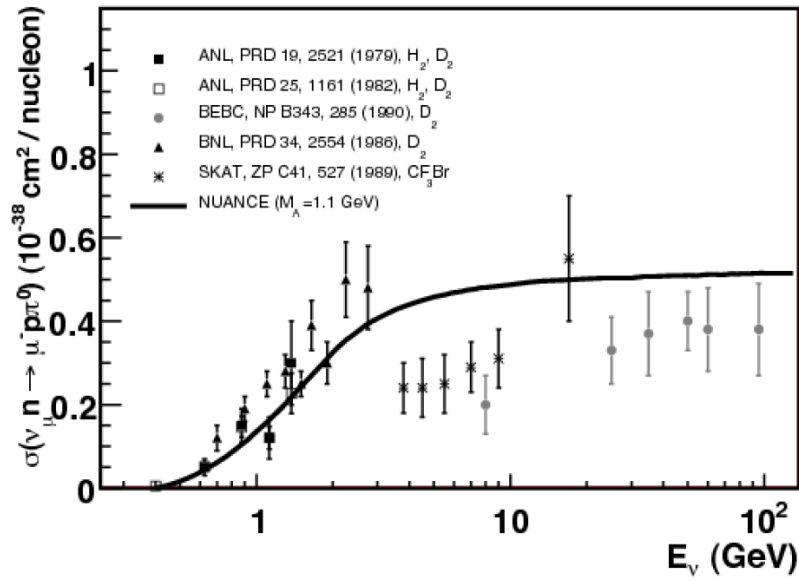


FIGURE 4.2: Historic CC1 $\pi^0$  cross-section measurements compared to the Nuance Monte Carlo generator prediction [90].

experiments. These are useful results but do not cover the neutrino energy region around 1 GeV as comprehensively, or with as small an uncertainty, as the MiniBooNE result. The work described in this thesis will contribute to increasing the understanding of CC $\pi^0$  production at T2K energies for more complex nuclei (Carbon) and ultimately result in a cross-sectional measurement which can be compared to the MiniBooNE result.

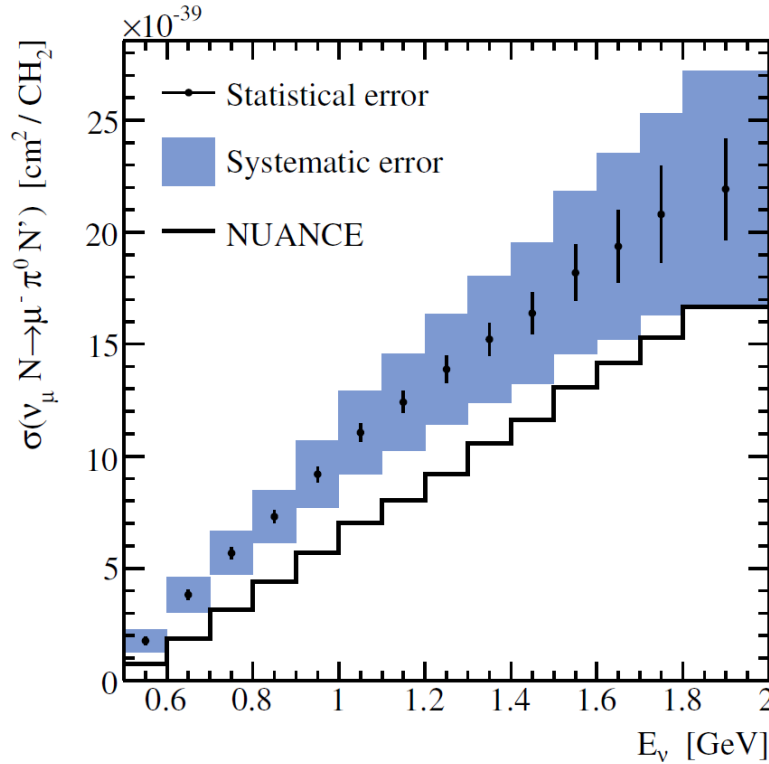


FIGURE 4.3: The MiniBooNE CC1 $\pi^0$ , flux averaged, differential cross-section measurement on a mineral oil target compared to the Nuance Monte-Carlo generator cross-section prediction [91].

## 4.2 Reconstructing Neutrino Energy in Events

The charged-current interaction is dominated by the quasi-elastic interaction (CCQE) below 1 GeV. This enables a precise determination of the energy of both  $\nu_\mu$  and  $\nu_e$ . This can be calculated by the formula:

$$E_\nu = \frac{m_N E_l - m_l^2/2}{m_N - E_l + p_l \cos\theta_l} \quad (4.1)$$

where  $m_N$  and  $m_l$  are the masses of the neutron and charged lepton ( $e^-$  or  $\mu^-$ ),  $E_l$ ,  $p_l$  and  $\theta_l$  are the energy, momentum, and angle of the charged lepton relative to the neutrino beam, respectively.

As stated, the CCQE interaction is the most common at T2K energies, but many other processes do occur (as illustrated in Figure 4.4). One important example is the charged-current single pion production mode (CC1 $\pi$ ), which occurs via the following :

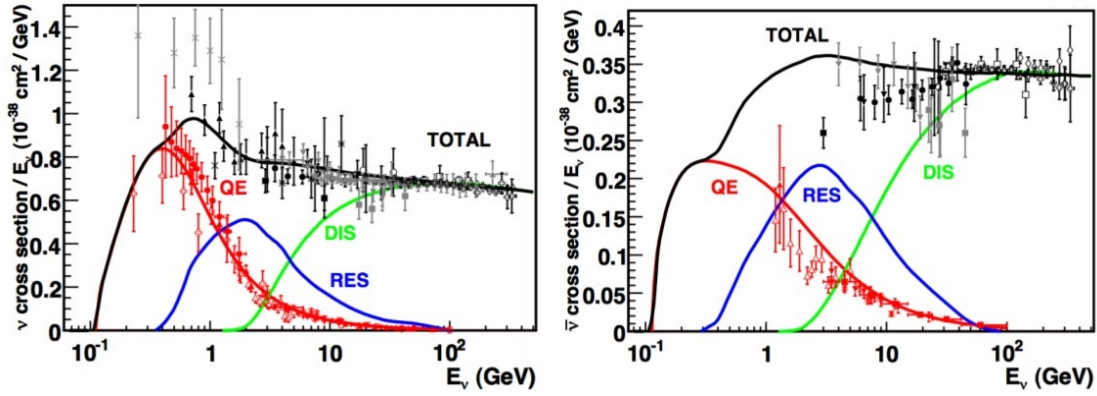


FIGURE 4.4: Neutrino and antineutrino charged-current cross-sections per nucleon for interactions as a function of neutrino energy. Cross-section measurements are shown for quasi-elastic interactions along with the total for all interactions from a selection of experiments. The Nuance [89] Monte Carlo generator cross-section prediction is shown for CCQE, CCRES and CCDIS interactions, along with the total [90]. Figure 2.18 can be used as a comparison to the NEUT MC generator, though in this case not delineated by interaction type.

$\nu_l + N \rightarrow l^- + N' + \pi$ , through the excitation of a  $\Delta$  resonance. Where  $\nu_l$  is the incoming neutrino,  $N$  is the target nucleus,  $l$  is the outgoing charged lepton,  $N'$  is an excited nucleus and  $\pi$  is a charged pion.

The fact that the pion is not reconstructed in the three-body final state means that the reconstructed energy of the initial neutrino is not just a function of the charged-lepton's direction and energy and the irreducible contribution from nuclear Fermi motion which also occurs in CCQE events. This has the undesirable effect of smearing out the reconstructed neutrino energy spectrum measurement, and consequently efforts are made to exclude these events from both near and far detector analyses. These events are irreducible in Super-K, but not in the ND280 where all charged particles can be seen. Rates of these interactions in the near detector must be well determined so that an accurate prediction can be made for the unoscillated events, occurring at Super-K. This procedure is common for all non-CCQE like events, which would result in backgrounds in Super-K.

### 4.2.1 Signal Definition

For this analysis, the signal is considered to be any  $\nu_\mu$  induced charged-current event, which produces at least one  $\pi^0$  in the final state. This can be expressed as :

$$\nu_\mu + n \rightarrow \mu^- + p + \pi^0 + X \quad (4.2)$$

where  $\nu_\mu$  is the incoming muon neutrino, n is a target neutron,  $\mu^-$  is the outgoing muon, p is the outgoing proton,  $\pi^0$  is the neutral pion produced, and X is either nothing or any other baryon/meson (potentially including another  $\pi^0$ ).

There are three dominant ways in which  $\pi^0$  decay  $\gamma$ s may convert in the ND280. These are the Tracker + Tracker, ECal + ECal and Tracker + ECal conversion topologies. Each of these defines where the final conversions from the two decay photons of a  $\pi^0$  take place. Examples of the two topologies not searched for in this analysis are shown in Figures 4.5 and 4.6, with a schematic of the signal topology shown in Figure 4.8.

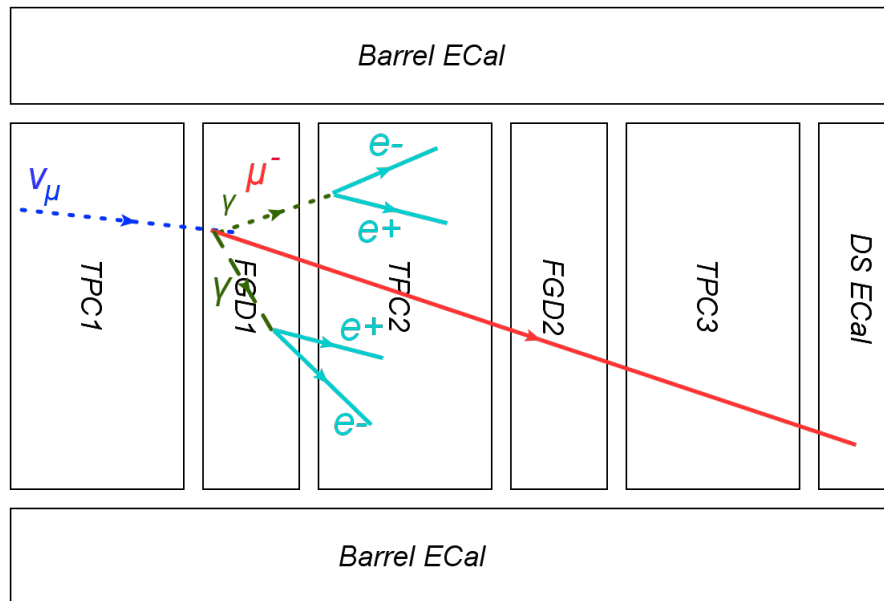


FIGURE 4.5: Schematic diagram representing a typical Tracker + Tracker  $\pi^0$  conversion in the ND280 detector.

The analysis described focuses primarily upon the reconstruction of the  $\pi^0$  candidate by detection of its decay products, in the form of electron and positron tracks in the

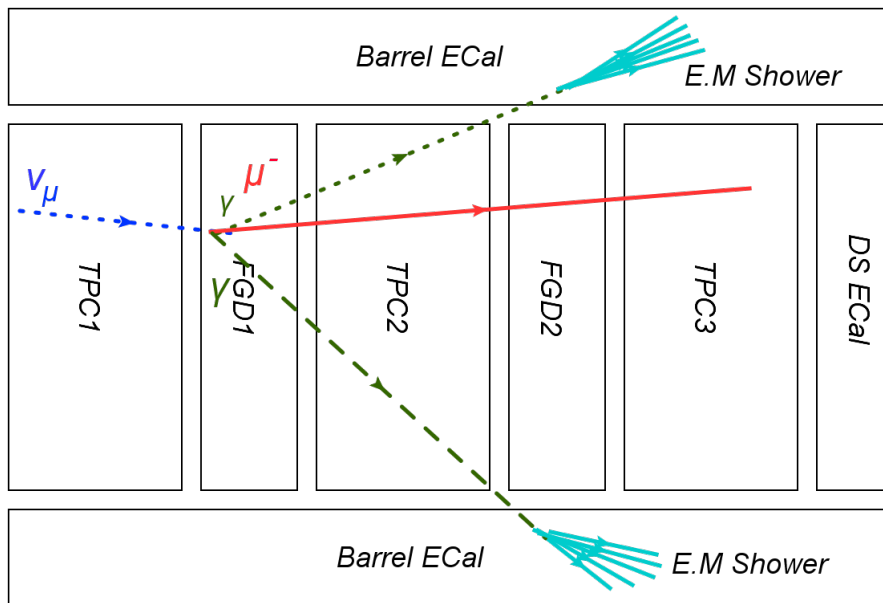


FIGURE 4.6: Schematic diagram representing a typical ECal + ECal  $\pi^0$  conversion in the ND280 detector.

tracker and  $\gamma$  showers in the ECal. Technically, four tracks (See Figure 4.7) would represent a clean  $\pi^0$  decay, one pair being a conversion of each decay photon. However, this analysis focuses on the Tracker + ECal  $\pi^0$  conversions, for which a clean signal would be two tracker tracks and one isolated ECal object (Figure 4.8). Additionally, we entertain the spurious idea that our detector may not be perfect, failing to reconstruct a low energy track from an asymmetric photon conversion, and so consider one additional reconstructed track and isolated ECal object as a further acceptable signal definition.

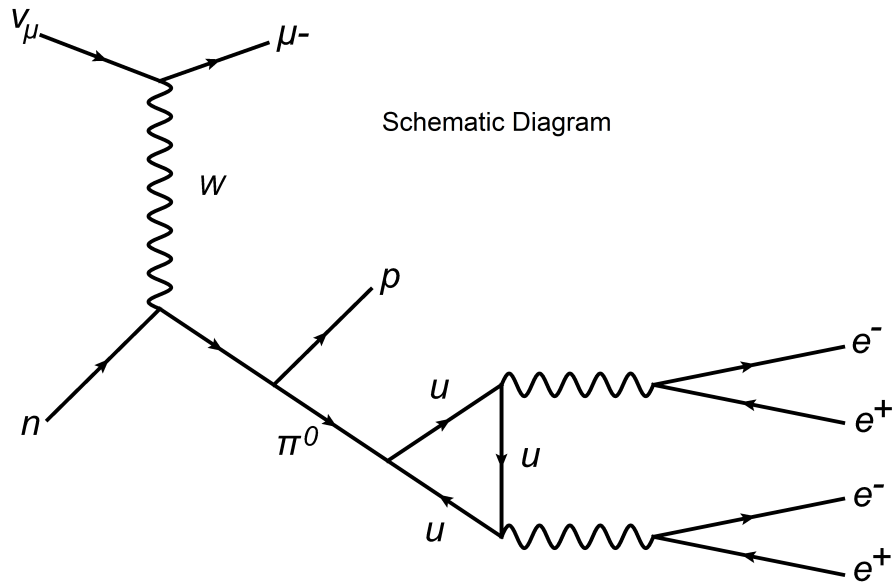


FIGURE 4.7: Schematic of a charged-current resonant neutrino interaction, producing a  $\pi^0$  and its subsequent decay to two photons and ultimately two  $e^+e^-$  pairs.

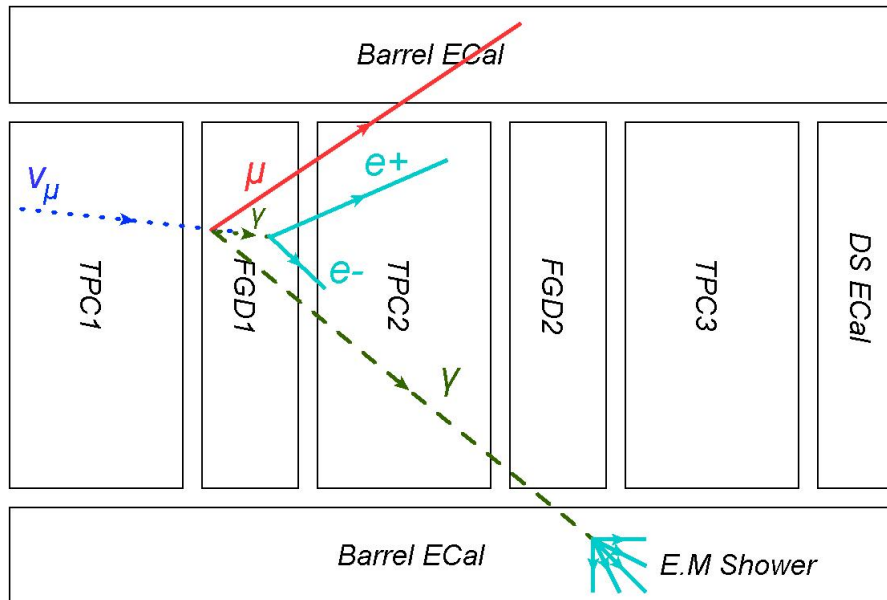


FIGURE 4.8: Schematic diagram representing a typical Tracker + ECal  $\pi^0$  conversion in the ND280 detector. Many other conversion topologies are possible for a Tracker + ECal  $\pi^0$  and are illustrated in the Appendix (A.1 to A.5)

### 4.3 Data and Monte Carlo Samples

The following Monte Carlo and Real Data Production was used to produce the final results. A much smaller Monte Carlo sample was used for optimisation. The Monte Carlo used was NEUT T2K Production 6B. Run 1 was not used as the barrel ECal was not installed at that time.

Run	Processed P.O.T	PØD Simulated Status
2	$11.14 \times 10^{20}$	Water In
2	$9.12 \times 10^{20}$	Water Out
3c	$9.93 \times 10^{20}$	Water Out
4	$32.89 \times 10^{20}$	Water In
4	$24.31 \times 10^{20}$	Water Out
Total	$87.39 \times 10^{20}$	-

TABLE 4.1: The P.O.T of the NEUT Monte Carlo samples used for this analysis.

Run	Run Period	Good Data P.O.T	PØD Status
2	Nov. 2010 - Feb. 2011	$4.28 \times 10^{19}$	Water In
2	Feb. 2011 - Mar. 2011	$3.53 \times 10^{19}$	Water Out
3c	Apr. 2012 - June. 2012	$13.48 \times 10^{19}$	Water Out
4	Oct. 2012 - Feb. 2013	$16.28 \times 10^{19}$	Water In
4	Feb. 2013 - May. 2013	$17.62 \times 10^{19}$	Water Out
Total	Nov. 2010 - May. 2013	$55.19 \times 10^{19}$	-

TABLE 4.2: The P.O.T of the data samples used for this analysis.

## 4.4 highland2

This analysis was completed utilising the bespoke software, highland2 (High Level Analysis at the ND280 Detector), which is currently the analysis framework of choice for T2K-ND280 analyses. It comprises a suite of connected classes, which help an analyst to construct a new analysis or selection using a prescribed process and generally is designed to simplify the process of analysing data in particle detectors. It integrates the existing ROOT Data Analysis framework, and gives the analyst access to myriad features within the highland2 package which should make it easier to produce an analysis and make a physics measurement.

The highland2 analysis framework is split into two core packages : Propagation of Systematics and Characterization of Events (PSyChE) which performs event selection and propagation of systematics and HighLAND which adds in any necessary corrections, FlatTree creation, MiniTree creation and tools for drawing. In practice PSyChE is part of the HighLAND distribution, and this analysis did not require in-depth investigation into the mechanisms of the underlying framework, only an understanding of implementing and validating an analysis.

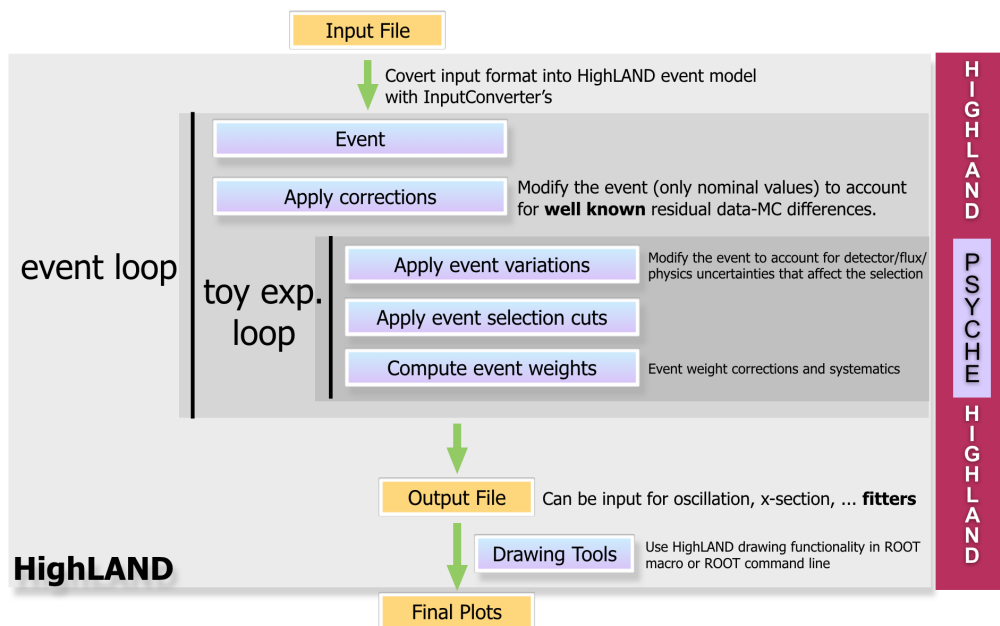


FIGURE 4.9: An overview of the data flow when running an analysis using highland2 [123].

As inputs, an analysis built in highland2 can take 4 formats; an oaAnalysis file (which is the conventional choice of data structure for past analysts who did not use highland2), a FlatTree (a reduced data structure, optimised for analysis running efficiency (now obsolete)), a MiniTree (an updated version of the FlatTree which provides intermediate data reduction), and a list of any of the previous. This analysis has been performed using a list of MiniTrees as the inputs for both Data and Monte Carlo, which have proven to dramatically reduce the required running time for the analysis. The improvement in running time has been indispensable, especially throughout the analysis development and optimisation, where changes must be made regularly and the analysis re-run. Proper parameters (contained in the highlandIO package) must be set when producing these MiniTrees, which were made in this instance using Condor [122], a batch processing system on the Lancaster University computing network, which allowed for fast final data quality checking and MiniTree creation.

At the core of the highland2 framework are the 'Actions and Cuts' which form the selection. These are applied on an event by event basis, and allow the analyst to preferentially select events of interest (signal) over events of no interest for this analysis (background). The entirety of this analysis was developed using only Monte Carlo (MC) data, with real data only being seen at the final stages, and used to make the plots which can be seen in Chapter 6. Reconstructed variables used in the selection are ones to which the ND280 detector is sensitive, and therefore those that can be used when running on real data, and true variables can only be accessed in Monte Carlo (i.e does this event truly contain a  $\pi^0$ ). True variables were used to optimise a selection, based on reconstructed physical quantities. Objects in a given event, and their properties, e.g. a track and its number of hits, determined charge, momentum etc, are stored in the 'toy-box' which is highland2 specific. A graphical overview of the workings of highland2 is shown in Figure 4.9.

There are detector systematic errors calculated as part of the analysis process. These are split into two types, 'Weight' and 'Variation' which both affect the number of events which will pass or fail a given selection for a given toy. The analyst determines which

systematics are required for a given analysis, for example an ECal object only analysis would not require systematics pertaining to the a TPC, and these are activated in parameters files. Additionally, a number of toys can be chosen (500 for this analysis), which represents the number of times the analysis is effectively re-run with changes to certain variables based on the active systematics. Systematic errors are discussed in more depth in Chapter 5.

The output of the analysis is in the form of a 'Microtree' which contains some information as standard, such as properties of certain tracks in the event (momentum, position, detector crossings etc), the events which pass each cut level and a header file containing information on the total Protons On Target (P.O.T) analysed and software versions used. The contents of this microtree are heavily expanded upon when creating an analysis, such that very specific quantities are represented and can be plotted easily. Additional data classes were written as part of this analysis, to encapsulate data concerning the neutral pion candidates and their constituents, and specific quantities contained therein were added to the output microtree for analysis.

The 'Drawing Tools' of *highland2* are possibly its most useful feature, offering a wide range of commands which once understood, can help an analyst to quickly and easily probe various details pertaining to a given analysis. The drawing tools are passed a data sample (Monte Carlo or Real Data Production), which can then be plotted in many useful forms, giving easy access to analysis variables, events passed for a given cut, truth information (often via the categories functionality) and selection efficiency and purity. The categories mentioned here are exceptionally useful for representing Monte Carlo data broken down into specific truth modes. For example, given a number of track objects being plotted against their momentum, the drawing categories could represent the true particle type of each object by colour (which would have been matched to a PDG particle code in the implementation).

Throughout this work, the drawing category used is called 'reactionpi0' is, an example of which can be found in Figure 4.11. This drawing category stratifies events by

: the number of  $\pi^0$ s produced in that event, whether or not that interaction was inclusive or exclusive, and other background options. A breakdown of the event properties which contribute to the drawing category are shown in Table 4.3.

Event Category	Description	Pre- $\pi^0$ Selection %
CC1 $\pi^0$	Charged-current event containing a $\mu^-$ , a proton and exactly one $\pi^0$	5.1
CCN $\pi^0$	Charged-current event containing a $\mu^-$ , a proton and more than one $\pi^0$	0.9
CC1 $\pi^0$ + X	Charged-current event containing a $\mu^-$ , a proton and exactly one $\pi^0$ + other particles	7.5
CCN $\pi^0$ + X	Charged-current event containing a $\mu^-$ , a proton and more than one $\pi^0$ + other particles	2.0
CC0 $\pi$	A typically clean CCQE signal with no additional particles emitted	49.2
CCOther	A Charged-current event producing a $\mu^-$ , a proton + other particles (no $\pi^0$ s)	25.5
Other	Any interaction not falling into any of the above categories (commonly neutral current interactions)	4.2
Out of FV	An interaction taking place outside the defined fiducial volume of the detector	5.6

TABLE 4.3: Definitions of the signals which define the subsets for the ‘reactionpi0’ drawing category, used throughout this analysis. All particles described are those present in the final state. ‘Other’ particles includes : charged-pions, neutral etas, neutral rhos, kaons, electrons, positrons and anti-muons. Percentage of events is passing muon selection.

## 4.5 Actions and Cuts in the $CC\pi^0$ Inclusive Analysis

In highland2, ‘Actions’ can be classed as methods which serve to obtain information about an event or the objects within that event, whereas ‘Cuts’ will act upon this information to retain or disregard certain events. In order to select charged-current events which contain at least one  $\pi^0$  in the final state, it is required to subject all events to a series of cuts which preferentially retain that signal. This process begins with a series of cuts, previously designed to select charged-current events (by searching for a  $\mu^-$ ) and are followed by cuts which aim to select the decay photons from a  $\pi^0$  candidate. This section provides an in-depth focus on each of the cuts and actions which comprise the selection, with special attention paid to the cuts used and their optimisation. This will be presented in a linear fashion, in the same way that the selection steps are linear. All optimisation was carried out using a Monte Carlo sample of Run 4 Air (Water Out) of  $4.27 \times 10^{20}$  P.O.T. All actions and cuts act on the final state particles existing in an event which are result from the interaction vertex producing the  $\mu^-$ . This process is identical for actual data using reconstructed physical quantities and running on Monte Carlo.

### 4.5.1 Selecting the Muon

Highland2 allows analysts to import cuts, actions and full selections into a new analysis. A well-established selection used by the T2K Experiment is the Charged-Current Inclusive analysis [124], which aims to select all events where a muon neutrino has interacted with a neutron in the scintillator target of FGD1 (FGD2 interactions can be found but this analysis focuses on FGD1), thus producing a muon which then continues through to the TPCs. As stated, this is an inclusive selection and thus should retain the events which also produce a neutral pion, at the same efficiency rate at which general charged-current events are retained. Track quality restrictions applied as part of this selection ensure that the main muon track candidate has 19 (out of 72) TPC segments [125], which ensures proper track reconstruction, and that it is not backwards going, i.e. it corresponds with the beam direction. This track quality restriction was established

using control samples, where 19 measurements of energy within the TPC was deemed to be the minimum necessary to accurately perform particle identification. A significant momentum bias for events with fewer than 18 hits in the TPC was determined, which would render momentum and PID determinations unreliable.

As can be seen in Figures 4.10 and 4.11, there is good agreement between the event rate predicted in the Monte Carlo and the data for this part of the selection. These plots do not take into account detector systematics and model uncertainties, which along with additional interactions such as meson exchange currents (MEC), may account for discrepancies in some of the bins. The 2p-2h effect is shown to lightly contribute to events in Figure 4.10, and is dominated by MEC, where 2-nucleon emission from the primary vertex occurs, instead of single nucleon emission from a typical CCQE interaction.

It can be seen in Figure 4.10 that the dominant contribution is from CCQE, where no secondary particles are produced from resonances. When this is broken down into the event categories described in Table 4.3, which shows the interaction contributions in terms of the number of  $\pi^0$ s produced (See Figure 4.11), we can see that only a fraction of events passing the  $\nu_\mu$  CC inclusive selection produce one or more  $\pi^0$ s (14.7%).

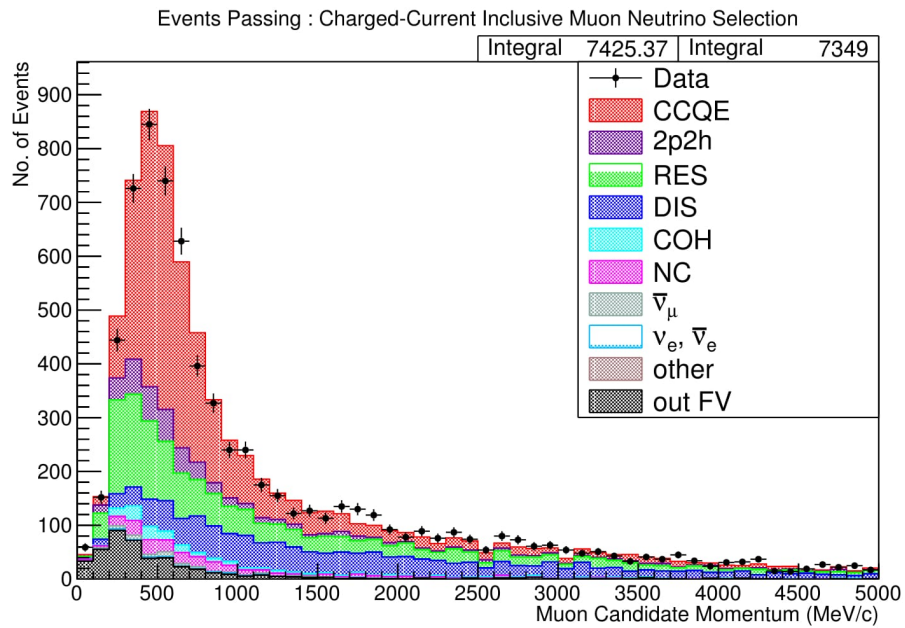


FIGURE 4.10: Momentum of muon candidates which pass the charged-current inclusive selection by interaction type.

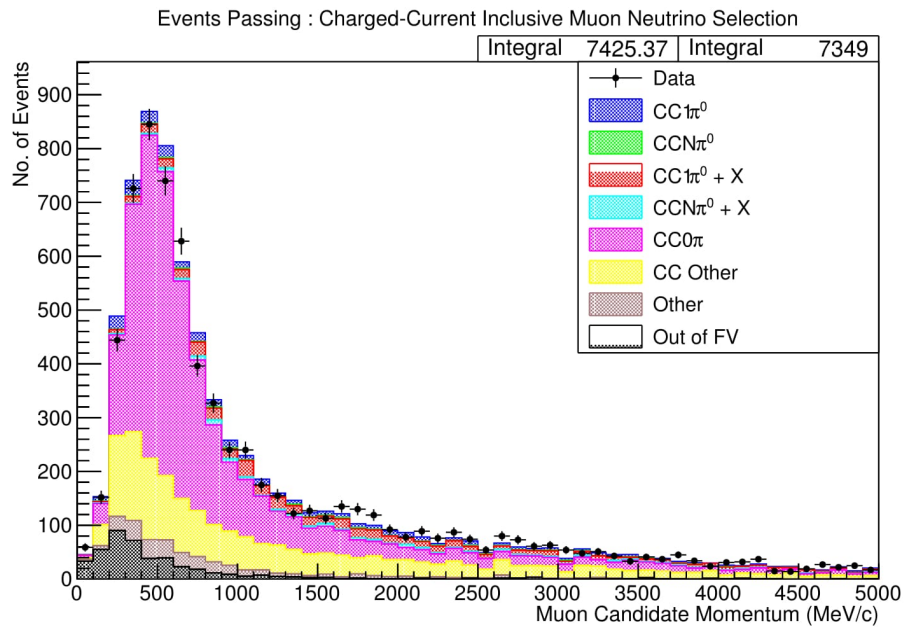


FIGURE 4.11: Momentum of muon candidates which pass the charged-current inclusive selection by  $\pi^0$  reaction type.

### 4.5.2 Finding True Vertex $\pi^0$ s

Once the muon has been selected, the next stage is to identify events which contain a  $\pi^0$ . To this end, the event level truth information is examined. In a given event, this action finds all of the true  $\pi^0$ s produced at the vertex which also produces the muon. This is information that we are only sensitive to in the Monte Carlo, which in real data, the selection process will aim to accurately predict. Unlike all other cuts and actions in the selection, this takes place only once per event, even in the case of multiple toy experiments, as regardless of systematic variations or weights, the number of true  $\pi^0$ s produced in a given event will remain constant.

This action first determines the primary vertex of the event, then iterates over all particles produced at that vertex. If any of the particles produced are  $\pi^0$ s, the counter keeping track of  $N\pi^0$ s is incremented and all of the information about this  $\pi^0$  is stored in a true  $\pi^0$  data class. This data class encapsulates qualities of the  $\pi^0$  object such as its unique ID, the number of 'child' decay products it has, and consequently the PDG codes and unique IDs of all of those. This process is repeated for as many true  $\pi^0$ s as there produced at the vertex of interest, i.e the muon vertex.

We can see here that events which pass the charged-current inclusive selection predominantly contain no  $\pi^0$ s. Only 12.2% of those events shown contain exactly one  $\pi^0$ , and 2.5% of events contain more than one  $\pi^0$ . Therefore it would be uninformative to simply use this existing CC inclusive selection when attempting to understand  $\pi^0$  events.

### 4.5.3 Finding Signal Relevant Objects

Firstly, all good quality track objects which were reconstructed for this event are accessed from a native highland2 data structure. This data structure contains objects which have passed data and track quality cuts. Tracks which begin in FGD1 and have a TPC component, are retained and split by charge into two toybox containers for electron candidates and positron candidates, where they remain for analysis to be conducted later in the selection. The track objects in these containers represent potential decay

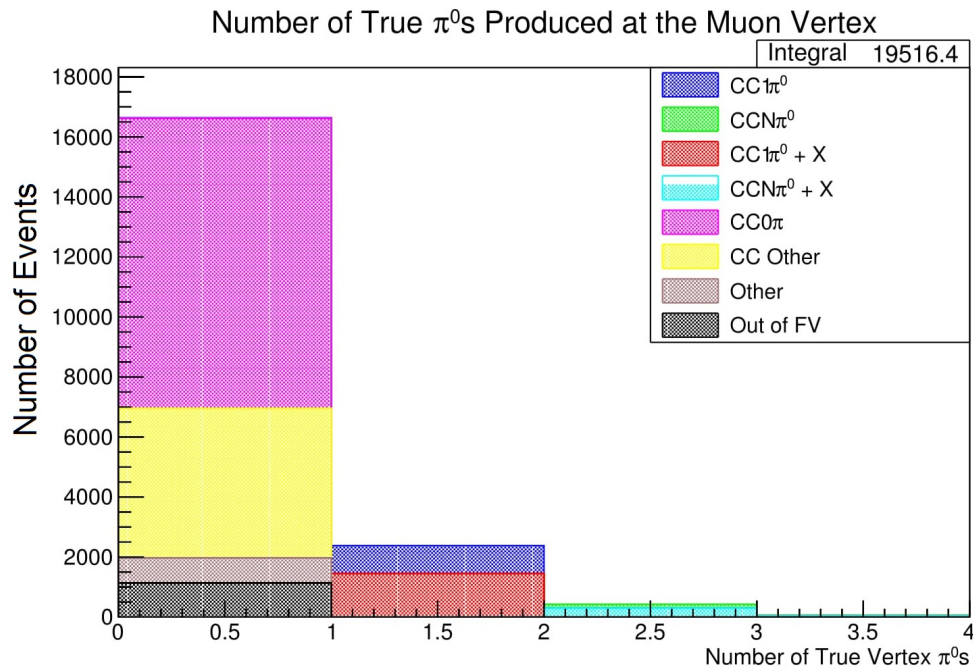


FIGURE 4.12: Number of True  $\pi^0$ s in Events Passing the Charged-Current Inclusive Selection

products of the decay photons produced by a  $\pi^0$ . Of course, the event muon candidate is excluded from this process, and all other actions after the initial charged-current selection has been passed.

We can see in Figure 4.13 that the majority of events do not contain any additional tracks beyond the muon, which originate in FGD1 and deposit enough energy over a certain distance in the TPC to pass the good quality requirement. For the  $\pi^0$  event contingent of this zeroth bin, it is likely that these are events containing only showers, which will be assigned to the ECal + ECal branch. For the events which comprise the CC Other contingent, these additional particles may stop fully in the FGD or also convert in an ECal. We can see here that requiring a minimum of one track here and a maximum of five would be a sensibly motivated restriction.

These are good quality tracks with a well reconstructed TPC segment, and so it is possible to perform reconstructed charge identification upon them, which will help later when pairing up  $e^+$  and  $e^-$  tracks to generate decay photon pair candidates.

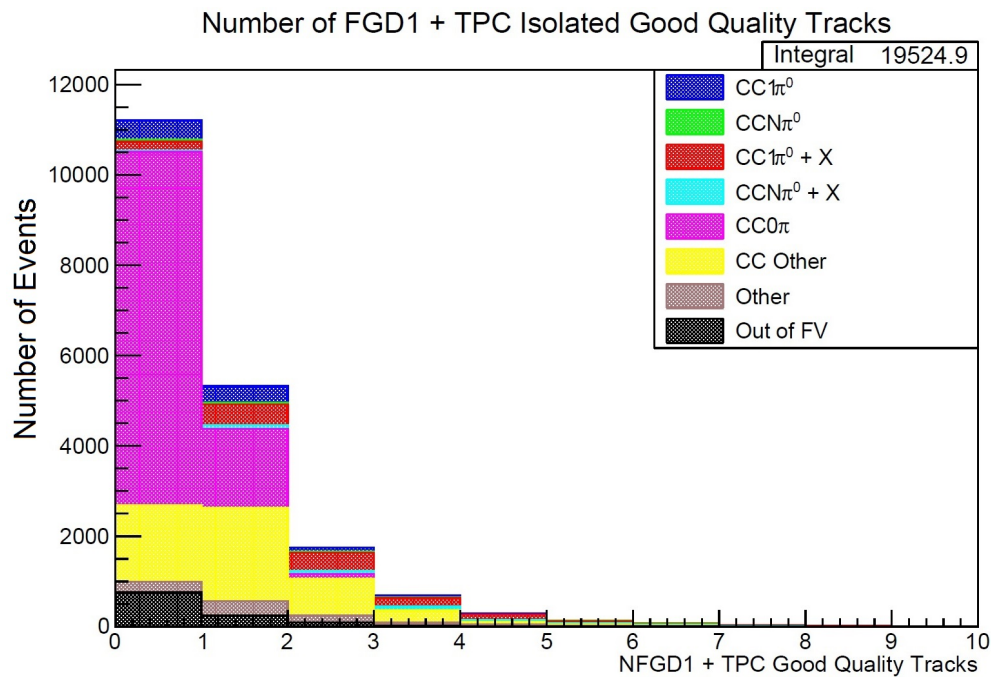


FIGURE 4.13: The number of tracks with both an FGD1 and TPC component, by number of events. This excludes the main muon track of the reconstructed charged-current interaction.

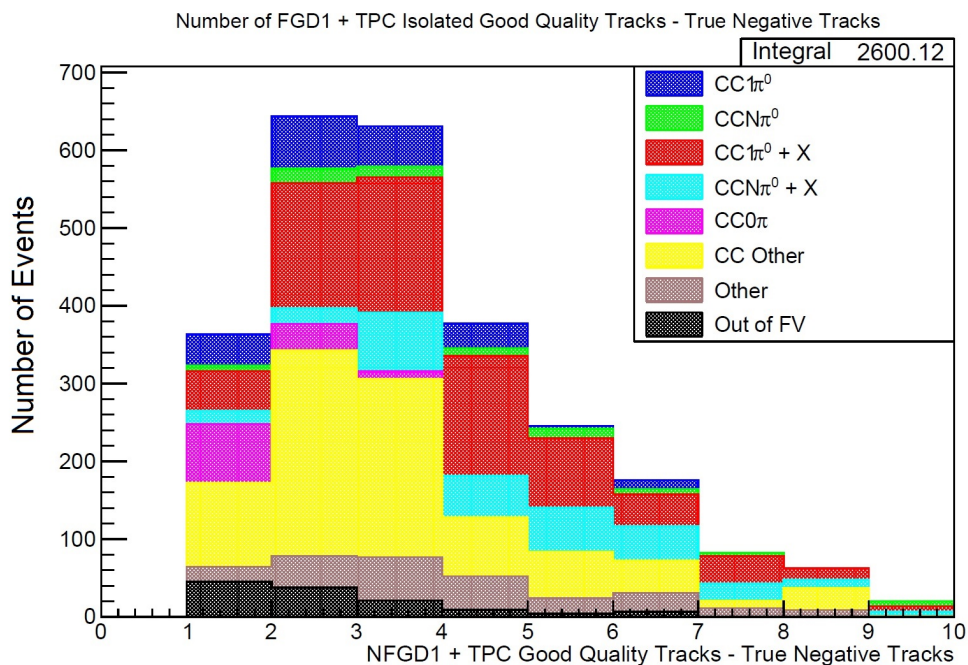


FIGURE 4.14: The number of true negative tracks with both an FGD1 and TPC component per event. This excludes the main muon track of the reconstructed charged-current interaction.

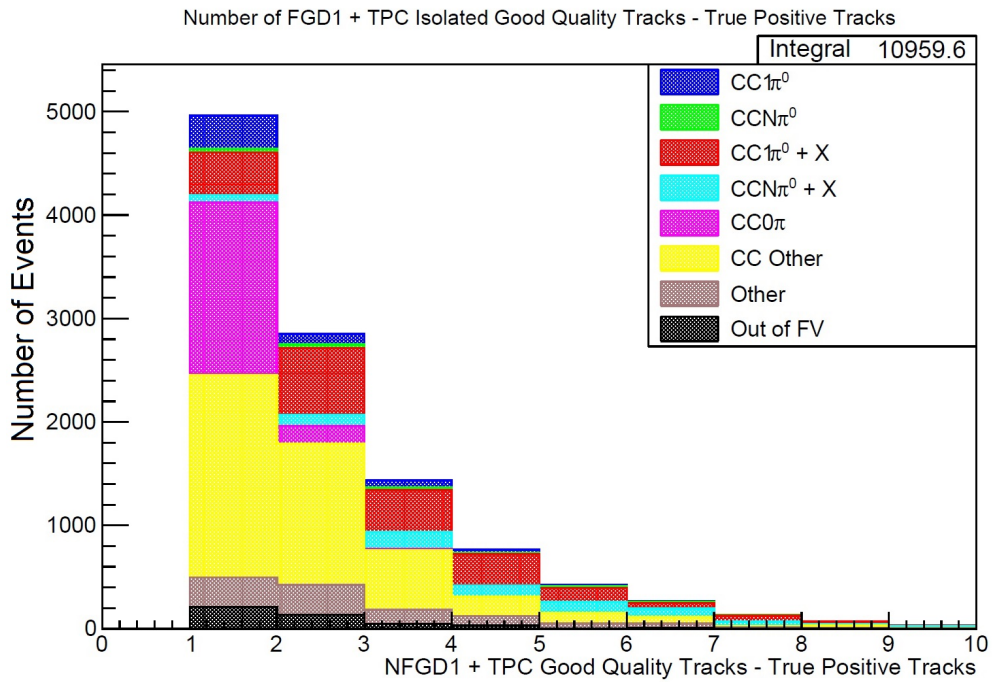


FIGURE 4.15: The number of true positive tracks with both an FGD1 and TPC component per event.

By comparing Figures 4.14 and 4.15, we can see that there are many more events which contain only one reconstructed true positive track than there are events which contain only one reconstructed true negative track, which is mainly due to the artificial removal of the  $\mu^-$  candidate from consideration.

To illustrate the effectiveness of the charge reconstruction, a comparison of true and reconstructed charge was carried out. This yielded that for the same track set as above, 97.4% of the time a positive track had its charge correctly identified and 88.0% of the time a negative track had its charge correctly identified. This is expected, as the charge reconstruction is a function of particle momentum [123] and would therefore be much more effective for heavy particles such as protons which we know make up a large portion (55.4%) of this sample. This illustrates that it is reasonable to use the reconstructed charge in the selection, an issue which is also addressed as a detector weight systematic - ‘Charge Identification Efficiency’.

The next action focuses only on procuring tracks which are fully contained within FGD1. Due to the limitations of the detector in this region, its main purpose being

as an active target, particle identification is not as effective for these tracks as those which have a good TPC component, and charge assignment can not be trusted, due to insufficient resolution and track curvature within the FGD. At this stage, these objects may represent  $\pi^0$  decay products, or other particles produced at the vertex, including the outgoing proton.

it can be seen in Figure 4.16 that the majority of events contain no isolated FGD1 tracks, which is expected as generally tracks will be energetic enough to travel into the TPC. There is a significant portion of  $\pi^0$  events in the zeroth bin, where presumably all tracks from photon conversions have made it out of FGD1.

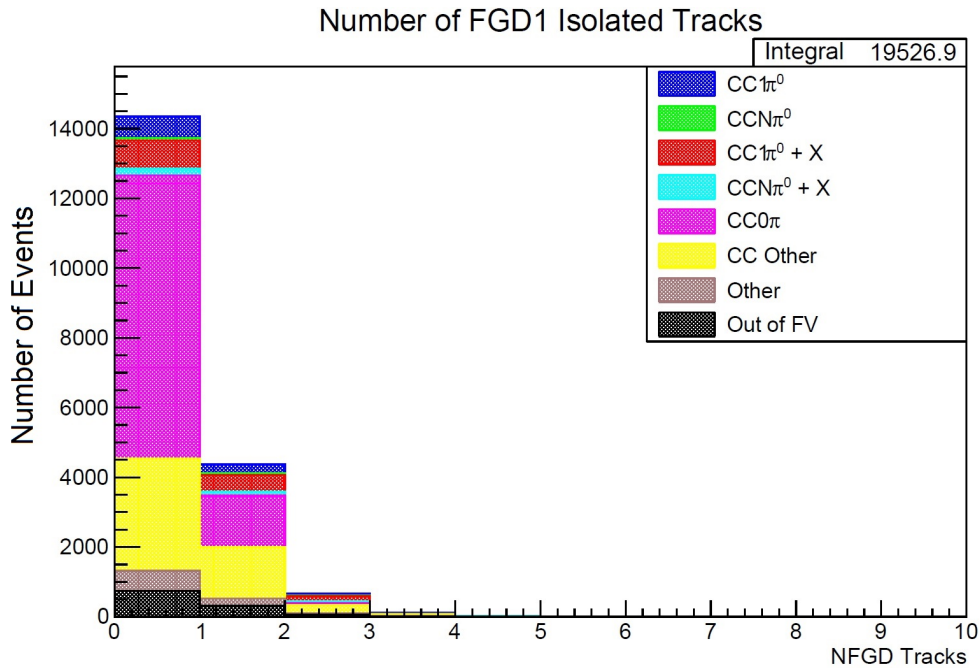


FIGURE 4.16: The number of reconstructed isolated FGD1 tracks per event.

As for the TPC tracks, charge reconstruction was investigated for the isolated FGD tracks, this yielded the conclusion that the current reconstruction almost always determines tracks as positive, and so it was decided not to rely on this.

At this point, all track objects of interest have been stored in containers for later use. Next, objects which are reconstructed in any of the ECals (Downstream or either Barrel) are accessed. These may be track or shower objects, but initially all objects are stored in one container, representing potential decay photons from a  $\pi^0$ . We know that any  $\pi^0$ s will be produced very close to the initial muon vertex and have a very short lifetime. Unless these photons pair convert or scatter in the FGD or TPC, they will be effectively invisible until they convert in an ECal, causing a shower. Therefore, any true  $\pi^0$  decay photons will only have an ECal component, making them effectively isolated. A check is performed at this point, which ensures that a reconstructed ECal object is not matched with an existing track object in the event. Only isolated ECal objects are retained in the aforementioned container, which helps to remove backgrounds from track objects which have both a tracker and ECal component. This does not help with

backgrounds from certain other processes, e.g. Bremsstrahlung.

#### 4.5.4 Building $\pi^0$ Decay Photon Candidates

The next step in the selection serves to cast the objects in the isolated ECal object container into  $\pi^0$  ECal decay photon candidate objects (DPCs). This is done using a bespoke data class, exclusive to this analysis, which allows complex objects to be built, giving access to information regarding the kinematic properties of that object (and its constituents), truth information and unique IDs which are assigned to each object in the Monte Carlo. The same data class is used later in the selection when building the tracker decay photon candidates, but it will be described now in its entirety.

The `AnaPi0DecayPhotonCandidate` data class, is at the very core of this analysis. It provides access to the reconstructed objects which combine to form a  $\pi^0$  candidate object, which in this analysis branch these are built from one tracker DPC and one ECal DPC. The data class is comprised of three core constructors, which serve to address each potential type of DPC.

Firstly, the ECal DPC constructor simply casts an isolated ECal object to an ECal DPC, this is done both for consistency and to give easy access to certain properties, such as energy, direction, start position and truth information. This particular constructor is not explored extensively in this branch of the analysis, but it used more thoroughly in the ECal + ECal branch, which uses a multivariate approach [126]. Better use of the properties of these objects might improve future analyses, in terms of which ECal DPCs are retained for building  $\pi^0$  objects.

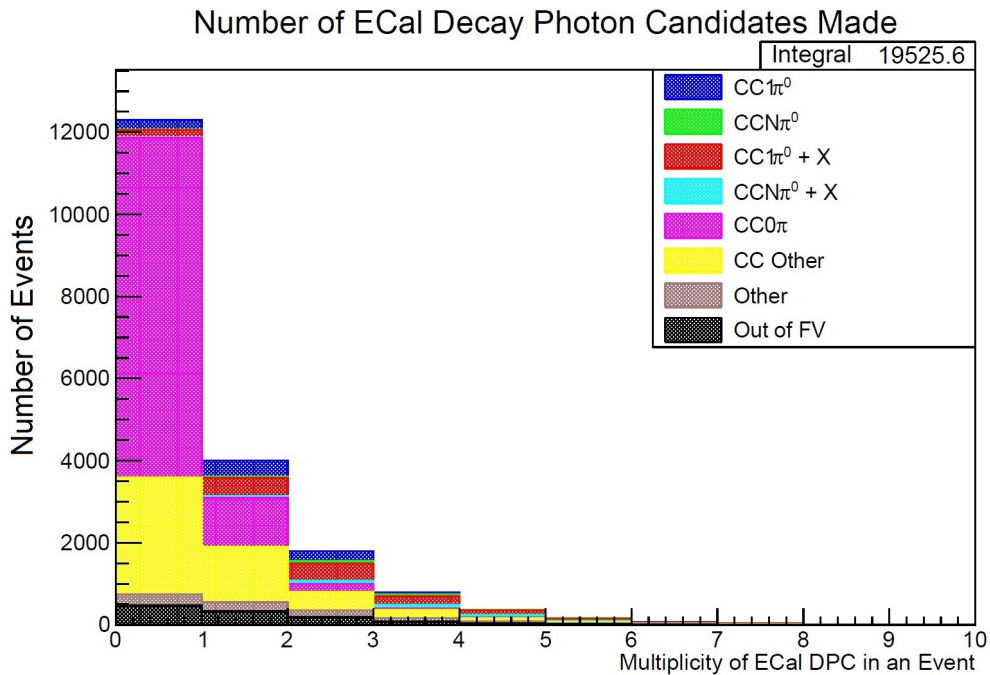


FIGURE 4.17: The number of ECal DPCs built in each event which pass the muon selection.

We can see in Figure 4.17 that for the majority of events, no ECal DPCs are built, and that in those events there is also a much smaller proportion of  $\pi^0$  events. It is likely that the majority of these events contain no isolated ECal objects, belong in the Tracker + Tracker branch, and will be ushered that way in upcoming cuts. It is possible that in events which do contain truly isolated objects, those reconstructed objects have been mis-attributed to reconstructed track segments and therefore not built into ECal DPCs. The bins of interest here contain events for which one or more ECal DPCs are made, where backgrounds such as CC Other still dominate, but which will be reduced throughout the course of the selection.

Secondly and thirdly, the tracker DPC constructor can be either : a constructor which takes two reconstructed track objects as input, or just one track, the motivation for which is explained in Subsection 4.2.1. The track constructors are called later in the selection, as mentioned above, and build very useful objects which are cut on throughout the selection by accessing various kinematic properties. The single track

constructor provides easy access to track properties such as momentum, energy, position and collinearity with the muon. The double track constructor adds to this by calculating and storing new properties such as pair separation, pair invariant mass and pair collinearity with the muon. All of the DPCs are imbued with information regarding true particle type (PDG code) for itself, its parent, grandparent and primary, which can be very useful in background discrimination and elimination.

#### 4.5.5 ECal and Track Object Multiplicity Cut

At this point in the process there are two important cuts which both serve a dual purpose. Firstly, this is a three branched analysis, although this work only focuses specifically on the development and usage of the Tracker + ECal branch. This means that when the analysis is run in its entirety, objects and events may be double counted, i.e. used in more than one branch. One way of circumventing this problem would be to use a wholly multivariate approach, discussed in Section 4.9. The most simple way would be to not have a branched selection at all, and build all  $\pi^0$ s in all three topologies for each event. However, this approach would likely result in more false combinatoric objects, thus further degrading the true understanding of our built objects and would certainly not allow us to probe any differences in each individual conversion topology. The chosen approach was to retain the three branches, but to make each one mutually exclusive from the others, by limiting the phase space of the number of allowed track objects and isolated ECal objects in a given topology.

	NECallsoObj	NTracks*
ECal+ECal	== 2	== 1
Tracker+Tracker	== 0	$\geq 3$ AND $\leq 5$
Tracker+ECal	== 1	$\geq 2$ AND $\leq 3$

TABLE 4.4: The number of minimum track and isolated ECal object requirements for each branch. \*NTracks is all tracker objects (TPC and FGD) and includes the main muon track.

The minimum requirement (Table 4.4) is, of course, very restrictive and only identifies the smallest number of objects of each type which would be required to have exactly one clean  $\pi^0$  decay in a given topology. The ranges reflect the fact that a tracker DPC can be built from one or two tracks. Upper limits to these parameters can be probed, as long as the branches remain exclusive, i.e. the phase space does not overlap.

### All Parameter Space Plot

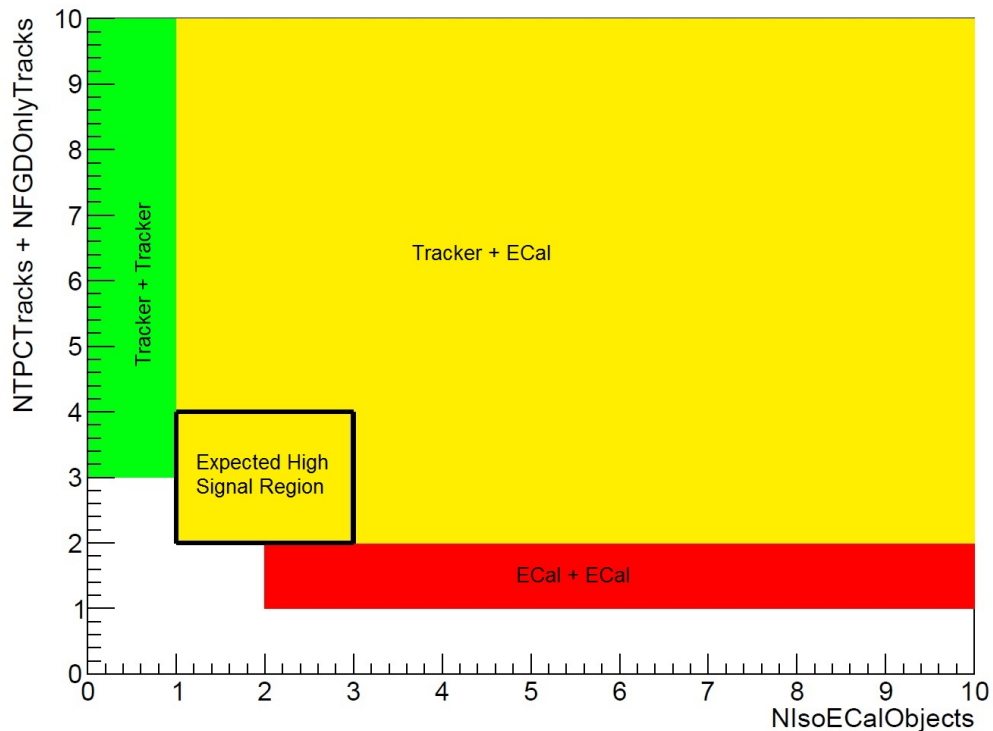


FIGURE 4.18: A visual representation of the track and isolated ECal object phase space which delineates each branch. The muon track is counted among NTPCTracks, therefore no charged-current muon neutrino events could occupy the bottom row.

As can be seen in Figure 4.18, each topology has a valid area of parameter phase space in which to expand, with the Tracker + ECal branch being allowed to expand in both directions. It may be that limiting the number of isolated ECal objects (Tracks) for the Tracker + Tracker (ECal + ECal) branch will prove to be too restrictive, i.e. if a Tracker + Tracker event has a bremsstrahlung shower it would be incorrectly pushed into the Tracker + ECal branch. However, barring a full multivariate approach, and with time constraints this compromise was a reasonable choice.

To confirm that these phase spaces were sensitive to the production of true  $\text{CCN}\pi^0$  events, similar plots to Figure 4.18 were produced which are broken down into signal and background. At this point we introduce the second purpose of these cuts, which is to limit backgrounds, namely the combinatoric effect, which arises from allowing many reconstructed objects to make up the  $\pi^0$  candidates. This number increases dramatically as the number of allowed tracks and isolated ECal objects increases.

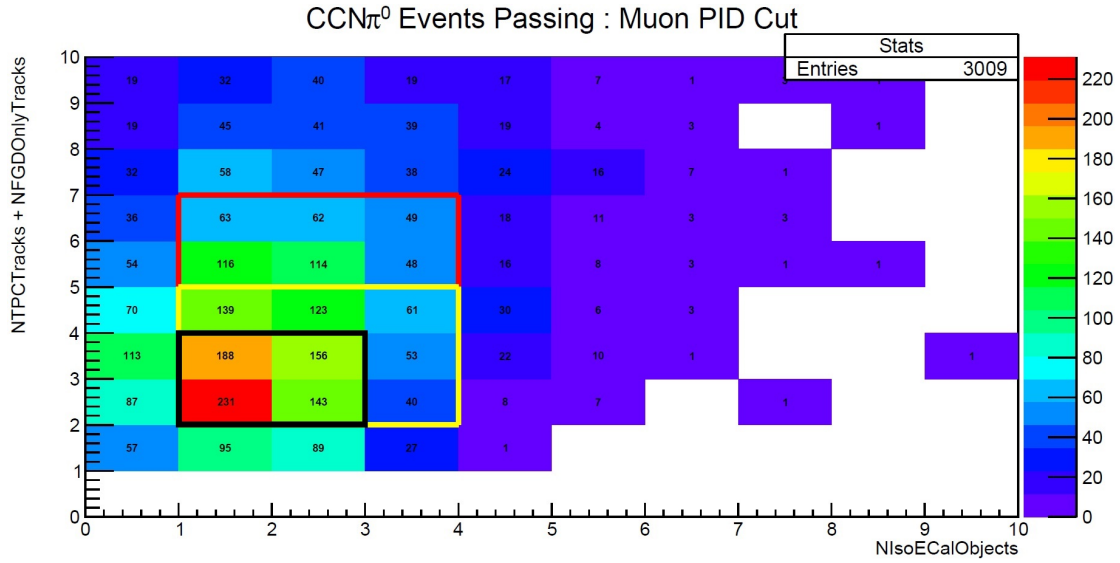


FIGURE 4.19: A visual representation of the track and isolated ECal object phase space for  $\text{CCN}\pi^0$  signal events. All events shown are those which contain at least one  $\pi^0$  in the MC truth. The black box shows an area of high signal, followed by the yellow and then red boxes. As the parameter space is expanded, more signal events are retained but this also leads to the inclusion of further backgrounds. The black, yellow and red boxes contain 23.9%, 37.7% and 52.7% of the total signal events respectively.

We can see in Figure 4.19 that the parameter space accessible to the Tracker + ECal branch does certainly provide sensitivity to  $\text{CCN}\pi^0$  events. By comparing with Figures 4.21 and 4.20, we see a motivation for limiting the number of allowed reconstructed objects to be within the red boxed region, which has the highest signal to signal + background ratio (purity) at 25.5%. We also see a hint here that disregarding events with two tracks may be beneficial, as while this would result in a lower efficiency (due to losing a significant source of  $\text{CCN}\pi^0$  events), it would overall increase the purity of the sample. If purity is considered to be important, this will have an effect at the optimisation stage.

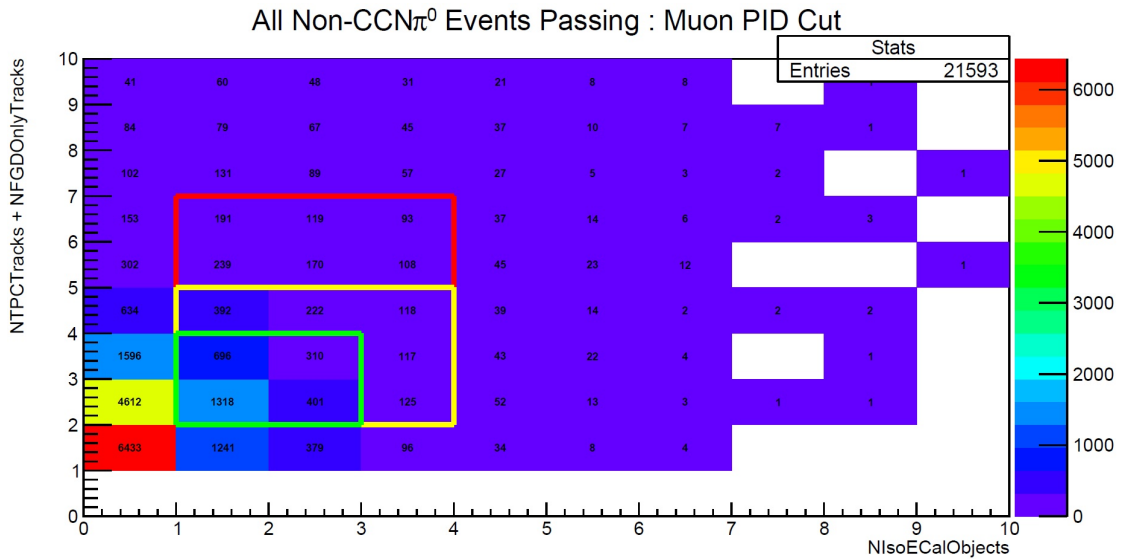


FIGURE 4.20: A visual representation of the track and isolated ECal object phase space for MC truth Non-CCN $\pi^0$ , i.e. background events. The green, yellow and red boxes contain 12.6%, 17.2% and 19.7% of the total background events respectively.

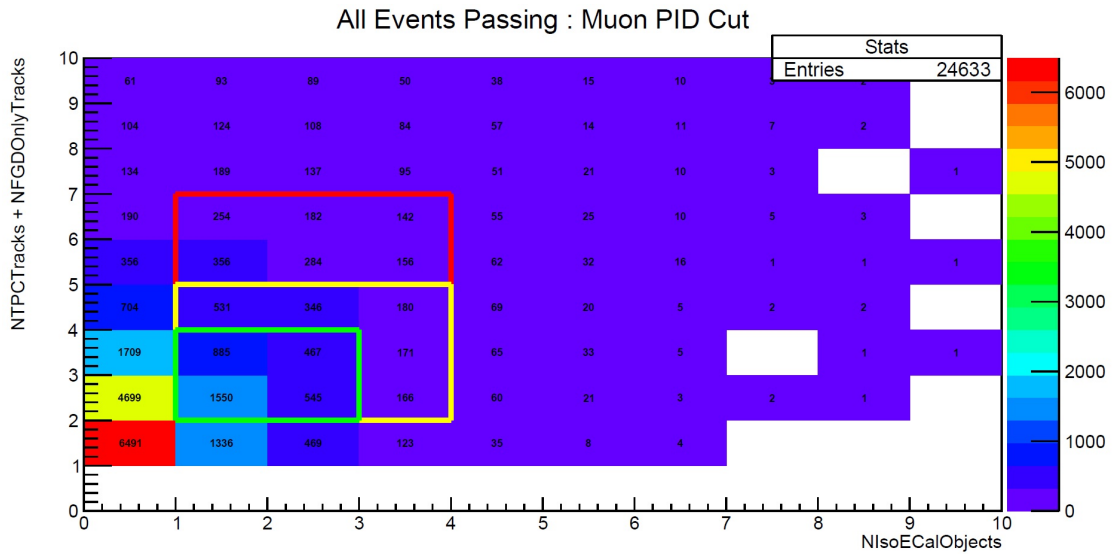


FIGURE 4.21: A visual representation of the track and isolated ECal object phase space for all events, both signal + background. The percentage of Signal/Signal + Background events in the green, yellow and red boxes is 20.8%, 23.4% and 25.5% respectively.

We can see in Figures 4.20 and 4.21 that the background events and total events have similar distributions (dominated by background) in the region of Tracker + ECal interest, steadily decreasing as the phase space box is expanded. Given the relatively

high backgrounds in the smallest box, it may prove that the larger phase spaces offer not only access to more events but in fact at a higher purity, as outlined in the caption of Figure 4.21. We can also illustrate here again that at this point, after the muon selection,  $\sim 12\%$  of the total events accessible in the full  $(10 \times 10)$  parameter phase space are  $\text{CCN}\pi^0$ .

#### 4.5.6 ECal Object Energy Cut

After the branch splitting stage, all actions and cuts now focus exclusively on the Tracker + ECal topology. Four cuts act upon the previously built ECal decay photon candidates. These begin with the energy cut, which is very straight forward and simply requires that the object must have deposited total energy within a given range (determined by signal optimisation), within the calorimeter. If it does not satisfy this requirement then it is removed from consideration as a constituent of a  $\pi^0$  candidate, and if there are no ECal DPCs left at this point, the cut returns false and the selection process will not continue.

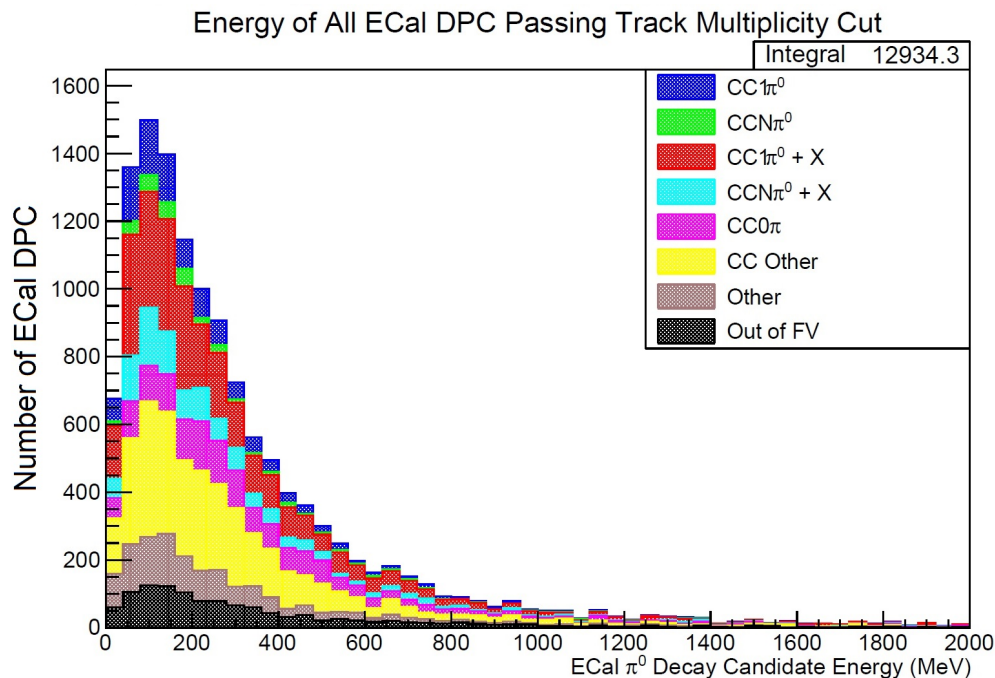


FIGURE 4.22: Distribution of the energies of all ECal DPC in events which have passed the multiplicity cuts.

In Figure 4.22 it is difficult to see if there is any preference for  $CCN\pi^0$  events to lie in any particular energy range for these ECal DPC. It would certainly be fair to implement a cut at 2000 MeV to cut out the long tail, and perhaps even 1000 MeV to ensure a cleaner signal.

Other restrictions include a lower energy limit of 30 MeV on these objects, which is due to limitations in the ECal reconstruction at very low energies. If the energy fit fails then a default value of  $\sim 28$  MeV is returned, irrespective of the objects true energy. Failure of this fit may occur if there are insufficient hits in the object. More detailed optimisation was achieved using a signal maximisation algorithm as will be explored in detail in the Section 4.6.

#### 4.5.7 ECal Object to Muon Vertex Distance Cut

To investigate if there is any preference of certain distance ranges from the muon vertex for true ECal DPCs, an analysis variable was added to the data class and analysis microtree for study. This distance will have a minimum, as it is constrained to begin in the ECal, and also have a maximum, defined by the outer dimensions of the detector. We expect a  $\pi^0$  produced at the muon vertex to decay almost immediately, and for its decay photons to fully convert before they leave the Tracker + ECal region. The fact that  $\pi^0$  decay photons are fully contained within the detector is an intentional consequence of the ECal design (See 4.5.7).

‘...the lead thickness of 1.75 mm was chosen based upon studies of  $\pi^0$  detection efficiency. The number of layers was determined by the requirement to have sufficient radiation lengths of material to contain electromagnetic showers of photons, electrons and positrons with energies up to 3 GeV [87].

The shape of the distribution in Figure 4.23 is as expected given the ND280 geometry. The distribution ‘switches on’ at just below 500 mm, which is the minimum distance between a muon vertex in FGD1 and the start of a shower in an ECal. This

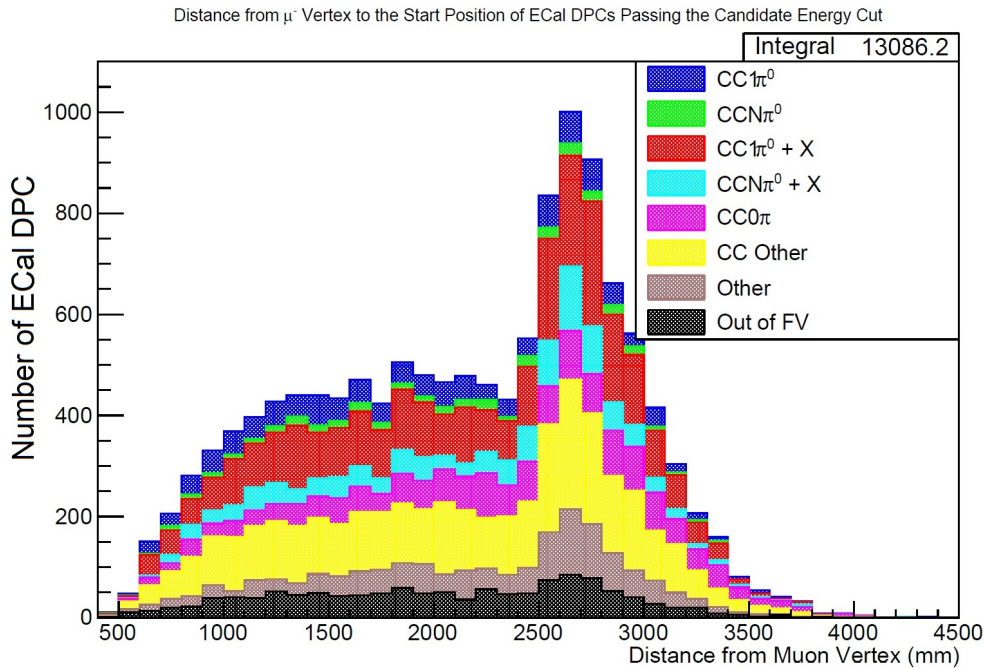


FIGURE 4.23: Distribution of the distance of the start position of all ECal DPCs from the  $\mu^-$  vertex.

is uniform and represents the barrel ECals accessible to these objects. It drops off at just above 3000 mm (not directly shown here), where it is obscured by the peak of ECal DPCs which make it to the Downstream ECal. At this point these objects could be from any particles and optimisation is needed to determine the validity of separating true  $\pi^0$  decay photons from background using this variable.

#### 4.5.8 ECal Object MIPeM Cut

Next we subject the remaining ECal DPCs to a MIPeM Cut. In 2012, a number of second generation ECal PID discriminators were developed [127].

These log-likelihood ratio variables can be used to :

- Distinguish showering particles such as electrons from non-showering particles, such as muons.
- Identify charged pions which behave like minimum ionising particles in the TPC.
- Identify low energy photons from  $\pi^0$  decay.

- Distinguishing highly ionising stopping particles (i.e. protons) from EM showers.
- Differentiate between EM and hadronic showers.

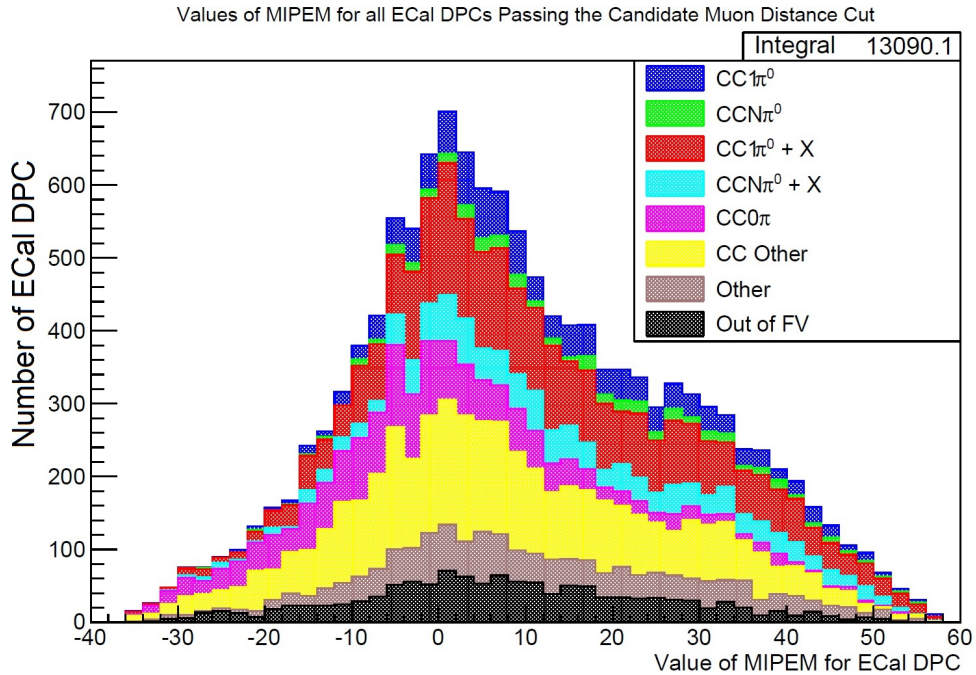


FIGURE 4.24: Values of MIPEM for all ECal DPC passing the unoptimised cut detailed in Subsection 4.5.7.

Electrons, positrons and gammas will be EM-like and shower, whereas muons, protons, pions etc will not. Discriminators are : MIPEM ( $e^+/e^-/\gamma$  and muon separation), EMHIP ( $e^+/e^-$  and protons separation), MIPPION (Pion and Muon separation). These PIDs could be extremely useful in this analysis, as we know that the showers of interest to us are caused by electromagnetic interactions and not minimum ionising particles. An assessment of all of the metrics mentioned above was carried out, but due to correlations, it was only practical to use one as each metric was a convolution of the same fundamental variables as the others. An analysis determined that MIPEM was the most effective metric to separate true electromagnetic showers from other background particles.

The MIPEM variable utilises a number of lower level variables which are used as inputs to an artificial neural network (ANN), the output of which is a likelihood PID.

Low level variables used include :

- Shower Opening Angle (mrad)
- Shower Width (mm)
- EM Energy Deposited (MeV)
- Axis Max Ratio - This gives a measure of how wide a cluster is relative to its length. It provides distinction between track-like (long-and-thin) and shower-like (short-and-wide) objects.
- Max Ratio - This exploits the difference in the longitudinal charge profiles of showering and MIP-like particles. The charge deposited in each layer of the ECal is calculated. Max Ratio is the ratio of charge in the highest charge layer to the charge in the lowest charge layer.

In future it may be effective to split the candidates by energy and preferentially use one metric over another, e.g. MIPEM Low for showers below 100 MeV. However a blanket approach was used for this analysis, using MIPEM for objects of all energies. Optimisation of the MIPEM cut is discussed in Section 4.6.

#### 4.5.9 ECal Object Collinearity Cut

This cut is the only one out of these four which (if effective) potentially has the power to discriminate electromagnetic showers from actual  $\pi^0$  decays from any other electromagnetic showers. It can do this by comparing the direction of the ECal shower with that of the direction of the vector which connects the muon vertex and the start position of that shower. If these two are close parallel (collinear) then we can say that it is likely that the source of the shower originated close to the source of the  $\pi^0$  decay, which is expected to be very close to the muon vertex. This method is explained in Subsection 4.5.14.

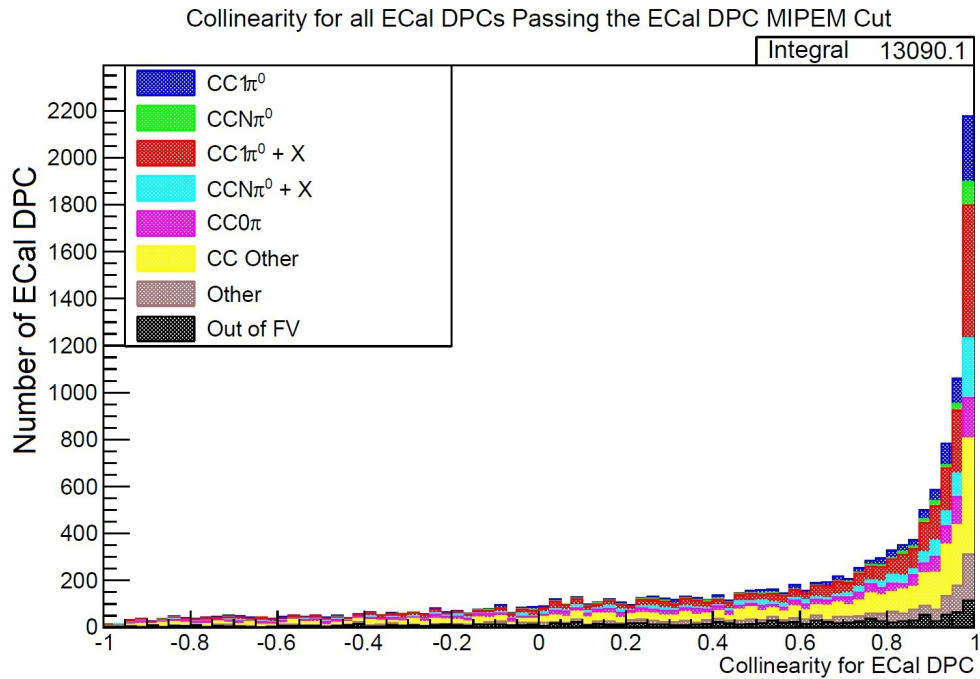


FIGURE 4.25: Collinearity for all ECal DPCs passing the unoptimised cut detailed in Subsection 4.5.8.

Candidates which are parallel with the muon-to-shower-start-position vector are expected to have a collinearity of 1. Figure 4.25 shows that very few events contain DPCs with collinearity less than zero, which would imply a directional vector heading back towards the muon vertex. However, unfortunately we see that the majority of candidates in all types of events seem to have a collinearity close to 1. This implies that this cut may not be very effective at removing false DPCs, providing very little discrimination in that region. This is likely due to the fact that if a charged particle is produced near to the vertex, then the direction of its consequent object in the ECal will have a collinearity close to 1. This cut should still theoretically be able to effectively remove Michel electrons or bremsstrahlung photons. Additionally, it is possible that there could be some discriminating power lost close to 1, due to the poorer direction resolution of the ECal when compared with the tracker.

#### 4.5.10 FGD1 Tracks Pion Pull Cut

A cut based on the particle identification of isolated FGD1 tracks, which are potential constituents of a Tracker DPC was explored. We know that we only wish to retain  $e^+$  and  $e^-$  tracks throughout the selection, and that other particle types can be produced at the vertex. Therefore some form of PID is needed to limit the number of Tracker DPCs.

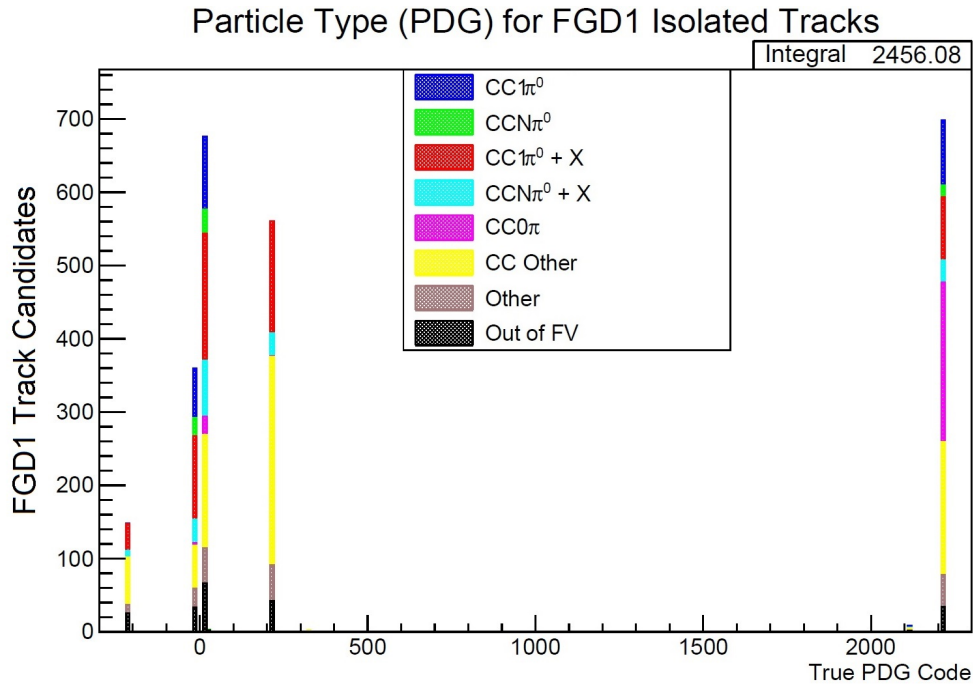


FIGURE 4.26: Full range of PDG codes which make up the FGD1 isolated tracks. This shows a large proportion of electrons and positrons ( $\pm 11$ ), but also large backgrounds from charged pions ( $\pm 211$ ) and protons (2212). The truth categories used are those described in Table 4.3.

In Figure 4.26 we can see that the major backgrounds are from protons (PDG = 2212), positive pions (PDG = 211), and negative pions (PDG = -211). With the peaks at PDG = 11 and PDG = -11 representing true electrons and positrons respectively. Looking in more detail in Figure 4.27, we can see a comparatively small contamination from muons at 13 and extremely small anti-muons contamination at -13. It is apparent from these plots that pions and protons provide the significant background for FGD1 isolated tracks.

In order to remove these backgrounds and preferentially retain useful signal, we

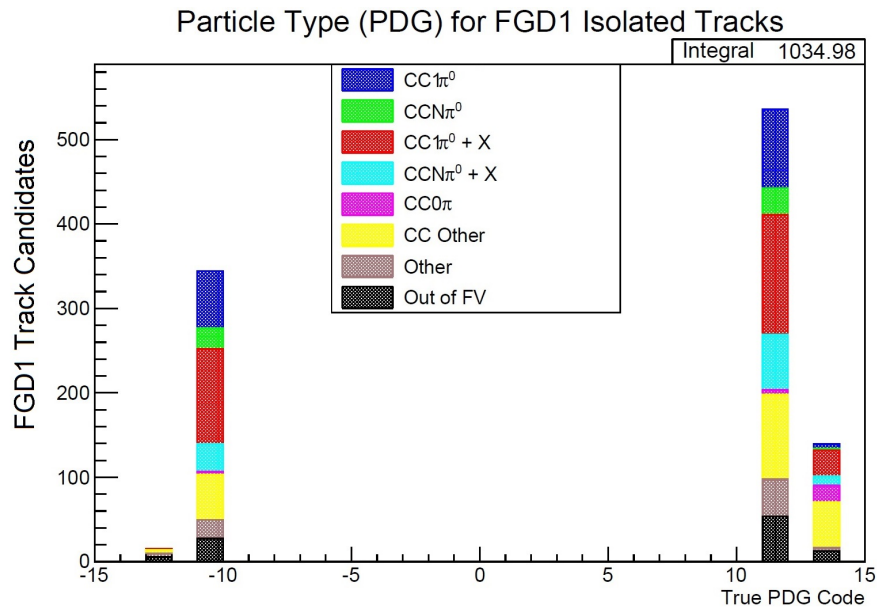


FIGURE 4.27: Restricted range of PDGs for FGD1 isolated tracks, showing  $\mu^-$  (and anti- $\mu^+$ ) contamination, as well as the electron and positron candidates. The truth categories used are those described in Table 4.3.

can use the ‘Pulls’ functions which exist natively for track objects in highland2. The pull value gives a measurement of how close a particle being analysed is to a particular particle hypothesis. These are calculated by comparing how much the energy of a given reconstructed particle deviates from that of a hypothetical particle probability density function for a determined track length and particle hypothesis. Ideally, the closer the likelihood of a reconstructed particle is to its hypothesis, the closer the pull will be to zero. In practice for real particles, many of the distributions for other particle types may be close to zero, but can still be very useful in separating these particles by pull values based on MC truth information.

As with the second generation ECal PID variables, there was more than once choice of FGD pull to use for this task, namely: FGD Proton Pull, FGD Muon Pull and FGD Pion Pull. The effectiveness of each of these pulls was assessed and FGD Pion Pull (Figure 4.28) was chosen as it seemed to be the best signal and background discriminator. This cut is unable to remove the electron and positron backgrounds produced by non- $CC\pi^0$  events.

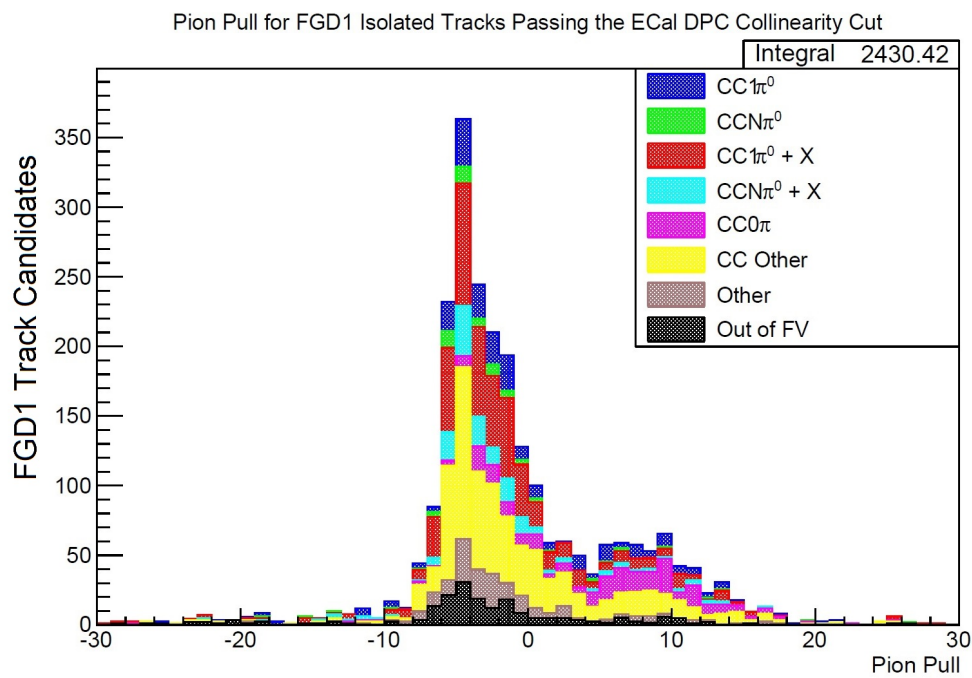


FIGURE 4.28: FGD track pion pull of all FGD1 isolated tracks passing the unoptimised cut detailed in Subsection 4.5.14. A large peak can be seen below zero and a smaller bump above. The large peak and the smaller bump are due to the way in which pion pull is calculated for particles of different species. True pions will tend to have a pull around zero (Figure 4.29, electrons and positrons less than zero (Figure 4.31) and protons larger than zero (although a significant portion may be mistaken for pions (Figure 4.29).

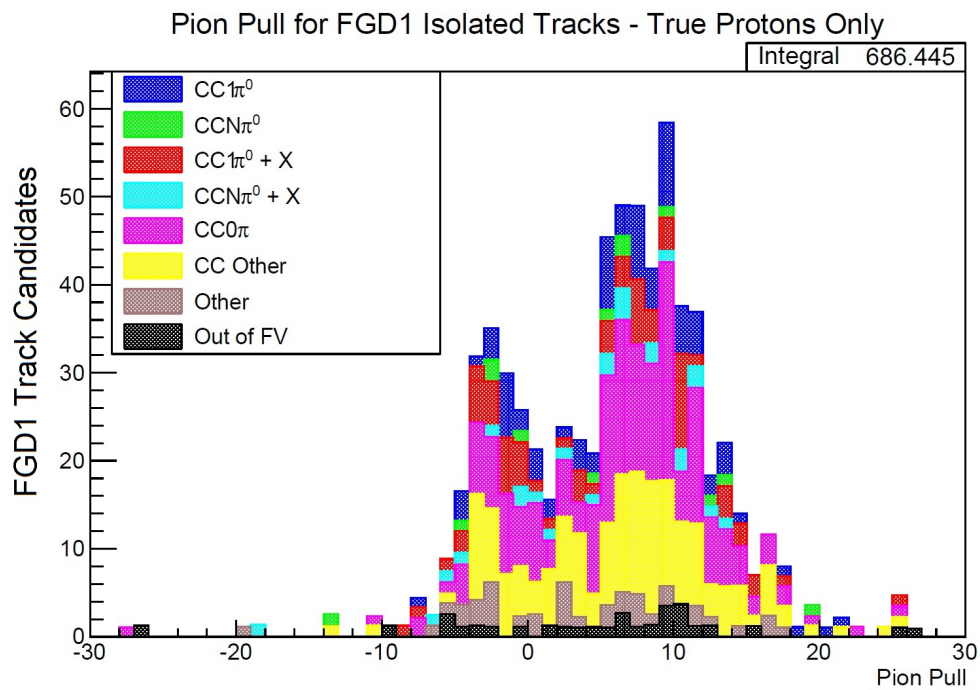


FIGURE 4.29: FGD track pion pull of true proton FGD1 isolated tracks passing the unoptimised cut detailed in Subsection 4.5.14. The true protons occupy a broad range of pulls, making some of them more difficult to remove using this variable than other particle species. The double peak is due to protons of certain momenta behaving in a similar fashion to pions in terms of  $dE/dx$ .

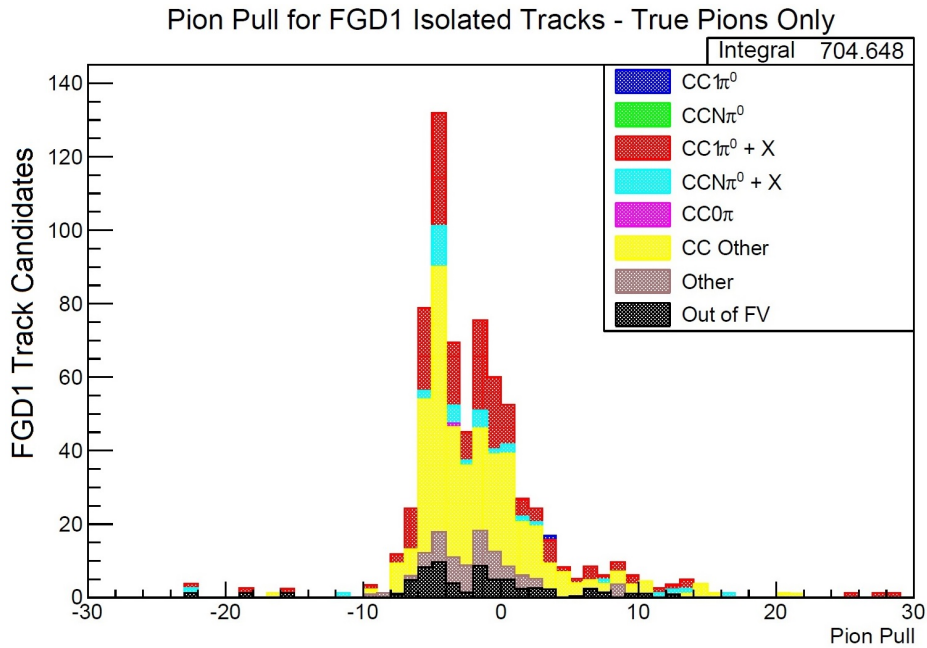


FIGURE 4.30: FGD track pion pull of true pion FGD1 isolated tracks passing the unoptimised cut detailed in Subsection 4.5.14. This is mostly centred around zero as we would expect for true pions matching the pull hypothesis. We can see that all events which contain a true pion track, necessarily satisfy an ‘Other’ event category.

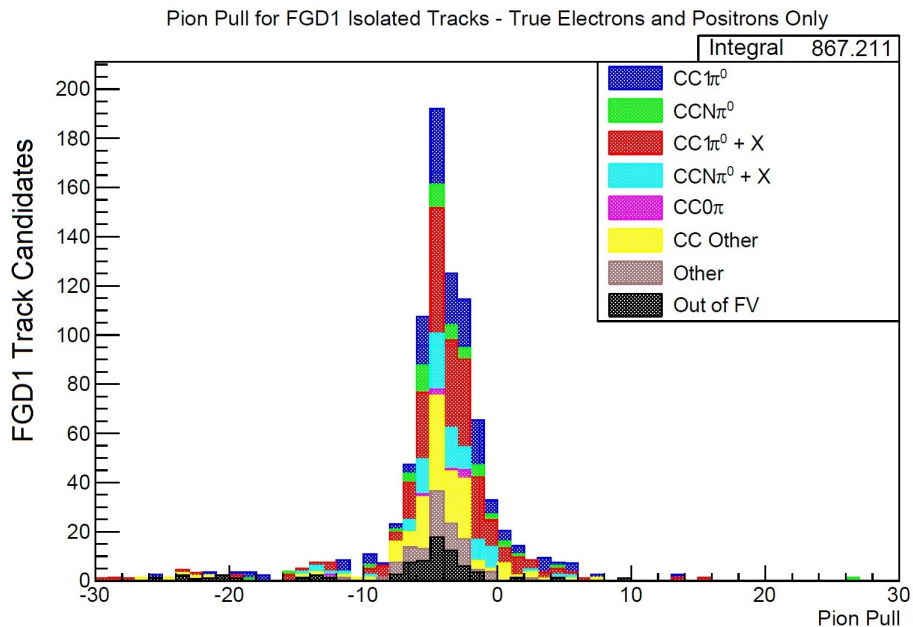


FIGURE 4.31: FGD track pion pull of true electron and positron FGD1 isolated tracks passing the unoptimised cut detailed in Subsection 4.5.14. This is a narrow peak predominantly below zero. By placing a sensible cut on FGD pion pull it is possible to remove a significant amount of proton background and a small amount of pion background.

By breaking down the tracks into the three main contributors, pions Figure 4.29 , protons Figure 4.30 and  $e^+/e^-$  Figure 4.31, it is clear from these Figures that there will be excellent discrimination of protons and  $e^+/e^-$  but sadly not as much for the background pions, which will need to be removed using further cuts. The range of values which maximised signal over background retention was determined during optimisation.

#### 4.5.11 TPC Tracks Likelihood Cut

Similar to the previous cut (FGD Pion Pull), the ‘TPC Track Likelihood Cut’, aims to preferentially remove background particle tracks over signal, however this cut acts upon tracks which have both an FGD1 and a good quality TPC component. Due to the higher resolution in this area of the tracker, determination of particle type should be more accurate for TPC tracks than FGD isolated ones. Rather than working on the basis of pulls, this cut uses the more common method for T2K analyses of likelihood functions, which benefit from additional information such as track curvature. For a given track, these likelihood functions return a probability that a given track is of a certain particle type (either Electron/Positron, Muon, Pion or Proton). If the probability of the particle being an  $e^+$  or  $e^-$  is lower than the chance of it being any one of the other three, then the track is removed from the box and therefore from future consideration as a Tracker DPC constituent. The effectiveness of these cuts is shown for negatively charged track candidates in Figures 4.32 and 4.33, and for positively charged candidates in Figures 4.34 and 4.35.

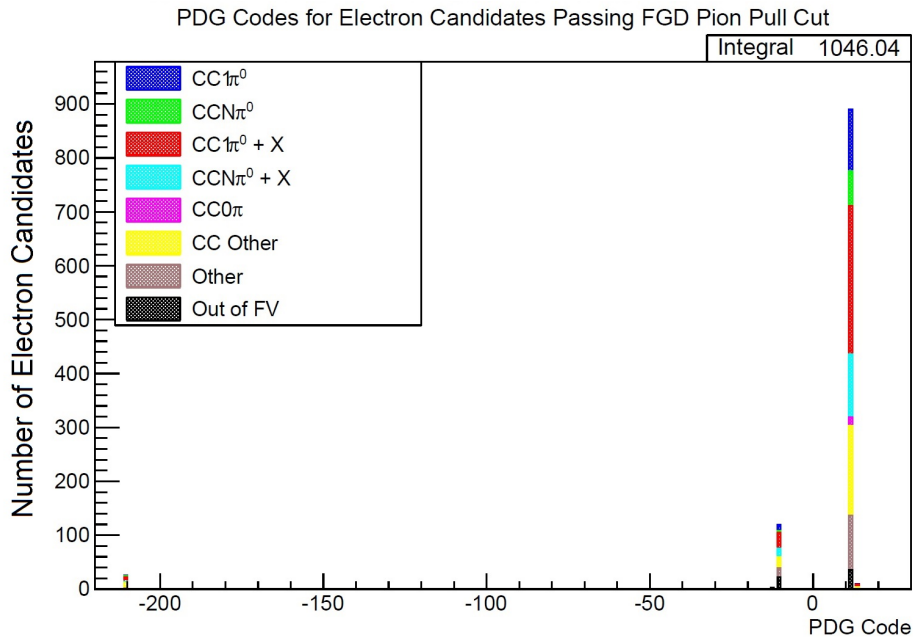


FIGURE 4.32: PDG Codes for TPC Electron Candidate Tracks before the cut detailed in Subsection 4.5.11. There are very few backgrounds for the negative tracks, the main one being positrons which are difficult to discern from electrons.

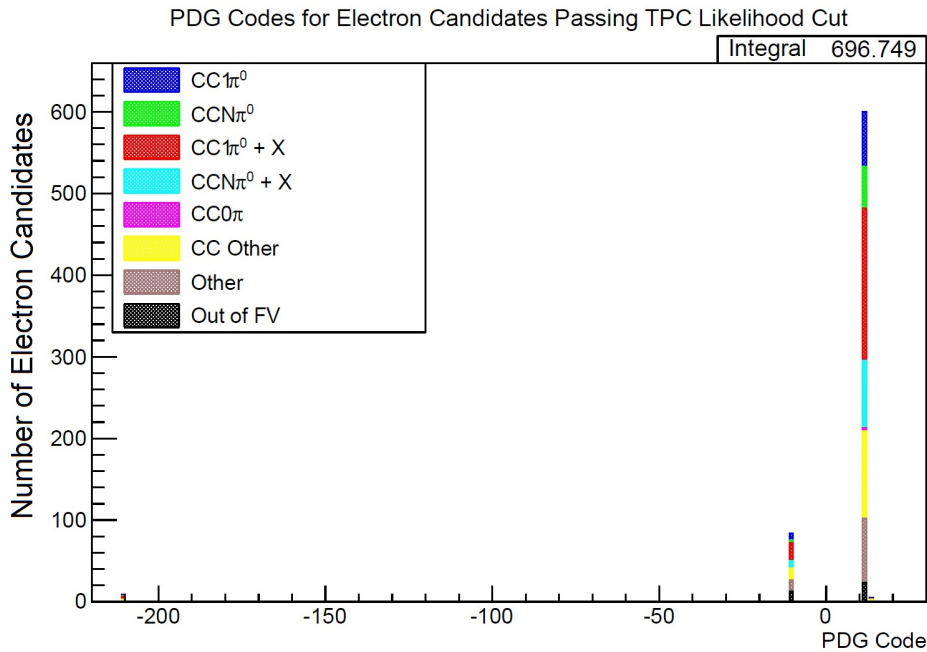


FIGURE 4.33: PDG Codes for TPC Electron Candidate Tracks after the cut detailed in Subsection 4.5.11. The likelihood cut fractionally decreases the positron and pion background, but significantly cuts out a large portion of potential signal. This cut is not worthwhile due to the initially low background.

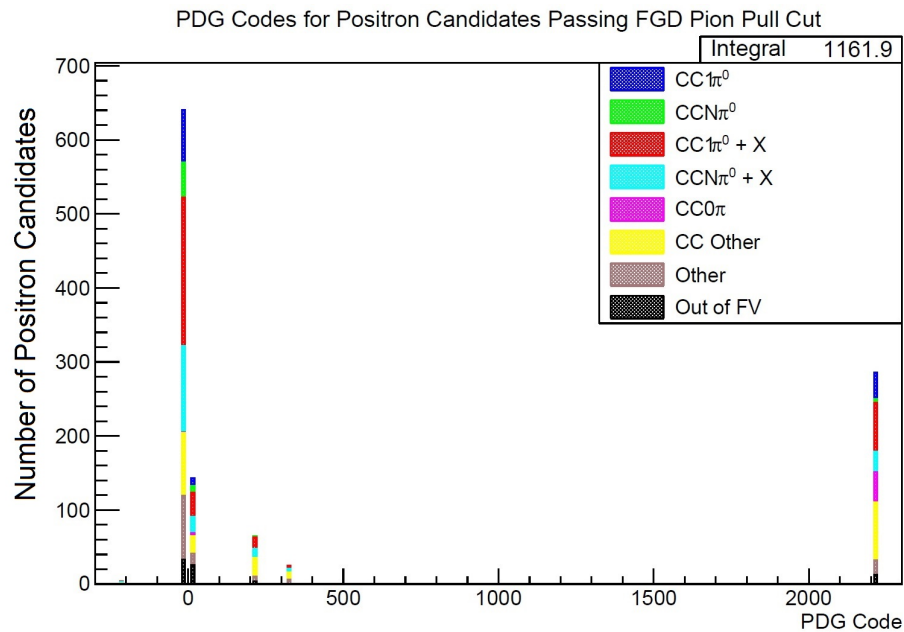


FIGURE 4.34: PDG Codes for TPC Positron Candidate Tracks before the cut detailed in Subsection 4.5.11. A large proton background and a small pion background can be seen for the positive track candidates.

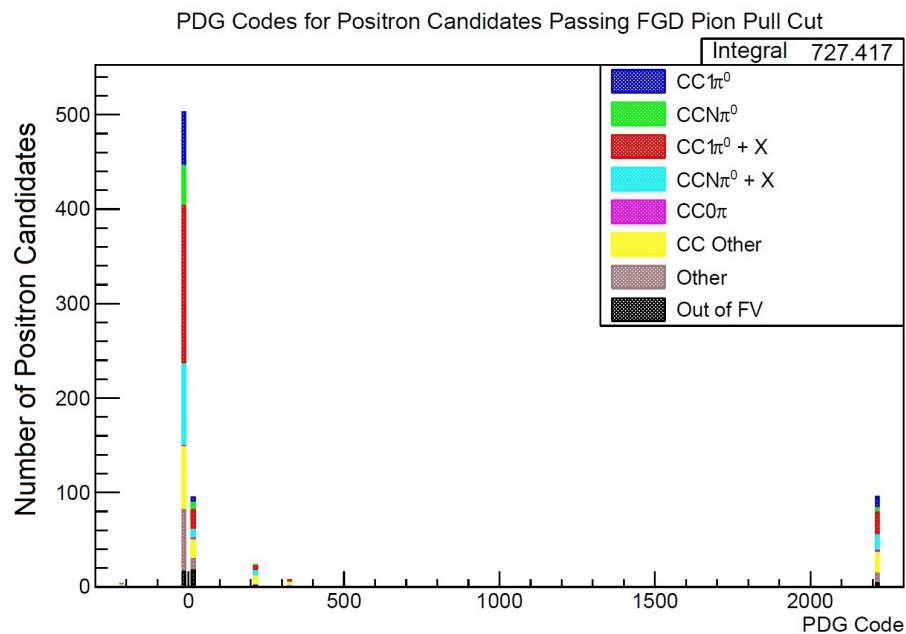


FIGURE 4.35: PDG Codes for TPC Positron Candidate Tracks after the cut detailed in Subsection 4.5.11. The proton and pion backgrounds which were present prior to the TPC track likelihood cut have been significantly reduced.

The ‘TPC Tracks Likelihood Cut’ does not have values to optimise, due to the likelihood functions being a hardwired feature of oaAnalysis. Initially these cuts were fully implemented for this analysis, but it became apparent that only the restriction for the positron candidates should remain. Due to the fact that there are very few negative, non-  $e^+/e^-$ , backgrounds, the effect of this cut on the electron candidates mostly served to reduce true  $e^+$  and  $e^-$ , which was not desirable. It was considered whether a PID cut on negative tracks is absolutely necessary, given the seemingly limited backgrounds, resulting in the removal of the negative track likelihood cut from the selection. The cut when applied to the positron candidates does seem to be effective, due to the large proton and pion contamination.

#### 4.5.12 Build Tracker Decay Photon Candidates

Once all low level cuts on the individual track objects has been completed, we move onto building the Tracker DPCs which will be combined with the ECal DPCs before the end of the selection, to form  $\pi^0$  candidates. This is actually achieved by five separate actions, producing DPCs of five different types. These can be formed from two tracks (TPC + TPC, FGDIso + TPC, FGDIso + FGDIso), or one (TPCIso, FGDIso). DPCs made from only one track object are accepted, due to the fact that some pair conversions can be heavily asymmetrical, imbuing one particle (i.e. an  $e^-$ ) with the majority of the momentum and the other (i.e. an  $e^+$ ) with very little. Due to limitations in reconstruction, this low momentum track may not be seen and therefore an opportunity to build a pair would be missed.

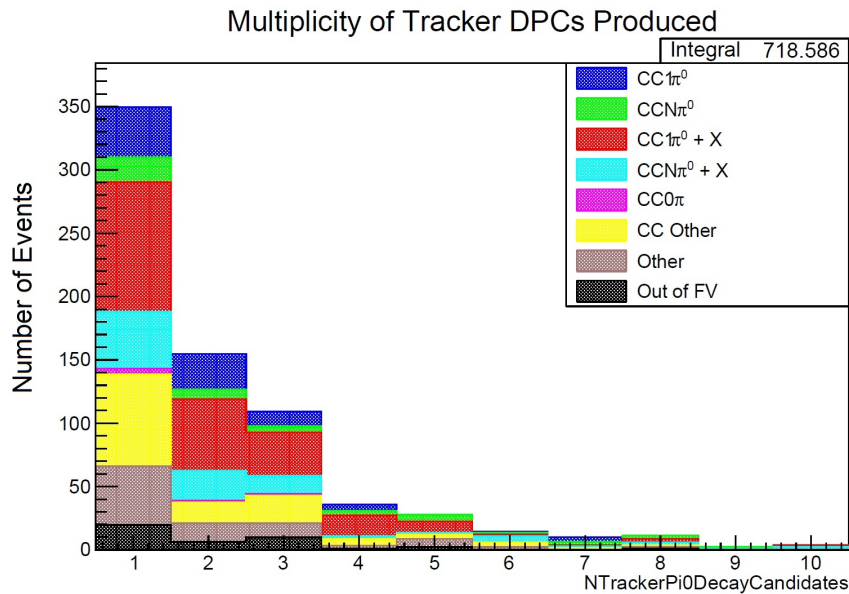


FIGURE 4.36: The multiplicity of NTrackerDPCs after all basic tracks cuts described in Section 4.5. Most events remaining contain one Tracker DPC, although non- $\pi^0$  backgrounds are large in this bin.

In Figure 4.36, in the majority of events at this point in the selection there is one Tracker DPC for use in combination with an ECal DPC to form a  $\pi^0$  candidate. However, we can see that there are background contributions pervading, especially in the one Tracker DPC regime. At first glance this may seem counter-intuitive, as we would expect a clean single  $\pi^0$  signal to be formed from one Tracker DPC and one ECal DPC. Contrarily,  $\pi^0$  events do tend to produce on average more tracks, and given that DPCs can be formed from isolated track, we would expect this effect to spill over into this area, generating more candidates. The single tracks from background sources also provide a large portion of the one Tracker DPC contribution. For this reason, the DPCs are subject to further cuts, while the selection only continues if there is at least one Tracker DPC remaining.

### 4.5.13 Tracker Decay Photon Candidate - Muon Vertex Distance Cut

In Subsection 4.5.7, a cut on the distance from the muon vertex was explained, for the ECal DPCs. A very similar cut is applied to the Tracker DPCs, in order to limit their number, increase the purity of built  $\pi^0$  objects and reduce combinatoric backgrounds.

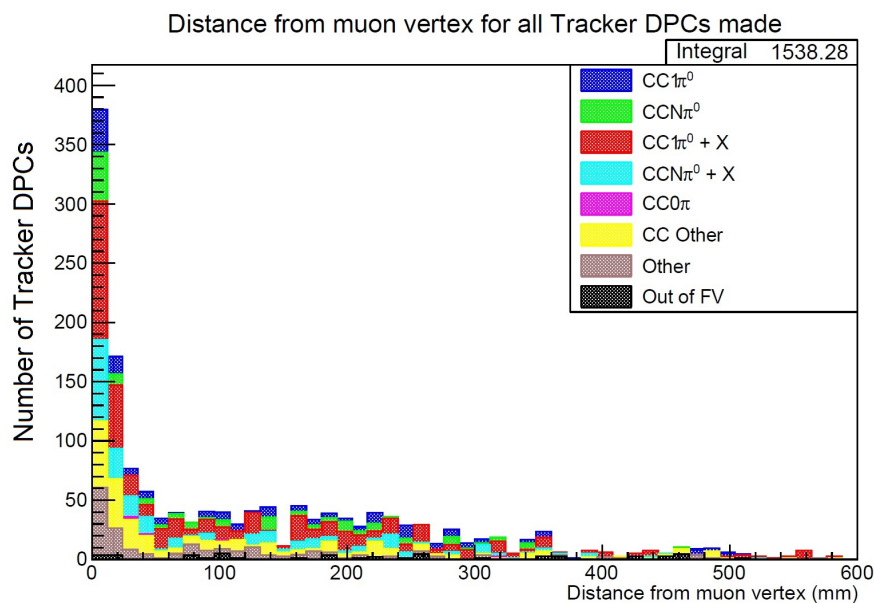
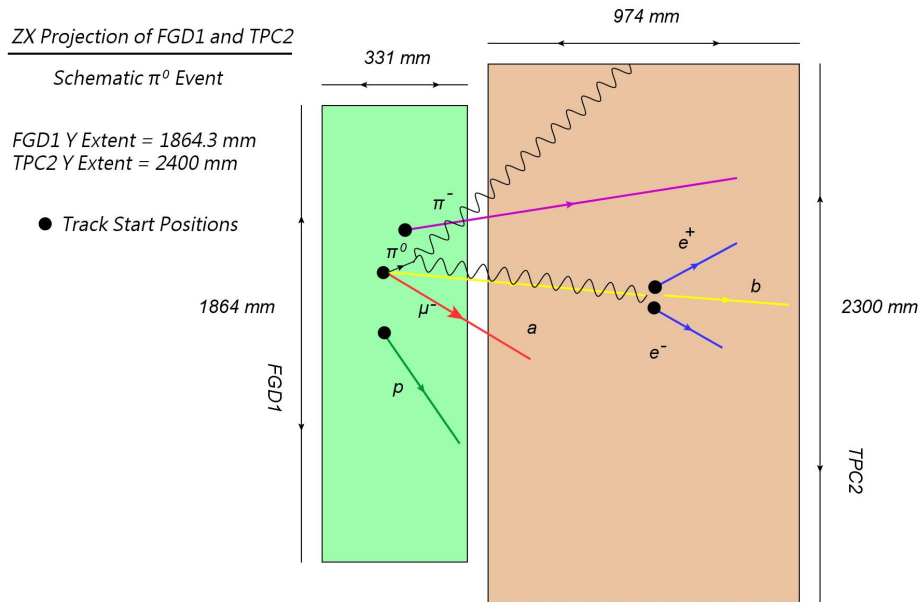


FIGURE 4.37: Distance to Muon Vertex for all Tracker DPCs Made. This represents all events (signal + background) which are retained after the basic track cuts described in Section 4.5. All optimisation was carried out using a Monte Carlo sample of Run 4 Air of  $4.27 \times 10^{20}$  P.O.T

Figure 4.37 shows that most Tracker DPCs are within 40 mm of the muon vertex, but there seems to be very little discrimination by event type for this variable. Optimisation of this variable, and others, was not conducted using event purity or event efficiency as the metric as this could potentially be a false economy. For the properties of objects such as this, the true signal is a decay photon which actually did originate from a  $\pi^0$ , and not just a decay photon which happens to exist within a  $\pi^0$  event.

#### 4.5.14 Tracker Decay Photon Candidate - Collinearity Cut

As with the ECal DPCs, the Tracker DPCs are now subject to a collinearity cut, which is explained in more detail here.



$a$  is a direction vector constructed from the start positions of the muon and the start position of the pair.  
 $b$  is a direction vector constructed from the 4 momenta of each of the pair constituents.

$$\text{Collinearity} = a \cdot b / |a||b| = \cos(\theta)$$

FIGURE 4.38: Schematic to show function of the tracker DPC collinearity cut. FGD1 and TPC2 are shown, with an illustrative event taking place, producing a  $\pi^0$  and other backgrounds. The converted pair (in blue) which has vector direction  $b$  (in yellow) should be close to the constructed vector direction  $a$  (also in yellow).

Figure 4.38 shows that the variable of collinearity is built by the comparison of two vectors (labelled  $a$  and  $b$  and designated yellow). In the case of a tracker DPC which has been built from only one tracker object, it is almost identical to the one used for the ECal DPCs, and therefore may fail to tracks which would also originate near the muon vertex. Aside from this strong background, the assumption used to justify the validity of this variable as an indicator of a true decay photon, is that the other ‘half of the pair’ has not been reconstructed due to low momentum. This would leave the majority of the momentum available for the portion which we do have access to and due to conservation of momentum, this should still be close to one for true  $\pi^0$  decay photons.

Due to the ambiguity in the effectiveness of this variable for single track DPCs, and the fact that few other cuts can be used to limit these types of objects, a very stringent range of values is ultimately used in those cases.

This variable performs best in the case where a tracker DPC is formed from two TPC tracks. It also works for pairs formed in the FGD, but the directional accuracy possible in the TPC is directly linked to its success in that situation. For a pair, the a vector is constructed using the muon vertex position and the pair start position (same as for a single track DPC), but the second vector b is formed from the linear superposition of the direction vectors of each pair constituent. If this resultant vector is parallel with a then it is a good indicator that the pair has been produced by a true  $\pi^0$  decay photon. Up until this point in the selection, it would be very easy to retain pair object DPCs which had been formed from stray background tracks. However, if pairing was performed at this stage, it is unlikely that such a pair would have a collinearity close to one. Optimisation of this was performed using true decay photon candidates as the signal, and split into two values for single track and pair DPCs.

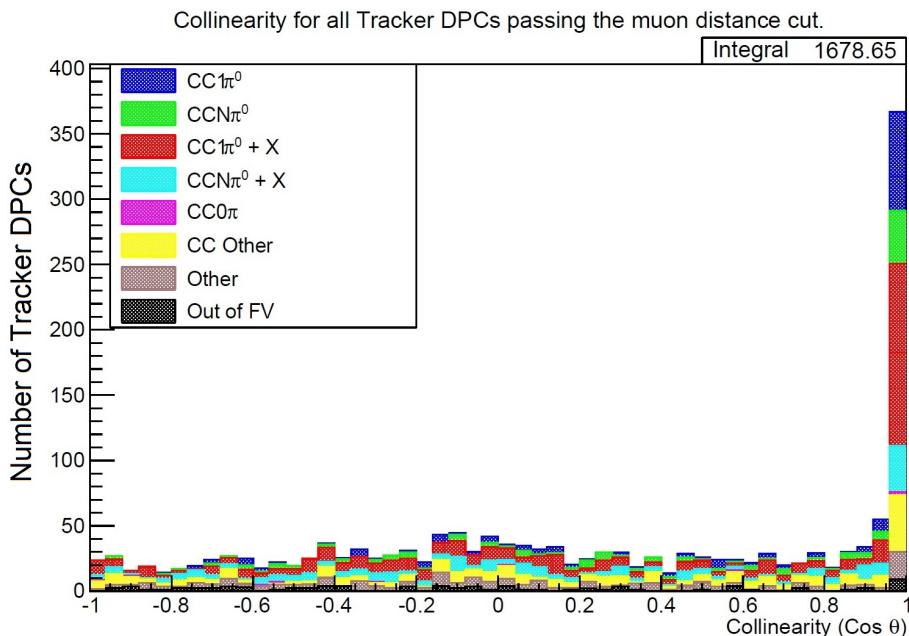


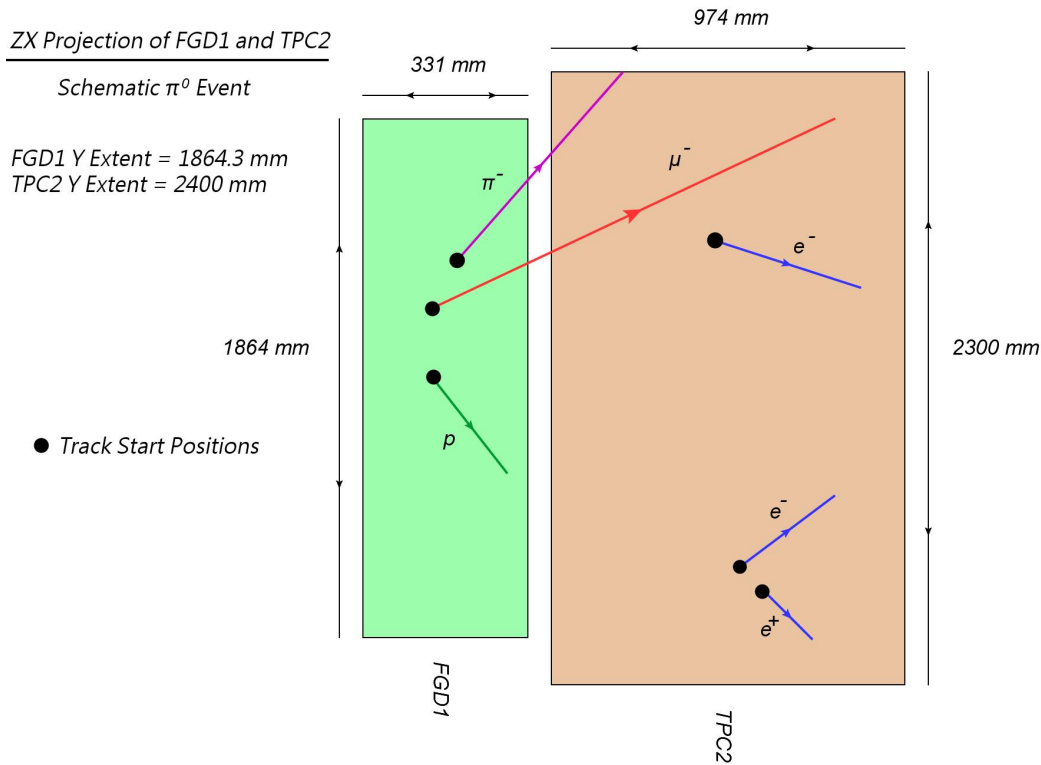
FIGURE 4.39: Collinearity of all tracker DPCs passing the muon distance cut. Most DPC candidates have a collinearity close to one, with event contributions being uniform for all values. No immediate analytical distinction can be seen for this variable.

Figure 4.39 shows that the majority of DPCs at this point in the selection do have a collinearity value close to 1 collinearity value, but that the event type to which the DPCs belong seems to be approximately uniform across the board. This was investigated in more detail and at higher resolution during optimisation.

#### 4.5.15 Tracker Decay Photon Candidate - Pair Separation Cut

As stated previously, tracker DPCs can be built from isolated tracks or pairs, a decision which was made to bolster the statistics possible for this  $\pi^0$  analysis, which are typically plagued by low statistics. The problem of low statistics is also worsened in this case, as this branch of the analysis only has access to Tracker + ECal converting  $\pi^0$ s, limiting the accessible phase space in that regard. With this in mind, it should be noted that it is not possible to subject these isolated track DPCs to the same battery of selection cuts which can be performed on pair DPCs. This has been illustrated somewhat in the previous cut, although a compromise was found by splitting that cut and being especially restrictive for non-pairs. For this and the next cut, we cannot cut on isolated track DPCs as two track constituents are explicitly required. Ultimately this means that greater confidence is bestowed in the truth of pair DPC objects which remain after these cuts, than non-pairs. This level of confidence is considered when the  $\pi^0$  candidates are built, and one is chosen.

The pair separation cut is self explanatory in that it is a distance cut, acting upon remaining tracker DPCs, which constrains the starting positions of pair constituents. This ensures that the start positions of the  $e^+$  and  $e^-$  candidates which form the DPC can only be separated by a maximum distance, determined by MC truth optimisation, as discussed in Section 4.6.



The three dimensional distance between the track start positions of any two constituents which form a pair (decay photon candidate) must not exceed 30 mm.

FIGURE 4.40: Schematic to show function of the tracker DPC pair separation cut. The pair converted in the lower part of TPC2 will have track start positions which are very close together. Whereas pairing up the negative pion and the upper electron track would result in a very large pair separation.

Figure 4.40 shows five tracks in this event (excluding the  $\mu^-$ ), which could be built into tracker DPCs. Three of these tracks are negative and two are positive, meaning that, assuming accurate charge identification, a total of 6 pair DPCs could be constructed. For the sake of this example it is assumed that the proton and pion have survived the PID cuts earlier in the selection. It is easy to see visually that for the conversion of a photon, we would expect the start positions of the  $e^+$  and  $e^-$  tracks to be close in 3-dimensional detector space, as is exemplified by the pair nearest to the bottom in of the TPC in the schematic. Therefore a simple cut to restrict the maximum separation between these two tracks should be effective, and dependent on stringency would negate up to five of those DPCs built. The allowed maximum distance was determined during selection optimisation.

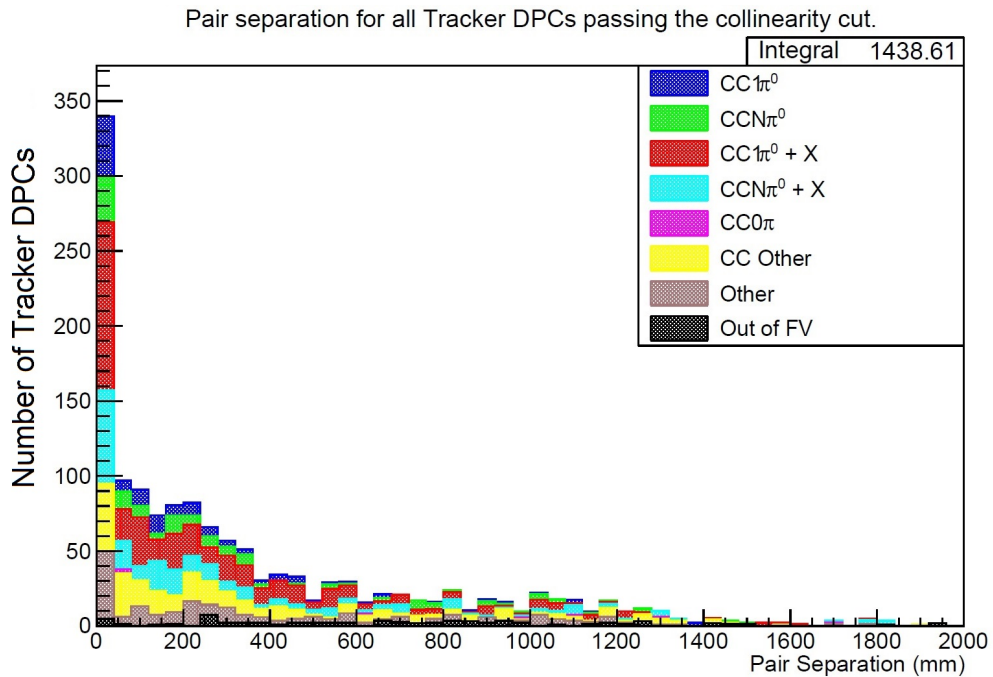


FIGURE 4.41: Pair separation for all tracker DPC candidates passing the collinearity cut. There is a large peak in the first bin, containing separation values of 0 to 40 mm. In terms of event category, the distribution seems to be even for all values, however this is somewhat meaningless and needs to be analysed in terms of a true DPC rather than a true  $\pi^0$  event.

In Figure 4.41 as expected we see many DPCs have a low value for pair separation, some of these belonging to background events. Once again, it is important to remember that this is plotted for all reconstructed DPCs and delineated by event type, not whether or not it is a true  $\pi^0$  decay photon. Optimisation for this variable yielded very good signal and background discrimination (See Section 4.6).

#### 4.5.16 Tracker Decay Photon Candidate - Pair Invariant Mass Cut

A thematically similar cut to the previous, we now cut on the reconstructed invariant mass of each remaining pair DPC. As photons are massless, pair production can only take place in the field of the nucleus or other charged particle, which must recoil to conserve momentum. Thus we expect the invariant mass of the  $e^+e^-$  pair to be small, i.e.  $\sim 0 \text{ MeV}/c^2$ .

$$M^2 = (E_1 + E_2)^2 - \|\mathbf{p}_1 + \mathbf{p}_2\|^2 \quad (4.3)$$

and

$$E^2 - \mathbf{p}^2 = M^2$$

where  $E_1$  is the energy of the first pair constituent,  $E_2$  is the energy of the second pair constituent,  $p_1$  is the momentum of the first pair constituent,  $p_2$  is the momentum of the second pair constituent, and  $M$  is the invariant mass of the system.

The four momentum of each track constituent can be reconstructed, and then be used to calculate the pair invariant mass. Within a sensible detector resolution and error this would be effectively 0 MeV, however this process can only occur in the field of the nucleus which contributes a small recoil, thus increasing this value.

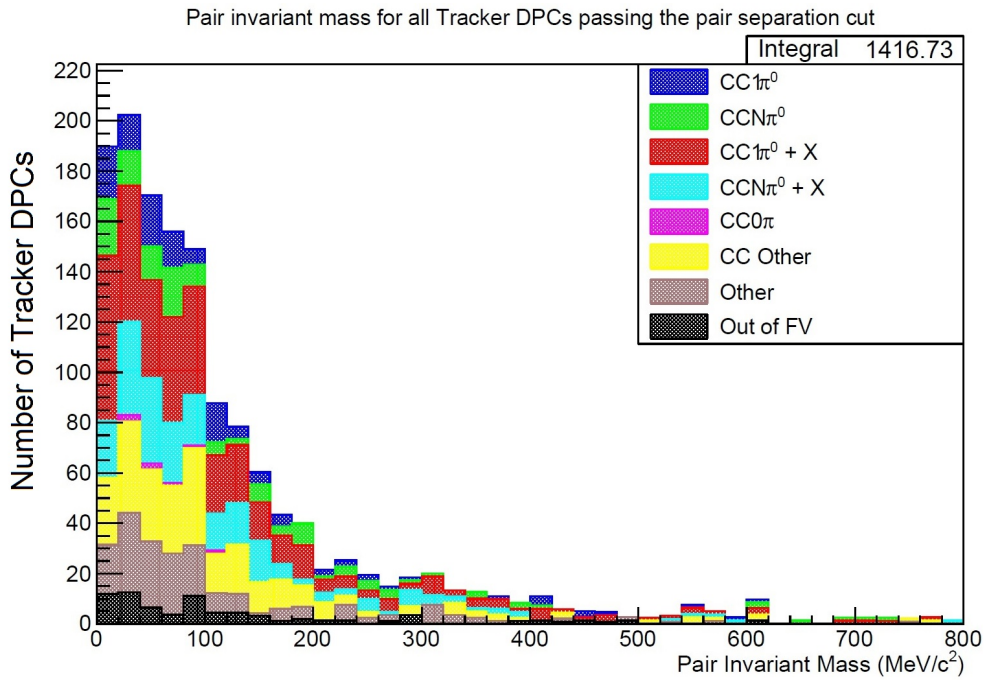


FIGURE 4.42: Pair invariant mass for all tracker DPC candidates passing the pair separation cut. Most DPC candidates have a reconstructed invariant mass of  $< 200 \text{ MeV}/c^2$ . The event category distribution is uniform.

We can see in Figure 4.42 that by far the majority of all pairs built have a total reconstructed pair invariant mass of under  $200 \text{ MeV}/c^2$  at this point in the selection, for the unoptimised (wide open) cuts. At the optimisation stage a fairly stringent range of values was determined for true decay photon pairs.

#### 4.5.17 Make Tracker + ECal $\pi^0$ s Candidates

The previous cut is effectively the last important one in the DPC selection, as now at this stage the  $\pi^0$ s candidates are built.

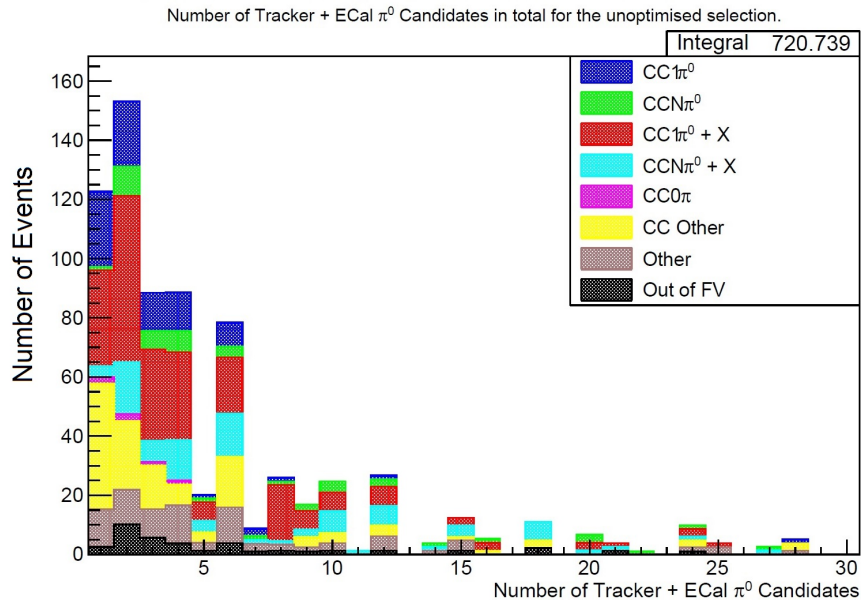


FIGURE 4.43: All possible  $\pi^0$ s candidates built for this sample for the unoptimised selection. This plot illustrates perfectly that the selection is in dire need of optimisation in order to construct only reasonable  $\pi^0$  candidates from which to choose. The fact that some events contain as many as 28  $\pi^0$  candidates illustrates the combinatoric problem appositely.

It is apparent from Figure 4.43 that a combinatoric problem exists. In stark contrast with Figure 4.12 which shows that producing more than two  $\pi^0$ s in an event, there are many reconstructed  $\pi^0$ s candidates being built, even as many as 28 in some cases. While the number of  $\pi^0$ s built drops off pretty sharply after 6 candidates, it is still apparent that the selection cuts are in dire need of optimisation, in order to reduce this number further. After this there are two simple cuts; the first simply requires that there is at least one  $\pi^0$  candidate (which there always should be); the second ensures that the  $\pi^0$ s candidate invariant mass is in the range of 0 MeV/ $c^2$  to 5000 MeV/ $c^2$ , which should not cut out many genuine  $\pi^0$  events.

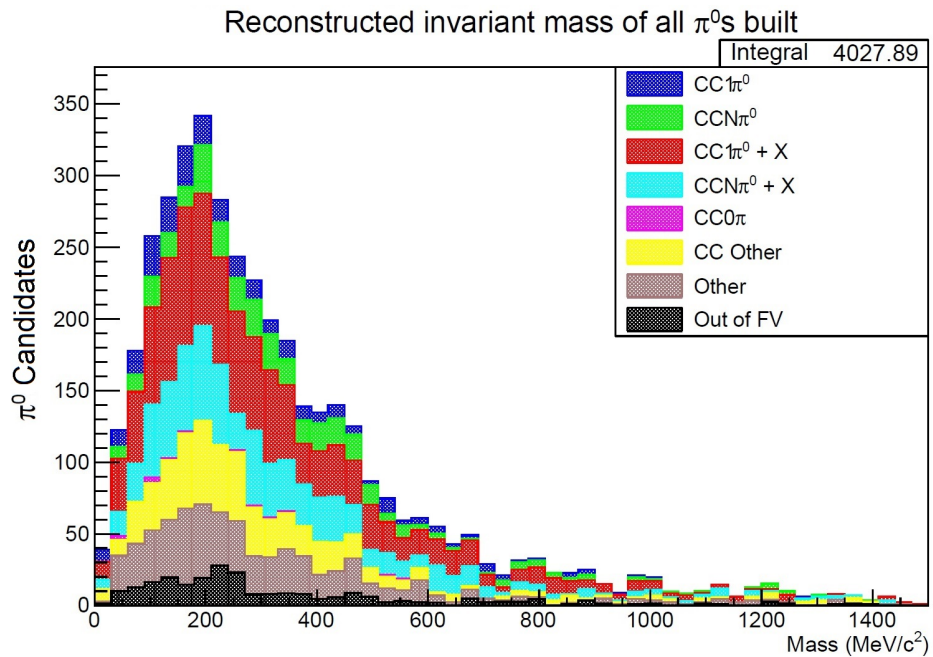


FIGURE 4.44: Reconstructed mass of all possible  $\pi^0$ s candidates built for this sample for the unoptimised selection. This has the expected wide gaussian profile and uniform event type distribution.

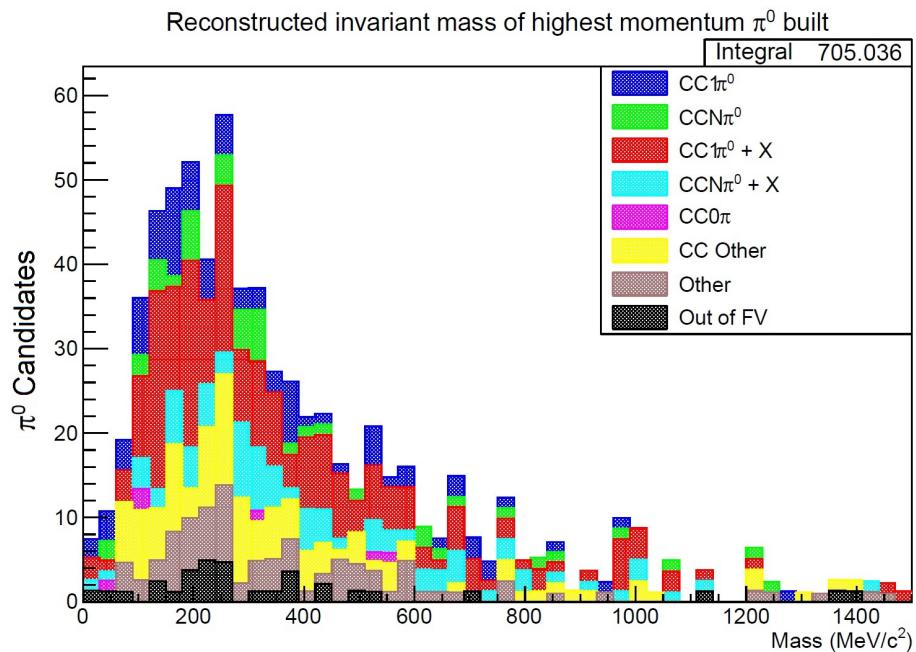


FIGURE 4.45: Reconstructed mass of the highest momentum  $\pi^0$ s candidate built for this sample for the unoptimised selection. Selecting only the highest momentum  $\pi^0$  in each event does not help to identify true  $\pi^0$  candidates.

For the unoptimised selection, if all possible  $\pi^0$  candidates are plotted (Figure 4.44), we see 4027  $\pi^0$  objects for the optimisation sample of  $4.27 \times 10^{20}$  P.O.T. If we arbitrarily decide to pick only the highest momentum candidate built in each event (Figure 4.45), we see 705  $\pi^0$  objects. This means that for every event which survives the complete unoptimised selection, there are on average 5.7  $\pi^0$  candidates reconstructed. We do see a peaked distribution around the known  $\pi^0$  mass of  $135 \text{ MeV}/c^2$ , even though we know that most of these candidates are false, and many belonging even to non- $\pi^0$  events. This is a broad distribution and some sort of combinatoric reduction is needed to limit the number of candidates and choose a likely one, even after optimisation.

## 4.6 Optimisation of Selection

The optimisation of the selection has been mentioned throughout this chapter, and now an in-depth description of the methods used and the results for each cut will be presented. The number of events passing any given cut in the selection can be plotted for a chosen variable, and by utilising the truth information available in the form of analysis flags, these distributions can be split into signal and background information. In some cases this was done by event type, in order to determine the range of values which would maximise the occurrence of our four signal event categories. This form of optimisation should only be used for event level variables, mostly ones which dictate how many of a given object should be allowed for the selection to continue (i.e. NTracks). In other cases this was done by particle type, simply accessing the native true PDG codes of tracks to maximise signal (electrons and positrons) over background (protons, pions, muons, kaons). In the final case, the true signal is represented by the true decay photon, stored in the bespoke data classes which were mentioned previously. As stated, all true  $\pi^0$ s produced at an FGD1 vertex and subsequent decay photons are stored at the beginning of each event (cleared post-event), so that the reconstructed objects can be compared to them to confirm their validity. In the case of the decay photons, a check is performed which confirms that all constituents of the DPC have the same parent (check

parent ID) and that this photon began with a true  $\pi^0$ . The truth of our reconstructed  $\pi^0$  objects can then be asserted by extension of the truth of its component DPCs.

Essentially, the algorithm which carries out the selection optimisation plots both signal and background (as defined by the user) for a given variable. The variable of interest is plotted on a one dimensional axis, e.g. Pair Separation (mm), Energy (MeV), Pull (Dimensionless Units), along the horizontal and the range of allowed values for both signal and background is varied. This variation is carried out by sampling every possible range (on a bin by bin basis) of the distribution. Each time a new range is sampled, a figure of merit is calculated which represents how much signal, background or both remain in that region.

All figures of merit which were considered are as follows :

$$(1) \text{ Efficiency} = \frac{\text{Retained Signal}}{\text{Total Sample Signal}}$$

$$(2) \text{ Purity} = \frac{\text{Retained Signal}}{\text{Retained Signal} + \text{Retained Background}}$$

$$(3) \text{ Efficiency} \times \text{Purity}$$

$$(4) \text{ Efficiency} \times \text{Purity}^2$$

Clearly, if efficiency alone was used this would result in retaining the entire range of values, or at least any range that included any signal at all. If purity alone was used this would likely result in an extremely restrictive sample, cutting out the majority of both the signal and background. A conventional choice is to use the product of these two metrics, striking a balance between signal retention and sample purity [128]. As stated,  $\pi^0$ s analyses do historically result in low statistics [126] and thus retaining as much signal as possible is important, implying that efficiency should be part of the

figure of merit chosen. However, this is offset by the combinatoric backgrounds and resultant impure samples which prevent a good physics understanding of the underlying processes. With this in mind, the decision was made to use Efficiency  $\times$  Purity<sup>2</sup> for the figure of merit for optimisation, a figure of merit which gives more power to the purity of the sample than the efficiency. This would be used as the figure of merits for all cuts, except in the cases when it is truly detrimental to signal efficiency to do so, i.e. 50% or more of the signal is lost).

Rather than showing the full optimisation treatment (each plot), the results are tabulated here :

Selection Cut	Optimised Range	Units	Efficiency	Purity
Number of FGD1 + TPC Tracks	3 to 8	None	42.5%	42.2%
Number of Isolated ECal Objects	3 to 6	None	53.4%	50.0%
FGD Track Pion Pull	-30 to -2	None	77.5%	56.9%
FGD1 + TPC Track Momentum	0 to 325	MeV/c	62.8%	60.0%
ECal DPC Energy	0 to 2750	MeV	100%	18.6%
ECal DPC MIPeM	-8 to 58	None	93.5%	58.8%
ECal DPC Collinearity	-0.66 to 1.0	$\cos(\theta)$	99.5%	18.6%
ECal DPC Muon Distance	0 to 3560	mm	99.5%	18.6%
Tracker DPC Muon Distance	100 to 340	mm	51.9%	24.3%
Tracker DPC Pair Separation	0 to 350	mm	92.6%	16.5%
Tracker DPC Pair Invariant Mass	0 to 470	MeV/c <sup>2</sup>	96.8%	15.3%
Tracker DPC Collinearity	0.944 to 1.0	$\cos(\theta)$	34.5%	30.0%
Number of Tracker + ECal $\pi^0$ Candidates	2 to 5	None	22.0%	55.8%
Post-Optimisation Selection	N/A	N/A	71.5%	9.8%

TABLE 4.5: Selection Optimisation Results - Figure Of Merit : Efficiency  $\times$  Purity<sup>2</sup>

. Note that this optimisation is for each independent cut and not done in a chronological order.

This optimisation represents independent variation of each variable considered, whereas in reality the values of these will affect the results of others. Therefore, a second round of optimisation was carried out, to further adjust these parameters, using the benefit of this ‘first-pass’ optimisation. In future this process could be repeated until there is very little variation in the returned values of an  $n$ th optimisation but only two rounds were completed in this case.

Additionally, some of the more restrictive values garnered from the first pass, namely the object multiplicity variables, were treated with scepticism, and loosened slightly for the next round. There are a number of reasonable rational justifications for this approach. Firstly the signal definition used for the object multiplicity cuts (any  $\pi^0$  in the event) does not take into account that the search in this branch is exclusively for Tracker + ECal  $\pi^0$ s and thus does not factor in the number of tracker and ECal objects which should be retained for specifically that focus. Secondly, for optimisation with a low number of bins, boundary errors are high and the signal and background can change rapidly, leading to an unreliable figure. Thirdly, a too restrictive approach for early cuts will indiscriminately cut out both background and signal objects early in the selection, where a more intelligent approach would be to use well motivated physical cuts later on. Finally, by limiting the range too heavily going into the second optimisation, we create an irretrievable loss of signal.

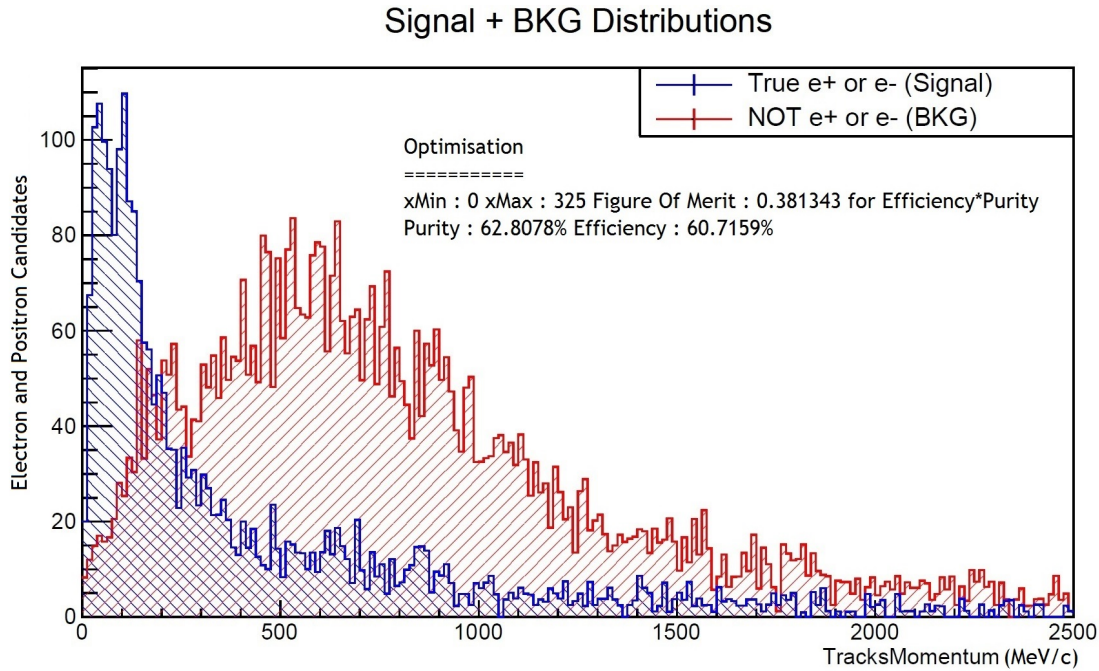


FIGURE 4.46: Momentum Optimisation for FGD1 + TPC Tracks in the Selection. Signal is shown in blue and background in red, illustrating that generally  $e^+$  and  $e^-$  particles have lower momentum than others. This does seem like a good candidate for a cut to preferentially retain signal over background. Values from the optimisation algorithm are superimposed on to the plot as text.

In Figure 4.46 it can be seen that ultimately good separation of signal particles such as  $e^+$  or  $e^-$  and background particles such as protons, pions and muons is achieved. This therefore would seem like an excellent selection cut, however a cut at the suggested value of  $325 \text{ MeV}/c^2$  would cut out many high energy electrons and positrons. This is a problem for this analysis due to the fact that photon conversions can be asymmetric and would therefore result in a low energy constituent (which would be retained) and a high energy one (which would be lost). A proper study of the momentum make-up of all pairs would illuminate this topic, but in this case a decision was made to remove this cut and simply retain the TPC Likelihood cut, which should fulfil the same purpose.

Before second optimisation, the overall event purity and efficiency of the event selection was assessed, giving 9.8% event purity and 71.5% event efficiency, retaining a large number of signal and background events, and not doing a very good job of preferentially retaining  $CC\pi^0$  events. Bear in mind that the event purity and efficiency maybe an important metric, but it was not used in the optimisation of all of the individual variables (as that would not make sense), and so these values are not to be compared with those from the optimisation results tables. These values further motivate the need for the second optimisation, the results of of which tabulated here :

Selection Cut	Optimised Range	Units	Efficiency	Purity
Number of FGD1 + TPC Tracks	3 to 6	None	42.5%	42.4%
Number of Isolated ECal Objects	3 to 6	None	53.4%	50.0%
FGD Track Pion Pull	-29.5 to -3	None	85.9%	64.5%
ECal DPC Energy	0 to 2750	MeV	100%	20.1%
ECal DPC MIPEM	-5 to 50	None	97.6%	61.5%
ECal DPC Collinearity	-0.66 to 1.0	$\cos(\theta)$	99.5%	18.6%
ECal DPC Muon Distance	580 to 3560	mm	99.5%	18.6%
Tracker DPC Muon Distance	105 to 400	mm	67.2%	50.0%
Tracker DPC Pair Separation	0 to 20	mm	52.3%	56.2%
Tracker DPC Pair Invariant Mass	0 to 40	MeV/c <sup>2</sup>	53.9%	52.4%
Tracker DPC Collinearity	0.944 to 1.0	$\cos(\theta)$	34.5%	30.0%
Number of Tracker + ECal $\pi^0$ Candidates	2 to 5	None	20.6%	54.5%
Post-Optimisation Selection	N/A	N/A	80.4%	3.6%

TABLE 4.6: Selection Second Optimisation Results - Figure Of Merit :  
Efficiency  $\times$  Purity<sup>2</sup>

. Note that this optimisation is for each independent cut and not done in a chronological order.

It is important to remember that the efficiencies and purities shown in the second optimisation results are based on the total amount of signal remaining, passed to it by events within the first-pass optimisation range. Therefore efficiencies can be higher

even for a seemingly more restrictive range of allowed values. Some specific examples of the optimisation procedure are shown in Figures 4.47 to 4.49.

### Signal + BKG Distributions

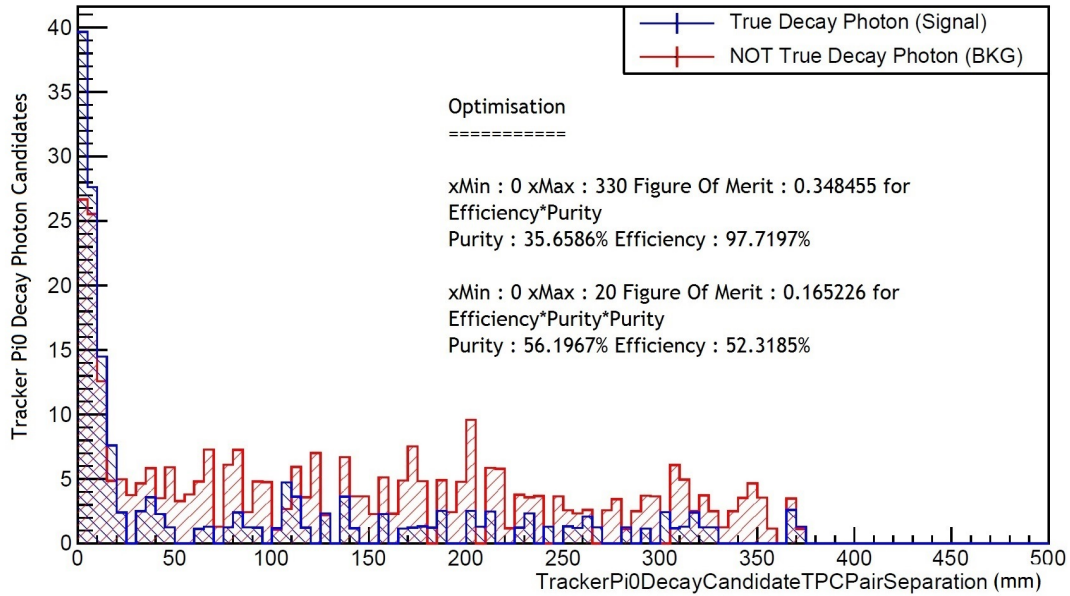


FIGURE 4.47: Optimisation of the Pair Separation for True and False Tracker DPCs. The majority of the signal exists for DPCs whose pair constituents are  $< 20$  mm apart. Values from the optimisation algorithm are superimposed on to the plot as text.

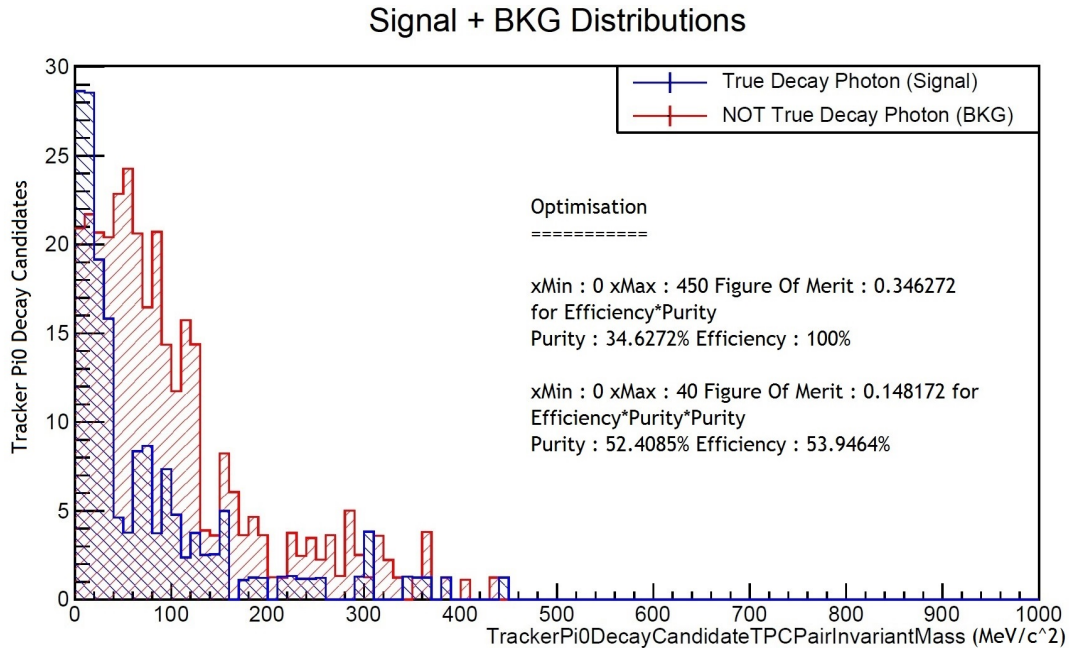


FIGURE 4.48: Optimisation of the Pair Invariant Mass for True and False Tracker DPCs. The amount of signal increases as the value of pair invariant mass tends to zero, with a reasonable maximum value of  $40 \text{ MeV}/c^2$  calculated by the optimisation process. Values from the optimisation algorithm are superimposed on to the plot as text.

We can see in Figure 4.47 that we can effectively use this variable to discern false pairs from true pairs by using the distance between the constituent's starting positions. The range is considerably tightened when invoking the metric which is dependent even moreso on purity. Unfortunately there is also an irreducible background which sits in the same region as that of the high signal. In Figure 4.48 there is reasonable signal to background separation (52.4% signal) at the lower values of pair invariant mass, as expected. The Efficiency\*Purity<sup>2</sup> metric returns 0 to  $40 \text{ MeV}/c^2$  for the range of retained DPCs.

Figure 4.49 illustrates a generally flat profile of signal and background up until the region close to one. However, this variable provided an expected duality of value when split into pairs or isolated tracks. Visual assessment of the optimisation plots showed that retaining pairs from  $-1$  to  $1 \cos(\theta)$  was prudent, while a heavy concentration of true DPCs for isolated tracks did inhabit the very high end of the spectrum (resulting in the value of 0.944 in optimisation). Due to this, two separate values were used for

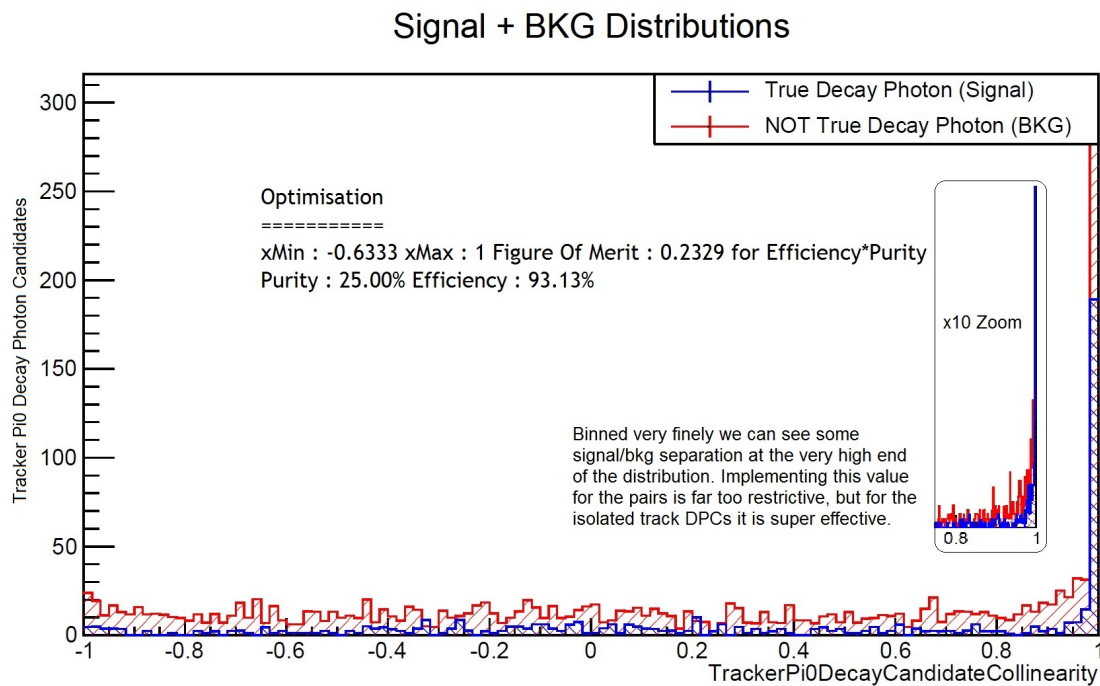


FIGURE 4.49: Optimisation of the Collinearity for True and False Tracker DPCs. Most DPC candidates for both signal and background have a value close to one. At extremely fine binning there is some separation, although this may be beyond the capability of the detector to resolve accurately. Values from the optimisation algorithm are superimposed on to the plot as text.

Tracker DPC collinearity. One value retains all pairs, with those DPCs subject to further, better motivated pair cuts. Another value removes a significant amount of isolated track background, which would otherwise remain throughout, for those DPCs built from only one track. Of course, the ECal DPC collinearity variable could not illustrate any such disunity.

A lower limit on the energy of the ECal DPCs was not indicated as necessary by the optimisation, however it is known that reconstruction of ECal objects which have are under 30 MeV in energy is unreliable (See Subsection 4.5.6). For this reason that minimum value is required in the selection going forward. As stated previously, the range of objects allowed in the early stages of the selection was deemed too restrictive, so events with as few as 2 tracks and 1 ECal object are retained at least to begin with. From this point, the analysis proceeded with those values ascertained by the second optimisation and outlined in Table 4.6 (aside from the exceptions mentioned).

## 4.7 Efficiency and Purity of Selection

The efficiency of the selection after the second optimisation and running on the same sample is 3.6%, the purity is 80.4%. A gradual increase (decrease) in purity (efficiency) can be seen as the selection of signal events is carried out. This results in a very pure event selection but admittedly at the cost of retaining only a small number of signal events. This bias towards purity results from intent of this analysis to allow good reconstruction of the actual  $\pi^0$ s in the events, for which it is requisite to be restrictive in terms of background.

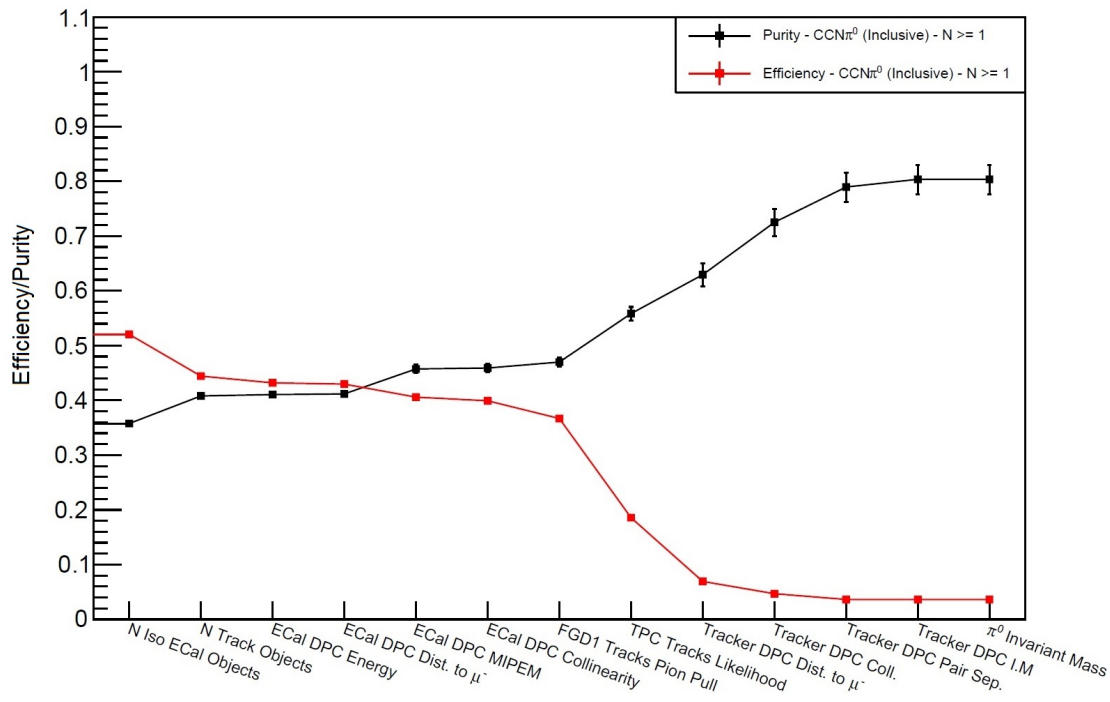


FIGURE 4.50: Efficiency and Purity of the Selection After Optimisation. The steady increase in signal event purity at each cut stage can be seen. This is accompanied by significant drops in signal efficiency, which is unavoidable for this type of analysis. Some cuts which do not seem to affect event purity, actually serve to reduce combinatoric backgrounds and increase object purity.

One particular feature of interest in Figure 4.50 is the sudden drop in efficiency which corresponds to the ‘TPC Tracks Likelihood’ cut. This is accompanied by an increase in event purity, though not quite at the same rate. Removal of this cut does have the expected effect of improving efficiency, with the resultant reduction of purity, but this is not the only consequence. In this form, the analysis still returns a number of combinatorically produced  $\pi^0$  objects for consideration post-selection. One of these must be chosen if any scientific assessment of the properties of  $\pi^0$ s produced in the events is possible. Removal of the cut in question decreases the probability of correctly picking the correct  $\pi^0$  reconstructed object in a  $\pi^0$  event at random from  $\sim 25\%$  to  $17\%$ . The TPC likelihood cut has such a large effect on purity due to the fact that it is the first cut which acts on any objects in the TPC (overwhelmingly the largest number of objects in

the analysis), and allows large backgrounds such as  $CC\pi^+$  events to be removed. Additionally, the TPC is very effective at removing non-electron events, which results in the removal of a large amount of background, but also some signal.

Selection Cut	Data Events	MC Events	100*MC/Data
Event Quality	450198	260058	57.8
> 0 Tracks	413300	227310	55.0
Quality + Fiducial	15273	14284	93.5
Veto	10836	10989	101.4
External FGD1	10630	10810	101.7
Muon PID	7758	7965	102.7
N Iso ECal Objects	2959	2864	96.8
N Track Objects	2166	2142	98.9
ECal DPC Energy	2098	2071	98.7
ECal DPC Dist. to $\mu^-$	2080	2054	98.8
ECal DPC MIPeM	1781	1746	98.0
ECal DPC Collinearity	1732	1711	98.8
FGD1 Tracks Pion Pull	1570	1536	97.8
TPC Tracks Likelihood	762	654	85.8
Tracker DPC Dist. to $\mu^-$	225	216	96.0
Tracker DPC Coll.	128	127	99.2
Tracker DPC Pair Sep.	90	90	100
Tracker DPC I.M	89	89	100

TABLE 4.7: The number of events in data and MC after each selection cut. All normalised to the P.O.T of the available Run 4 Air RDP -  $1.76 \times 10^{20}$ .

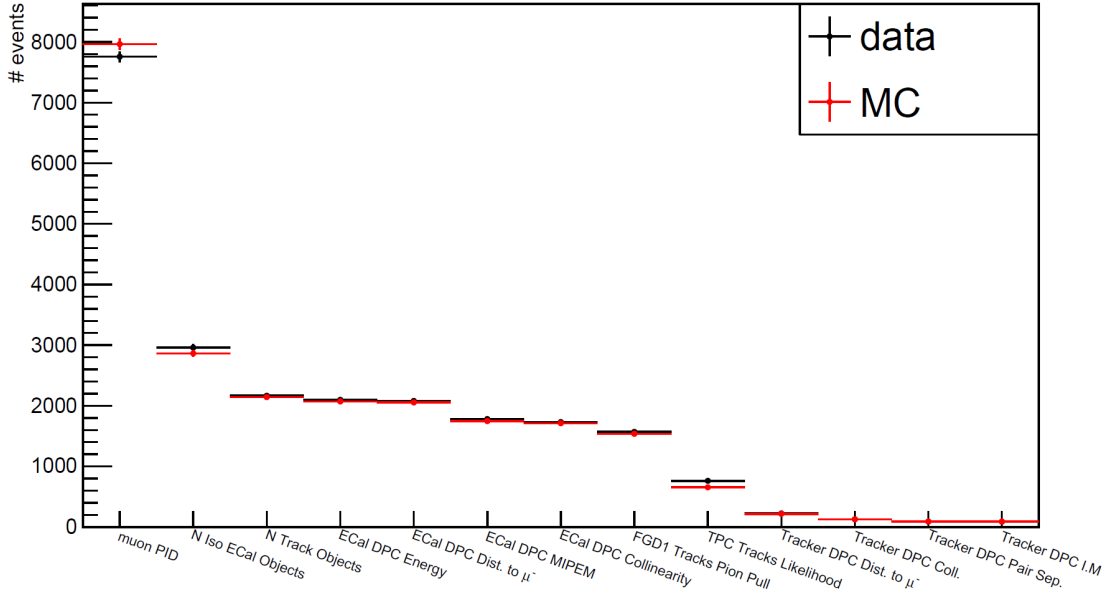


FIGURE 4.51: Accompanying plot to Table 4.7 showing the number of events surviving each selection cut in data and MC. The selection here starts after the Charged-Current pre-selection has been applied. There is very good agreement between data and MC throughout for the Run 4 Air sample (normalised to  $1.76 \times 10^{20}$  P.O.T).

It can be seen in Table 4.7 that there is a large discrepancy between the number of data and MC events very early on in the selection, although this is quickly rectified by the Quality and Fiducial Volume cut. There is a slight discrepancy after the TPC Likelihood cut, but again this disappears after the subsequent cut. A full breakdown of the contributing event categories from Monte Carlo truth can be found in Table 4.8.

#### 4.7.1 Acting upon Selection Objects in Addition to Events

A differential analysis carried out in terms of the reconstructed kinematics of the selected  $\pi^0$  would be incorrect if the object had been built from erroneous constituents. Given that reconstruction of the true  $\pi^0$  object is a concern, the event efficiency and purity are not necessarily the best figures of merit on which to focus. However, in order to gain access to  $\pi^0$  objects, first these events must be selected. Additionally, optimisation was not simply carried out with respect to signal event retention, it did heavily consider reconstruction of a true  $\pi^0$ , especially in the case of the DPC cuts.

Selection Cut	CC1 $\pi^0$	CCN $\pi^0$	CC1 $\pi^0 + X$	CCN $\pi^0 + X$	CC0 $\pi$	CCOther	Other	Out of FV
Quality + Fiducial	489	84	707	199	4105	2266	764	5670
Veto	461	78	675	185	4025	2179	730	2656
External FGD1	458	77	668	183	4019	2170	721	2515
Muon PID	393	63	607	156	3911	2046	344	445
N Iso ECal Objects	293	61	526	144	537	826	224	253
N Track Objects	204	53	485	132	218	713	191	145
ECal DPC Energy	200	52	468	130	208	688	187	137
ECal DPC Dist. to $\mu^-$	198	52	466	129	205	680	187	137
ECal DPC MIPEM	186	51	436	126	125	530	170	122
ECal DPC Collinearity	183	51	426	126	120	519	169	118
FGD1 Tracks Pion Pull	156	45	400	122	76	482	157	99
TPC Tracks Likelihood	64	24	199	79	14	174	62	39
Tracker DPC Dist. to $\mu^-$	27	12	70	27	1	39	24	17
Tracker DPC Coll.	21	9	47	16	0	17	11	7
Tracker DPC Pair Sep.	18	8	36	10	0	11	5	3
Tracker DPC I.M	18	8	36	10	0	10	5	3

TABLE 4.8: Breakdown of the Monte Carlo for Run 4 Air Optimisation Sample (Normalised to  $1.76 \times 10^{20}$  P.O.T as in Table 4.7 and Figure 4.51) in terms of the possible reactionpi0 event categories. Illustrated at each stage in the selection process to convey the effect which each cut has on the relative signal and background contributions. Full descriptions of each of the contributing categories can be found in Table 4.3.

As in the case of the ‘TPC Tracks Likelihood’ cut, there is quite a dramatic drop in efficiency associated with the ‘Tracker DPC Dist. to  $\mu^-$ ’ cut. This drop may be somewhat misleading, as due to the fact that this is chronologically the first cut acting upon tracker DPCs, it bears the responsibility of acting on the largest amount of signal. The mechanics of highland2 and specifically this type of plot, impose a chronological structure to the selection which is not necessary. A better representation of the selection would be in an ‘N-1 form’ which shows the individual effectiveness of each cut as if entirely independent from the others. We can, of course, see from the optimisation which cuts are truly cutting out what amount of our chosen signal for each cut.

Again, bearing in mind that Figure 4.50 only represents  $\pi^0$  events and not objects, the cuts which act on certain objects (Tracks and DPCs) are doing more than simply improving the selection event purity, they are improving the chance that the candidate eventually chosen is the true  $\pi^0$ .

## 4.8 Reconstructed $\pi^0$ Candidates

By keeping track of the kinematics of the constituent objects which are formed into the  $\pi^0$  candidates, a number of reconstructed variables can be assessed for the built objects. In this analysis we have access to : the momentum of the muon which initiated a charged-current interaction, producing a  $\pi^0$ , the momentum of the reconstructed  $\pi^0$  object, the invariant mass of the reconstructed  $\pi^0$  object, and the angle of that  $\pi^0$  with respect to the muon. All of these reconstructed quantities will be shown in the results section, but the reconstructed invariant mass will be shown here for the standard optimisation sample used.

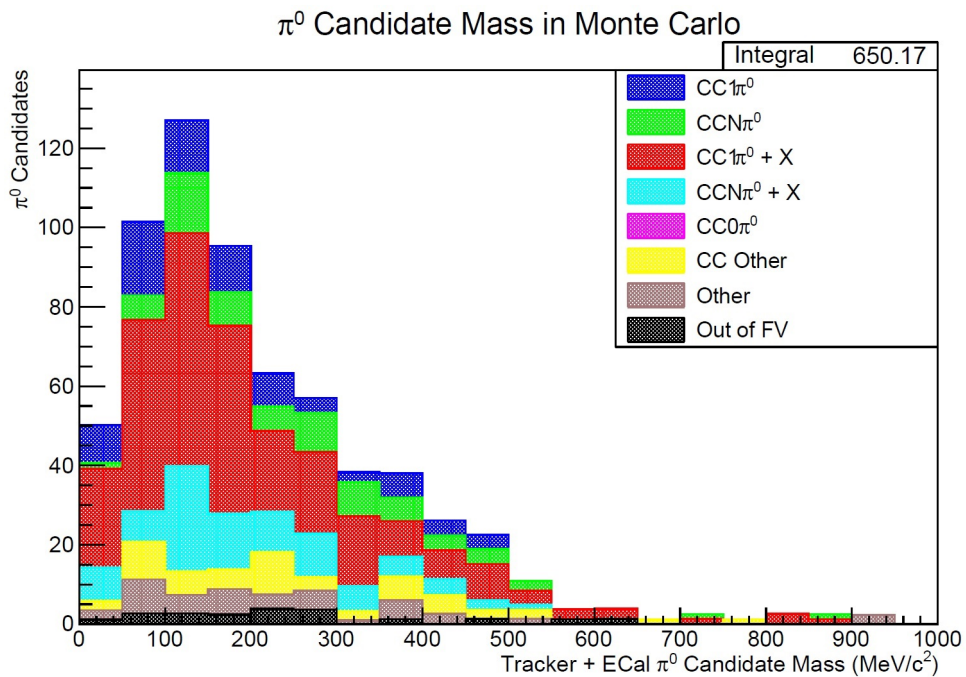


FIGURE 4.52: Reconstructed invariant mass of all  $\pi^0$ s passing the selection. This appears to have the expected peak at the known  $\pi^0$  mass of  $135 \text{ MeV}/c^2$ , which implies that the actual  $\pi^0$  objects are being correctly built. There is an associated width which could be due to detector resolution smearing or wrong combinations of  $\pi^0$  decay particles. Additionally, the 80.4% purity can be seen, with the background event contributions being flat (not peaked at  $135 \text{ MeV}/c^2$ ).

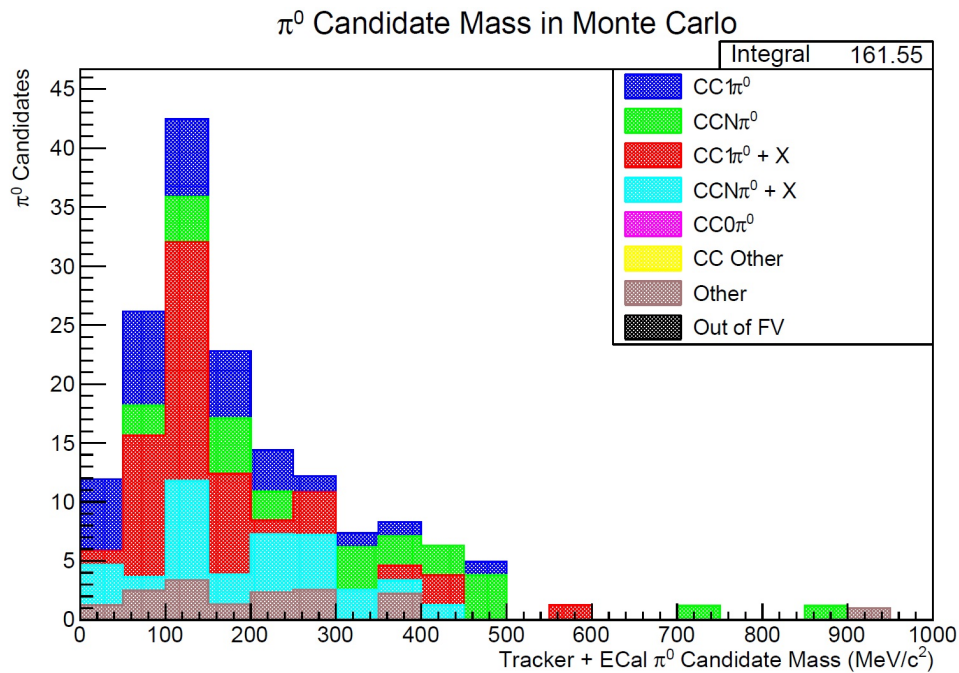


FIGURE 4.53: Reconstructed invariant mass of all true  $\pi^0$ s passing the selection. This shows a very well defined peak as expected. However, this does illustrate that even for true  $\pi^0$ s there is an associated width, and a contribution from 'Other', due to neutral current interactions.

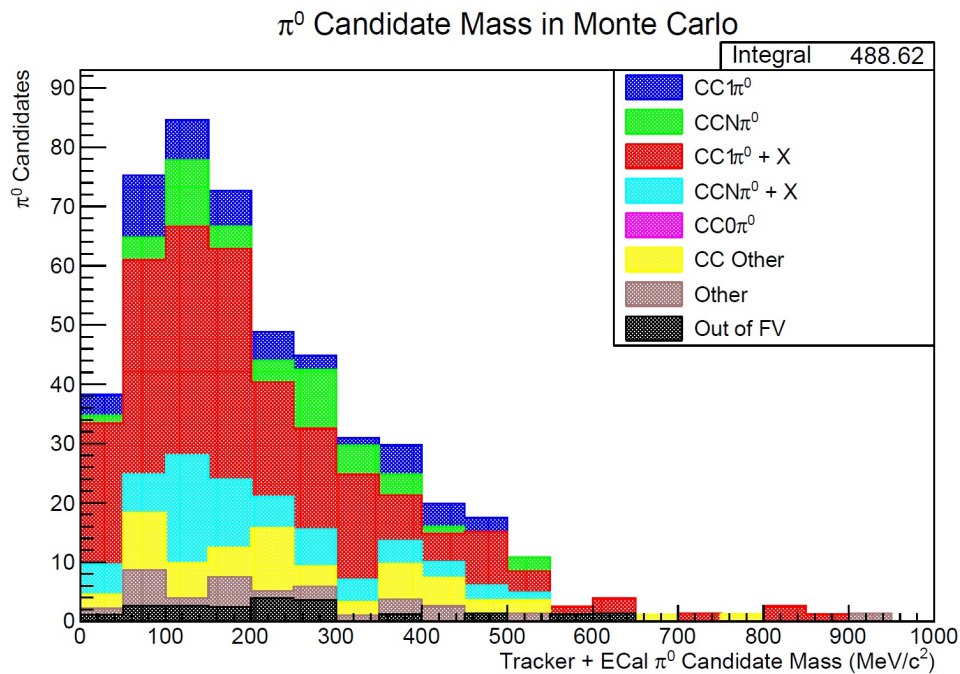


FIGURE 4.54: Reconstructed invariant mass of all false  $\pi^0$ s passing the selection. A broad peak built from the incorrect combination of  $\pi^0$  decay products in (mostly) actual  $\pi^0$  events. This represents one of the biggest hurdles to overcome in this and future  $\pi^0$  analyses.

Figures 4.52, 4.53 and 4.54 show all possible combinatoric  $\pi^0$  objects built for the optimised selection for this sample. These have been split into all, true, and false  $\pi^0$ s respectively, based on the event level truth information. As expected we see a very sharp invariant mass peak around  $135 \text{ MeV}/c^2$  for the true  $\pi^0$ s, and a broader distribution when plotting all candidates. Interestingly, even in the case of the false  $\pi^0$  objects, a very broad peak around  $135 \text{ MeV}/c^2$  has emerged. Many of the  $\pi^0$  candidates shown in this distribution may be partially built from track objects and DPCs which originated with true  $\pi^0$ s, but unless it is fully and accurately reconstructed from all true  $\pi^0$  decay products, it is not classed as a true  $\pi^0$  in this regard (possibly leading to a soft mass peak). In the case where we have plotted all of the reconstructed  $\pi^0$  objects (Figure 4.52) we see that the event background categories contribute a generally flat profile (certainly not peaking around  $135 \text{ MeV}/c^2$ ), which also supports the soft mass peak from half-correctly-built  $\pi^0$ s. The worry that the selection cuts are somehow ‘chiseling’ a mass peak out of the combinatoric  $\pi^0$  objects is somewhat assuaged by Figure 4.58, which shows the reconstructed invariant mass for all the false combinatoric  $\pi^0$  objects passing the selection (in the MC). This distribution does not seem to indicate a peak around  $135 \text{ MeV}/c^2$ , unlike the true and half-true  $\pi^0$  objects.

## 4.9 Choosing a $\pi^0$ Candidate

It is expected due to combinatorics and evident in the comparison of Figure 4.52 and Figure 4.53 that despite best efforts to restrict backgrounds and limit reconstructed objects, the selection still yields  $\sim 3$  additional false reconstructed  $\pi^0$  objects for each one that is true. This problem could potentially be solved by using a multivariate analysis where the properties of objects in a selected event are used actively as inputs to an boosted decision tree, ultimately ranking the resultant  $\pi^0$  objects built by likelihood of their truth. Such a sophisticated approach was beyond the time constraints of this analysis, though a small number of naive ranking systems were developed, simply as it is necessary to pick one  $\pi^0$ .

Metrics investigated for this purpose were choosing : the highest momentum  $\pi^0$ , the  $\pi^0$  built with the highest energy ECal DPC, the  $\pi^0$  built with the smallest pair separation, the  $\pi^0$  built with the smallest pair invariant mass, the  $\pi^0$  closest to the known  $\pi^0$  invariant mass, and one from a naive multivariate (nMVA) approach.

The naive multivariate approach is not particularly well motivated in its construction, but future work could use a similar (better researched) approach to choosing a  $\pi^0$  if faced with a similar combinatoric background. The nMVA used minimised the value of :

$$\text{nMVA Metric} = \frac{\text{Pair Separation} \times \text{Pair Invariant Mass}}{\text{ECal DPC Shower Energy}}$$

Any metric which resulted in more than one  $\pi^0$  being selected, i.e. more than one  $\pi^0$  candidate could be formed from the same tracker DPC but a different ECal DPC, would defer to the highest momentum one of those remaining. Additionally, any metric which requires the use of a pair will preferentially pick pair-built  $\pi^0$ s over ones formed with an isolated track DPC. In these cases where there are only isolated track DPCS available, these metrics would simply again defer to the highest momentum  $\pi^0$ .

Results from this sample illustrate that were a  $\pi^0$  candidate to be randomly chosen post-selection, this would correctly pick the true  $\pi^0$  23.5% of the time. Table 4.9 shows the effectiveness of performing that task for all metrics considered.

From Table 4.9 we can see that there is very little difference in the effectiveness of the metrics used for this sample. A preference for using the candidate closest to the  $\pi^0$  invariant mass can be seen, so this metric will be used going forward to identify the  $\pi^0$  used for results and measurements, with the additional loose restriction of retaining only candidates with an invariant mass of under  $500 \text{ MeV}/c^2$ . Of course this means that we cannot perform any measurements related to determining this mass, but as this is a well-known value, this is not an issue.

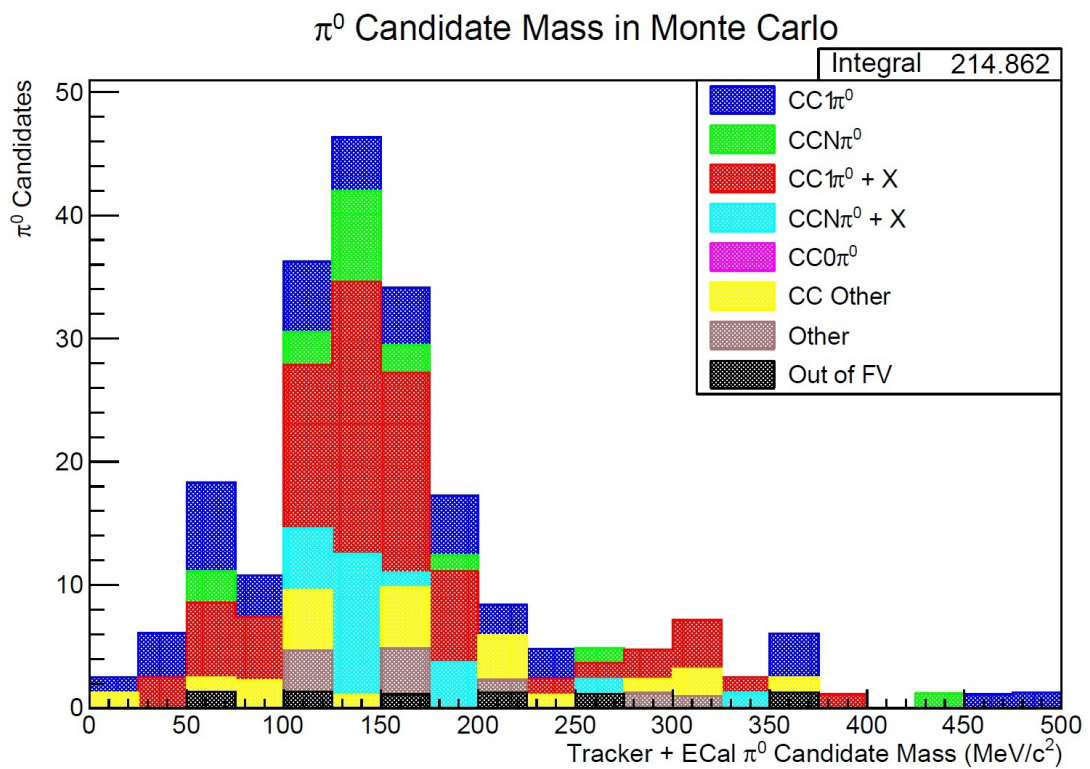


FIGURE 4.55: The  $\pi^0$  candidate with the invariant mass closest to that of the known  $\pi^0$  mass in a given event is chosen and plotted here. We see the characteristic  $\pi^0$  mass peak around  $135 \text{ MeV}/c^2$ . Of course we cannot use this to measure the  $\pi^0$  mass as we are now biased, but it is a useful metric which helps to correctly identify the true  $\pi^0$ .

Choosing Metric	P(True $\pi^0$ )
Selected at Random	23.5%
nMVA	23.6%
Highest Momentum $\pi^0$	23.1%
Smallest Pair Separation	22.5%
Smallest Pair Invariant Mass	22.5%
Closest to $\pi^0$ Invariant Mass	27.4%
Highest Energy ECal DPC	23.8%

TABLE 4.9: Probability of correctly identifying the true  $\pi^0$  in a selected event. All values subject to a statistical error of  $\pm 6.7\%$  for this sample. These values may seem low as often only one of the two true  $\pi^0$  decay photons are correctly identified.

#### 4.9.1 Half the Photons Away

At this stage it is likely that many of the combinatoric false  $\pi^0$  candidates in actuality are built containing one correct  $\pi^0$  decay photon. We can investigate this by plotting all built  $\pi^0$  candidates for the cases where : Both photons are from a true  $\pi^0$  (Figure 4.56), one photon is from a  $\pi^0$  (Figure 4.57), neither photon is from a  $\pi^0$  (Figure 4.58). Each of these cases has a share of the total number of candidates of 25.3%, 55.0% and 19.6% respectively. This illustrates that out of all built  $\pi^0$  candidates, at least one true decay photon is selected in 80.3% of cases in 100% of the selected events (which does include backgrounds).

As expected, in Figure 4.56 we see a clear mass peak representing the true selected  $\pi^0$ s. All contributions to the events are from ones which have produced at least one  $\pi^0$ s, including the 'Other' category (neutral-current produced pions).

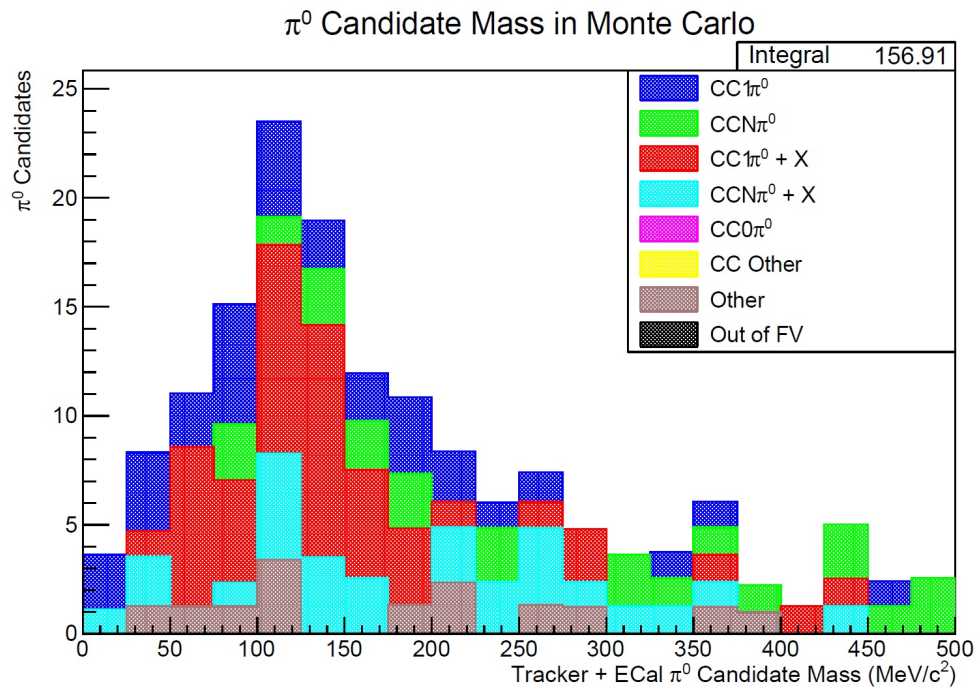


FIGURE 4.56: Reconstructed  $\pi^0$  candidates where both photons are from a true  $\pi^0$ . For all candidates within the 0 to 500  $\text{MeV}/c^2$  range.

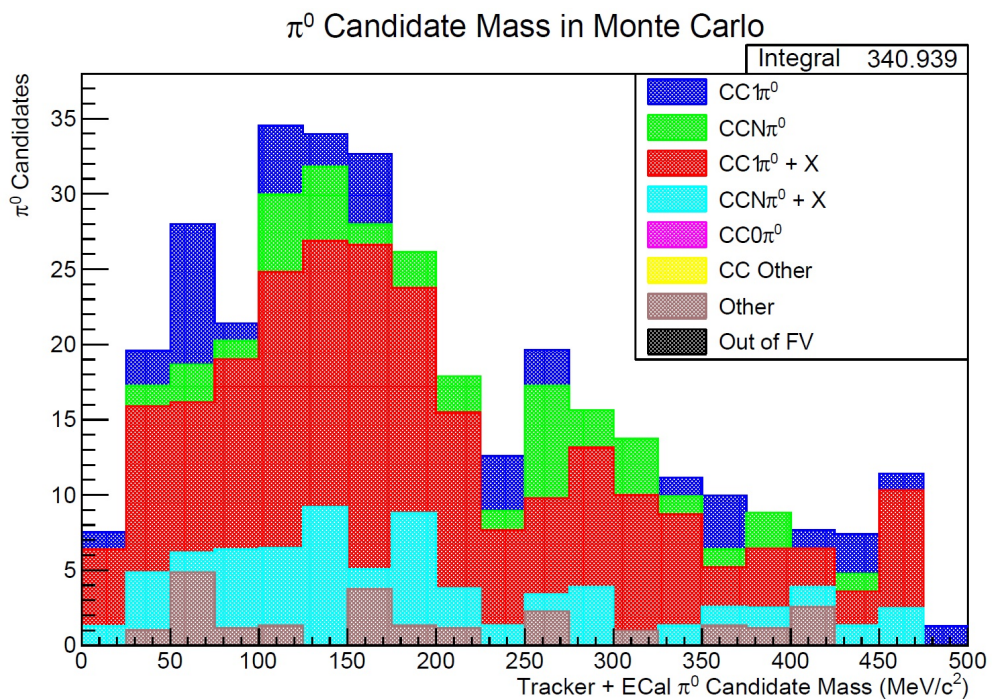


FIGURE 4.57: Reconstructed  $\pi^0$  candidates where exactly one photon is from a true  $\pi^0$ . For all candidates within the 0 to 500  $\text{MeV}/c^2$  range.

A  $\pi^0$  is also always required in the events shown in Figure 4.57 and a broad mass peak can be identified, due to 50% of the object being accurately reconstructed as the true  $\pi^0$ . The second true DPC may not have been reconstructed and built into these candidates, due to the low energy of its decay constituents, therefore the true DPC which is used will provide the majority of the contribution to the invariant mass.

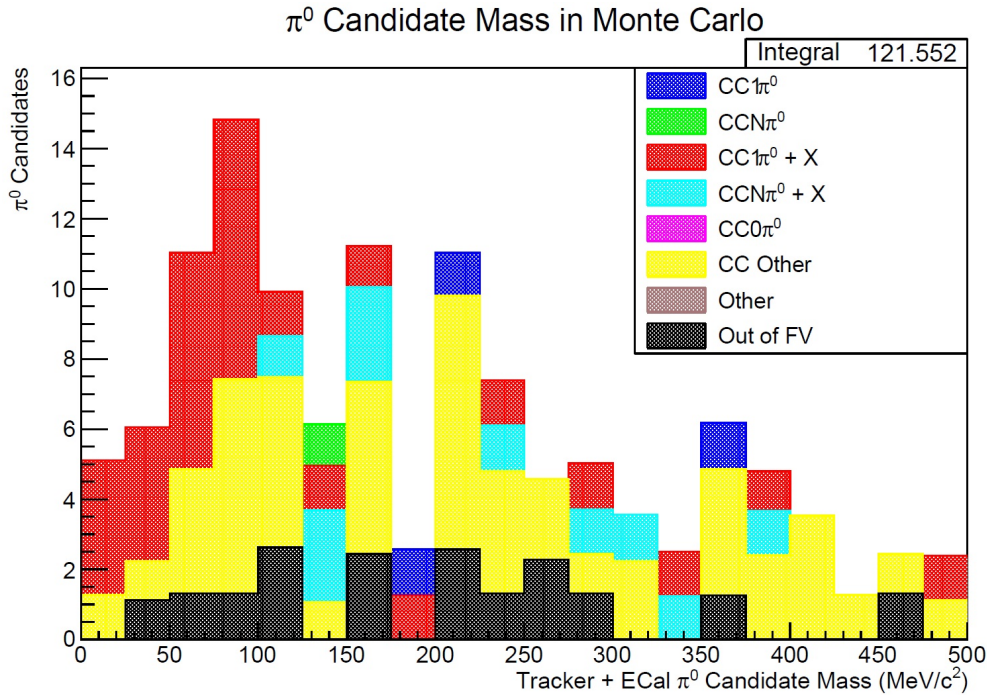


FIGURE 4.58: Reconstructed  $\pi^0$  candidates where neither photon is from a true  $\pi^0$ . For all candidates within the 0 to 500  $\text{MeV}/c^2$  range. This is low statistics (due to the high event purity of the selection) and has an irregular structure. These objects are mostly built from ‘Other’ particles.

Figure 4.58 shows the cases where the  $\pi^0$  candidate was reconstructed from two non- $\pi^0$  incorrect DPC objects. This conveys that this mostly happens in non- $\pi^0$  events (58.5% of the time) and less frequently in true  $\pi^0$  events (41.5% of the time). The sources of these false objects is quite evident in  $\pi^0$  events, as the great majority includes one or more additional particles, which the reconstruction has failed to correctly identify and thus remove from consideration.

In conclusion, for the selection, we can say that by use of the metric which picks the closest candidate to the known  $\pi^0$  mass, and by only considering true  $\pi^0$  events

---

(in which regard the selection is 80.4% pure), we accurately reconstruct  $\pi^0$  candidates containing one or more actual  $\pi^0$  decay photons 89.9% of the time, and fully accurately reconstructed in 31.1% of cases.



## Chapter 5

# Systematic Uncertainties

In order to fully understand the role of systematic uncertainties in neutrino experiments, we must take a step back and re-assess what our goal is and evaluate the experimental and mathematical framework which we have to achieve that goal. We know that neutrino oscillation experiments require measurements of charged-current and neutral-current event rates of interactions occurring within their detectors in order to determine flux and beam properties. Generically, we can describe this process as :

$$R(\mathbf{x}) = \Phi_\nu(E_\nu) \times \sigma(E_\nu, \mathbf{x}) \times \epsilon(\mathbf{x}) \times P(\nu_A \rightarrow \nu_A), \quad (5.1)$$

where  $R$  is the reconstructed event rate (a function of the reconstructed variables in a given analysis,  $\mathbf{x}$ ),  $\Phi_\nu$  is neutrino flux (a function of the true neutrino energy),  $\sigma$  is the neutrino interaction cross-section (dependent on neutrino energy and the reconstructed kinematic detector variables),  $\epsilon$  is the detector efficiency (a function of the reconstructed variables) and  $P(\nu_A \rightarrow \nu_A)$  is the oscillation probability to remain in its initial state. (in the case of T2K this would commonly be a  $\nu_\mu$ ).

It is clear from 5.1, that in order to accurately measure any oscillation effects, the other variables ( $\Phi_\nu$ ,  $\sigma$  and  $\epsilon$ ) must be known to a reasonable degree. For the purpose of this analysis, which does not seek to directly gain any understanding of neutrino oscillation, we can discount this final term. Knowing that our result in real data will be a number of selected events (framed as distributions reconstructed kinematic variables which are presented in Chapter 6), we can see that to make a valid comparison to

the predicted Monte Carlo number of selected events and relevant distributions, these three remaining factors on the right-hand side of 5.1 must be well-understood. Simply stated, in order to inform current models of neutrino interaction, we should understand the flux, cross-section and detector response. While these will never be precisely understood, they should fall within sensibly motivated systematic errors, which will be discussed in this chapter. By improving the understanding of neutrino interaction models [129] i.e. final state interactions, interaction potentials, resonances etc, this analysis will contribute to improving future oscillation analyses.

However, ultimately, we must acknowledge that this analysis is only capable of reconstructing (however effectively) the  $\pi^0$ s whose photons convert in the Tracker + ECal regions of the detector (by design). Therefore, an extrapolation of this result to a meaningful physics quantity such as a  $\pi^0$  cross-section binned in neutrino energy, would be prohibitively difficult, requiring dramatic phase-space and efficiency corrections and resulting in errors so large, as to negate the worth of the result. The obvious and simple solution is to consider the entire  $\pi^0$  conversion phase space by running the complete analysis (all three branches, as discussed in 4.5.5) and extracting the total number of events from that combined assessment. Additionally, it would be worthwhile considering phase space restrictions for the  $\pi^0$ s which ensure that they are detectable, such as focusing only on ones above a certain momentum and within a given angular range. Both of these tasks will be undertaken by future analysts working within the  $\pi^0$  group, as discussed in Chapter 7.

## 5.1 Detector Systematics

A major benefit of using the Highland2 analysis framework is the native inclusion of systematic errors for detector sources. These detector systematics take into consideration a wide range of effects and can be turned on or off in a given analysis by the use of parameter switches. The propagation of a given detector error means determining the effect which it has on certain objects, (i.e. tracks or showers, and following this through to determine how this affects the total number of selected events at a given stage in the selection, up to and including the final stage.

The two methods used to evaluate systematic errors in the Highland2 framework are weights and variations. Variations modify properties of objects within the event, such as momentum, energy deposition and magnetic field strength (or shape), whereas weight systematics alter the final weight of the event passing the selection, but leave the event properties untouched. This means that each time we apply a systematic variation, the entire selection must be run again. As weights do not affect properties within an event, the selection does not need to be re-done. Some systematics could be potentially be propagated both as a weight or as a variation, while others can only be propagated in one way. Systematics which affect a continuous property of the event, e.g. momentum resolution, momentum scale, particle identification variables etc, must be implemented as variations. Systematics which affect a binary property of the event e.g. charge confusion, tracking efficiencies etc, can be implemented both as weights or variations. And systematics that affect only the event normalisation, e.g detector mass, pile up etc, can be exclusively implemented as weights.

The efficiency-like method, used for propagating the object level weight systematics is based on studies comparing data and Monte Carlo predictions for well-known control samples. A plethora of control samples have been used to determine the proper figures, including one containing exclusively through-going single muon tracks [123]. All of the muons that sample have originated from interactions which occur in the sand surrounding the detector and cover a restricted phase space (usually high energy and small angle). These control samples cannot possibly fully represent the complexities which

will occur in a given selection (i.e. in the muon sample there would be no interaction of multiple tracks) which would affect the efficiencies. Track efficiencies and efficiencies for matching between sub-detectors are calculated using the redundancy between detectors. For example, the TPC2 track efficiency can be computed using tracks with segments in FGD1 and FGD2. Similarly, the FGD1 track efficiency can be computed using tracks with segments in TPC1 and TPC2. For these reasons it is possible that the efficiencies computed using those control samples do not correspond to the ones of the analysis samples. Consequently, a model to extrapolate the control sample efficiency to the analysis sample is needed. The simplest model is the one assuming that the ratio between the efficiencies in data and MC is the same in both the analysis and control samples. The efficiency in the MC analysis sample can be computed using the truth information (given a true GEANT4 trajectory, it is always possible to know whether or not a track or shower has been correctly reconstructed). The predicted efficiency in the analysis data sample is calculated using a comparison of the reconstruction efficiency in both MC and data control samples. The systematics applied are propagated through in Highland2, by using the built-in toy experiment functionality. In this analysis, 500 toy experiments was chosen to reasonably determine the level of uncertainty. In each of these toy experiments, each reconstructed variable subject to a detector systematic either contributes to an event weight or directly towards the number of events passing a selection cut (variation).

Of course, not all of the systematics available within Highland2 are appropriate for this selection, so only relevant ones were activated. In addition to this, systematics should be applied to only the relevant objects. In this selection it is important that all tracks and ECal objects are subject to proper systematic assessment, but not all objects would necessarily be subject to all systematics. For example, it is not necessary to apply the TPC PID systematic to isolated FGD1 tracks, or the TPC momentum resolution systematic to the ECal showers. In order to address this problem, Highland2 incorporates functionality for the analyst to manually state which objects should be subject to which systematics.

Table 5.1 lists all of the detector systematics used in this analysis, whether they are weight or variation and whether they are applied at an object level or an event level. Variation systematics include Magnetic Field, Momentum Scale, Momentum Resolution, Momentum Bias From Vertex Migration, TPC PID, FGD PID, ECal Electromagnetic Energy Resolution, ECal Electromagnetic Energy Scale.

Systematic	Applied To	Applied As	Relative Error (%)
Pion Secondary Interactions	Object	Weight	5.22
Proton Secondary Interactions	Object	Weight	3.17
Variation Systematics	Object	Variation	2.18
Charge Identification	Object	Weight	0.36
TPC Track Efficiency	Object	Weight	2.85
FGD Track Efficiency	Object	Weight	6.04
TPC + FGD Matching	Object	Weight	0.76
Out Of Fiducial Volume	Event	Weight	0.22
Pile Up	Event	Weight	0.28
FGD Mass	Event	Weight	0.58
Sand Muons	Event	Weight	< 0.01%
TPC Cluster Efficiency	Object	Weight	1.85
TPC + ECal Matching Efficiency	Object	Weight	2.69
ECal PID	Object	Weight	5.34
Total Relative Error	-	-	11.14 ( $\sim \pm 5.6\%$ )

TABLE 5.1: Detector Systematics in the  $\nu_\mu CC\pi^0$  Inclusive Selection. Each of the fundamental error sources was varied to  $\pm 1\sigma$  uncertainty level. It is detailed whether each error source is applied at the object or event level, and implemented as a variation or weight systematic. This total relative detector error translates to a propagated associated uncertainty of  $\sim \pm 5.1\%$  on the final result.

### 5.1.1 Discussion of Completeness and Importance of Detector Systematics

An extensive range of systematic errors is available in the Highland2 analysis framework. Each potential source of error is considered, and ultimately a variation or event weight is applied due to that source. The completeness of the set of detector systematics can be illustrated in a number of ways. Firstly, an attempt is made to describe all potential sources of fundamental error, such as momentum resolution and known track efficiency uncertainties. As stated, many of these are informed by control samples, used to definitively understand the behaviour of the detector and certain particles at the required energy scales. These fundamental errors will affect higher level objects within the analysis, and this is handled by keeping track of the basic objects and their associated systematics, when these objects are built into more complex data classes (for example a shower being stored as an isolated ECal object). All errors are propagated in this way to ensure that no high level objects escape their inherent error derived from their fundamental components. There are other types of errors which are due to the physics occurring rather than limitations within the detector. Errors such as pion and proton secondary interactions are also only considered for relevant cases (i.e. a true proton or true pion in the event), and some additional mathematical modelling of the transport of these particles in the detector is included in the calculation of these error sources. In addition to the comprehensive attempts to cover every error source and the control samples used to inform these, the completeness of this set can be justified by comparison with other similar physics analyses within T2K, which state similar scales and sources of error [141] [126].

The highest contributor of detector error in this analysis is FGD Track Efficiency. This is to be expected as every retained signal event contains at least one object (the muon) which has segments in the FGD, with a high likelihood that many other objects used throughout the selection (FGDIso and FGD+TPC tracks) also have an FGD component. A similar justification can be used for the fifth largest source of detector error, TPC + ECal Matching Efficiency. The second highest source of detector error is ECal PID. Again, this is reasonable due to the fact that each signal event must contain at

least one isolated ECal object, with the additional concern that many of these objects may be considered throughout the selection, with cuts based on the ECal reconstruction and PID ability being used to remove unwanted objects. The third largest source is Pion Secondary Interactions. We can see in Figure 4.26, that at an early stage in the selection there is a large contamination of charged pions in the optimisation sample, which illustrates clearly that there is the potential for secondary interactions with these particles within the detector, which may cause confusion regarding object reconstruction. This justification also stands for the fourth largest detector error source, Proton Secondary Interactions.

## 5.2 Validation of Detector Systematics

Three methods were used to verify that the detector systematics were implemented correctly in the Highland2 framework, and that they were producing a reasonable variation in the number of selected events. Commonly for all three methods, the analysis was run using  $87.39 \times 10^{20}$  P.O.T NEUT on T2K production 6B (See Table 4.1), over 500 toy experiments, with all relevant systematics switched on.

The resulting analysis file was used for all of the three following methods :

- A plot showing number of events at each cut level for each of 500 toy experiments was produced.
- Histograms showing the relative error contribution from each detector systematic source were produced and the integral value extracted. For this method, the analysis run over the same MC sample again, with each individual detector systematic exclusively activated (a total of 23 times).
- A manual assessment of the effect of the systematics on certain example variables was carried out by counting the number of events which fall in/out of the specified cut range for that example variable for each toy.

Overall, this resulted in a large number of histograms ( $O \sim 1000$ ), only the most salient of which will be shown here.

### 5.2.1 Assessment of Individual and Total Systematics

There is a built-in function in Highland2, which allows the analyst to plot the error (relative to a single event) for any analysis variable. The analysis was run 23 times, one for each individual systematic, and these contributions plotted independently. As the relative errors are in terms of events, it is irrelevant which reconstructed quantity is used for the distribution (in fact it is not even necessary to plot them in this way). However, for the sake of simplicity, the relative error for each individual detector systematic was plotted in terms of the  $\mu^-$  candidate momentum. This was done for each stage in the selection for posterity, but only the value at the final selection stage was used. The relative error for five of the major detector systematic contributors are shown in Figures 5.2 to 5.6), followed by the total relative detector error in Figure (5.7).

It is not of great importance to show the detector errors in terms of binned reconstructed variables, as only a total MC/Data comparison is quoted as the final result of the analysis, and this is based on a number of events rather than kinematic comparisons. However, as these errors are illustrated in this section in terms of ‘Muon Candidate Momentum’, the pertinent distribution of all muon candidates passing the selection is shown in Figure 5.1. Figure 5.1 illustrates that there are relatively few events and thus muon candidates remaining in the total MC after the selection, especially in the lower populated bins. This situation gives rise to large statistical errors in some of the bins, which when applied to Figures 5.2 to 5.7 may explain some of the discrepancies in corresponding and neighbouring bins. The percentage statistical error on each bin is shown in Table 5.2.

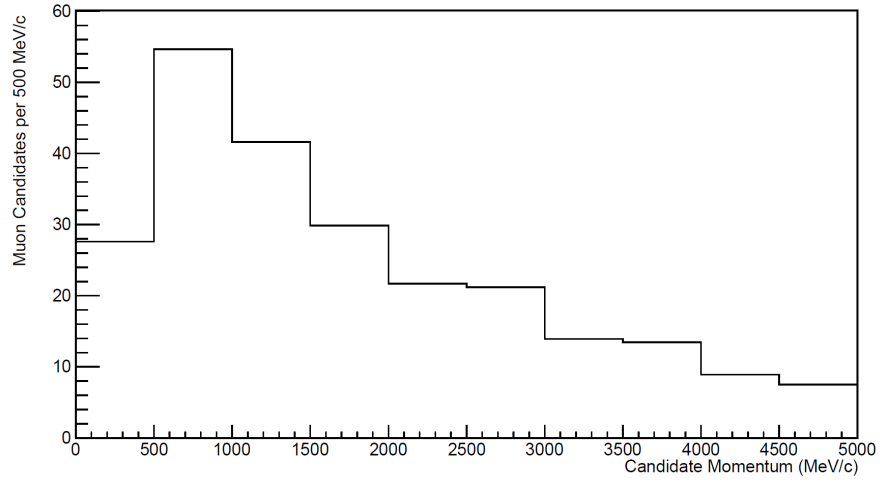


FIGURE 5.1: The distribution of all muon candidates passing the selection for the entirety of the Monte Carlo used for this analysis result ( $87.39 \times 10^{20}$  P.O.T)

Bin	Statistical Error (%)
$0 \leq x < 500$ MeV/c	$\pm 18.9$
$500 \leq x < 1000$ MeV/c	$\pm 13.5$
$1000 \leq x < 1500$ MeV/c	$\pm 15.5$
$1500 \leq x < 2000$ MeV/c	$\pm 18.3$
$2000 \leq x < 2500$ MeV/c	$\pm 21.3$
$2500 \leq x < 3000$ MeV/c	$\pm 21.3$
$3000 \leq x < 3500$ MeV/c	$\pm 26.4$
$3500 \leq x < 4000$ MeV/c	$\pm 26.4$
$4000 \leq x < 4500$ MeV/c	$\pm 32.0$
$4500 \leq x < 5000$ MeV/c	$\pm 35.0$

TABLE 5.2: Monte Carlo statistical errors in the muon momentum bins for candidates passing the selection.

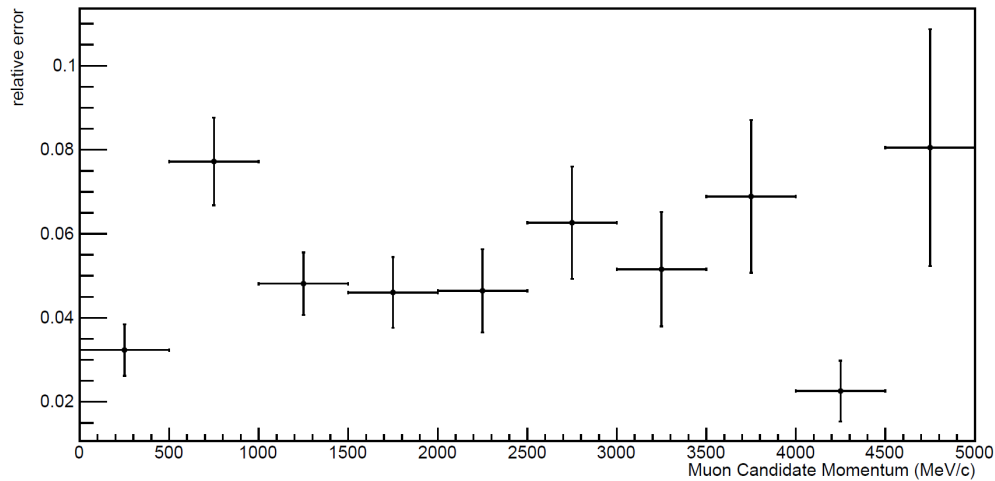


FIGURE 5.2: The detector error which defines secondary pion interactions is expectedly high in this analysis (due to pions providing a major background to the positive tracks being built to form decay photon candidates), however it is reasonably stable at lower energies. The total relative error contribution from this source is  $\sim 5\%$

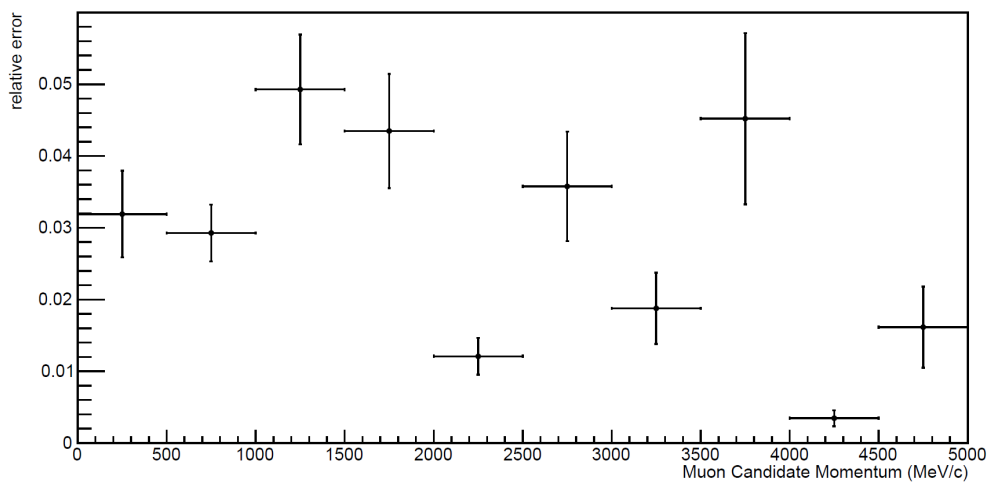


FIGURE 5.3: The secondary interaction proton detector error becomes erratic at high momenta, due to low statistics. Perhaps limiting the upper momentum of the muon candidate to 2 GeV would be beneficial. The error contribution from this source is  $\sim 3\%$

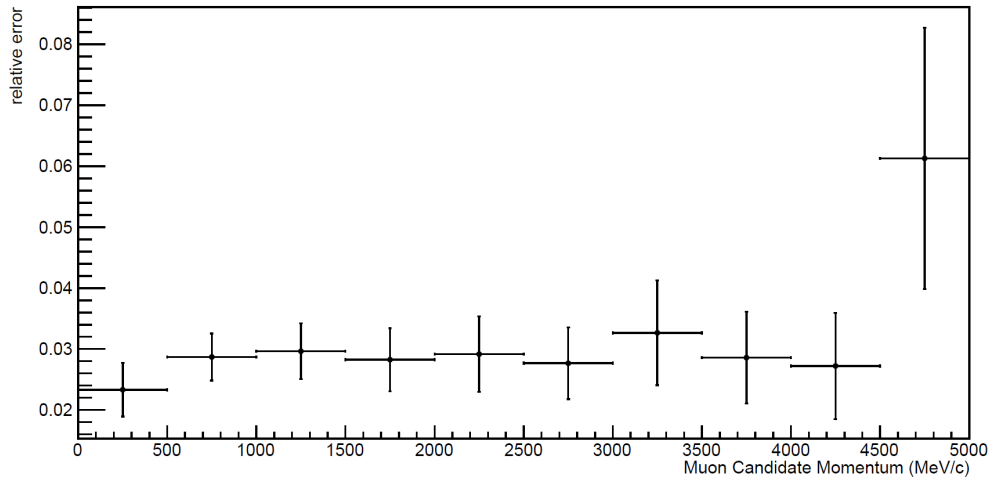


FIGURE 5.4: TPC Track Efficiency is an unavoidable systematic in any T2K analysis which utilises the tracker. The error here is relatively uniform except at very high momenta, which is likely due to the low number of events in that bin. The overall contribution from this source is ( $\sim 3\%$ )

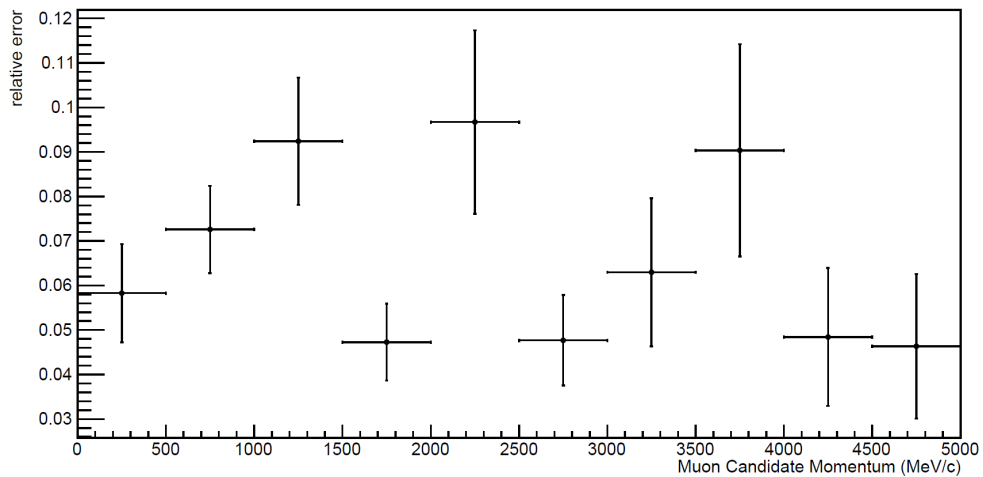


FIGURE 5.5: FGD Track Efficiency turns out to be the highest source of detector uncertainty in this analysis ( $\sim 6\%$ ). This is not too surprising given that all track objects used must begin within FGD1. In future it should be considered whether the statistics boost gained from reconstructing  $\pi^0$  decay products which fully convert in FGD1 (FGDIso DPCs) is well-motivated, and worth the added error.

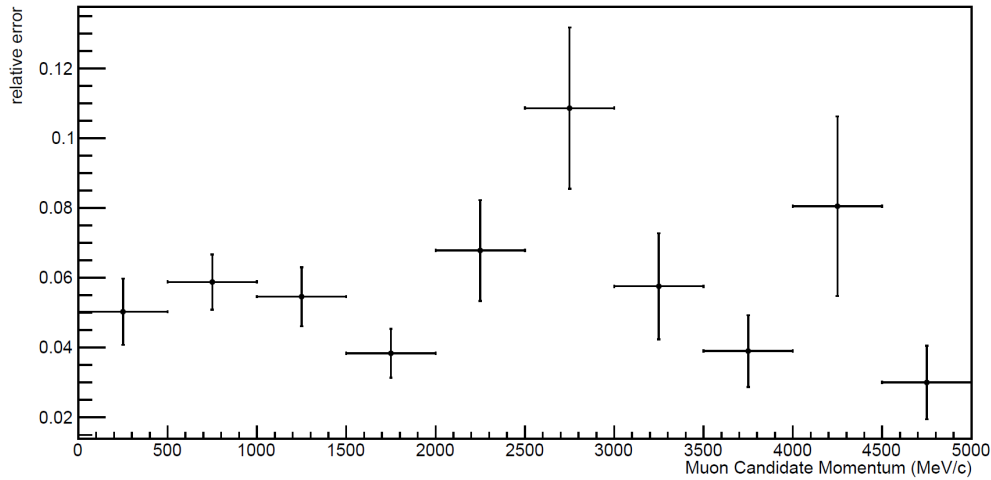


FIGURE 5.6: The relative error contribution from the determination of ECal PID. This is one of the highest sources of detector systematic in this analysis, due to the importance of ECal objects. The averaged error contribution is  $\sim 5\%$ , which potentially could be mitigated by limiting the analysis to muon candidates with momentum of 2 GeV and under.

By plotting each of the individual systematic contributions over one continuous bin (for events passing the final selection cut), a series of average integral relative errors were obtained. These were summed in quadrature and compared to the integrated sum over all bins for the total error (ran as an independent analysis). These figures were in agreement, both being  $\sim 11\%$  (Figure 5.7 and Table 5.1). The assumption that these errors can be justifiably added in quadrature in order to calculate a total detector error is supported by the fact that each source of error is independent. This has been illustrated by the fact that each was run separately for the selection, as well as collectively, with both yielding the same result. Additionally, each source of error arises from an independent variation of an underlying physical quantity which does not affect others.

It is clear that a thorough assessment of the systematic errors can provide valuable insight into potential avenues of future improvement for an analysis. In this case, had the systematics assessment been completed earlier, overall reduction of the detector systematics may have been possible with only a few simple steps. However, due to time constraints this is not possible and will be left to a future analyst.

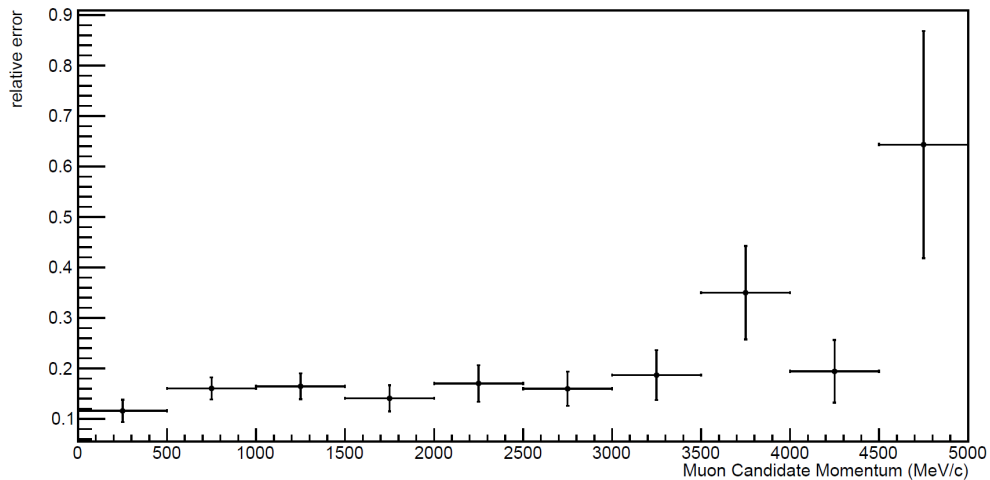


FIGURE 5.7: The total relative error contribution from all sources of detector error. The total averaged differential error for this is in agreement with other methods, at  $\sim 11\%$  ( $\sim \pm 5.5\%$ ). Once again there is a dramatic increase in error for events with a high momenta muon candidate. In a future analysis it could be beneficial to cut off this high muon energy tail, although in reality it is unlikely to contain many selected events.

### Assessing Systematic Impact on Specific Toy Variables

The efficiency and purity of the selection depend on how many signal events are passed and not passed throughout the selection. Whether an event passes or not depends on the value of certain reconstructed quantities for certain variables (i.e. TPC Pair Invariant Mass, Electron Likelihood etc). If the detector systematics are being properly applied in Highland2, then a variation in the value of reconstructed quantities should be seen. In order to test this, toy variables were added to the analysis output microtree, which represented particular physical quantities of interest (i.e. FGD Track Pion Pull, Reconstructed  $\pi^0$  Invariant Mass). The reconstructed properties of the objects in each toy throw of the selection should be different from one another, due to the effect of the detector systematics. All of the systematics outlined in Table 5.1 were switched on for this process.

FGD Track Pion Pull is well-understood (See Subsection 4.5.10), and so this was used as the test variable for this hypothesis. Using the optimised values for this variable (Table 4.6), it can be seen how many events fall in and out of that optimised range

for each toy experiment. This effectively generates a distribution of events which would pass/not pass this cut, directly dependent on the variation in the physical reconstructed quantity due to the detector systematics. The changes in the shape of the variable distribution and the variation in the number of retained events can be seen in Figure 5.8, where 4 examples of the 500 toy experiments thrown for this analysis are shown.

Utilising the number of retained events provided by these plots for each toy, a distribution which represented the variation in number of retained events for all 500 toys thrown was produced (See Figure 5.9). This was largely Gaussian in shape and centred around the mean, implying a reasonable variation in the reconstructed quantities.

### Events Passing The Selection For Each Toy Experiment

Once again using a built-in Highland2 drawing tool, it was easy to plot the number of events which passed each stage of the selection (for a given branch) for each toy experiment throw (incorporating all switched-on detector systematics). This was done for all selection cut stages in the analysis, in order to rule out any strange behaviour at specific cut levels, but only the surviving events passing the final stage of the selection will be shown here.

Figure 5.10 shows that the distribution of events at the final stage of the selection for 500 toys is reasonable (moderately gaussian). The RMS is  $\sim 20$ , which also agrees with the total detector systematic from other methods of  $\sim 11\%$  ( $\sim \pm 5.5\%$ ).

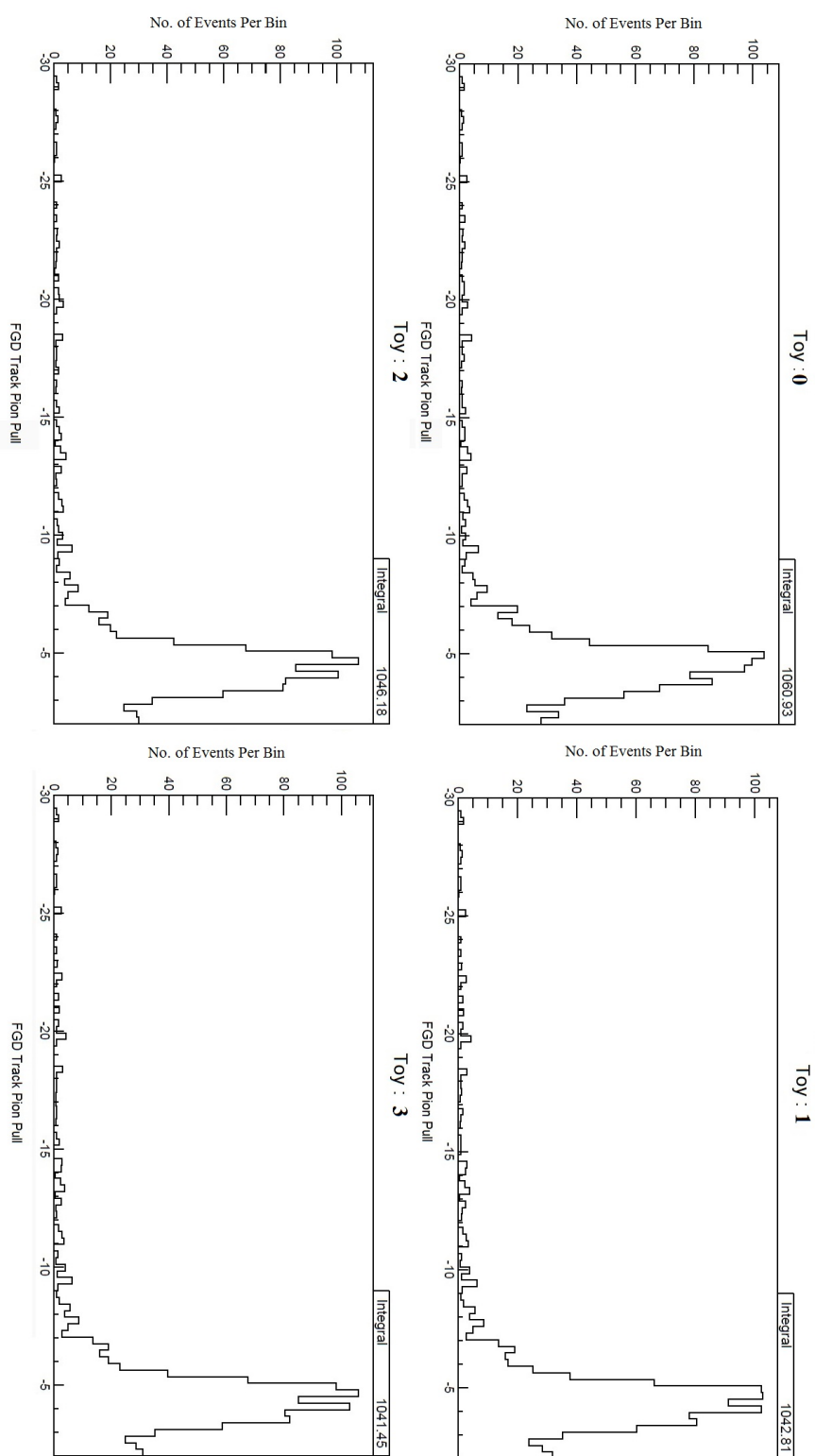


FIGURE 5.8: The reconstructed FGD track pion pull for the first four toys, variation in the shape and the number of events retained can be seen.

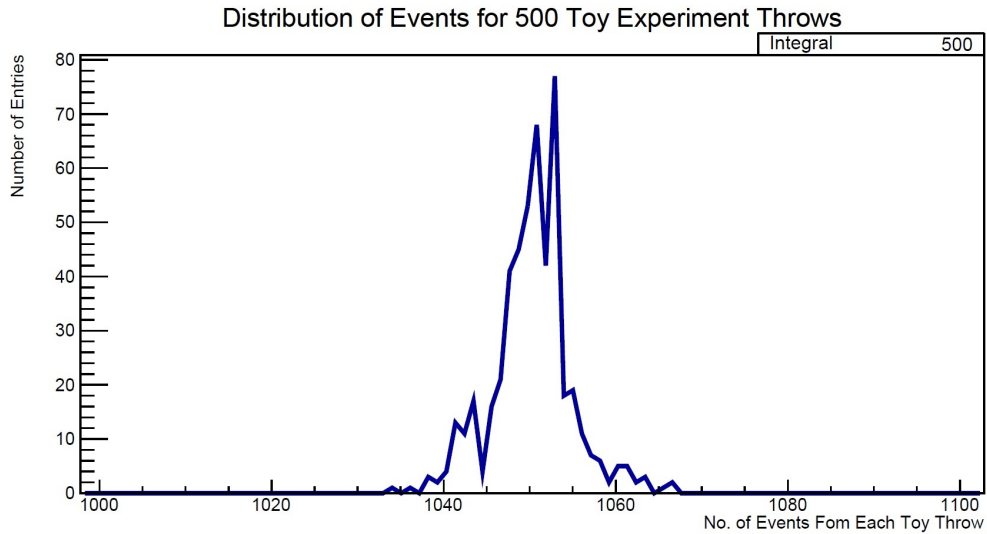


FIGURE 5.9: The number of events passing the FGD track pion pull for each toy was plotted. This variation illustrates that the systematics are having an effect, and that it is within expectations. We would not expect estimate of the error from this figure to be in-keeping with the overall  $\sim 11\%$  ( $\sim \pm 5.5\%$ ), as this is early in the selection and only takes into account systematics which affect this specific variable. However, it is reasonably Gaussian, with a mean of 1050, a standard deviation of 4.5 and a variance of 20.6.

### Sand Muon Contamination

It is possible that the analysis could be contaminated by the effect of ‘Sand Muons’. These are muons originating in the area around the detector due to  $\nu_\mu$  interactions in the surrounding rock and sand, which could possibly masquerade as charged-current muon tracks or other backgrounds. In order to rule this out, an  $2.67 \times 10^{20}$  P.O.T MC sample of exclusively sand muons was used for the analysis. This quickly demonstrated that the effect of this background is negligible in this selection, with zero sand muon events passing the selection. This negligible contribution to the overall detector systematic is reflected as  $< 0.01\%$  in Table 5.1. Neutrino interactions which occur in other non-fiducial sources such as the ECal or magnet, are modelled as part of the NEUT MC generator and handled within the FLUKA software. These types of interactions are cut out early in the selection by quality and fiducial cuts, and also have a  $< 0.01\%$  contribution. These events are considered in the ‘Out of Fiducial Volume’ category in this analysis.

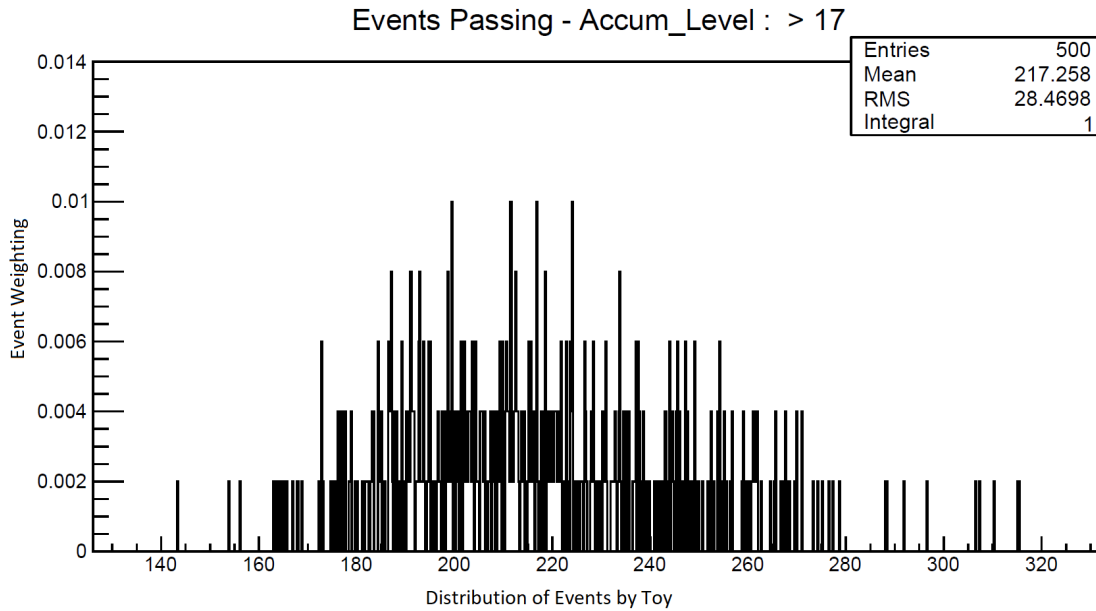


FIGURE 5.10: The number of events passing the entire selection for 500 toy throws of the experiment (all detector systematics switched-on) is shown. A reasonably gaussian distribution can be seen, centred around a mean of  $\sim 217$  events. The weight contribution to each toy is shown, with the integral of all events summing to one.

### 5.3 Flux Systematics

A major source of uncertainty in this analysis, and all ND280 analyses is in the modelling of the neutrino flux. The flux simulation and its associated uncertainties are driven by primary proton beam profile measurements, measurements of the focusing horns' magnetic fields, and hadron production data. Overall, the flux modelling can be considered in two parts : firstly that of the flux simulation and tuning (which can be handled by the use of a flux tuning file) while at the analysis selection stage in Highland2; Secondly that of the flux uncertainties, calculated by the beam group and handled in the T2KReWeight [130] package.

#### 5.3.1 Flux Simulation and Tuning

The Monte Carlo is generated using a given flux model, an approximation which may not fully represent the reality of the experiment. Measurements from beamline monitors, muon monitors (at the end of the decay volume) and INGRID (on-axis detector

at 280 m) are used to improve the accuracy of the the flux model in the MC. In this section, the processes used to simulate the T2K neutrino flux in the Monte Carlo are described. Flux tuning techniques, which involve updating an existing flux model and errors using new information from sources such as control samples are also described. Events are weighted in Highland2, using an existing flux tuning file, which is produced by the beam group. In this analysis, the following flux tuning file was used : ‘tuned13av1.1\_13anom’.

As outlined in Section 2.3, the neutrino beam is produced by the interaction of a 30 GeV proton beam with a graphite target, the initial stages of which is simulated for the Monte Carlo by FLUKA [97]. Control samples of hadron production data are essential in order to properly constrain neutrino flux. These are supplied by the NA61/SHINE [131] experiment at CERN, which specifically investigates hadron production for the total kinematic range of interest to T2K, and for a thin target, and has good agreement with the FLUKA simulation.

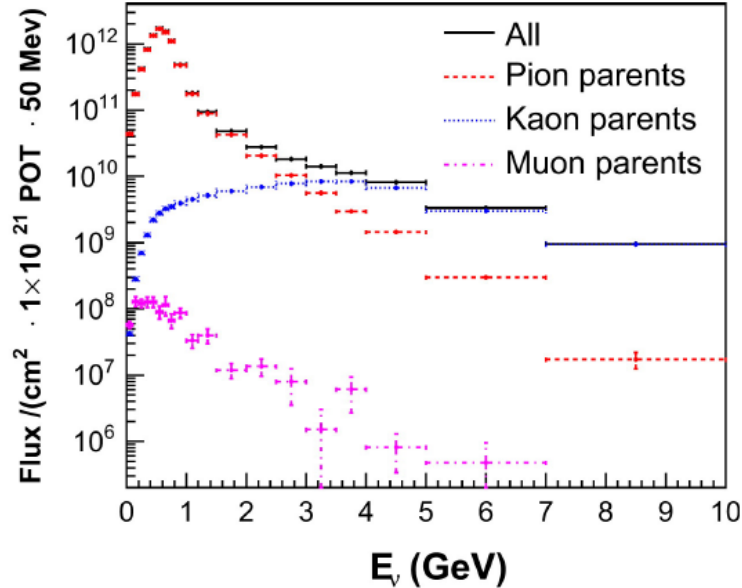


FIGURE 5.11: The Fluka2008.3b neutrino flux prediction for the ND280 detector for  $\nu_{\mu}$ , re-weighted to the NA61 target data. The contribution from pion, kaon and muon decays to the total neutrino flux are shown [132].

The FLUKA simulation produces an array of particles (including pions and kaons),

whose kinematic information is subsequently passed to the JNUBEAM [132] software. JNUBEAM is a GEANT3 [98] Monte Carlo simulation of key components in the secondary beam-line including the baffle, target, horn magnets, helium vessel, decay volume, beam dump, and muon monitor [133]. The geometry of these components as used by JNUBEAM is based as precisely as possible on the final mechanical drawings of the constructed beamline. JNUBEAM also includes the INGRID, ND280, and SK detectors, which are positioned in the simulation according to the latest geographical survey results. In JNUBEAM, particles passed from FLUKA are propagated through the simulated horn magnetic field, and may interact with the horn material in the target station. Particles are propagated in this way through the decay volume until they interact or decay. The properties (kinematic variables, decay phase-space density, branching fraction) of all simulated neutrinos produced in this way are saved. Thus the variables of interest to the experiment (neutrino flux and energy spectrum) are obtained from simulated events by weighting according to these probabilities. Additionally, salient information regarding the initial proton and the full interaction chain which lead to production of the neutrino is saved to allow for re-weighting of the proton beam profile and primary hadronic interactions.

The final stage of the flux simulation is the modelling of hadronic interactions using GCALOR [132] which is within JNUBEAM. While the NA61/SHINE models the the initial protons on carbon interaction well, this is only for a thin target, which is not exactly the same as the target used in the T2K beam. The chain of hadronic interactions for each simulated event producing a neutrino is saved, and re-weighting based on hadron interaction measurements is applied to the simulated events. Secondary hadrons are designated as such if they are produced in interactions of the original protons, whereas tertiary hadrons are those produced by interactions of hadrons other than the original proton. These additional hadronic interactions and multiplicity probabilities modify the likelihood of a neutrino being produced and the resultant energy spectrum.

All of the simulated processes discussed allow a model comparison to the NA61/SHINE data, which can then be propagated into a parameter shift, which is expressed in terms

of weights in neutrino energy bins. These weights files represent the flux tuning, which are curated by the beam group and periodically updated to reflect the most recent studies and model information. In terms of implementation in Highland2, the beam group provides histogram tuning files, which are automatically applied at the proper stage in an analysis, to help to more accurately model the beam flux.

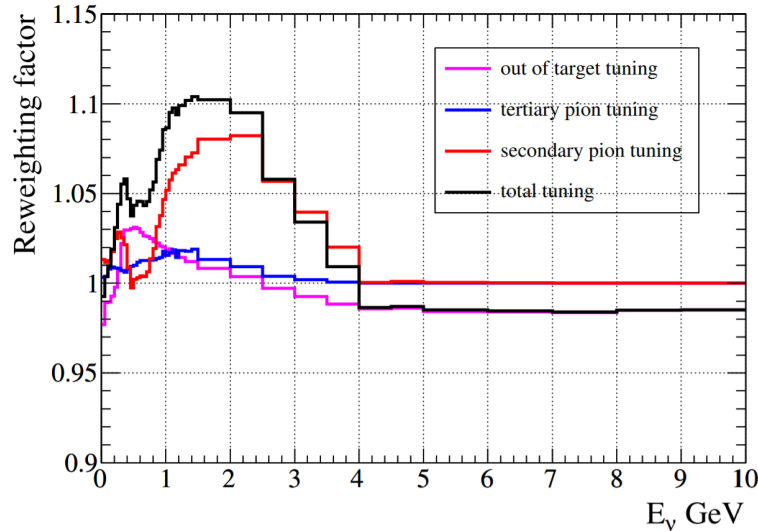


FIGURE 5.12: The final tuning weights for the flux predictions at the ND280 for  $\nu_\mu$ . The secondary pion tuning is substantial, and without it the neutrino flux would be considerably underestimated [70].

### 5.3.2 Flux Uncertainties

The flux tuning allows analysts to use an up to date modelling of the neutrino beam flux. However, the initial simulation and subsequent tuning does not take into consideration the systematic uncertainties on a number of variables which could cause variation in that prediction. Flux fluctuations affect the number of selected events, efficiency and integrated flux predicted by the nominal MC. The systematics considered by the beam group include uncertainties in the following :

- Pion production multiplicity in both the primary and secondary interactions
- Kaon production multiplicity in the primary and secondary interactions
- Interaction cross-sections of  $p, \pi^\pm, K^\pm$

- Off-axis angle
- Primary beam optics
- Horn alignment
- Target alignment
- Horn current
- Horn field asymmetry (magnetic field distribution)

Once intrinsic uncertainties within these areas are understood, they can be propagated to obtain variations in the flux prediction. For example, the neutrino flux can be calculated using different horn currents to estimate the effect of the horn current uncertainty. This would involve  $N$  toy throws within the uncertainty distribution for the horn current, propagated to a flux value, the resultant distribution of which supplies the flux uncertainty for that particular source. The systematics related to hadron interactions/production provide some additional complexity, due to their distribution over many bins in momentum and angle, which also introduce correlations. The contributions to the flux error are summed into categories and shown in Figure 5.13.

Uncertainty in all of the above variables is propagated into a covariance matrix (binned in neutrino energy) which represents the modified weighting of each event. This covariance matrix is supplied by the beam group. An example of a flux covariance matrix can be seen in Figure 5.14, taken from the 2013 T2K neutrino flux prediction paper [70].

The next stage in the process of applying flux uncertainties to a given selection, is to determine the event weightings, which are based on these inputs. This can be achieved by using the functionality of T2KReWeight [130]. This same procedure is used for cross-section, final state interactions (FSI) and flux uncertainties, and is described in the Section 5.5. The neutrino flux uncertainty covariance matrix used in in this analysis is passed to T2KReWeight and used to apply weights to each event passing the selection,

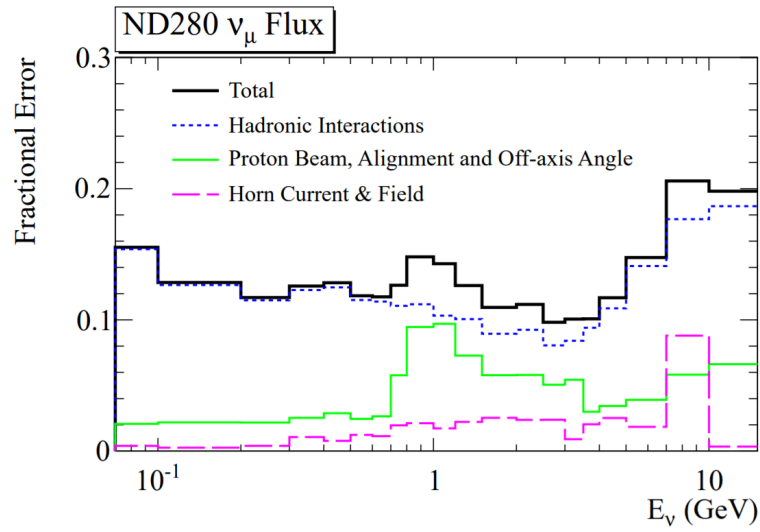


FIGURE 5.13: The fractional error for the total neutrino flux uncertainty, for a wide range of energy. Also shown are the individual contributions from three primary sources of uncertainty : hadronic interactions, beam parameters and horn current [70].

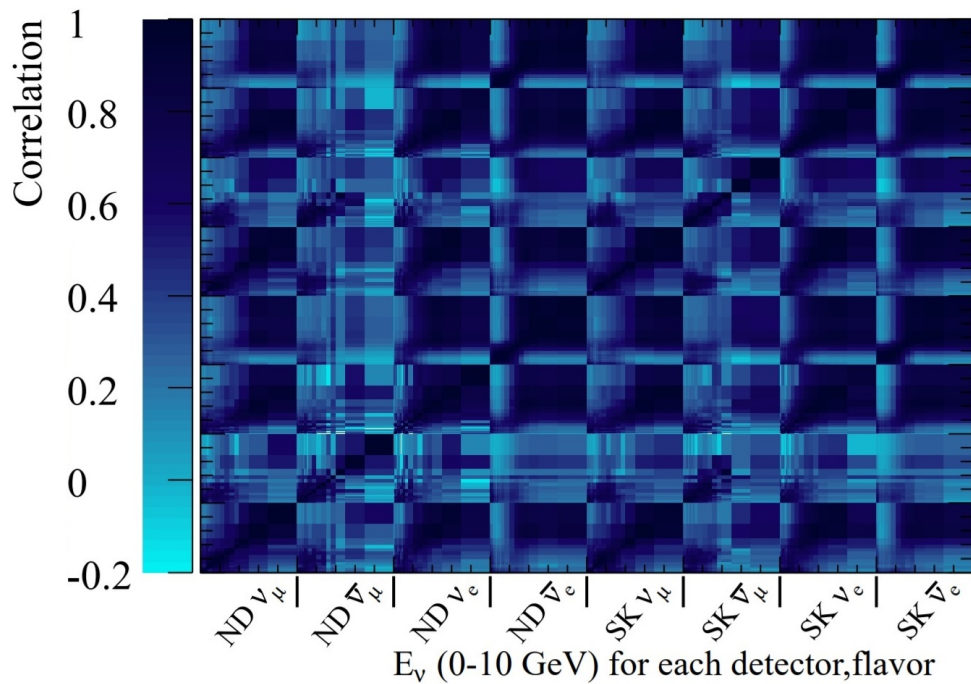


FIGURE 5.14: Correlations of the flux for a given flavor, energy and detector. The binning on the y-axis is identical to the binning on the x-axis. [70]

for specific ranges of neutrino energy. This has been extracted and plotted in Figure 5.15. The total MC flux error  $\pm 5.8\%$ .

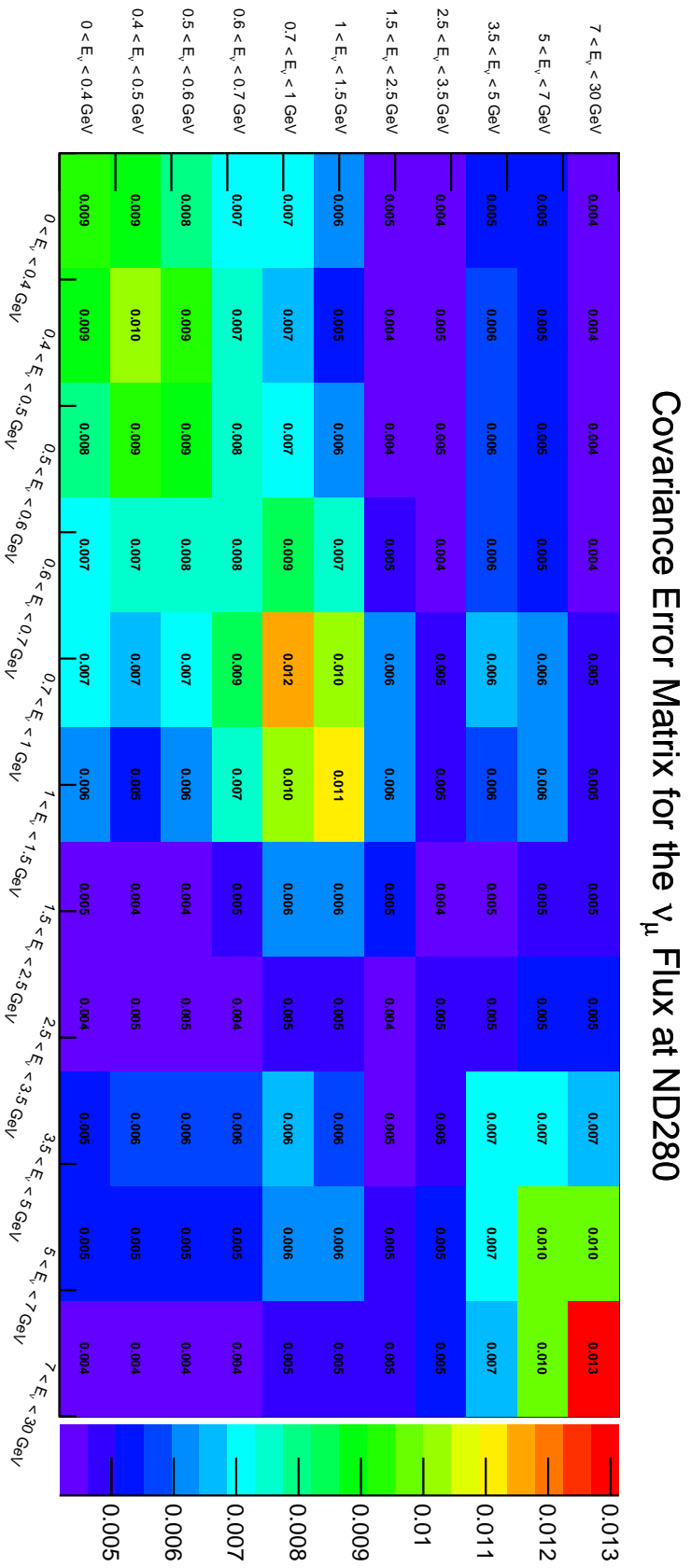


FIGURE 5.15: Correlations of the flux uncertainties for a range of neutrino energy.

## 5.4 Neutrino Interaction Uncertainties

A notable source of uncertainty in any physics analysis is that of the model parameters which help form a description of the physical (particle) world. These model parameters mostly concern neutrino interaction parameters, nuclear final state interactions (FSI) and cross-sectional parameters.

The Neutrino Interactions Working Group (NIWG) within T2K, focuses primarily on estimating prior uncertainties on cross-section model parameters, driven by external data constraints, such that a more accurate model of our physics understanding can be used in T2K analyses (including this one). This procedure includes modifying re-weighting using uncertainties in model parameters in T2KReWeight, and then fitting the NEUT Monte Carlo model to publicly available data when possible. The results of this fitting are then used to select an appropriate cross-section model for analyses and determine values for the prior inputs and errors for that model. By 2014, many changes had been made since the start of T2K to the NEUT model, including modifications to the description of CCQE interactions, np-nh and resonant single pion interactions. There had also been an expansion to the available data sets which could be used to more accurately understand and parameterise these models, being provided by experiments such as MiniBooNE [134], *Minerva* [135] and DUET [136]. Therefore, this was an opportune time to re-evaluate the interaction based model uncertainties which were employed in the T2K analyses of the time. After a thorough study, the NIWG produced updates to the model parameters, which have been summarised in a weights file and utilised in this analysis, and many others.

Parameter	Units	Prior Mean	Error	NEUT Nominal
$M_A^{QE}$	GeV/c <sup>2</sup>	1.15	0.07	1.2
$p_F^{12C}$	MeV/c	223	13	217
$M_A^{RES}$	GeV/c <sup>2</sup>	0.95	0.15	0.95
$E_B^{12C}$	MeV	25	9	25
MEC <sup>12C</sup>	None	27%	29%	100 %
$C_5^A$	None	1.01	0.12	1.01
CC Coherent <sup>12C</sup>	None	1.0	1.0	1.0
NC Coherent	None	1.0	0.3	1.0
NC Other	None	1.0	0.3	1.0
$BG_{RES}$	None	1.3	0.2	1.3
$DIS_{MP}^{ISHP}$	None	0	0.4	0
FSI Inelastic Low E	None	0	0.41	0
FSI Inelastic High E	None	0	0.34	0
FSI Pion Absorption	None	0	0.41	0
FSI Pion Production	None	0	0.50	0
FSI Charge Exchange Low E	None	0	0.57	0
FSI Charge Exchange High E	None	0	0.28	0

TABLE 5.3: Parameters and relevant values of the NIWG group 2015 model parameter covariance matrix. The values shown here are consistent with those plotted in the model error covariance matrix used for this analysis. More detail can be found in the T2K technical note [137].

The cross-section model and FSI uncertainty covariance matrix which was used in this analysis (See Figure 5.16), is contained within the flux and model errors file, passed to T2KReweight and used to apply reasonable weights to each event passing the selection, to account for discrepancies between our Monte Carlo models and reality.

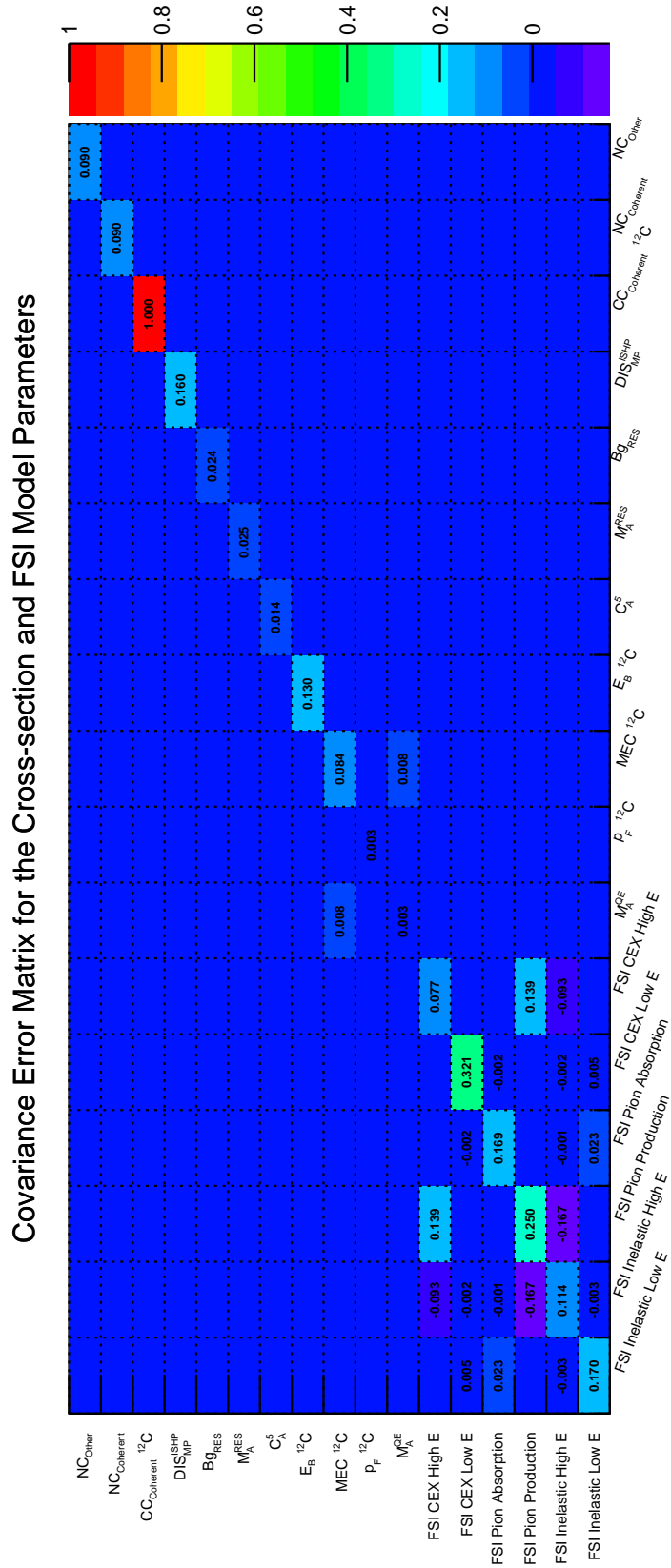


FIGURE 5.16: Correlations of the interaction and FSI uncertainties considered in this analysis.

### 5.4.1 Most Relevant Neutrino Interaction Uncertainties

A wide range of error sources (Table 5.3) are considered in order to determine the level of uncertainty provided by nuclear model and interaction assumptions. In this analysis, the magnitude of each individual error source contribution is not known, and a deconvolution of a single source from the many would be much more complex for model uncertainties than for flux (which is generally applied linearly). However, based on our understanding of the underlying processes involved in this analysis, assumptions can be made as to which of these model and interaction error sources are most relevant. When an interaction of interest occurs, additional effects may occur within the nucleus involved. Firstly, FSI Pion Absorption, Production and Charge Exchange are likely to be important. These parameters affect how pions can be absorbed, scattered and produced. Possibly most importantly, these pions can exchange charge with the nucleus, resulting in the appearance or disappearance of a neutral pion in the final state. For example, a CCRES interaction could proceed, which produces a neutral pion, only to have that absorbed and a charged pion emitted, making the final state invalid for this analysis. Conversely, an interaction such as DIS, may produce a charged pion, which is then involved in a charge exchange FSI process, resulting in a final state which is eligible for the selection, though not due to the expected interaction process. The  $M_A^{RES}$  (axial form factor for resonant pion production) and  $C_5^A$  (normalisation factor for  $M_A^{RES}$ ) parameters will also have an impact on the neutral pion production rate from resonant interactions, and specifically may affect the kinematics of the final state neutral pions (which in turn could have an impact on selection efficiency), this is discussed in more detail in Section 6.2.2. The total MC error from interaction uncertainties is  $\pm 6.7\%$  and FSI is  $\pm 6.9\%$ .

## 5.5 Propagation of Systematic Errors Using T2KReWeight

To propagate systematic errors coming from cross-section, FSI and flux uncertainties, the software package T2KReWeight is used. Specifically, a pre-made script ‘Create

Weights' can be used to produce appropriate weights files, which can then be applied to the events passing the selection, such that reasonable error bands for a number of systematic sources can be plotted. As input, the weights macro takes a given analysis output file (microtree) and a file which contains the values and uncertainties of model parameters, in the form of the covariance matrices shown in Figures 5.15 and 5.16.

From this, a unified weights file is produced which contains calculated weights for a pre-defined number of toy throws (500 in this case) for each event. The weights histograms in the produced unified weights ROOT file represent the nominal case, as well as the flux, FSI and Cross-Section errors for both reconstructed and true quantities. Error contributions from the sources discussed in this chapter are shown in 5.4, with the total propagated error for this analysis applied to results in Chapter 6.

Source of Error	Size (%)
MC FSI	$\sim \pm 6.9$
MC Interaction	$\sim \pm 6.7$
MC Flux	$\sim \pm 5.8$
MC Detector	$\sim \pm 5.5$

TABLE 5.4: All sources of systematic error which affect the NEUT Monte Carlo are shown. These are separated into four major sources, which are all similar in scale.



## Chapter 6

# Results

### 6.1 Overview

In this chapter the final results of the  $\nu_\mu$  Charged-Current  $\pi^0$  analysis are presented. All MC and data shown is for events passing the entire selection (described in Chapter 4), for the  $87.39 \times 10^{20}$  NEUT T2K Production 6B P.O.T (Table 4.1) and  $55.19 \times 10^{19}$  T2K Real Data Production (RDP) P.O.T (Table 4.2). The number of events passing the entire selection in both data and MC for the total available P.O.T and scaled to the lower amount is shown in Table 6.1. This shows a prediction of  $262.1 \pm 32.8$  (Stat. + Det. + Flux + Model Error) events being selected for the NEUT Monte-Carlo, and a total of  $316 \pm 17.8$  events being selected within the real data.

The table is also reflected in Figure 6.2, which shows the progression of events in both data and MC as each selection cut is passed. It illustrates that predominantly there is good agreement between the two, with a slight discrepancy initially arising from the N Iso ECal object cut, which is temporarily assuaged by subsequent cuts, until further tension is introduced by the TPC likelihood cut. This is the only cut in the  $\pi^0$  selection which was not optimised specifically for this analysis, due to the likelihood values being a hard-coded part of oaAnalysis and thus Highland2. These cuts did not have such an obvious effect in the Run 4 air sample used to optimise the analysis, but this could be due to an introduced bias, and it is for this exact reason that most of the MC and all data was not seen until this stage to preserve objectivity. Quantitatively, before the TPC likelihood cut there is a 98.0% match between data and MC, which is reduced to 84.2% after, introducing a disparity from which the selection does not recover. This may be further exacerbated by subsequent cuts such as the TPC pair invariant mass cut, though seemingly to a lesser extent. It is difficult to tell however, as the selection cuts (although mostly independent in action), are necessarily executed in a linear fashion and are not evaluated non-chronologically here. The final match of data and MC post-selection and  $\pi^0$  candidate choice stands at 82.9%. Without including all known sources of systematic error and uncertainty (See Section 6.3 for the final result), it can be said that after the selection there are 262 events remaining in the Monte Carlo and 316 in the RDP, which may seem in tension, though this is refuted by the inclusion of errors.

Selection Cut	Data Events	MC Events
Event Quality	1416001	822013
> 0 Tracks	1298963	719364
Quality + Fiducial	47974	44320
Veto	34050	33875
External FGD1	33429	33345
Muon PID	24396	24500
N Iso ECal Objects	9120	8756
N Track Objects	6652	6518
ECal DPC Energy	6445	6329
ECal DPC Dist. to $\mu^-$	6402	6279
ECal DPC MIPEM	5458	5322
ECal DPC Collinearity	5329	5228
FGD1 Tracks Pion Pull	4853	4754
TPC Tracks Likelihood	2310	2012
Tracker DPC Dist. to $\mu^-$	725	628
Tracker DPC Coll.	441	375
Tracker DPC Pair Sep.	331	271
Tracker DPC I.M	329	269
Post-Selection $\pi^0$ Mass Cut	316	262

TABLE 6.1: The number of events in data and MC after each selection cut for  $87.39 \times 10^{20}$  NEUT T2K Production 6B MC P.O.T and  $55.19 \times 10^{19}$  T2K Real Data Production (RDP) P.O.T. This represents 0.66% of the events passing the quality and fiducial cuts for the RDP and 0.59% for the NEUT MC.

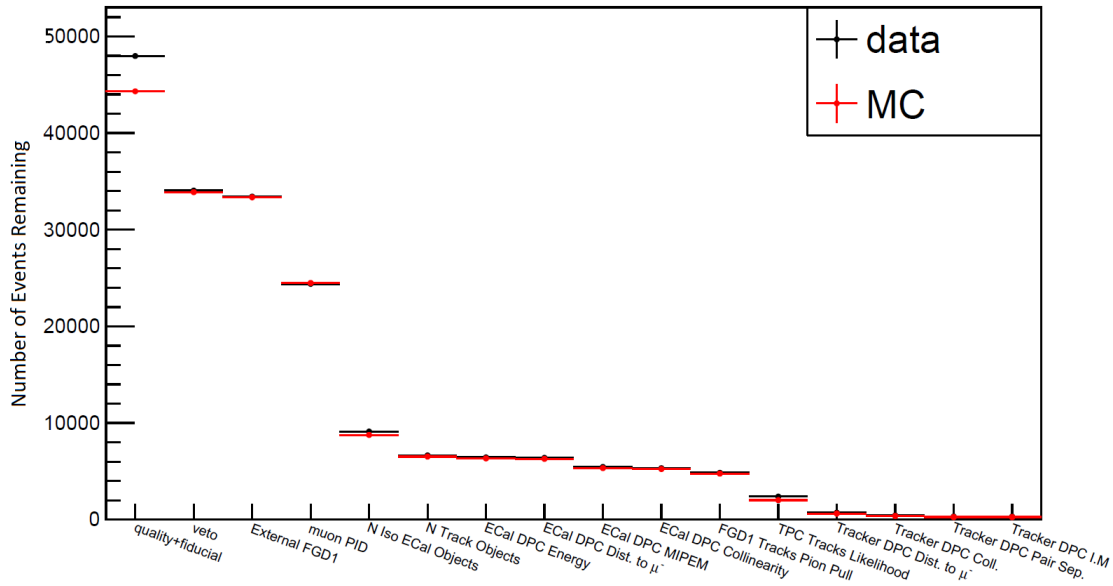


FIGURE 6.1: The number of events in data and MC after each selection cut for  $87.39 \times 10^{20}$  NEUT T2K Production 6B MC P.O.T and  $55.19 \times 10^{19}$  T2K Real Data Production (RDP) P.O.T. The first two cuts, which can be seen in Table 6.1 have been intentionally removed from this plot in order to focus more clearly on the later stages of the selection. As stated, these first two stages show a large data/MC disparity, which is largely rectified by the quality and fiducial volume cuts.

Each of the kinematic distributions is represented in two ways, firstly using the native Highland2 drawing tools to represent the interaction classification, and secondly with errors representing the total MC systematic error and the statistical RDP error (plotted using the basic ROOT framework [115]). Dividing the results into two types of plots allows information regarding the distributions to be presented comfortably, without over-crowding the plots. The native Highland2 plots each illustrate a given variable distribution, and show the number of events which passed the selection in both RDP and MC (normalised to data P.O.T). The surviving events are broken-down into the same event categories used throughout the analysis (see Chapter 4), primarily distinguishing between events which contain a  $\pi^0$  in the MC truth information, those with more than one, and those with none. Secondly, the distributions are also shown with surviving event/candidate rate for both RDP and MC normalised to 'per  $10^{18}$ ' P.O.T. These 'Error-Band' plots convey the total systematic uncertainty from the

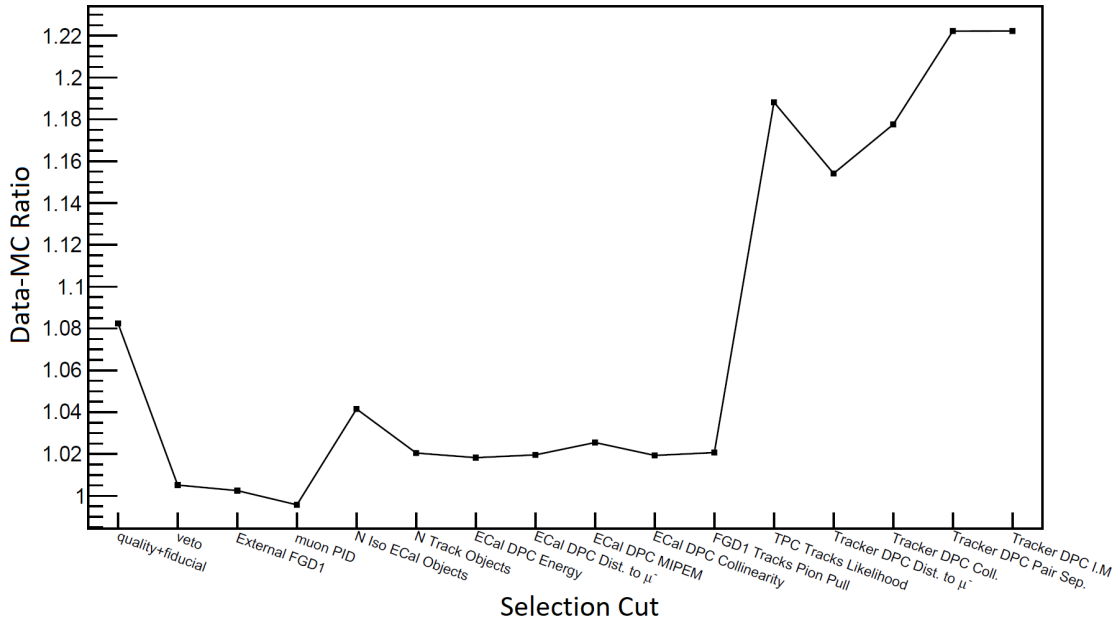


FIGURE 6.2: The ratio of remaining events in data and MC after each selection cut for  $87.39 \times 10^{20}$  NEUT T2K Production 6B MC P.O.T and  $55.19 \times 10^{19}$  T2K Real Data Production (RDP) P.O.T. The first two cuts, which can be seen in Table 6.1 have been intentionally removed from this plot in order to focus more clearly on the later stages of the selection. It can clearly be seen that the later stages of the selection, specifically the TPC Tracks Likelihood cut, introduce a data/MC disparity. The post-selection cut which selects the  $\pi^0$  candidate is not shown, but brings the ratio to 1.21, as outlined in the results.

following sources : Detector, MC Statistical, Final State Interactions, Neutrino Interactions, Flux and (as also on the Highland2 plots) RDP statistical. A breakdown of these errors is shown in separate plots (Figures 6.4 to 6.8) for the  $\pi^0$  invariant mass distribution, which defines the final result. For the remaining kinematic distributions only the total MC error and data statistical is shown for each.

For both types of plot, the RDP and MC shown is identical. Slight differences in the MC are due to the additional Neutrino Interaction Working Group (NIWG) tuning applied in the error band plots. In the case of the  $\pi^0$  distributions, one  $\pi^0$  candidate from each event has been chosen using the metric which selects the candidate having the reconstructed invariant mass closest to the known  $\pi^0$  mass, as justified in Section 4.9. For the distributions concerning  $\mu^-$  candidates, it would be extremely rare to have an event where multiple  $\mu^-$ s could be considered to be the highest momentum negative

track (the standard condition for identifying a  $\mu^-$  produced in a charged-current  $\nu_\mu$  interaction), regardless the  $\mu^-$  candidate used is determined by the standardised T2K Highland2  $\nu_\mu$  selection [124], which forms the foundation of this analysis. As exactly one candidate is chosen per surviving event for both  $\mu^-$  and  $\pi^0$ s, we can consider the number of events identical to the number of candidates <sup>1</sup>.

## 6.2 Kinematic Distributions

The five kinematic distributions presented in this chapter all focus on variables which can be of use in informing MC models, whether by providing some confirmation of their accuracy (in the case of agreement) or by implying some lack of understanding (in areas of tension or disagreement).

---

<sup>1</sup>A non-integer number of candidates in the MC for the distributions may seem counter-intuitive, but this is caused by event weighting due to detector systematics and flux tuning.

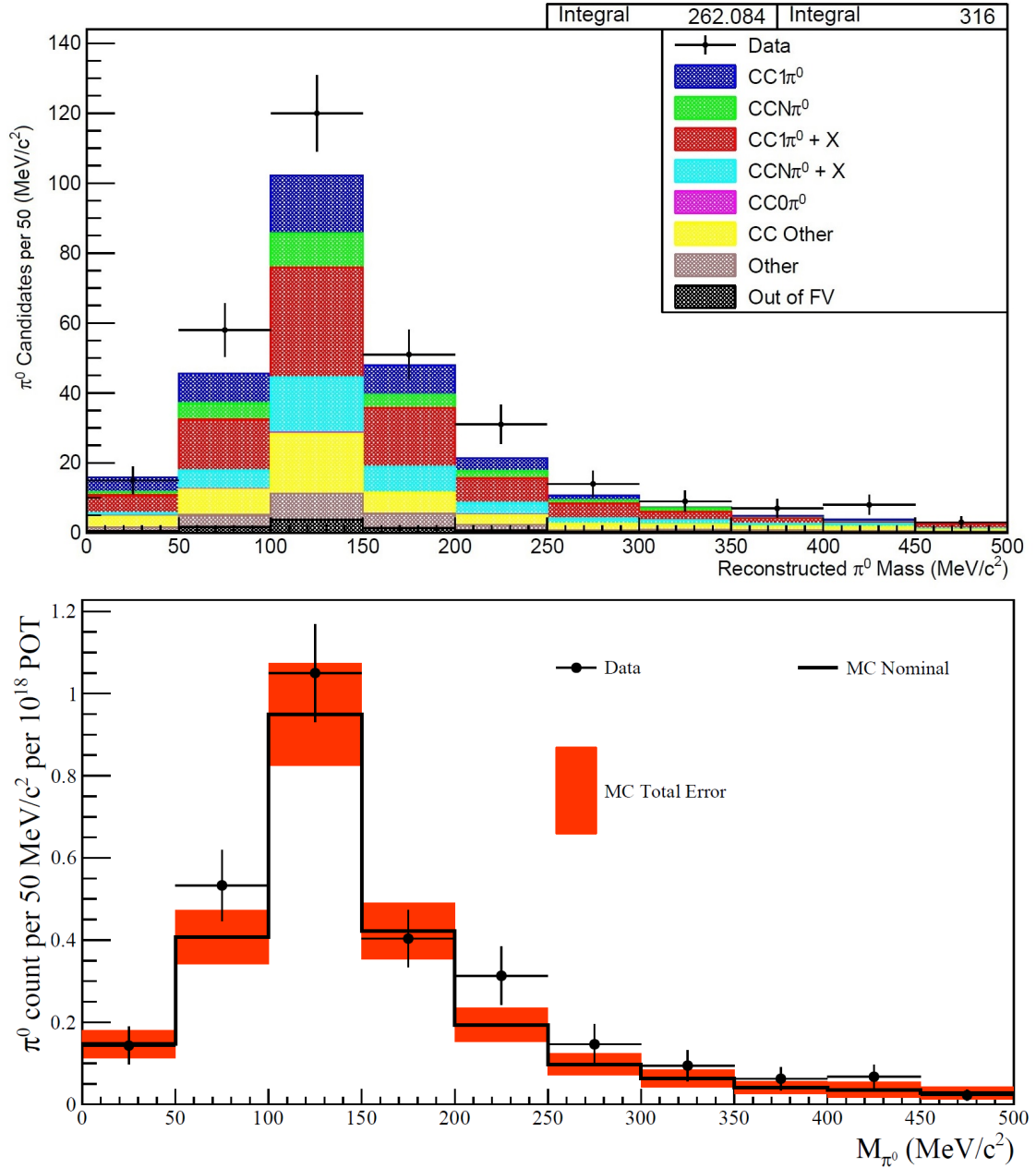
6.2.1  $\pi^0$  Invariant Mass

FIGURE 6.3: Reconstructed invariant mass distribution of  $\pi^0$  candidates passing the selection, scaled to  $55.19 \times 10^{19}$  P.O.T of RDP from T2K Runs 2-4. Compared with  $87.39 \times 10^{20}$  P.O.T of NEUT Monte Carlo from T2K Runs 2-4 Production 6B. The total RDP statistical error corresponds to  $\pm 8.6\%$  and the total MC error is  $\pm 12.5\%$ .

We know that the invariant mass of the  $\pi^0$  meson is  $135 \text{ MeV}/c^2$  [77]. Therefore if we correctly identify and reconstruct the  $\pi^0$  candidate from the selection process, we would expect to see a defined peak centred around that value, with an expected width due to the detector resolution when reconstructing the decay products, even if they have been correctly identified. This provides confidence that the correct  $\pi^0$  candidate has been selected. However, it cannot truly be said that the real  $\pi^0$  has been identified solely by observation of this quintessential peak, as there is a heavy bias imposed when choosing the  $\pi^0$  candidate closest to the known  $\pi^0$  invariant mass, which can result in non- $\pi^0$  decay products being built into these candidates. The fact that there are non- $\pi^0$  backgrounds present in Figure 6.3 illustrates that backgrounds can be mis-reconstructed into  $\pi^0$ s. Specifically, contributions from ‘CCOther’ and ‘Other’<sup>2</sup> are present. However, from the work described in Chapter 4, we know that according to the truth-matching used in this analysis, in the MC, the  $\pi^0$  built uses at least one of the correct decay photons  $\sim 80\%$  of the time, which is in-keeping with the non- $\pi^0$  event contamination observed. The efficacy of the truth matching is discussed further in Chapter 7.

The decision to choose the  $\pi^0$  candidate closest to the known  $\pi^0$  invariant mass is used to improve confidence that the correct candidate has been selected. However, of course this choice has an effect on the results of the analysis in terms of the shapes of various distributions and even the overall rate measurement. In terms of the kinematic distribution shapes, the  $\pi^0$  invariant mass,  $\pi^0$  momentum and  $\pi^0 \cos(\theta)$  with respect to  $\nu_\mu$  beam direction can be affected by the choice of  $\pi^0$  candidate, whereas the  $\mu^-$  momentum and  $\mu^- \cos(\theta)$  with respect to  $\nu_\mu$  beam direction are solely dictated by the event and therefore are unchanged. The three distributions which can be affected by this choice are included in the Appendix (Figures A.6 to A.11) for all possible metrics available within this analysis framework. The only distribution which can affect the final result of this analysis (the data/MC rate comparison) is the  $\pi^0$  invariant mass, which may be susceptible to candidates (and thus events) falling out of the prescribed

<sup>2</sup>Albeit ‘Other’ may contain neutral current  $\pi^0$ s which have slipped through the muon selection.

0 to 500  $\text{MeV}/c^2$  binning. As can be seen from the relevant plots in the Appendix (Figures A.6 to A.11), the number of MC events in these distributions varies from 243 to 262, with a standard deviation of 6.2 (2.5%). The number of data events varies from 283 to 316, with a standard deviation of 10.4 (3.5%). These errors could be incorporated into the final rate measurement, but they are correlated and this could be a complex process best left to a future analyst. Each of these distributions is very similar when picking any metric which does not bias towards the true  $\pi^0$  mass, although this mainly manifests in the broadening of the peak (in the case of the mass and momentum plots) due to false combinatorics. The  $\pi^0 \cos(\theta)$  distributions are all almost identical regardless of metric choice, likely due to the inherent similarity in the direction of candidates passing the selection and the limitations in reconstructing such directionality with high precision for composite objects in ND280.

A breakdown of each systematic source of error for the  $\pi^0$  invariant mass distribution (Figure 6.3) is shown here in Figures 6.4 to 6.8.

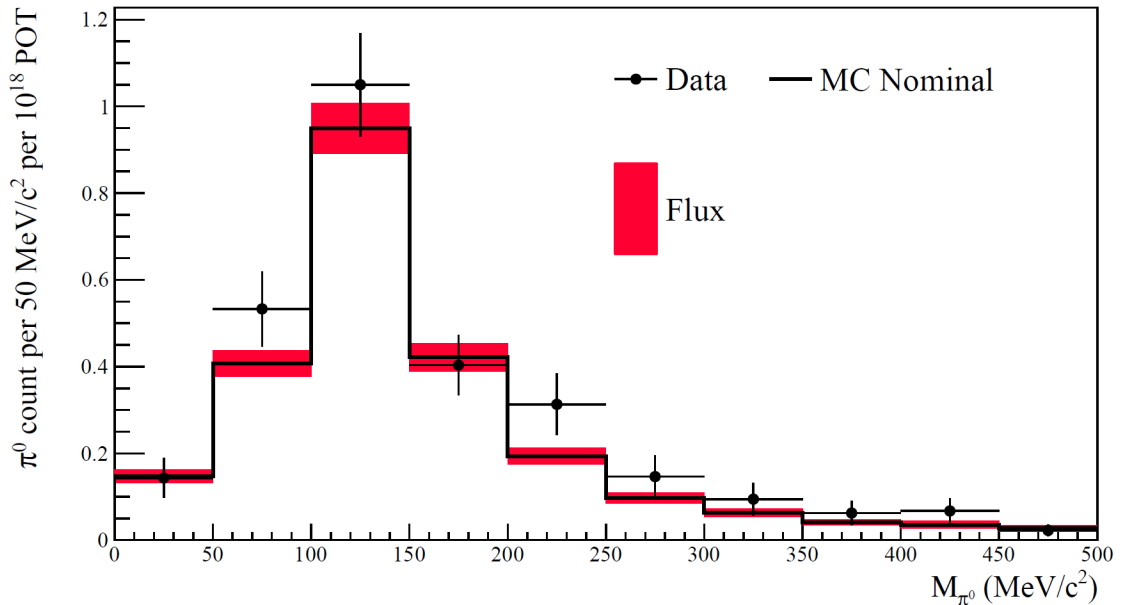


FIGURE 6.4: Reconstructed invariant mass distribution of  $\pi^0$  candidates passing the selection, scaled to  $55.19 \times 10^{19}$  P.O.T of RDP from T2K Runs 2-4. Compared with  $87.39 \times 10^{20}$  P.O.T of NEUT Monte Carlo from T2K Runs 2-4 Production 6B. Only the MC flux source of error is shown, which corresponds to  $\pm 5.8\%$ .

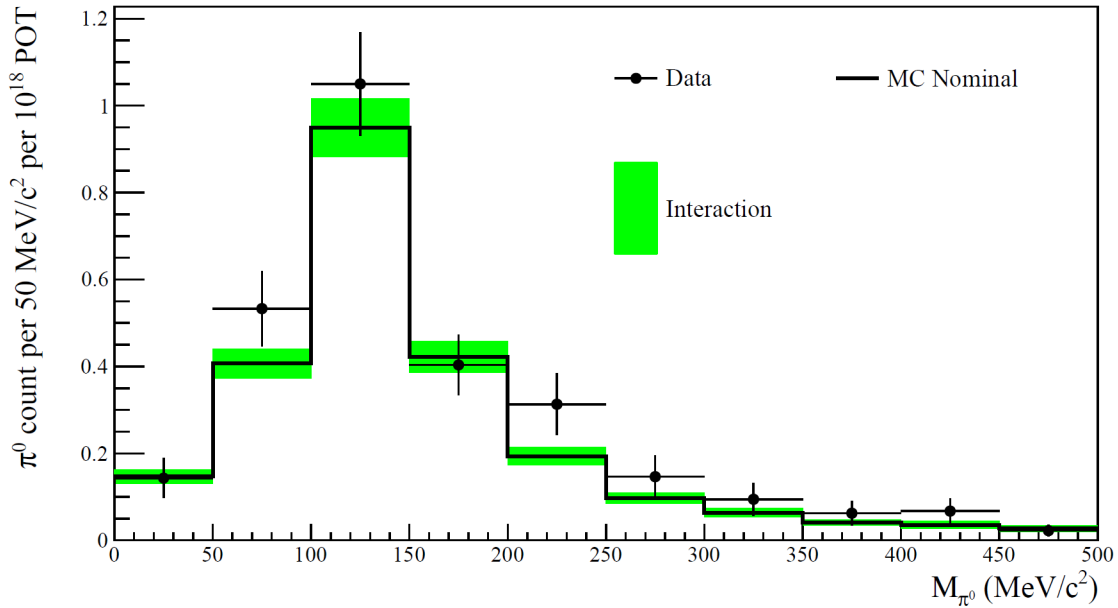


FIGURE 6.5: Reconstructed invariant mass distribution of  $\pi^0$  candidates passing the selection, scaled to  $55.19 \times 10^{19}$  P.O.T of RDP from T2K Runs 2-4. Compared with  $87.39 \times 10^{20}$  P.O.T of NEUT Monte Carlo from T2K Runs 2-4 Production 6B. Only the MC interaction source of error is shown, which corresponds to  $\pm 6.7\%$ .

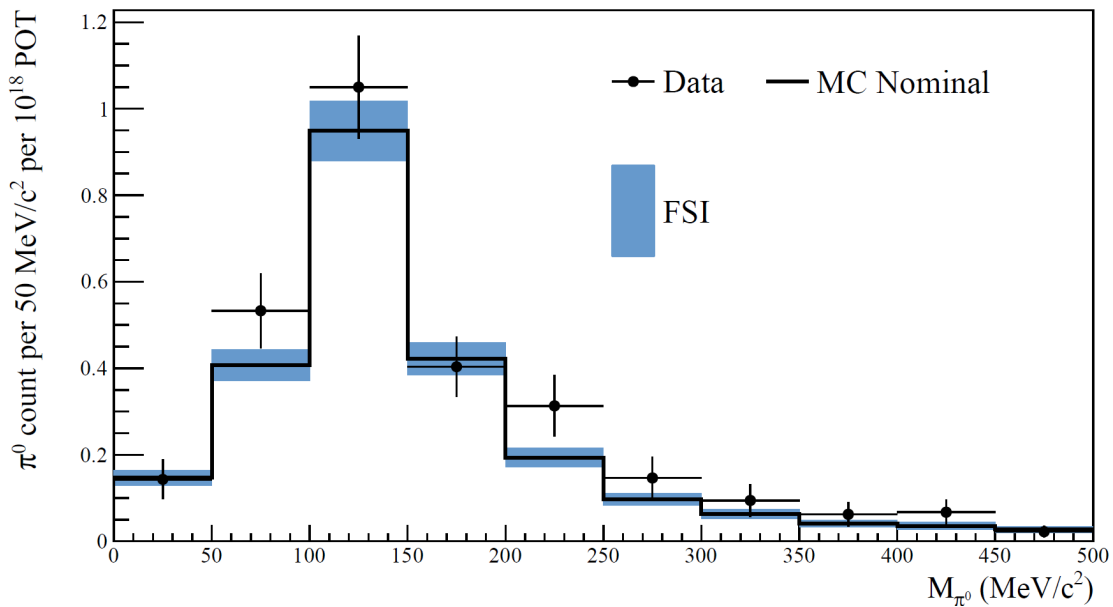


FIGURE 6.6: Reconstructed invariant mass distribution of  $\pi^0$  candidates passing the selection, scaled to  $55.19 \times 10^{19}$  P.O.T of RDP from T2K Runs 2-4. Compared with  $87.39 \times 10^{20}$  P.O.T of NEUT Monte Carlo from T2K Runs 2-4 Production 6B. Only the MC FSI source of error is shown, which corresponds to  $\pm 6.9\%$ .

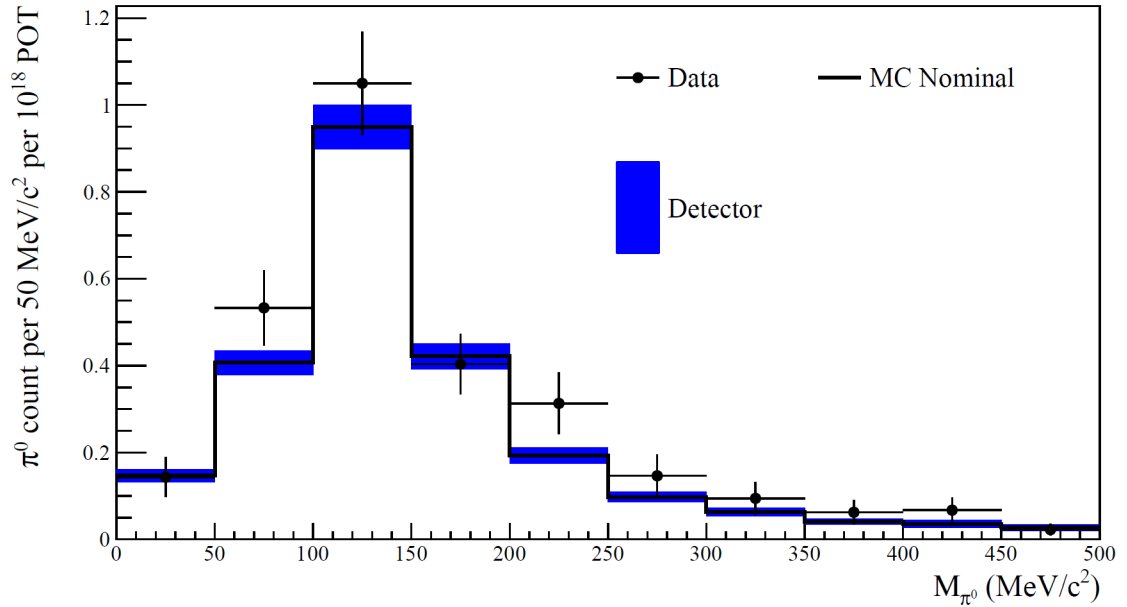


FIGURE 6.7: Reconstructed invariant mass distribution of  $\pi^0$  candidates passing the selection, scaled to  $55.19 \times 10^{19}$  P.O.T of RDP from T2K Runs 2-4. Compared with  $87.39 \times 10^{20}$  P.O.T of NEUT Monte Carlo from T2K Runs 2-4 Production 6B. Only the MC detector source of error is shown, which corresponds to  $\pm 5.1\%$ .

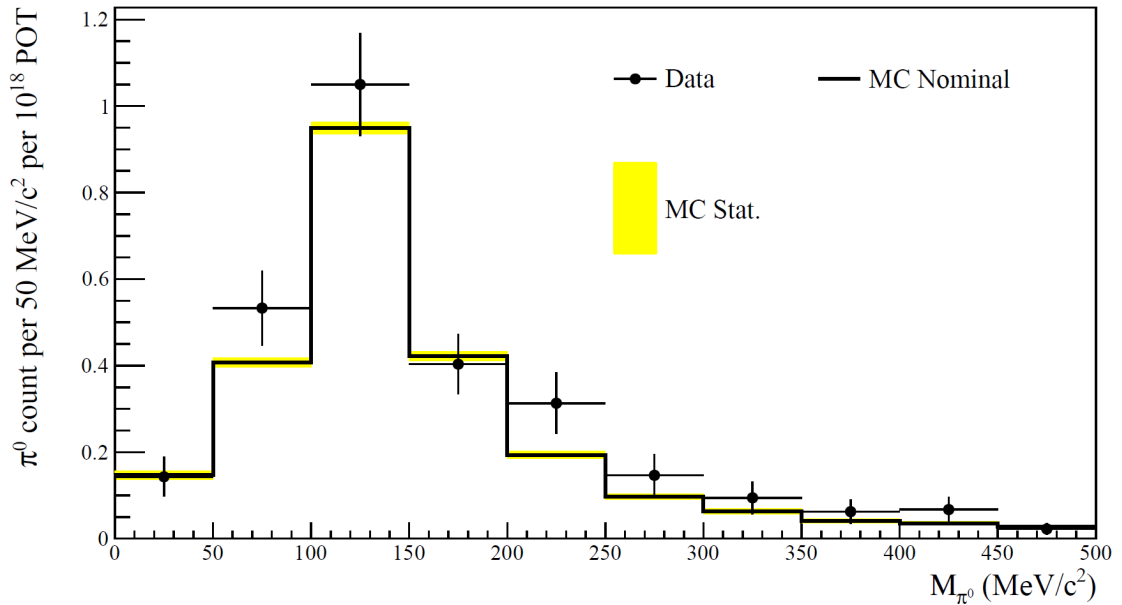


FIGURE 6.8: Reconstructed invariant mass distribution of  $\pi^0$  candidates passing the selection, scaled to  $55.19 \times 10^{19}$  P.O.T of RDP from T2K Runs 2-4. Compared with  $87.39 \times 10^{20}$  P.O.T of NEUT Monte Carlo from T2K Runs 2-4 Production 6B. Only the MC statistical source of error is shown, which corresponds to  $\pm 1.5\%$ .

### 6.2.2 $\pi^0$ Momentum

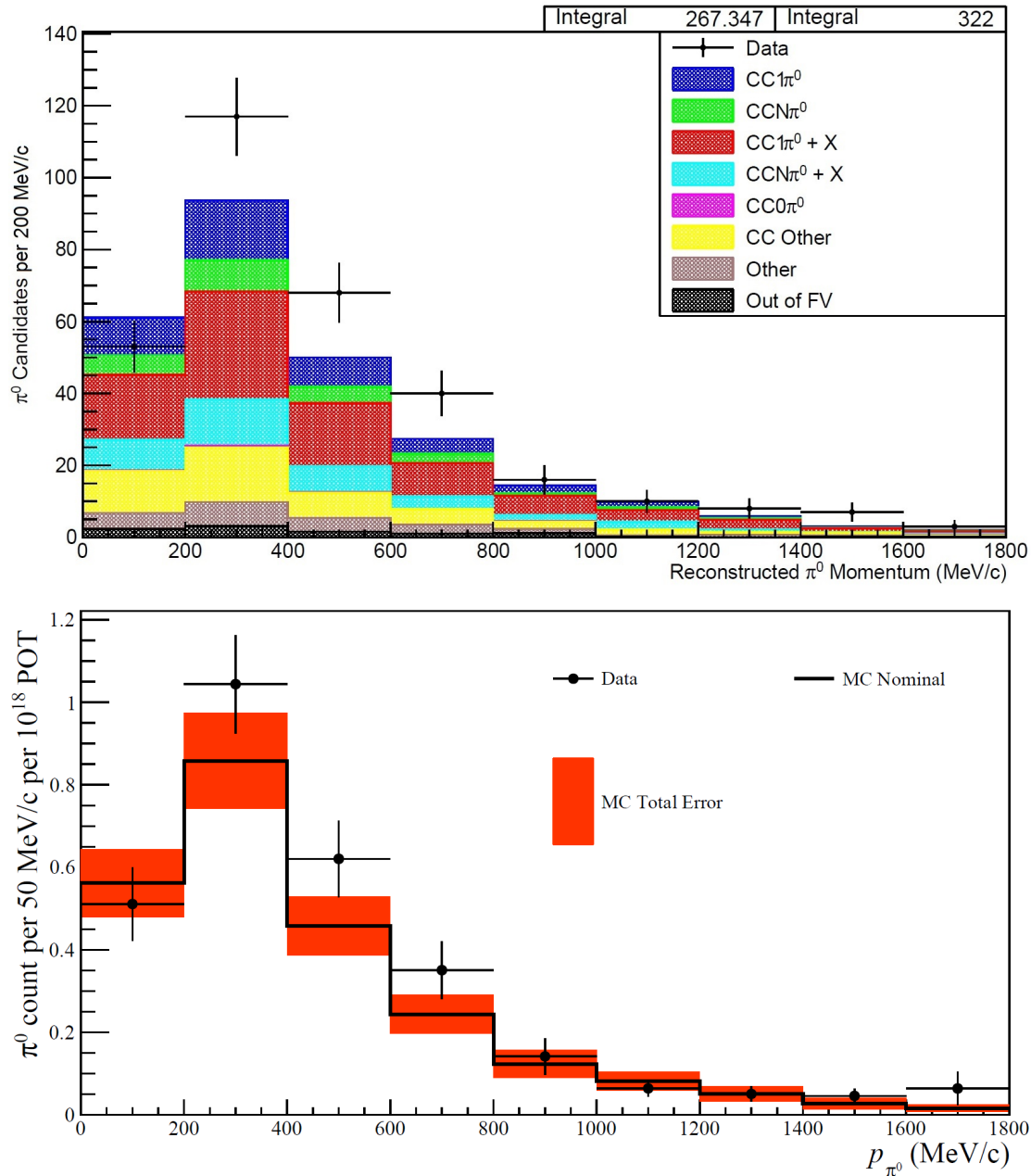


FIGURE 6.9: Reconstructed momentum distribution of  $\pi^0$  candidates passing the selection, scaled to  $55.19 \times 10^{19}$  P.O.T of RDP from T2K Runs 2-4. Compared with  $87.39 \times 10^{20}$  P.O.T of NEUT Monte Carlo from T2K Runs 2-4 Production 6B.

There have been few direct measurements (some at MiniBooNE [138] and Minerva [139]) of the momentum of neutral pions produced in charged-current neutrino interactions [90]. Comparisons of the distributions of this reconstructed quantity in data and Monte Carlo could provide insight into model discrepancies for general neutral pion production, as well as the specific  $\pi^0$  production modes which contribute in distinctive ways. In addition to measuring the overall rate at which certain interactions occur as a subset of charged-current interactions (i.e.  $CC\pi^0$  interactions), it is important to understand the mechanisms by which these specific interactions proceed. In terms of  $\pi^0$  production, the core modelled interactions are Resonant  $\pi^0$  Production and Deep Inelastic Scattering (DIS) (all via the charged-current channel).

In general in the NEUT model, the mode in which neutral pion production is achieved depends on the invariant mass of the hadronic system in its final state, as well as the pion multiplicity [100] [140]. The resonance mode for charged current  $\pi^0$  production occurs as :

$$\nu_\mu + n \rightarrow \mu^- + p + \pi^0 \quad (6.1)$$

Where  $\nu_\mu$  is a muon neutrino,  $\mu^-$  is a muon, n is a neutron, p is a proton, and  $\pi^0$  is a neutral pion.

This is for the case where one pion is produced and the invariant mass of the final system was  $< 2$  GeV and the Rein-Seghal model was used [140], which proceeds via a two-step process. Firstly the neutrino induced baryon resonance is modelled, secondly this resonance decays to the final state shown in Equation 6.1. An example of a model specification which can only be probed experimentally is the phenomenological parameter of single pion axial vector mass ( $M_A^{RES}$ ), which is set to 1.1 GeV/ $c^2$  in NEUT. As the value of  $M_A^{RES}$  increases, interactions with higher  $Q^2$  values, and consequently larger scattering angles, are enhanced<sup>3</sup>. This means that it is possible to use the kinematic distributions of neutral pion momentum and  $\pi^0 \cos(\theta)$ , taken w.r.t the neutrino beam direction, to probe information about the true value of  $M_A^{RES}$ . However,

<sup>3</sup>In  $\nu$ -nucleon scattering,  $Q^2$  is the four-momentum transfer between the leptonic and hadronic system.

without unfolding the reconstructed distribution to the actual kinematics (via means of inverting the detector response (discussed further in Chapter 7), it would be difficult to claim this effect as a direct result of  $M_A^{RES}$ . Perhaps the best way to assess this systematically would be to produce a range of samples each with a different value of  $M_A^{RES}$  and compare each with data to determine the most likely value. Alternatively MC produced using different neutrino generators (NEUT [100], GENIE [101], NuWro [102] etc), which each utilise a different value of  $M_A^{RES}$  could be used to determine which value provides a best fit to the data.

For the case of the production of  $\pi^0$ s in conjunction with another  $\pi^0$ , a charged pion or one of many mesons, the DIS model is used. This proceeds as :

$$\nu_\mu + n \rightarrow \mu^- + N' + \pi^0 + \pi \quad (6.2)$$

Where  $\nu_\mu$  is a muon neutrino,  $\mu^-$  is a muon, n is a neutron,  $N'$  is an excited baryon,  $\pi^0$  is a neutral pion, and  $\pi$  is a charged pion.

or

$$\nu_\mu + n \rightarrow \mu^- + N' + \pi^0 + X \quad (6.3)$$

Where  $\nu_\mu$  is a muon neutrino,  $\mu^-$  is a muon, n is a neutron,  $N'$  is an excited baryon,  $\pi^0$  is a neutral pion, and X is any meson or none.

All entries are for the same  $\pi^0$  candidates selected as depicted in the  $\pi^0$  Mass (Figure 6.3) and  $\pi^0 \cos(\theta)$  w.r.t the  $\nu_\mu$  beam direction (Figure 6.10) distributions (i.e. candidates closest to known  $\pi^0$  invariant mass). There appears to be reasonable agreement between the MC NEUT model and the data. There is mild tension in bins 2-4 in Figure 6.9, but this may disappear in the case where the analysis is run over a larger data set, as the statistical errors on data are large. The slight discrepancy in the final bin, which alters significantly due to the additional NIWG tuning, may be disregarded due to the extremely low statistics ( $O \sim 1$  event). However, this does raise the issue of the efficacy of that tuning in the low statistics regime. The mild data excess seems to be consistent,

---

implying a normalisation effect, possibly inherent in the MC or as some function of the event weighting inherent in the Highland2 systematics approach. For the Monte Carlo, detector, model and flux errors dominate, and in total these are similar in scale to the statistical errors for the data. Overall, all values show reasonable agreement, leading to the conclusion that data and MC agree. Quantitatively, the MC and Data agree within  $1.4 \sigma$ , assuming all relevant uncertainties associated with the MC.

### 6.2.3 $\pi^0 \cos(\theta)$ With Respect to $\nu_\mu$ Beam Direction

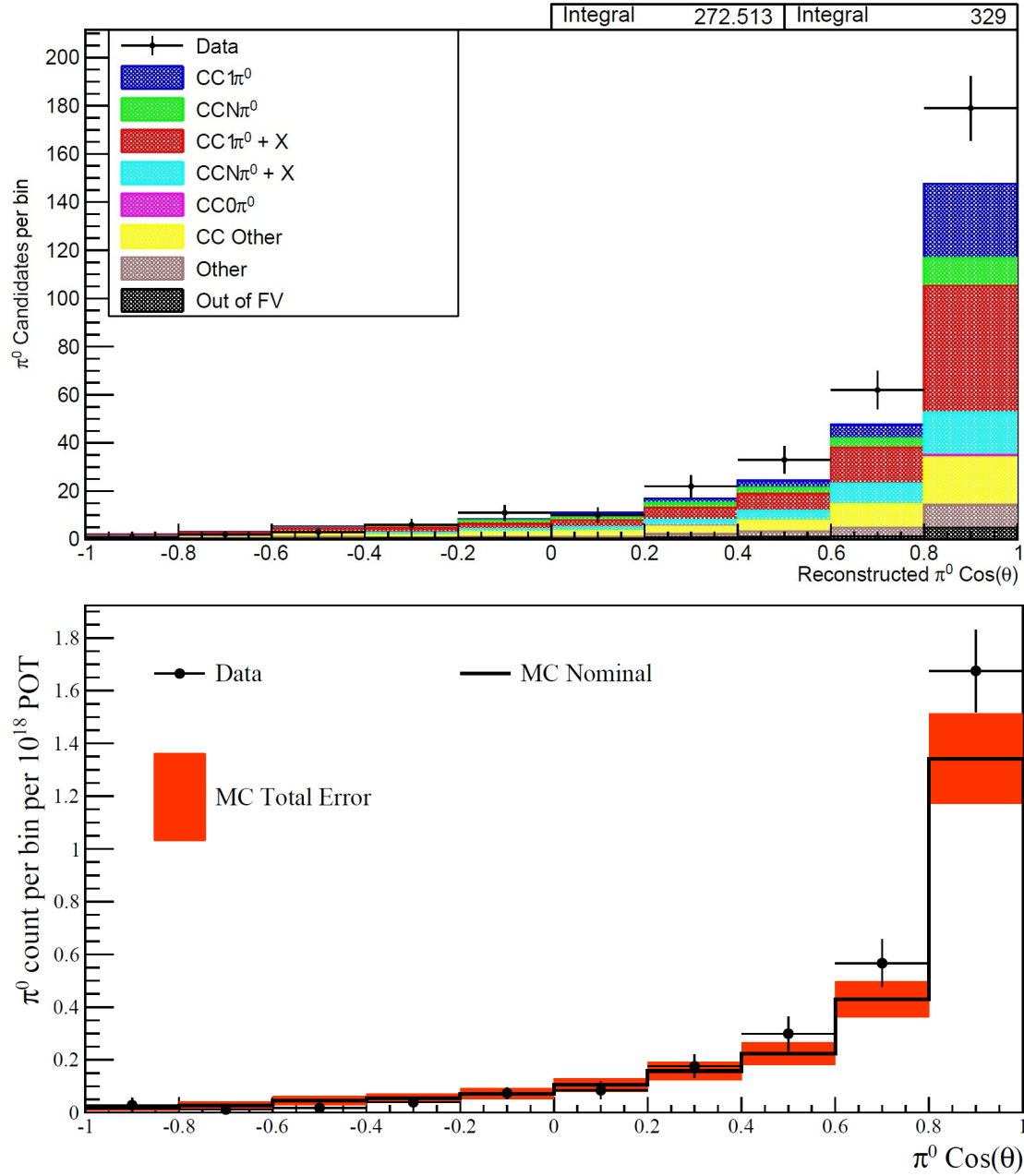


FIGURE 6.10: Reconstructed  $\cos(\theta)$  distribution of  $\pi^0$  candidates passing the selection, scaled to  $55.19 \times 10^{19}$  P.O.T of RDP from T2K Runs 2-4. Compared with  $87.39 \times 10^{20}$  P.O.T of NEUT Monte Carlo from T2K Runs 2-4 Production 6B.

As stated in Subsection 6.2.2, the MC model used can be probed for accuracy and precision by constructing distributions of kinematic regions of interest. In this case, the angle between the assumed neutrino beam direction, which is along the z-axis of the detector, and the resultant relative angle of the reconstructed  $\pi^0$  is plotted as a function of cosine. All entries are for the same  $\pi^0$  candidates selected as depicted in the  $\pi^0$  Mass (Figure 6.3) and  $\pi^0$  Momentum (Figure 6.9) distributions, i.e. closest to known  $\pi^0$  invariant mass.

Entries of  $\pi^0 \cos(\theta) < 0$  are candidates which have a reconstructed angle going back towards the beam origin. From the MC truth  $\pi^0$  reaction categorisation, we can see that these candidates are more likely to belong to ‘CCOther’ (events containing no  $\pi^0$ s) than the more forward going candidates ( $\sim 36\%$  background below zero,  $\sim 27\%$  background above zero). This provides a motivation to use  $\pi^0 \cos(\theta)$  in future analyses as a true  $\pi^0$  discriminator, although this would need confirmation for  $\pi^0$  objects as well as events. The legitimacy of focusing on only forward-going  $\pi^0$ s is further compounded by the fact that the ND280 and Highland2 is inherently biased to search for forward going objects. It would not be unfair to exclusively focus on  $\pi^0$  candidates both in MC truth and reconstruction, which have a  $\cos(\theta) > 0$  and a well-defined minimum momenta. These considerations fall into the realm of detector and analysis sensitivity, and are known as phase-space considerations, a facet of this analysis which could be investigated further in future work. However, great care would have to be taken to ensure that any such restriction did not favour one production mode over any other.

There is a mild data excess, particularly for the more forward-going candidates. In the case of an actual Data-MC discrepancy, this excess could be due to a tendency for the MC to produce more isotropic candidate, however more statistics are required to make this claim. This could be due to a prevalence of DIS produced  $\pi^0$ s over resonant production, or maybe even directly due to an overestimation of  $M_A$ , leading to interactions with higher  $Q^2$  values and therefore higher scattering angles.

By plotting the  $\pi^0 \cos(\theta)$  against  $\pi^0$  momentum in a two-dimensional plane, perhaps more useful comparisons can be made between the data and MC, which could

inform models and contribute to oscillation analyses. Two dimensional distributions were produced using MC and data for the events and candidates passing the selection for the following pairs of variables :  $\pi^0$  invariant mass vs  $\pi^0$  momentum,  $\pi^0 \cos(\theta)$  vs  $\pi^0$  momentum, and  $\mu^- \cos(\theta)$  vs  $\mu^-$  momentum. These distributions can be found in the appendix (Figures A.18 to A.23). A cursory visual analysis of these distributions does not provide any immediately obvious areas of discrepancy, although there are minor differences, which would likely be ameliorated by more statistics.

In Figure 6.10, the MC errors are dominated by detector and model systematics, which are overall similar in scale to the data statistical errors.

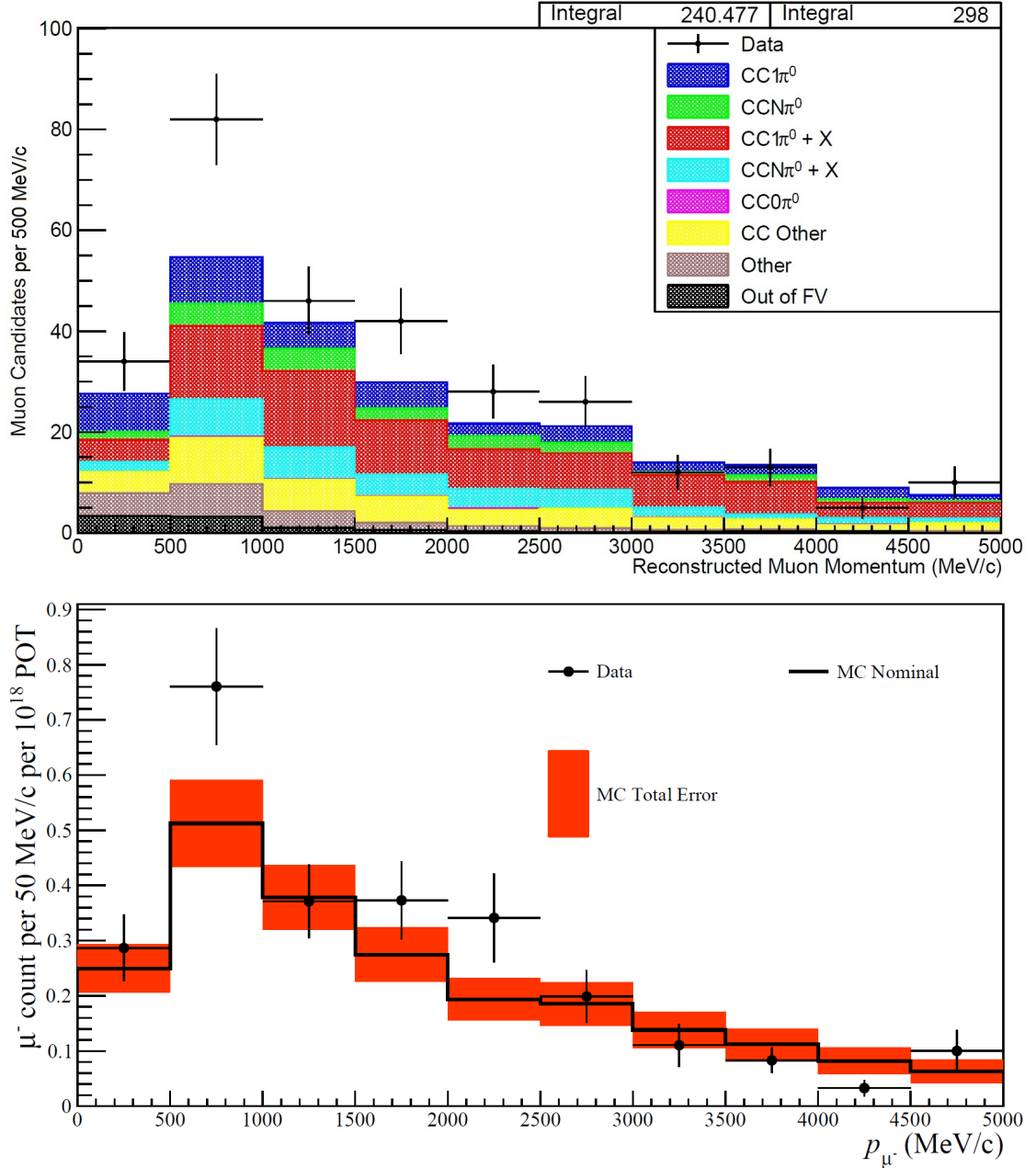
6.2.4  $\mu^-$  Candidate Momentum

FIGURE 6.11: Reconstructed momentum distribution of  $\mu^-$  candidates passing the selection, scaled to  $55.19 \times 10^{19}$  P.O.T of RDP from T2K Runs 2-4. Compared with  $87.39 \times 10^{20}$  P.O.T of NEUT Monte Carlo from T2K Runs 2-4 Production 6B.

The distribution in Figure 6.11 shows the momentum distribution for the muon candidate for events passing the selection. These are predominantly charged-current events, with minor contributions from ‘Other’ and ‘Out of FV’ interactions, which overall produced a  $\pi^0$  ( $\sim 72\%$  of the time). There is agreement within errors between data and MC for this variable, with three exceptions in the 2nd, 5th and 9th bins. In general for normally distributed data, we would expect to see 68.7% agreement within one standard deviation, which does hold for this variable. It would certainly be worthwhile to compare this distribution to others from similar analyses, and to the reconstructed muon momentum distribution for this analysis, in the case where only the initial stages i.e. selecting any charged-current event, have been passed. Further to this, and running with more statistics, it would be prudent to assess the results of the selection at each accumulation level, in order to determine if a particular cut is responsible for the departure of the data from MC. The MC errors are dominated by MC mode, flux and detector, and are similar in scale to the data statistical errors.

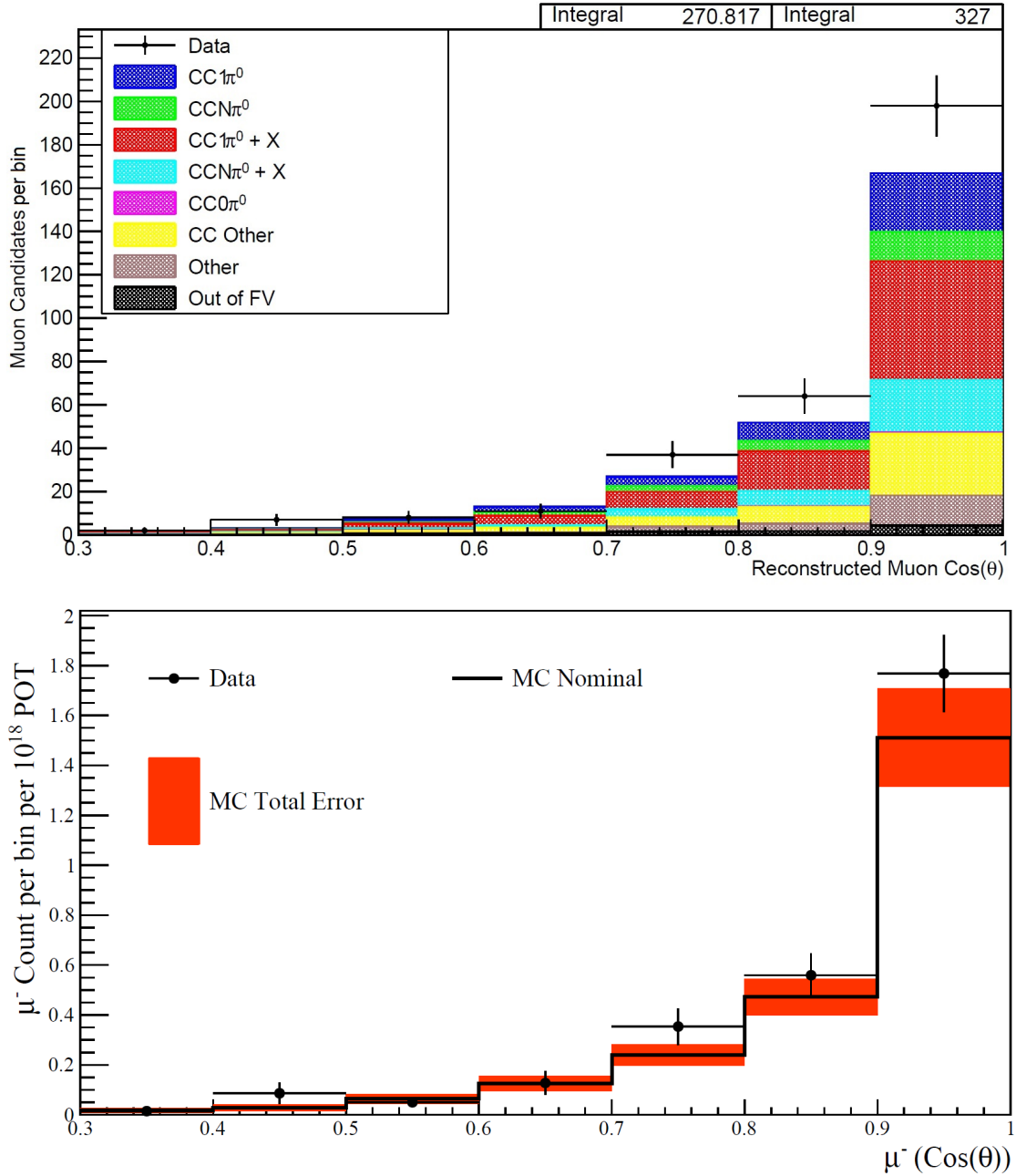
6.2.5  $\mu^- \cos(\theta)$  With Respect to  $\nu_\mu$  Beam Direction

FIGURE 6.12: Reconstructed  $\cos(\theta)$  distribution of  $\mu^-$  candidates passing the selection, scaled to  $55.19 \times 10^{19}$  P.O.T of RDP from T2K Runs 2-4. Compared with  $87.39 \times 10^{20}$  P.O.T of NEUT Monte Carlo from T2K Runs 2-4 Production 6B.

The distribution in Figure 6.12 shows the angle between the reconstructed muon candidate, which is indicative of a  $\nu_\mu$  charged-current induced event, and the neutrino beam direction, presented as a function of cosine<sup>4</sup>. There is good agreement between MC and data, both in shape and scale, with a fairly consistent very mild data excess for the most forward going muons. As with the  $\pi^0$  kinematics, plotting the  $\mu^- \cos(\theta)$  against  $\mu^-$  momentum in a two-dimensional plane may provide useful comparisons between the data and MC, which could inform models. The MC errors are dominated by model, flux and detector systematics, and are similar in scale to the real data statistical errors.

---

<sup>4</sup>There were no events for both MC and data of  $\mu^- \cos(\theta) < 0.3$ , hence the curtailed range. This is due to the preferential selection of events containing forward going muon candidates

### 6.3 Summary of Results

Analysis of a Monte Carlo data set equivalent to  $87.39 \times 10^{20}$  P.O.T, yields an event selection efficiency of  $3.2\% \pm 0.1\%$  and a  $CC\pi^0 + X$  event purity of  $71.7\% \pm 0.7\%$ . These values and errors are directly obtained from the T2K analysis software framework, Highland2. The total number of MC events passing the selection for the RDP equivalent P.O.T of  $55.19 \times 10^{19}$  P.O.T, which contain a  $\pi^0$  candidate with invariant mass of 0 MeV/c<sup>2</sup> to 500 MeV/c<sup>2</sup> is 262.1. The number of data events for the same P.O.T and containing an equivalent  $\pi^0$  candidate is 316. Systematic errors calculated using methods described in Chapter 5, are given for this analysis in Table 6.2 and Table 6.3.

Source of Error	Size (%)
RDP Statistical	$\pm 5.6$

TABLE 6.2: The statistical error for the real data production is shown here. This is comparable to the Monte Carlo errors, and can be mitigated in future by the use of more data.

Source of Error	Size (%)
MC FSI	$\pm 6.9$
MC Interaction	$\pm 6.7$
MC Flux	$\pm 5.8$
MC Detector	$\pm 5.1$
MC Statistical	$\pm 1.5$
Total MC Error	$\pm 12.5$

TABLE 6.3: All sources of systematic error which affect the NEUT Monte Carlo are shown. These are separated into five major sources, with comparable contributions from all stated sources aside from MC statistical.

The number of MC events passing the selection can then be stated as  $262.1 \pm 32.8$ , with the number of RDP events being  $316 \pm 17.8$ . This illustrates that the data and MC are in very slight tension, however this is well within  $2\sigma$  and should not be considered as proof any model discrepancy. This result can be quoted as a data/MC ratio of :

- $1.21 \pm 0.07$  (Data Statistical)  $\pm 0.15$  (Total MC Error)

Previous work for all conversion topologies has showed a 10% excess of data events over MC [141].

This chapter has presented an overview of several reconstructed kinematic quantities for events passing the described selection. These serve to illustrate general agreement with the NEUT T2K Production 6B Monte Carlo used [142], with minor discrepancies in some specific areas. In order to present any of these distributions in terms of the underlying interaction cross-section probability, it would be necessary to disentangle the detector effects from the reconstructed quantities by using an inversion of a constructed detector response matrix. This was beyond the scope of this first generation analysis in terms of time available, but certainly provides a valuable goal to attain for future work. Additionally, reconstructing the incident neutrino energy for charged-current interactions resulting in inclusive  $\pi^0$  production would be a worthwhile focus.

## Chapter 7

# Conclusions and Future Work

This thesis has described a first generation Tracker + ECal  $\nu_\mu$  Charged Current  $\pi^0$  analysis. The analysis was carried out using a bespoke T2K ND280 analysis package, highland2, with several major contributions made by the author, to this and potential future  $\pi^0$  analyses. In this chapter, conclusions will be drawn and areas of future work is highlighted.

### 7.1 Future Work

This first generation analysis has nonetheless utilised a multitude of pre-existing useful tools, designed and implemented by previous and present contributors to T2K. This analysis can be described as first generation due to the comprehensive  $CC\pi^0$  package being built anew in its entirety in the developing highland2 analysis framework, and the fact that it focuses explicitly on the Tracker + ECal  $\pi^0$  conversions. A significant amount of time was spent in the development and optimisation of this package, which will be used for future analyses. A description of potential improvements and future work are now presented, for the benefit of completeness and as a road-map for other analysts.

#### 7.1.1 Completion of a full branched analysis

There are three potential avenues of conversion for the decay photons of a  $\pi^0$  in the ND280, as described in 4.2.1. Prior to this analysis, splitting a  $\pi^0$  analysis into multiple

sub-detector driven branches in order to investigate potential phase space differences in  $\pi^0$  conversion had been only considered in the work of Dr. Matt Lawe's thesis [126], which focused on ECal + ECal  $\pi^0$  conversions. Learning from these specific topologies, both individually and in combination was the driving force which led to the development of the highland2 framework which contains the described Tracker + ECal  $\pi^0$  analysis. This framework now houses the ECal + ECal branch, which was migrated into highland2 and improved from its original state (an early version of the original highland), the completed Tracker + ECal branch (developed by the author), and the unfinished Tracker + Tracker branch.

One of the great benefits of using this framework for future  $\pi^0$  analyses is the modular nature of the selections and general structure of highland2. In real terms this means that the Tracker + ECal analysis benefits from particular selection actions designed for the ECal + ECal branch, which provide early identification of isolated ECal objects in an event. More extensive than this, almost all of the selection actions and cuts designed for the Tracker + ECal branch can be used interchangeably with the Tracker + Tracker branch. This would require arrangement of the necessary actions and cuts into an explicit Tracker + Tracker branch, which would then be followed when specific event conditions (i.e. simplistically, multiplicity of tracks and isolated ECal objects in an event) are fulfilled. Additionally, a cycle of optimisation would need to be completed for the specific photon conversion topology, and parameters added in to represent that branch.

In order to ensure that all three branches could be run simultaneously over the same event, an intelligent determination of the branch (or multiple branches in the case of multiple  $\pi^0$ s) in which an event and  $\pi^0$  candidate should be placed, needs to be undertaken. This has been naively presented using mutually exclusive conditions but could possibly be better accomplished by following all branches simultaneously and implementing a retrospective Multivariate Analysis (MVA) which could determine the likelihood of each built candidate belonging to a given branch. Of course, care must be taken to ensure that no  $\pi^0$  candidate remains in more than one branch, being double counted. Once this is completed, a full comparison of each conversion phase space

could be made with a total  $\pi^0$  phase space measurement, possibly revealing interesting physics, model information or detector bias.

### 7.1.2 Moving Towards Modular $\pi^0$ Analyses

As stated in the previous section, many of the actions, cuts and systematic error methods which form a  $\pi^0$  analysis for T2K in the highland2 framework, are in fact small modular platform-specific classes which can be reused in other physics analyses. These would be especially useful for their intended purpose of identifying  $\pi^0$  candidates and also for vetoing  $\pi^0$ s in certain event topologies. In regards to this usefulness, the C++/Highland2 code is fully committed to a shared T2K repository, which is accessible to all members of the experiment. It would be beneficial for a future analyst to develop a broad purpose, well-documented  $\pi^0$  analysis framework by extending the current one and adding further functionality. This would give other analysts direct and easy access to pre-existing coded functions, actions and cuts which have been well-tested and understood, thus reducing repetition of effort and allowing more specific analyses to be carried out, without reinventing the wheel. Alongside this, prescribed optimisation algorithm scripts should be made available, which generically solve optimisation problems for at least one and two-dimensional restrictions. Highland2 has provided the majority of the work towards this goal, which would be suited to an incoming T2K PhD student, who could then benefit directly from their construction in producing a specific analysis.

### 7.1.3 Combinatorics and MVAs

A key issue which emerged throughout the development of this analysis was that of combinatorics, and the resultant high multiplicity of potential  $\pi^0$  candidates. Best efforts were made to limit the number of objects built and thus select true  $\pi^0$  events by imposing a series of cuts on reconstructed event variables, such that only  $\pi^0$ -like objects survived the selection. This linear approach was effective at limiting the objects and certainly at selecting  $\pi^0$  events, nonetheless a choice remained to be made in

the final stages of the selection in order to choose the most-likely  $\pi^0$  candidate built. In this analysis a number of metrics were developed, none of which seemed to radically improve the probability of picking the correct  $\pi^0$  from those built. With respect to this, a Multivariate Analysis (MVA) should be constructed for the intended combined three-branched analysis, which keeps track of all possible relevant properties of the constituents of built  $\pi^0$  candidates, and defines a likelihood ranking system for the consequent products based on combinations of these properties. Additionally, this MVA need not be limited by the analyst's decisions (and time) on what would constitute an effective ranking system or even what constitutes relevant input to this metric, if a machine learning approach is used. Machine learning techniques are now being investigated globally in physics analyses and event reconstruction and triggers, and are proven to be effective and efficient [143].

#### 7.1.4 Running with more data

*“ ‘Data! data! data!’ he cried impatiently. ‘I can’t make bricks without clay.’ ”*

*- Arthur Conan Doyle, The Adventure of the Copper Beeches*

As with any experiment, the more data collected, the better the precision of the result. As stated in Table 4.2, the equivalent of  $55.19 \times 10^{19}$  P.O.T was used for this analysis. At the time of writing, the T2K experiment has produced  $14.93 \times 10^{20}$  P.O.T equivalent of  $\nu_\mu$  data, a process which has taken  $\sim 7$  years to accomplish. Using only the data currently available would result in a multiplicative improvement of  $\sim 2.6$ , resulting in lower statistical errors and allowing anomalous features to be ruled out or investigated further. Beyond this, proposals for T2K's future operation request an extended run to  $20^{21}$  [67] (and higher in the long term), which assuming half  $\nu_\mu$ -running and half  $\bar{\nu}_\mu$ -running, would result in a improvement in statistical errors for this analysis of  $\sim \times 17.9$ . Alongside this analysis, this increased P.O.T would be highly beneficial for many other T2K key analyses in myriad areas, including : CP Violation, Mass Hierarchy, the size and octant of  $\theta_{23}$ , and whether a 3-flavour mixing model really does fit the data [67].

### 7.1.5 Run Analysis on $\bar{\nu}_\mu$ Data

- Arthur Conan Doyle, *The Adventure of the Copper Breeches*

“Data! data! data!, he cried impatiently. I can’t make bricks without clay.”

Since the T2K experiment has been running in  $\bar{\nu}_\mu$ -mode for an appreciable amount of time in recent years (illustrated in Figure 2.2). It would be a waste if running this analysis using anti-neutrino MC and Data was not considered. The total P.O.T for normal mode neutrinos used in this analysis was  $55.19 \times 10^{19}$  P.O.T (although much more is available now). The total  $\bar{\nu}_\mu$ -mode P.O.T currently available is  $7.62 \times 10^{20}$  P.O.T, which is approximately 7.6 times more normal mode P.O.T than was used in this analysis, a testament to the hard work and dedication of the beam group in achieving this feat in recent years.

As stated in Chapter 2, T2K has made large strides to exposing CP Violation in the lepton sector by comparison of  $\nu_e$  and  $\bar{\nu}_e$  appearance due to differences in neutrino oscillation for anti-matter. Probing other avenues of matter/anti-matter asymmetry could be done by analysing events containing interactions producing third party particles, such as  $\pi^0$ s, induced by both  $\nu_\mu$  and  $\bar{\nu}_\mu$  and comparing the two. Naively, this could hypothetically be achieved with relative ease by utilising the existing selection and simply replacing the pre-selection block (which is currently the standard highland2 T2K  $\nu_\mu$ CC even selection) with the standardised  $\bar{\nu}_\mu$ CC selection. Of course, in addition to this, the selection would require re-optimisation and a new assessment of backgrounds. This approach could potentially provide some very interesting comparisons of  $\pi^0$  production rate and kinematic properties for  $\nu_\mu$ -mode and  $\bar{\nu}_\mu$ -mode MC and data. Further to this, the results of such an analysis could be compared with another independently developed  $\bar{\nu}_\mu$ CC $\pi^0$  analysis, which is presently being built [144].

### 7.1.6 Improved Detector Reconstruction

In conjunction with utilising more beam data, comes the benefit of improvements to the Monte Carlo and analysis tools, which have been added over time. The analysis

described in this work used the equivalent of  $87.39 \times 10^{20}$  simulated P.O.T, which was split into Run's 2-4. At this point, run periods 5-7 have been completed and run 8 is well underway. The MC production used for this work was 6B, whereas the current MC version exceeds production 7, and significant improvements to Highland2 have been made. Regarding improvements to the MC, this analysis would particularly benefit from improvements to the low energy reconstruction of  $e^+/e^-$  tracks in the tracker region, and electromagnetic showers in the ECals. The mis-mapping work described in Chapter 3 will help in this regard, and other techniques such as the integration of improved ECal reconstruction techniques will contribute to better recognition of  $\pi^0$  events and (possibly) more importantly, better reconstruction of good  $\pi^0$  objects. Specifically, the identification and reconstruction of 'soft' gammas in asymmetric  $\pi^0$  decays will be improved, which will ultimately lead to better event/object identification and improved reconstruction of kinematic variables, i.e a more accurate and precise  $\pi^0$  candidate mass peak (less smearing).

### 7.1.7 Improved Truth Matching

In order to build an accurate analysis, the complex information from the Monte Carlo needs to be accessed and understood properly. The truth matching in this analysis was sufficient, although it certainly could be improved. On the event level, the truth matching 100% accurate in terms of extracting the information from the NEUT Monte Carlo. This means that the simple event category delineation which has been used throughout this work (and for the highland2 style results plots in Chapter 6), which was determined by the multiplicity of all particles produced at the neutrino interaction vertex, is flawless. However, this category is determined by counting all  $\pi^0$ s produced and not all those which have resultant conversions in the chosen Tracker + ECal topology. A specific category system (used for both drawing and signal optimisation) could be designed to track the final positions of each of the  $\pi^0$  decay objects, but given the number of potential re-scatters this could be complex. Ultimately this may not be necessary,

given that the end goal of a combined measurement would require only the existing event truth information.

Additionally, one emerging theme of this analysis was that the candidate  $\pi^0$  construction was being partially neglected (in that the focus was on event type identification over object). The combinatoric side to this has been well-documented, whereas the object truth matching has not been discussed. The basics of the truth matching ensure that the constituent parts of the  $\pi^0$ s built, are of the correct PDG code (i.e. electron, positron or photon), and whose primary particle was a  $\pi^0$ . These two conditions are checked by using built-in `oaAnalysis` functionality, which is very useful. However, this method does not give us any information about the generation to which this constituent belongs, i.e. is an electron candidate a direct daughter of a decay photon or has it been scattered? This effect could be minor in the case of a small number of scatters or electromagnetic conversions, but for far removed constituents this could form a major issue in terms of skewing reconstructed (in the MC) quantities with respect to the data. Essentially, a comparison could be made of  $\pi^0$  conversions where all constituents have very few scatters, and those which have many. Cleaner signals may provide better defined distributions for the reconstructed kinematic variables for events passing the selection. This process could be potentially achieved by use of a recursive class which iterates over constituents and their parents until reaching the primary particle, all the while counting the levels through which it has ascended.

### 7.1.8 More detailed assessment of systematic errors

This analysis benefits strongly from the pre-existing systematic error classes and event weight propagation which is inherent in `highland2`. Fairly recent additions to this framework have even included classes which determine ECal reconstruction errors (ECal Energy, ECal PID etc), which removed the necessity of designing new, analysis-specific error classes. However, it is possible that not all sources of detector error were fully taken into account, especially in terms of the amalgam objects which form a large

proportion of this analysis. This may not be a large issue if the errors on the more fundamental objects were propagated correctly, nonetheless re-running the analysis in a newer more sophisticated version of highland2 alone, may yield improvements. If not, the larger task of designing new systematic error classes which specifically pertain to quantities only considered in this analysis should be undertaken. Additionally, a more comprehensive study should be done to confirm whether the statistical boon of utilizing decay photon candidates which convert fully in FGD1 is outweighed by the large associated systematic error in this regime.

### 7.1.9 Cross-section Measurement

Ultimately, the major goal of many analyses is to determine the interaction cross-section (i.e. the rate at which an interaction occurs) for a specific signal. In this case that would be to measure directly the rate at which  $\pi^0$ s are produced in charged-current events, induced by a muon neutrino. The first stage in accomplishing this would be to make a measurement combining the three-branched selection, as mentioned above. This would allow for a measurement of the total  $\pi^0$  production cross-section (with the benefit of being able to analyse the individual contributions). The second barrier to producing a valid cross-section is to accurately build good  $\pi^0$  objects, a topic which has been discussed at length in this thesis. Having a good event purity and object purity will mitigate the need for dangerous model dependent corrections when constructing a cross-section, and help to improve the accuracy of any differential cross-section (binned in useful kinematic variables). Additionally, limitations may need to be set on the phase space of the signal and selection, which will then proliferate through to the cross-section measurement. Discussions with other analysts and decisions made in previous  $\pi^0$  analyses [141], indicate that four restrictions of signal phase space would be effective in ensuring that there is minimal dependence on the neutrino-nucleus scattering model used in the MC. These restrictions need to be further validated but are naively : applying both a minimum momenta and a  $\cos(\theta)$  cut (to ensure that they are forward going) to

both the  $\mu^-$  and  $\pi^0$  candidates. Further acceptance concerns are regarding the identification efficiency of  $\gamma$ s and  $e^+/e^-$ , and are also addressed in other sections of this chapter (specifically the detector and MC improvements outlined in Subsection 7.1.6).

The major difficulty in producing a model independent cross-section is that of ‘unfolding’ or ‘de-convoluting’ to real physics from the measured case, which is essentially real physics  $\times$  detector response. This can hypothetically be achieved by effectively modelling the detector response as a ‘smearing matrix’ and inverting this to create an ‘unfolding matrix’ which allows de-convolution of measured data to real physics. Accurately building the entries of this matrix can be a very complex process, but can possibly best be achieved by a thorough comparison of various reconstructed quantities in multiple neutrino generators (GENIE, NEUT, NuWro) with data, leading to a reasonable interpretation of the actual detector response. Once this unfolding matrix is constructed, it would be required to use T2K’s bespoke software, ‘XSTools’ [145] to produce a cross-section, binned in a useful variable, to be considered at the time. XSTools provides a similar functionality to other software used throughout this analysis (such as the bespoke software used for the generation of the error bands and Highland2 detector systematic toys), by applying the inverted smearing matrix to the data for many systematic throws. Additionally, some background subtraction may be necessary, which gives even more credence to a high purity event selection with well-understood  $\pi^0$  candidates. Due to this high purity (and proportional low efficiency), more MC and data will also be required in order to make a reasonable cross-section measurement, but this has been discussed in an Subsection 7.1.4.

#### 7.1.10 Including FGD2

When the ND280 detector was designed, it was in a such a way that many interesting physics measurements could potentially be made, using a varied suite of sub-detectors. One of which is the PØD, designed to specifically detect  $\pi^0$ s, but which unfortunately

is not very effective at identifying charged-current  $\nu_\mu$  events, and is therefore commonly used as an upstream activity veto. Uncertainties in nuclear models play a significant role in the measurement of a neutrino-nucleus interaction, therefore it is important to have measurements conducted on different target materials. The PØD was designed with an optional Water In/Water Out functionality which would allow for cross-sectional measurements on both of these nuclear mediums. However, as this is not usable in a charged-current analysis, it is fortunate that a similar design was built into the FGDs, where FGD1 is composed solely of alternating scintillator bars and FGD2 additionally contains 6 water modules. FGD2 is partially composed of water because the detector at Super-Kamiokande is water-based, but as a consequence, cross-section measurements on carbon and on water can be determined from a comparison of neutrino interactions in the two FGDs.

The selection developed and described in this work could be altered to run on either FGD or both, due to a parameter driven functionality in highland2. However, before any useful information could be gained from such comparisons, there would need to be significant alterations and additions to the analysis in order to allow the more general use of the existing actions and cuts. It would be a useful task for a future analyst to undertake, especially in the case where the existing framework is modularised and used generically in  $\pi^0$  analyses going forward.

### 7.1.11 Run Analysis Using Multiple Neutrino Generators

A very direct way of determining the physics cause of discrepancies between Data and MC, is to re-run an analysis using Monte Carlo generated from a different source. There exist a number of credible neutrino generators which could be used for this task (among them GENIE, NEUT and NuWro), which use variations of different generally accepted physics models. Highland uses a homogenised MC input format (minitree) which can be produced using input from multiple generator formats, such that running the analysis over GENIE MC at least, would not be prohibitively difficult.

## 7.2 Conclusions

The results shown in Chapter 6 illustrate good agreement between the NEUT T2K production 6B Monte Carlo and T2K real data production (RDP) Rruns 2-4 (See Tables 4.1 and 4.2). Presented as a function of several kinematic variables, qualities of the MC which are model dependent have been probed, with data and MC agreeing within one standard deviation. Any discrepancies which are present in these distributions may be due to statistical fluctuation, and this analysis would certainly benefit from more data.

Regarding the Tracker + ECal branch conversions which were the specific focus of this analysis, there seems to be broad agreement, approaching a mild data excess. Previous work in the ECal + ECal topology regime [126], yielded data-MC agreement in all but one specific topology, FGD1 Barrel + Barrel photon conversions, which illustrated a significant data excess. Previous work which focused on all CC inclusive  $\pi^0$ s produced (i.e. in any topology), found that there was a data excess in events of  $\sim 10\%$  [141], which would be in-keeping with the result of this analysis. An analysis completed in the established Highland2 framework, focusing explicitly on the Tracker + Tracker  $\pi^0$  conversions would provide a useful comparison to the other topology specific analyses and an overall CC $\pi^0$  production measurement.

As stated in Section 7.1, in addition to running with more data, there is lots of potential for future work for this analysis, which will help to improve its accuracy and precision. A solid foundation has been laid for a next generation analysis which will yield a cross-section result.



## Appendix A

# Appendix

TABLE A.1: Selection Optimisation Results - Figure Of Merit : Efficiency  
× Purity

Selection Cut	Optimised Range	Units	Efficiency	Purity
Number of FGD1 + TPC Tracks	2 to 8	None	75.6%	27.0%
Number of Isolated ECal Objects	2 to 6	None	35.9%	84.8%
FGD Track Pion Pull	-30 to -1.5	None	82.8%	54.8%
FGD1 + TPC Track Momentum	0 to 362.5	MeV/c	64.1%	49.8%
ECal DPC Energy	0 to 2750	MeV	100%	18.6%
ECal DPC MIPEM	-18 to 58	None	98.4%	57.1%
ECal DPC Collinearity	-0.74 to 1.0	None	99.9%	18.6%
ECal DPC Muon Distance	0 to 3920	mm	100%	18.5%
Tracker DPC Muon Distance	0 to 477.5	mm	99.8%	16.7%
Tracker DPC Pair Separation	0 to 490	mm	99.8%	15.7%
Tracker DPC Pair Invariant Mass	0 to 470	MeV/c <sup>2</sup>	96.8%	15.3%
Tracker DPC Collinearity	-1.0 to 1.0	None	100%	16.5%
Number of Tracker + ECal $\pi^0$ Candidates	0 to 5	None	100%	14.8%

TABLE A.2: Selection Second Optimisation Results - Figure Of Merit :  
Efficiency  $\times$  Purity

Selection Cut	Optimised Range	Units	Efficiency	Purity
Number of FGD1 + TPC Tracks	2 to 6	None	75.0%	27.4%
Number of Isolated ECal Objects	2 to 6	None	86.5%	35.5%
FGD Track Pion Pull	-29 to -2	None	93.4%	61.5%
ECal DPC Energy	0 to 2750	MeV	100%	20.1%
ECal DPC MIPeM	-7 to 50	None	98.5%	61.4%
ECal DPC Collinearity	-0.66 to 1.0	$\cos(\theta)$	100%	20.1%
ECal DPC Muon Distance	0 to 3560	mm	99.8%	20.1%
Tracker DPC Muon Distance	100 to 340	mm	100%	61.2%
Tracker DPC Pair Separation	0 to 215	mm	92.7%	58.0%
Tracker DPC Pair Invariant Mass	0 to 230	MeV/ $c^2$	100.0%	53.2%
Tracker DPC Collinearity	0.942 to 1.0	$\cos(\theta)$	97.5%	63.2%
Number of Tracker + ECal $\pi^0$ Candidates	0 to 5	None	100%	15.8%

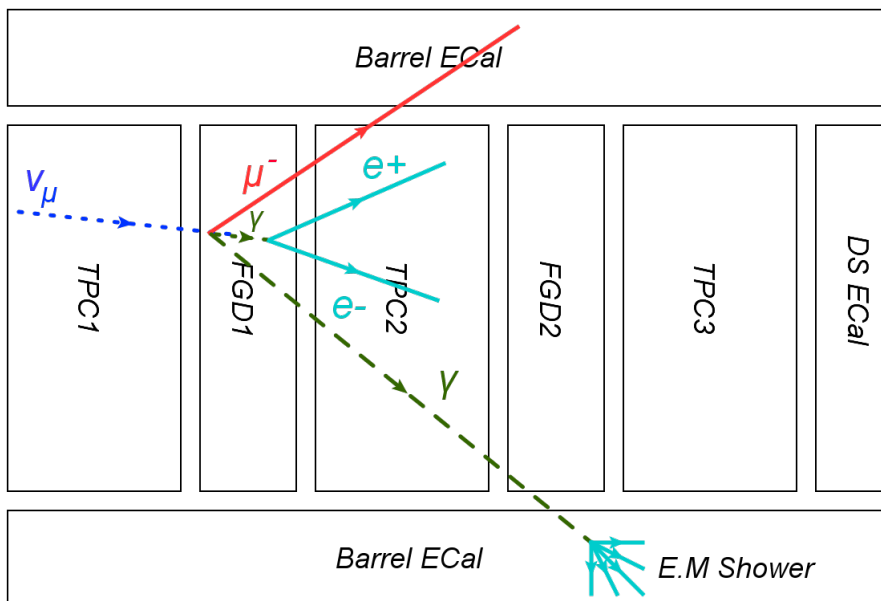


FIGURE A.1: This represents the ideal circumstance for a ND280 Tracker+ECal  $\pi^0$  conversion, where there is a clear TPC Pair which forms a pair. These tracks may have FGD and TPC components, but it is possible that the photon has entirely converted in the TPC, thus giving the tracks only TPC components.

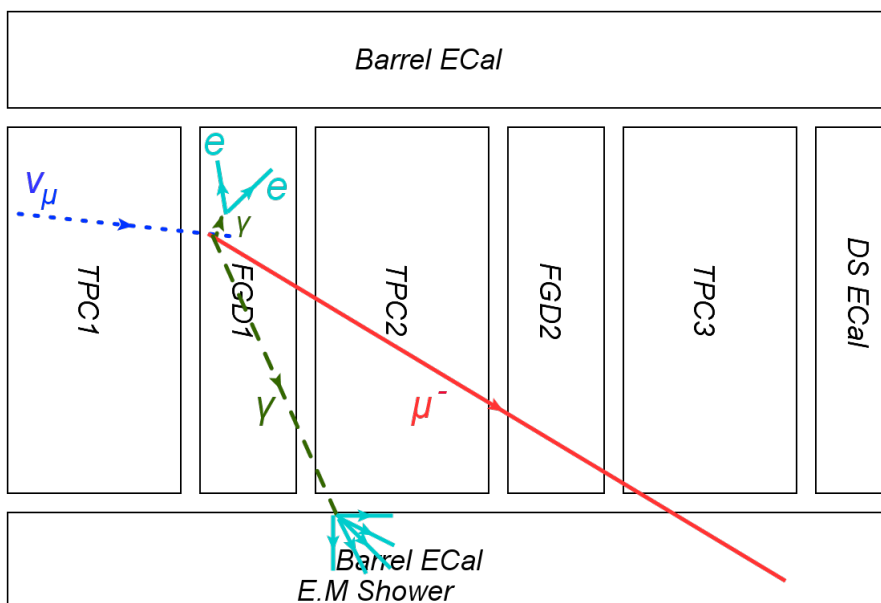


FIGURE A.2: In this instance the Tracker DPC has fully converted in FGD1 and the tracks produced by this photon are also entirely contained there. Although this is a pair, it may not result in building an ideal  $\pi^0$  candidate, due to the inferior reconstruction capabilities when compared with the TPC. For example, charge reconstruction is not reliable in the FGD.

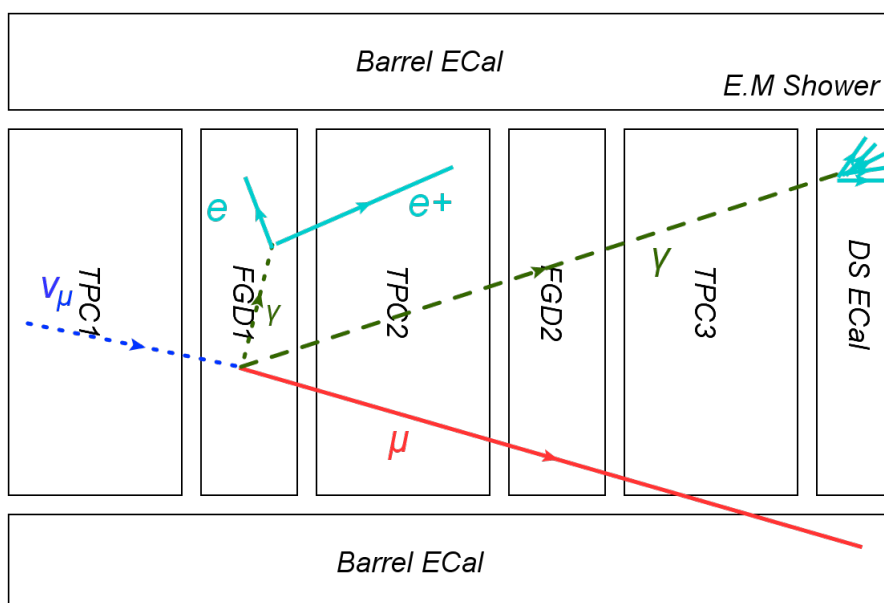


FIGURE A.3: In this instance the Tracker DPC photon has converted in FGD1 but one of the resultant tracks is fully contained within FGD1 and the other in TPC2. The underlying idea is that these are from the same pair and can be reconstructed as such. Additional complications do arise due to the dead space between the subdetectors, as well as the lack of reliable charge reconstruction in the FGD. An isolated track in the FGD (passing cuts) will be matched up with all available tracks in the TPC to form Tracker DPC Pair candidates.

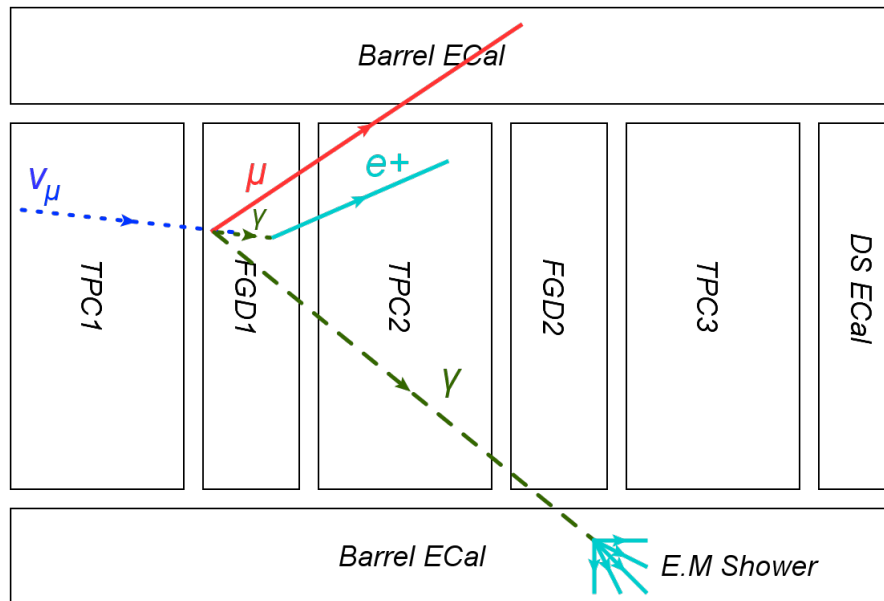


FIGURE A.4: In this instance the assumption is being made that the photon conversion has resulted in an asymmetric electron/positron pair, such that only one of the tracks is reconstructed (and the other missed due to a sufficient number of track segments in the FGD+TPC). The particular DPC built from this track will not be subject to a number of the cuts which can act only on pairs, meaning that it is likely to build a less reliable  $\pi^0$  object.

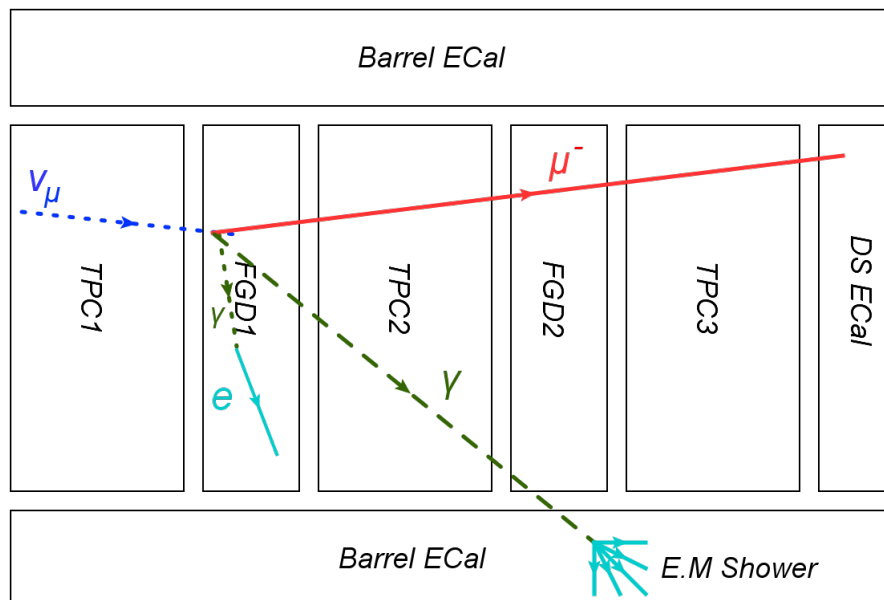


FIGURE A.5: In this instance the assumption is being made that the photon conversion has resulted in an asymmetric electron/positron pair, such that only one of the tracks is reconstructed (and the other missed due to a sufficient number of track hits in the FGD). This topology would likely not result in a good Tracker DPC and thus  $\pi^0$  object, due to the lack of a complementary pair track and inferior reconstruction.

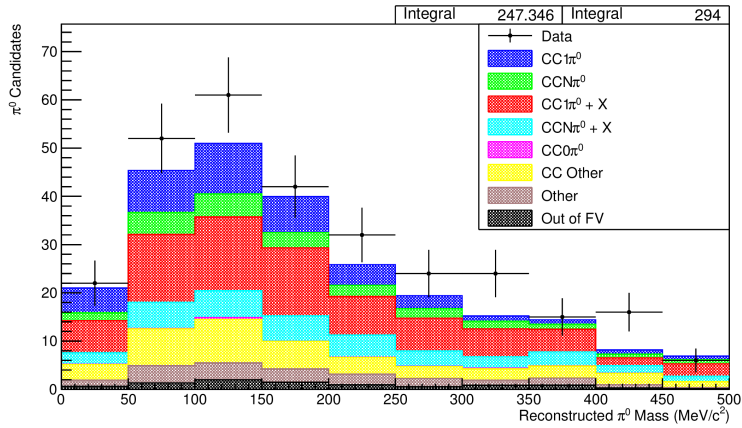


FIGURE A.6: Reconstructed invariant mass of highest momentum  $\pi^0$  candidates passing the selection.

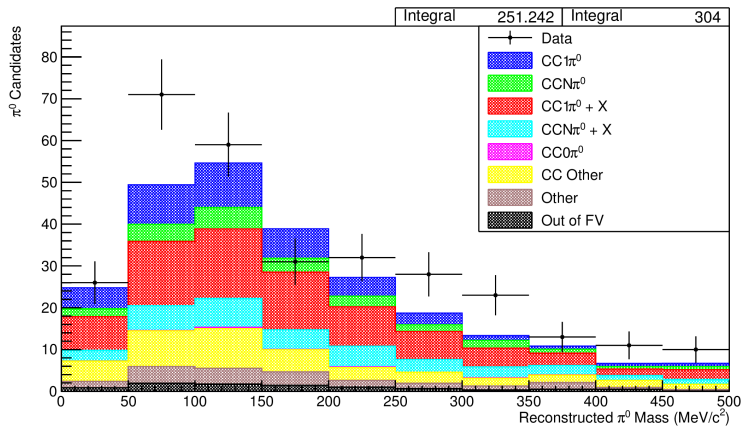


FIGURE A.7: Reconstructed invariant mass of randomly selected  $\pi^0$  candidates passing the selection.

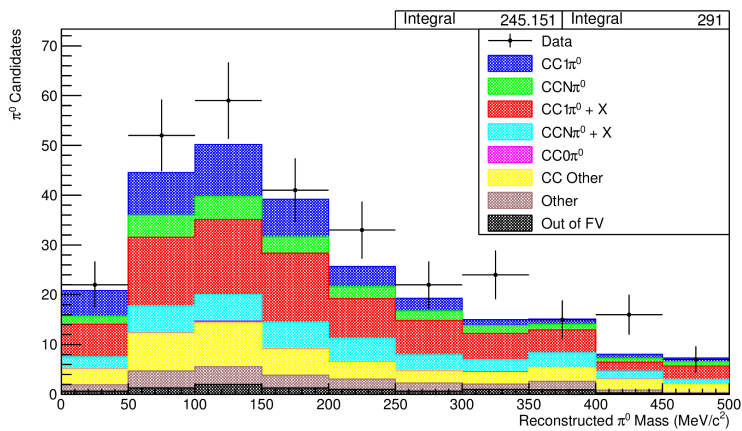


FIGURE A.8: Reconstructed invariant mass of  $\pi^0$  candidates passing the selection which are selected by the nMVA.

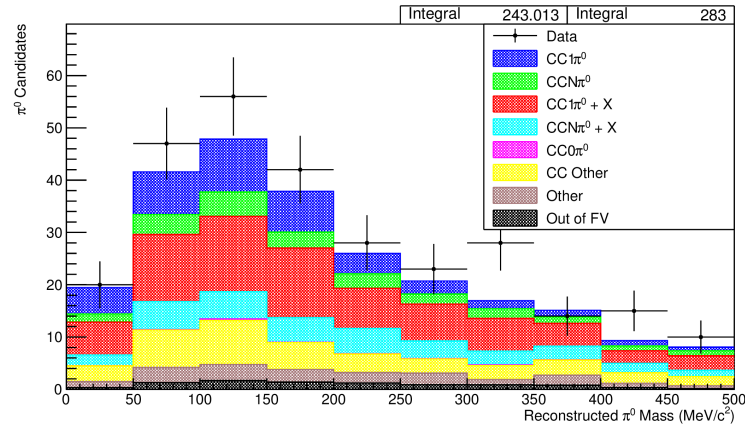


FIGURE A.9: Reconstructed invariant mass of  $\pi^0$  candidates passing the selection, whose ECal DPC has the highest energy.

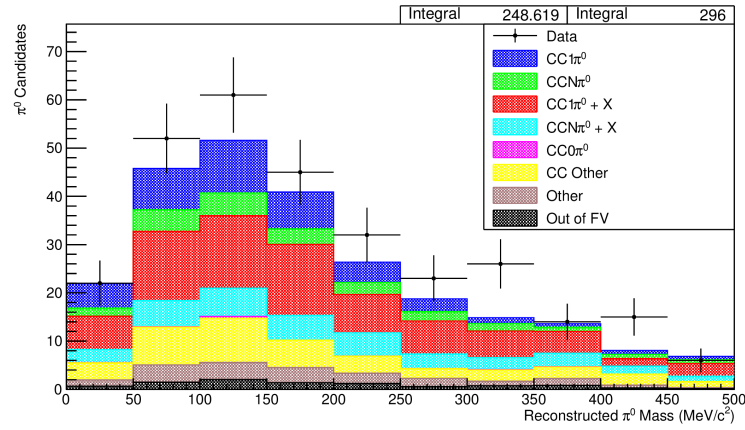


FIGURE A.10: Reconstructed invariant mass of  $\pi^0$  candidates passing the selection, whose Tracker DPC has the smallest TPC pair invariant mass.

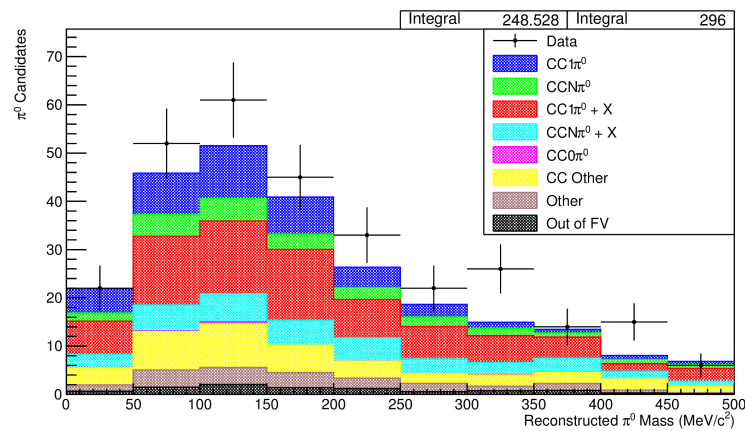


FIGURE A.11: Reconstructed invariant mass of  $\pi^0$  candidates passing the selection, whose Tracker DPC has the smallest TPC pair separation.

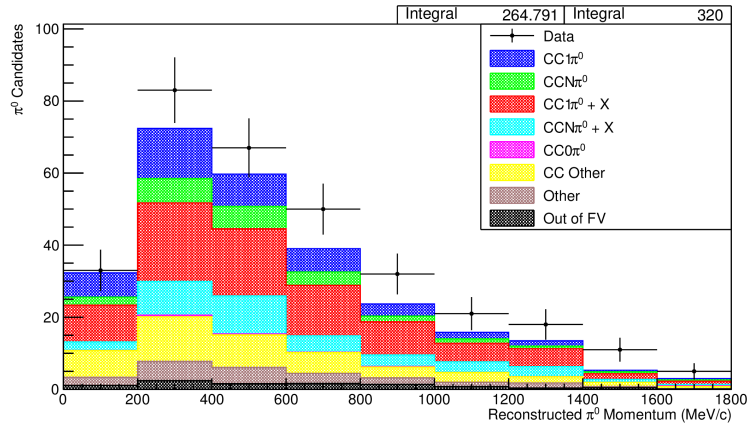


FIGURE A.12: Reconstructed momentum of highest momentum  $\pi^0$  candidates passing the selection.

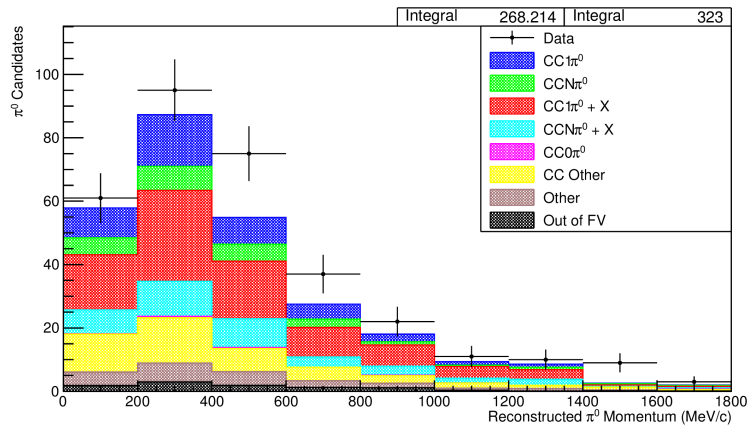


FIGURE A.13: Reconstructed momentum of randomly selected  $\pi^0$  candidates passing the selection.

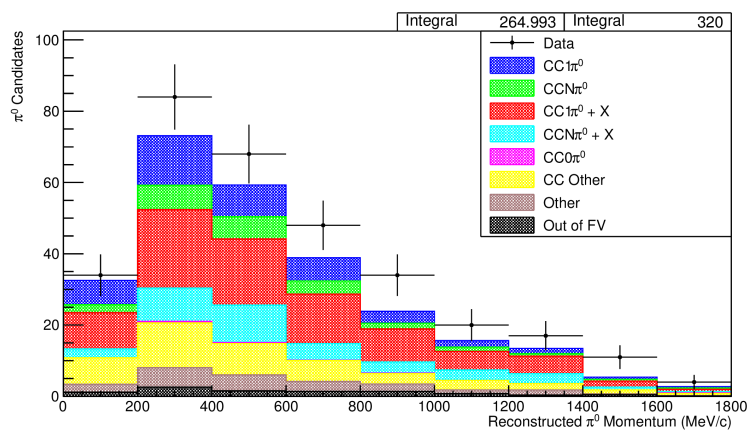


FIGURE A.14: Reconstructed momentum of  $\pi^0$  candidates passing the selection, which are selected by the nMVA.

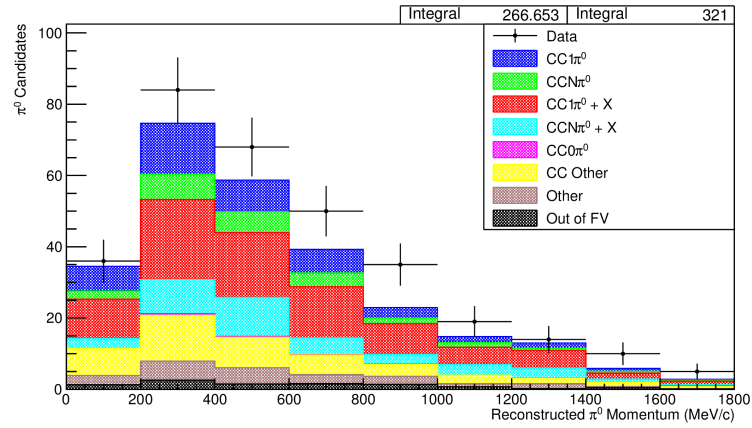


FIGURE A.15: Reconstructed momentum of  $\pi^0$  candidates passing the selection, whose ECal DPC has the highest energy.

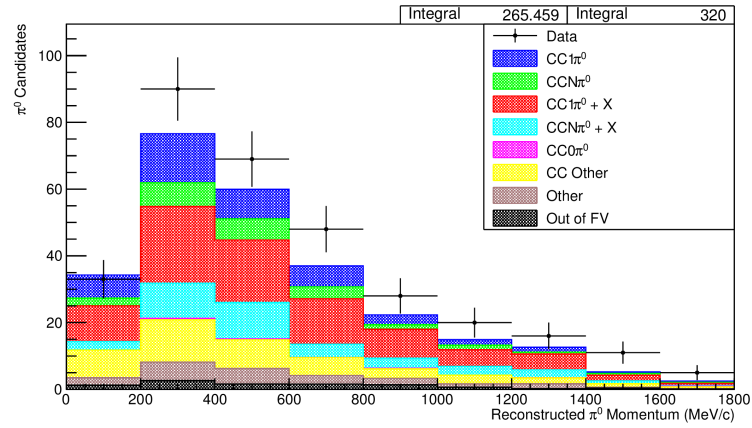


FIGURE A.16: Reconstructed momentum of  $\pi^0$  candidates passing the selection, whose Tracker DPC has the smallest TPC pair invariant mass.

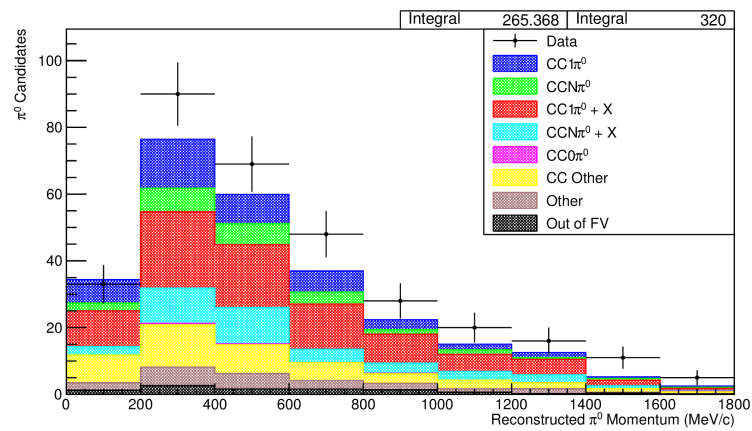


FIGURE A.17: Reconstructed momentum of  $\pi^0$  candidates passing the selection, whose Tracker DPC has the smallest TPC pair separation.

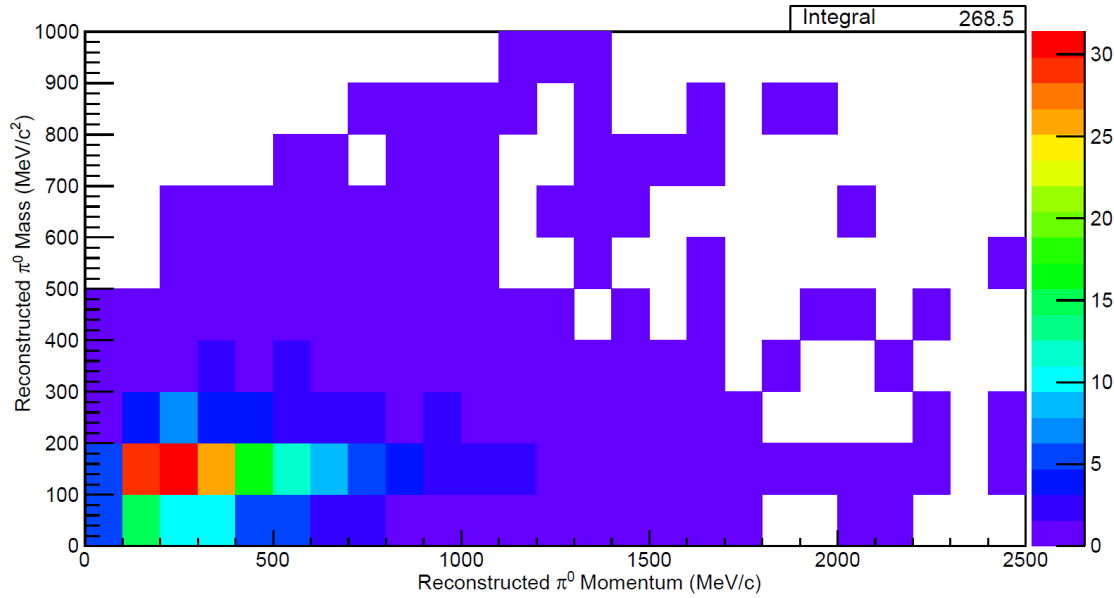


FIGURE A.18: Two dimensional distribution of the reconstructed invariant mass vs reconstructed momentum for selected  $\pi^0$  candidates passing the selection in the NEUT MC. There does not appear to be any obvious sources of discrepancy between the MC and data, although this would benefit from higher statistics.

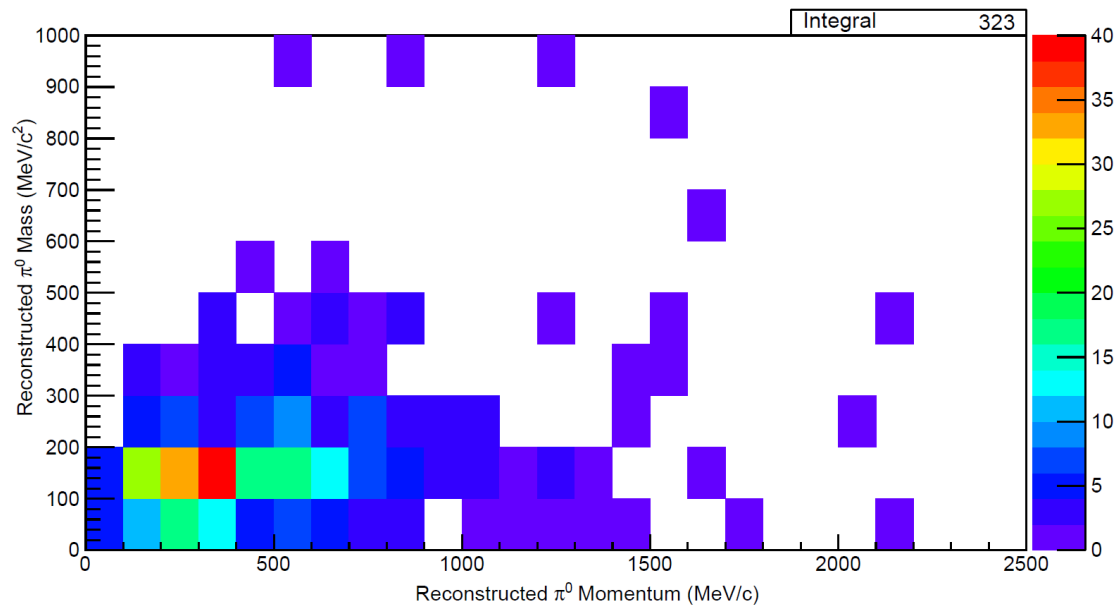


FIGURE A.19: Two dimensional distribution of the reconstructed invariant mass vs reconstructed momentum for selected  $\pi^0$  candidates passing the selection in the observed data. There does not appear to be any obvious sources of discrepancy between the MC and data, although this would benefit from higher statistics.

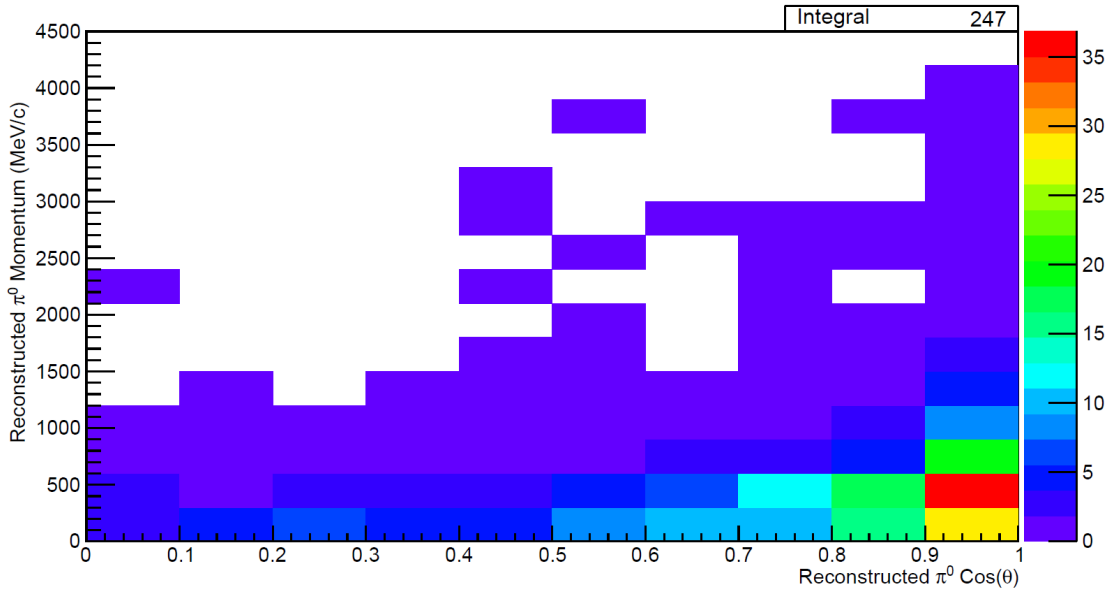


FIGURE A.20: Two dimensional distribution of the reconstructed momentum vs reconstructed  $\cos(\theta)$  (w.r.t to  $\mu^-$  direction) for selected  $\pi^0$  candidates passing the selection in the NEUT MC. There does not appear to be any significant sources of discrepancy between the MC and data, although this would benefit from higher statistics.

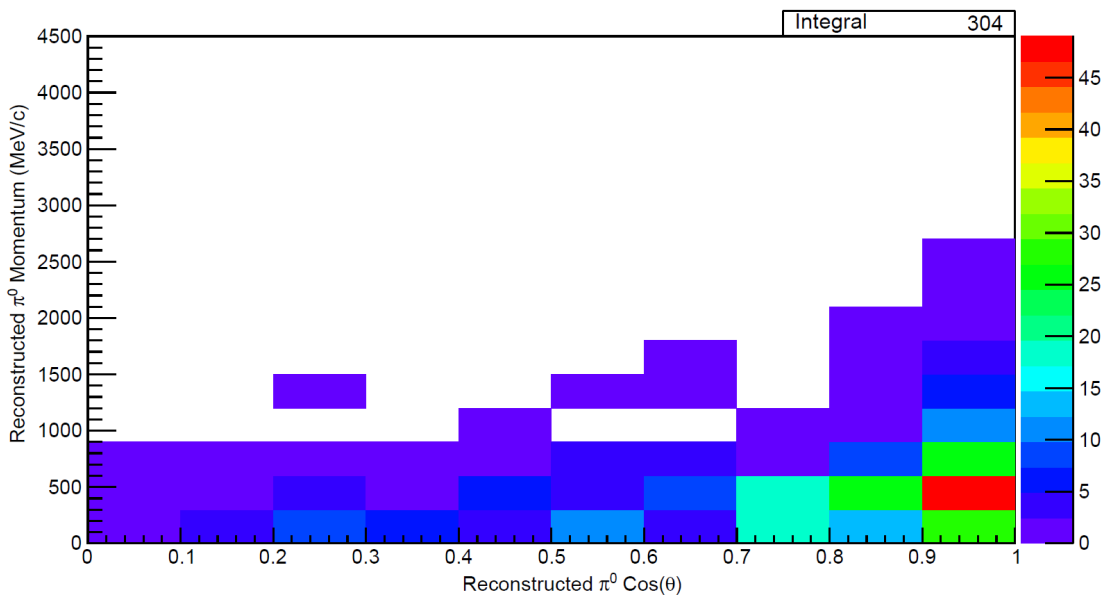


FIGURE A.21: Two dimensional distribution of the reconstructed momentum vs reconstructed  $\cos(\theta)$  (w.r.t to  $\mu^-$  direction) for selected  $\pi^0$  candidates passing the selection in the observed data. There does not appear to be any significant sources of discrepancy between the MC and data, although this would benefit from higher statistics.

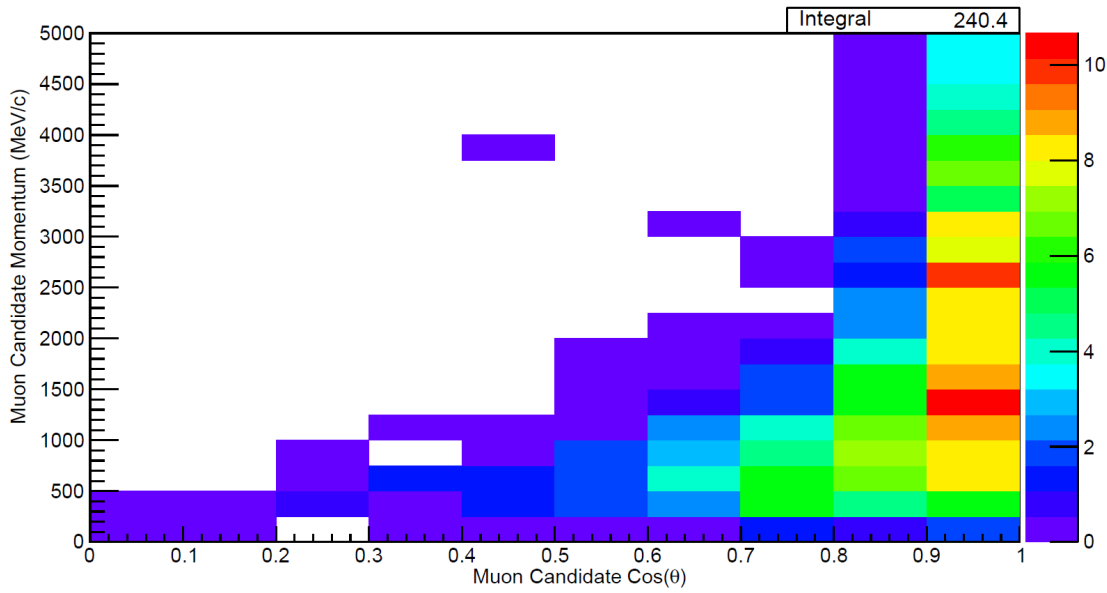


FIGURE A.22: Two dimensional distribution of the reconstructed momentum vs reconstructed  $\cos(\theta)$  (w.r.t to the assumed neutrino beam direction) for all  $\mu^-$  candidates passing the selection in the NEUT MC. There does not appear to be any significant sources of discrepancy between the MC and data, although this would benefit from higher statistics.

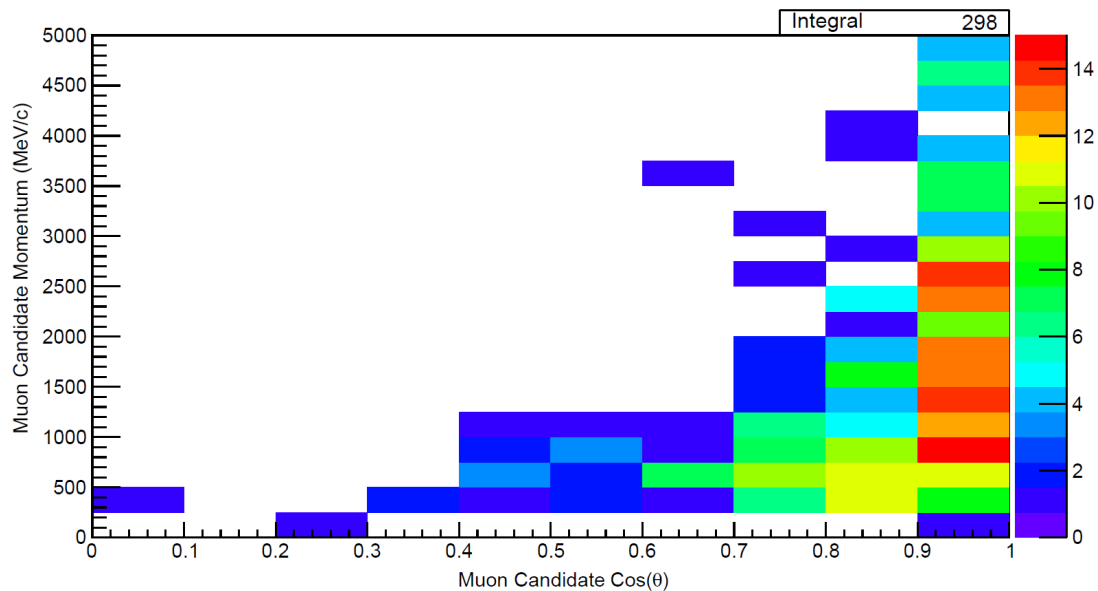


FIGURE A.23: Two dimensional distribution of the reconstructed momentum vs reconstructed  $\cos(\theta)$  (w.r.t to the assumed neutrino beam direction) for all  $\mu^-$  candidates passing the selection in the observed data. There does not appear to be any significant sources of discrepancy between the MC and data, although this would benefit from higher statistics.

RMM Number	TFB Number	Channel Number	Swapped with Channel
0	23	5	7
1	0	12	28
1	5	61	63
3	6	16	24
3	6	32	41
3	6	48	53
3	6	37	45
4	4	26	27
4	34	16	31
4	34	17	30
4	34	18	29
4	34	28	19
4	34	20	27
4	34	21	25
4	34	22	26
4	34	23	24
5	0	60	61
5	17	27	28
5	17	44	45
5	19	62	63
5	23	37	39
8	4	1	4
8	14	34	36
8	21	43	45
8	22	32	33
8	23	20	21
9	1	45	46
9	20	59	61
10	24	19	21
10	36	41	42

TABLE A.3: Mis-mappings found in the work described in Chapter 3.



# Bibliography

- [1] Q.R. Ahmad, et al., 'Direct evidence for neutrino flavor transformation from neutral-current interactions in the Sudbury Neutrino Observatory.' *Physical Review Letters* 89, 011301 (2002).
- [2] 'The Standard Model' [en.wikipedia.org/wiki/StandardModel](http://en.wikipedia.org/wiki/StandardModel)
- [3] Sutton, Christine. *Spaceship neutrino*. Cambridge University Press, 1992.
- [4] Frank Close, 'Neutrino' (2013) ISBN: 9780199695997
- [5] The T2K Experiment. 'A Brief History of Neutrinos'. <http://t2k-experiment.org/neutrinos/a-brief-history/>
- [6] Fermi, E. (1933). 'Tentativo di una teoria dei raggi  $\beta$ '. *La Ricerca Scientifica*
- [7] Pais, Abraham (1986). *Inward Bound*. Oxford: Oxford University Press. p. 418. ISBN 0-19-851997-4.
- [8] Wikipedia. 'The Quark'. <http://en.wikipedia.org/wiki/Quark-mediaviewer/File:Beta-Negative-Decay.svg>
- [9] The Reines-Cowan Experiments - Detecting the Poltergeist Los Alamos Science Number 25 1997 <http://library.lanl.gov/cgi-bin/getfile?00326606.pdf>
- [10] Reines, Frederick, and Clyde L. Cowan. 'The neutrino.' *Nature* 178, no. 4531 (1956): 446-449.
- [11] Leon Lederman, Melvin Schwartz and Jack Steinberger 'Observation of High-Energy Neutrino Reactions and the Existence of Two Kinds of Neutrinos' (1962) doi:10.1103/PhysRevLett.9.36
- [12] DONUT Collaboration 'Observation of Tau Neutrino Interactions' (2000) arXiv:hep-ex/0012035
- [13] Stephen Myers and Emilio Picasso 'The LEP Collider' *Scientific American* Vol. 263, No. 1 (JULY 1990), pp. 54-61
- [14] ALEPH, DELPHI, L3, OPAL, and SLD Collaborations, and LEP Electroweak Working Group, and SLD Electroweak Group, and SLD Heavy Flavour Group, *Phys. Reports* 427, 257 (2006).
- [15] L3: M. Acciarri et al., *Phys. Lett.* B431, 199 (1998); DELPHI: P. Abreu et al., *Z. Phys.* C74, 577 (1997); OPAL: R. Akers et al., *Z. Phys.* C65, 47 (1995); ALEPH: D. Buskulic et al., *Phys. Lett.* B313, 520 (1993)

- [16] Cyburt, Richard; et al. (2005). 'New BBN limits on physics beyond the standard model from He-4'. *Astropart. Phys.* 23 (3): 313-323. arXiv:astro-ph/0408033
- [17] Komatsu, Eiichiro; et al. (2010). 'Seven-Year Wilkinson Microwave Anisotropy Probe (WMAP) Observations: Cosmological Interpretation'. *The Astrophysical Journal Supplement Series* 192 (2): 18. arXiv:1001.4538
- [18] Planck Collaboration 'Planck 2015 results. XIII. Cosmological parameters' (2015) <https://arxiv.org/abs/1502.01589>
- [19] Davis Jr, Raymond, Don S. Harmer, and Kenneth C. Hoffman. 'Search for neutrinos from the sun.' *Physical Review Letters* 20, no. 21 (1968): 1205.
- [20] Wikipedia. 'Proton-proton chain reaction'. <http://en.wikipedia.org/wiki/Proton-protonchainreaction-mediaviewer/File:Proton-proton-cycle.svg>
- [21] 'Cryogenic particle detection - Solar neutrino problem' [www.kip.uni-heidelberg.de/tt-detektoren/neutrinos.php?lang=en](http://www.kip.uni-heidelberg.de/tt-detektoren/neutrinos.php?lang=en)
- [22] Pontecorvo, B., 1958. Inverse *beta* Processes and non-conservation of lepton charge. *Zhur. Eksptl'. i Teoret. Fiz.*, 34.
- [23] M. Kobayashi, T. Maskawa 'CP-Violation in the Renormalizable Theory of Weak Interaction' (1973), *Progress of Theoretical Physics.* 49 (652-657) doi:10.1143
- [24] La, HoSeong, and Thomas J. Weiler. 'Simple Mass Matrix Ansätze for Neutrino Mixing.' arXiv preprint arXiv:1311.1550 (2013).
- [25] Abe, K., N. Abgrall, H. Aihara, Y. Ajima, J. B. Albert, D. Allan, P-A. Amaudruz et al. 'The T2K experiment.' *Nuclear Instruments and Methods in Physics Research Section A: Accelerators, Spectrometers, Detectors and Associated Equipment* 659, no. 1 (2011): 106-135.
- [26] Buchmuller, Wilfried, Pasquale Di Bari, and Michael Plumacher. 'Cosmic microwave background, matter-antimatter asymmetry and neutrino masses.' *Nuclear Physics B* 643, no. 1 (2002): 367-390.
- [27] W. Buchmuller, R. D. Peccei, T. Yanagida 'Leptogenesis as the origin of matter' (2015) arXiv:hep-ph/0502169
- [28] 'T2K presents hint of CP violation by neutrinos' (04/08/2017) <http://t2k-experiment.org/2017/08/t2k-2017-cpv/>
- [29] 'Introduction to Neutrino Oscillations', University of Kyoto (2016)
- [30] Ratoff, P. 'Long Base-line Neutrino Experiments'. SUSY2014.
- [31] Fukuda, Y., T. Hayakawa, E. Ichihara, K. Inoue, K. Ishihara, H. Ishino, Y. Itow et al. 'Evidence for oscillation of atmospheric neutrinos.' *Physical Review Letters* 81, no. 8 (1998): 1562.

- [32] Ahmad, Q. R., R. C. Allen, T. C. Andersen, J. D. Anglin, J. C. Barton, E. W. Beier, M. Bercovitch et al. 'Direct evidence for neutrino flavor transformation from neutral-current interactions in the Sudbury Neutrino Observatory.' *Physical Review Letters* 89, no. 1 (2002): 011301.
- [33] Abe, K., J. Adam, H. Aihara, T. Akiri, C. Andreopoulos, S. Aoki, A. Ariga et al. 'Measurement of neutrino oscillation parameters from muon neutrino disappearance with an off-axis beam.' *Physical review letters* 111, no. 21 (2013): 211803.
- [34] Abe, K., J. Adam, H. Aihara, T. Akiri, C. Andreopoulos, S. Aoki, A. Ariga et al. 'Precise Measurement of the Neutrino Mixing Parameter  $\theta_{23}$  from Muon Neutrino Disappearance in an Off-Axis Beam.' *Physical review letters* 112, no. 18 (2014): 181801.
- [35] The T2K Experiment. <http://t2k-experiment.org/neutrinos/beyond-the-standard-model/>
- [36] Daya Bay Collaboration. 'Results from Daya Bay' (2014)
- [37] Particle Data Group 'Neutrino Mixing' (2016) [pdg.lbl.gov/2017/reviews/rpp2016-rev-neutrino-mixing.pdf](http://pdg.lbl.gov/2017/reviews/rpp2016-rev-neutrino-mixing.pdf)
- [38] Rosen, S., Peter, and James M. Gelb. 'Mikheyev-Smirnov-Wolfenstein enhancement of oscillations as a possible solution to the solar-neutrino problem.' *Physical Review D* 34, no. 4 (1986): 969.
- [39] Fritzsche, Harald, and Zhi-Zhong Xing. 'Lepton mass hierarchy and neutrino oscillations.' *Physics Letters B* 372, no. 3 (1996): 265-270.
- [40] Julien Lesgourgues, Sergio Pastor. ( 26 Dec 2012) 'Neutrino mass from Cosmology' arXiv:1212.6154
- [41] KATRIN Collaboration (A. Osipowicz et al.) 'KATRIN: A Next generation tritium beta decay experiment with sub-eV sensitivity for the electron neutrino mass.' (2001) arXiv:hep-ex/0109033
- [42] E. W. Otten, C. Weinheimer (Submitted on 11 Sep 2009) 'Neutrino mass limit from tritium beta decay' arXiv:0909.2104
- [43] 'The story of anti-matter' <https://timeline.web.cern.ch/timelines/The-story-of-antimatter>
- [44] S. Fukuda et al. (Super-Kamiokande Collaboration) 'Solar Boron 8 and hep Neutrino Measurements from 1258 Days of Super-Kamiokande Data' *Phys. Rev. Lett.* 86, 5651 (2001)
- [45] 'Carl Anderson' [www.aps.org/programs/outreach/history/historicsites/](http://www.aps.org/programs/outreach/history/historicsites/)
- [46] Ahrens, J., John N. Bahcall, X. Bai, R. C. Bay, T. Becka, K-H. Becker, D. Berley et al. 'Sensitivity of the IceCube detector to astrophysical sources of high energy muon neutrinos.' *Astroparticle Physics* 20, no. 5 (2004): 507-532.

- [47] Ananthaswamy, Anil. 'Ice-bound hunter sees first hint of cosmic neutrinos.' *New Scientist* 218, no. 2915 (2013): 15.
- [48] IceCube Collaboration 'Determining neutrino oscillation parameters from atmospheric muon neutrino disappearance with three years of IceCube DeepCore data' (2014) *Phys. Rev. D* 91, 072004 (2015)
- [49] Daya Bay Collaboration (2012). "Observation of electron-antineutrino disappearance at Daya Bay". *Physical Review Letters*. 108 (17): 171803. arXiv:1203.1669
- [50] Boger, J., R. L. Hahn, J. K. Rowley, A. L. Carter, B. Hollebone, D. Kessler, I. Blevins et al. 'The Sudbury neutrino observatory.' *Nuclear Instruments and Methods in Physics Research Section A: Accelerators, Spectrometers, Detectors and Associated Equipment* 449, no. 1 (2000): 172-207.
- [51] Kraus, Christine, and Simon JM Peeters. 'The rich neutrino programme of the SNO+ experiment.' *Progress in Particle and Nuclear Physics* 64, no. 2 (2010): 273-277.
- [52] Josh Klein 'Results and prospects with the Sudbury Neutrino Observatory' (2010)
- [53] Sudbury Neutrino Observatory Laboratory. 'The SNO Detector'. <https://www.snolab.ca/content/sno-detector>
- [54] Bilenky, S. M. 'Neutrinoless double beta-decay.' *Physics of Particles and Nuclei* 41, no. 5 (2010): 690-715.
- [55] Patterson, R. B. 'The NOvA experiment: status and outlook.' *Nuclear Physics B-Proceedings Supplements* 235 (2013): 151-157.
- [56] P. Adamson et al. (NOvA Collaboration) 'First measurement of muon-neutrino disappearance in NOvA' (2016) *Phys. Rev. D* 93, 051104
- [57] P. Adamson et al. (NOvA Collaboration) 'First Measurement of Electron Neutrino Appearance in NOvA' (2016) *Phys. Rev. Lett.* 116, 151806
- [58] 'DUNE - The Deep Underground Neutrino Experiment' <http://www.dunescience.org/>
- [59] 'The Hyper-Kamiokande Experiment' M.Hartz, NuFact (2016) [http://vietnam.in2p3.fr/2016/nufact/transparencies/5\\_friday/3\\_Hartz.pdf](http://vietnam.in2p3.fr/2016/nufact/transparencies/5_friday/3_Hartz.pdf)
- [60] Araki, T.; et al. (KamLAND Collaboration) (2005). 'Measurement of neutrino oscillation with KamLAND: evidence of spectral distortion'. *Physical Review Letters*. 94 (8): 081801-081806
- [61] 'The Borexino Experiment' <http://borex.lngs.infn.it/> (2008)
- [62] Abe, Y.; et al. (Double Chooz Collaboration) (2012). 'Reactor disappearance in the Double Chooz experiment'. *Physical Review D*. 86 (5): 052008. arXiv:1207.6632
- [63] Forero, D. V., M. Tortola, and J. W. F. Valle. 'Global status of neutrino oscillation parameters after Neutrino-2012.' *Physical Review D* 86, no. 7 (2012): 073012.

- [64] Abe, K., J. Adam, H. Aihara, T. Akiri, C. Andreopoulos, S. Aoki, A. Ariga et al. 'Observation of electron neutrino appearance in a muon neutrino beam.' *Physical review letters* 112, no. 6 (2014): 061802.
- [65] M. Batkiewicz 'Cross-section measurements of neutral pion production in neutrino-nucleus scattering in T2K' (2014) 11th International Workshop on Neutrino-Nucleus Scattering in the Few-GeV Region - NuInt 2017
- [66] D. Dewhurst 'Searches for sterile neutrinos using the T2K off-axis near detector.' (2015) arXiv:1504.08237
- [67] K. Abe et al, 'Proposal for an Extended Run of T2K to  $20 \times 10^{21}$  POT' (2016) <https://arxiv.org/abs/1609.04111>
- [68] Steve Boyd. 'Neutrino Oscillations : Theory and Present' - Warwick Week (2014)
- [69] Wikipedia. 'Pi Plus Decay'. <http://en.wikipedia.org/wiki/Pion>
- [70] K. Abe et al. 'The T2K Neutrino Flux Prediction' <https://arxiv.org/pdf/1211.0469.pdf>
- [71] Takatomi Yano. 'The Design of T2K Off-Axis Near Detector and The Basic Beam Property Measurements at T2K'. February 2012. <http://www.t2k.org/docs/talk/087/LLWI12Yano>
- [72] Tsuyoshi Nakaya and Robert K Plunkett 'Neutrino oscillations with the MINOS, MINOS+, T2K, and NO $\nu$ A experiments' (18 January 2016) *New J. Phys.* 18 (2016) 015009
- [73] Fukuda, S., Y. Fukuda, T. Hayakawa, E. Ichihara, M. Ishitsuka, Y. Itow, T. Kajita et al. 'The super-kamiokande detector.' *Nuclear Instruments and Methods in Physics Research Section A: Accelerators, Spectrometers, Detectors and Associated Equipment* 501, no. 2 (2003): 418-462.
- [74] Jelley, John Vernon. 'Cherenkov radiation and its applications.' (1958).
- [75] 'Events at Super-K' (2010) <http://www-sk.icrr.u-tokyo.ac.jp/sk/detector/display-e.html>
- [76] Super-Kamiokande Collaboration 'Evidence for the Appearance of Atmospheric Tau Neutrinos in Super-Kamiokande' *Phys. Rev. Lett.* 110, 181802 (2013)
- [77] <http://pdg.lbl.gov/2014/listings/rpp2014-list-pi-zero.pdf>
- [78] 'Searches for Nucleon Decay at Super-Kamiokande' <http://nngroup.physics.sunysb.edu/sk/physics/nucleon-decay/>
- [79] Wilking, M. 'A New Method for Event Reconstruction in Large Cherenkov Detectors' (2013)
- [80] Karlen, D. 'Near detectors for the T2K experiment.' *Nuclear Physics B- Proceedings Supplements* 159 (2006): 91-96.

- [81] Abe, K., N. Abgrall, Y. Ajima, H. Aihara, J. B. Albert, C. Andreopoulos, B. Andrieu et al. 'Measurements of the T2K neutrino beam properties using the IN-GRID on-axis near detector.' *Nuclear Instruments and Methods in Physics Research Section A: Accelerators, Spectrometers, Detectors and Associated Equipment* 694 (2012): 211-223.
- [82] Kudenko, Yury. 'The near neutrino detector for the T2K experiment.' *Nuclear Instruments and Methods in Physics Research Section A: Accelerators, Spectrometers, Detectors and Associated Equipment* 598, no. 1 (2009): 289-295.
- [83] Assylbekov, S., G. Barr, B. E. Berger, H. Berns, D. Beznosko, A. Bodek, R. Bradford et al. 'The T2K ND280 off-axis pi-zero detector.' *Nuclear Instruments and Methods in Physics Research Section A: Accelerators, Spectrometers, Detectors and Associated Equipment* 686 (2012): 48-63.
- [84] Abgrall, N., B. Andrieu, P. Baron, P. Bene, V. Berardi, J. Beucher, P. Birney et al. 'Time projection chambers for the T2K near detectors.' *Nuclear Instruments and Methods in Physics Research Section A: Accelerators, Spectrometers, Detectors and Associated Equipment* 637, no. 1 (2011): 25-46.
- [85] Amaudruz, P-A., M. Barbi, D. Bishop, N. Braam, D. G. Brook-Roberge, S. Giffin, S. Gomi et al. 'The T2K fine-grained detectors.' *Nuclear Instruments and Methods in Physics Research Section A: Accelerators, Spectrometers, Detectors and Associated Equipment* 696 (2012): 1-31.
- [86] Aoki, S., G. Barr, M. Batkiewicz, J. Blocki, J. D. Brinson, W. Coleman, A. Dabrowska et al. 'The T2K side muon range detector (SMRD).' *Nuclear Instruments and Methods in Physics Research Section A: Accelerators, Spectrometers, Detectors and Associated Equipment* 698 (2013): 135-146.
- [87] Allan, D., C. Andreopoulos, C. Angelsen, G. J. Barker, G. Barr, S. Bentham, I. Bertram et al. 'The electromagnetic calorimeter for the T2K near detector ND280.' *Journal of Instrumentation* 8, no. 10 (2013): P10019.
- [88] 'Hamamatsu PMT Modules' <https://www.hamamatsu.com/eu/en/3003.html>
- [89] Casper, D. 'The nuance Neutrino Simulation, and the Future' (2002) arXiv:hep-ph/0208030
- [90] J. A. Formaggio and G. P. Zeller, 'From eV to EeV: Neutrino cross sections across energy scales,' *Rev. Mod. Phys.*, vol. 84, pp. 1307-1341, Sep 2012.
- [91] A. A. Aguilar-Arevalo et al., 'Measurement of charged-current induced neutral pion production cross sections on mineral oil' *Phys. Rev. D*, vol. 83, p. 052009, Mar 2011.
- [92] J. Catala-Perez, 'Measurement of neutrino induced charged current neutral pion production cross section at SciBooNE', PhD thesis, Universitat de Valencia, 2014.
- [93] C. Mariani et al., 'Measurement of inclusive  $\pi^0$  production in the Charged-Current Interactions of Neutrinos in a 1.3-GeV wide band beam,' *Phys. Rev. D*, vol. 83, p. 054023, 2011.

- [94] Finch, A. 'T2K Software Explained' (Access available on request)
- [95] 'Midas Documentation' [midas.triumf.ca/MidasWiki/index.php/Midas\\_documentation](http://midas.triumf.ca/MidasWiki/index.php/Midas_documentation)
- [96] Sam Short 'Study of Neutrino-Induced Neutral Current Neutral Pion Production in the T2K Near Detector' (2013)
- [97] G. Battistoni et al. 'Overview of the FLUKA code', *Annals of Nuclear Energy* 82, 10-18 (2015)
- [98] *Nuclear Instruments and Methods in Physics Research A* 506 (2003) 250-303
- [99] H. Gallagher, Y. Hayato, 'Monte Carlo Neutrino Event Generators' <http://pdg.lbl.gov/2013/reviews/rpp2013-rev-mc-nu-event-gen.pdf> (2013)
- [100] Hayato, Yoshinari. (2009). A Neutrino Interaction Simulation Program Library NEUT. *Acta Physica Polonica B - ACTA PHYS POL B*. 40
- [101] Andreopoulos, C. 'The GENIE Neutrino Monte Carlo Generator PHYSICS USER MANUAL' (2015) <https://arxiv.org/pdf/1510.05494.pdf>
- [102] Zmuda, J. 'NuWro Monte Carlo generator of neutrino interactions - first electron scattering results' (2015) <https://arxiv.org/abs/1510.03268>
- [103] Abe, K., N. Abgrall, Y. Ajima, H. Aihara, J. B. Albert, C. Andreopoulos, B. Andrieu et al. 'Indication of electron neutrino appearance from an accelerator-produced off-axis muon neutrino beam.' *Physical Review Letters* 107, no. 4 (2011): 041801.
- [104] Abe, K., N. Abgrall, Y. Ajima, H. Aihara, J. B. Albert, C. Andreopoulos, B. Andrieu et al. 'First muon-neutrino disappearance study with an off-axis beam.' *Physical Review D* 85, no. 3 (2012): 031103.
- [105] Abe, K., N. Abgrall, H. Aihara, T. Akiri, J. B. Albert, C. Andreopoulos, S. Aoki et al. 'Evidence of electron neutrino appearance in a muon neutrino beam.' *Physical Review D* 88, no. 3 (2013): 032002.
- [106] Daya Bay Collaboration (2012). 'Observation of electron-antineutrino disappearance at Daya Bay'. *Physical Review Letters*. 108 (17) arXiv:1203.1669 doi:10.1103/PhysRevLett.108.171803
- [107] Abe, K., J. Adam, H. Aihara, T. Akiri, C. Andreopoulos, S. Aoki, A. Ariga et al. 'Measurement of neutrino oscillation parameters from muon neutrino disappearance with an off-axis beam.' *Physical review letters* 111, no. 21 (2013): 211803.
- [108] Abe, K., J. Adam, H. Aihara, T. Akiri, C. Andreopoulos, S. Aoki, A. Ariga et al. 'Measurement of the intrinsic electron neutrino component in the T2K neutrino beam with the ND280 detector.' *Physical Review D* 89, no. 9 (2014): 092003.
- [109] Abe, K., N. Abgrall, H. Aihara, T. Akiri, J. B. Albert, C. Andreopoulos, S. Aoki et al. 'Measurement of the inclusive  $\nu_\mu$  charged current cross section on carbon in the near detector of the T2K experiment.' *Physical Review D* 87, no. 9 (2013): 092003.

- [110] K. Abe, J. Adam, H. Aihara, T. Akiri, C. Andreopoulos, S. Aoki et al. 'Measurement of the Inclusive Electron Neutrino Charged Current Cross Section on Carbon with the T2K Near Detector' *Phys. Rev. Lett.* 113, 241803 (2014)
- [111] Chris Walter on behalf of the T2K Collaboration. 'Results from T2K.' *Neutrino 2014*. <https://indico.fnal.gov/getFile.py/access?contribId=268sessionId=18resId=0materialId=slidesconfId8022>
- [112] ECal Low Energy Task Force 'ECal Low Energy Photon Reconstruction' (2014)
- [113] Dolan, S. 'POD ECal Simple Track Fitter' (2015) [t2k.org](http://t2k.org) (access available on request)
- [114] T. Maryon 'Development of Particle Reconstruction in the T2K ND280 Electromagnetic Calorimeters and an early study into neutrino induced charged current single pion events' <http://www.t2k.org/docs/thesis/048/TomMaryonsThesis>
- [115] ROOT : An Analysis Framework. <http://root.cern.ch/drupal/>
- [116] L. Pickering 'An optional extension to the Simple Track Fitter' (2015)
- [117] D.Shaw, H.O'Keeffe, Re-mapping channels in the ND280 ECal, (T2K-TN-260) (2015) (Access available on request)
- [118] Wilkinson, C., Layer Efficiency - Investigating swaps on RMM3 TFB6 <http://www.t2k.org/nd280/ecal/Meetings/premeeting-2013-05-13/layerefficiency/view>
- [119] T2K Light Injection System <http://www.t2k.org/nd280/ecal/Meetings/premeeting-2012-04-20-talks/shefliupdatecollab/view>
- [120] Dr. Jon Perkin [www.t2kuk.org/wiki/LI:TheMovie](http://www.t2kuk.org/wiki/LI:TheMovie)
- [121] R. Bjorklund, W. E. Crandall, B. J. Moyer; H. F. York (1950). 'High Energy Photons from Proton-Nucleon Collisions'. *Physical Review*. 77 (2): 213–218. doi:10.1103/PhysRev.77.213.
- [122] 'Computing with HTCondor' <https://research.cs.wisc.edu/htcondor/>
- [123] Finch, A. 'ND280 Highland2 Documentation' (Access available on request)
- [124] T2K ND280 Charged-Current Inclusive Highland2 Analysis <https://repo.nd280.org/viewvc/ND280/highland2/numuCCAnalysis/> (Access available on request)
- [125] Claudio Giganti, Marco Zito 'Particle Identification with the T2K TPC' (2009) [https://www.t2k.org/docs/technotes/001/dEdxnote\\_v2](https://www.t2k.org/docs/technotes/001/dEdxnote_v2) (Access available on request)
- [126] M. Lawe 'Study of Charged Current Neutral Pion Production in the T2K Near Detector' (2014) <https://www.t2k.org/docs/thesis/051>

- [127] G. Barker et al 'Implementation of the Second Generation PID for the ND280 Tracker ECals' (2012) [https://www.t2k.org/docs/technotes/111/ecalPidTechNote\\_v1r0](https://www.t2k.org/docs/technotes/111/ecalPidTechNote_v1r0) (Access available on request)
- [128] R. P. Lichfield 'Neutrino induced events in the MINOS detectors' (2008) <http://minos-docdb.fnal.gov/cgi-bin/ShowDocument?docid=4646>
- [129] Pilar Coloma, Patrick Huber, Chun-Min Jen, Camillo Mariani 'Neutrino-nucleus interaction models and their impact on oscillation analyses' (2014) arXiv:1311.4506
- [130] Sheffield University Particle Physics Group 'Neutrino-Nucleus Interactions' [www.sheffield.ac.uk/physics/research/pppa/nugroup/t2k/](http://www.sheffield.ac.uk/physics/research/pppa/nugroup/t2k/)
- [131] Raul R. Prado, for the NA61/SHINE Collaboration 'Measurements of Hadron Production in Pion-Carbon Interactions with NA61/SHINE at the CERN SPS' (2017) arXiv:1707.07902
- [132] N. Abgrall et al., 'Pion emission from the T2K replica target: Method, results and application' Nuclear Instruments and Methods in Physics Research Section A: Accelerators, Spectrometers, Detectors and Associated Equipment, vol. 701, pp. 99-114, 2013.
- [133] K. Matsuoka 'Design and performance of the muon monitor for the T2K neutrino oscillation experiment' (2010) arXiv:1008.4077
- [134] MiniBooNE Collaboration 'The Neutrino Flux prediction at MiniBooNE' (2009) arXiv:0806.1449
- [135] MINERvA Collaboration 'Neutrino Flux Predictions for the NuMI Beam' (2016) arXiv:1607.00704
- [136] Elder Pinzon for DUET Collaboration 'Measurement of Charged Pion Absorption and Charge Exchange Cross Sections' (2013) [indico.ihep.ac.cn/event/2996/session/6/contribution/154/material/slides/0.pdf](http://indico.ihep.ac.cn/event/2996/session/6/contribution/154/material/slides/0.pdf)
- [137] A. Bercellie et al. 'Cross section parameters for 2014 oscillation analysis' (2014) <https://www.t2k.org/docs/technotes/192/version22>
- [138] O. Lalakulich, 'U. Mosel Pion production in the MiniBooNE experiment' (2013) arxiv.or:1210.4717
- [139] T. Le et al. 'Single neutral pion production by charged-current  $\nu_{\mu}$  interactions on hydrocarbon at  $E_{\nu} = 3.6$  GeV' (2015) arxiv:1503.02107
- [140] C. Mariani 'Measurement of inclusive  $\pi^0$  production in the Charged-Current Interactions of Neutrinos in a 1.3-GeV wide band beam' (2011) arxiv:1012.1794
- [141] M. Batkiewicz 'Production of  $\pi^0$  mesons in  $\nu_{\mu}$  CC interactions in the tracker part of the near detector of the T2K experiment' (2016) (Access available on request)

- 
- [142] Callum Wilkinson 'NEUT development for T2K and relevance of updated 2p2h models' (2015) arxiv:1505.07994
- [143] A. Aurisano, A. Radovic, D. Rocco, A. Himmel, M. D. Messier, E. Niner, G. Pawloski, F. Psihas, A. Sousa, P. Vahle 'A Convolutional Neural Network Neutrino Event Classifier' (2016) arXiv:1604.01444
- [144] Sergey Suvorov 'Anti-Nu CC Pi Zero Analysis Update' (2017) (Access Available On Request)
- [145] 'A short tutorial for using the xsTool' nd280.lancs.ac.uk/stable/invariant/xsTool/ (Access available on request)